UCGE Reports
Number 20144

Department of Geomatics Engineering

Reliable and Continuous Urban Navigation Using Multiple GPS Antennas and a Low Cost IMU

(URL: http://www.geomatics.ucalgary.ca/GradTheses.html)

by

Rakesh Ammunje Nayak

October 2000

THE UNIVERSITY OF CALGARY

Reliable and Continuous Urban Navigation Using Multiple GPS Antennas and a Low Cost IMU

by

Rakesh Ammunje Nayak

A THESIS

SUBMITTED TO THE FACULTY OF GRADUATE STUDIES

IN PARTIAL FULFILMENT OF THE REQUIREMENTS FOR THE

DEGREE OF MASTER OF SCIENCE

DEPARTMENT OF GEOMATICS ENGINEERING

CALGARY, ALBERTA

OCTOBER, 2000

© Rakesh A. Nayak 2000

ABSTRACT

The research presented in this thesis focuses on the feasibility of using multiple antennas to isolate and detect multipath on pseudoranges, and the impact of using multiple antennas along with some statistical reliability measure to detect blunders on pseudorange measurements, such that blunders can be rejected before they contaminate the estimated vehicle positions. The latter part of the thesis addresses the integration of differential GPS (DGPS) and a low cost IMU for reliable and effective navigation in an urban vehicular environment, which is motivated by the significant accuracy degradation that can exist due to satellite shading and multipath effects.

A series of tests were conducted in and around Calgary whereby the shading effects ranged from open sky to significant shading to about 30 degrees in elevation. Four NovAtel GPS receivers and antennas along with a low cost IMU were mounted on the roof of the vehicle. The effects of multipath, its temporal and spatial decorrelation properties among closely spaced antennas in various environmental conditions were studied. Statistical test were performed to detect multipath in the form of blunders. Constraints were also applied between antennas to make use of the inter antenna geometry. An improvement of 10%-40% in position accuracy and greater than 50% in reliability was achieved under different conditions

A three-axis micro-machined solid-state IMU from Systron Donner was then integrated with the system. The resulting integrated positions are computed and compared with a digital road map of Calgary and accuracy statistics are presented. Subsets of antennas (i.e. one, two and three antennas) are used with the IMU to determine the performance as a function of the number of GPS receivers utilized. In addition, the ability of the IMU to bridge GPS outages, poor geometry, and significant multipath is also assessed. The overall performance as a function of the shading environment (open sky versus urban) is computed and the effectiveness of the IMU to aid GPS is described. The test results show that the position accuracies vary significantly with the number of antennas used, the reliability test and also with inertial aiding. The augmentation of GPS with INS resulted

in an improved availability of position. Availability improvements of 10% were observed by limiting the prediction interval to 20 s and 100% availability is achievable, with reduced accuracy improvement resulting from the poor quality of sensors used.

ACKNOWLEDGEMENTS

I would like to express my heartfelt gratitude to my supervisor Dr Elizabeth Cannon, for her support, and guidance through out my M.Sc. program. I would also like to thank her for providing me the opportunity for me to come here and experience the pulse of GPS first hand. I am also thankful to DaimlerChrysler Research and Technology North America for funding most of this work, especially Mr. Christopher Wilson. I am extremely grateful to Prof. Oleg Salychev and Dr. Vladimir Voronov for their patience during the innumerable discussions we had on inertial navigation concepts and software. I am also grateful to all the staff and the course instructors for imparting quality education and make this a very memorable learning experience.

There are many among my friends who have been there whenever I need some help both technical and non-technical. These include, Jayanta Ray, Sam Ryan, Mark Petovello, Georgia Fotopoulos, Luiz Fortes, Luo Ning, and Huming Wu. I am extremely grateful to Kyle O′keefe, Ron Ramsaran, Naga Ravi, and Junjie Liu without whose help the field trials would not have been possible. Thanks guys. Accord Software and Systems Pvt Ltd, is also thanked for introducing me to the exciting field of GPS.

Finally I would like to thank my parents and my brother for their unconditional support and being with me and supporting me all through my life.

TABLE OF CONTENTS

APPROVAL PAGE ..... **ii**
ABSTRACT ..... **iii**
ACKNOWLEDGEMENTS ..... **v**
TABLE OF CONTENTS ..... **vi**
LIST OF TABLES ..... **ix**
LIST OF FIGURES ..... **x**
ACRONYMS ..... **xiii**
NOTATIONS ..... **xv**

Chapter 1 Introduction **1**
1.1 Background 1
1.2 Literature Review 2
1.3 Research Objectives 4
1.4 Thesis Outline 5

Chapter 2 Fundamentals of GPS and INS **7**
2.1 Introduction 7
2.2 Fundamentals of GPS 7
2.2.1 Space Segment 8
2.2.2 Control Segment 8
2.2.3 User Segment 9
2.2.4 GPS Signal Structure 9
2.2.5 Typical Receiver Architecture 11
2.3 GPS Observables and Error Sources 12
2.3.1 Orbital Errors 13
2.3.2 Clock Errors 13
2.3.3 Selective Availability 14
2.3.4 Ionospheric Error 14
2.3.5 Tropospheric Error 15
2.3.6 Multipath Errors 16
2.3.7 Receiver Noise 18
2.3.8 Error Summary 19
2.4 Fundamentals of INS 20
2.4.1 Mechanization and Error Models 22
2.5 Initialization 25
2.5.1 Calibration 25
2.5.2 Alignment 26

Chapter 3 System Realization and Inertial Sensors 30

3.1 Test Vehicle and GPS Receivers 30
3.2 Inertial Sensor 32
3.2.1 Accelerometer 32
3.2.2 Gyroscopes 34
3.2.3 MotionPak™ Characteristics 35
3.3 Inertial Augmentation Setup 36
3.4 Test Route Description 38
3.4.1 Section 1 [Open sky and suburban conditions] 38
3.4.2 Section 2 [Downtown section] 39
3.4.3 Section 3 [Foliage section] 40
3.4.4 Section 4 [open sky and suburban conditions] 41

Chapter 4 Code Multipath Characterization 43

4.1 Introduction 43
4.2 Code Multipath 43
4.3 Code Multipath Characterization 46
4.3.1 Multipath Correlation 50
4.3.2 Other Effects 51
4.4 Results 53
4.4.1 Tracking Performance in Section 1 [Open Sky] 53
4.4.2 Tracking Performance in Section 2 [Urban Canyon] 56
4.4.3 Tracking Performance in Section 3 [Dense Foliage] 59
4.4.4 Tracking Performance in Section 4 [Semi-urban conditions] 62
4.4.5 Code Multipath Error in Section 1 [Open sky] 63
4.4.6 Code Multipath Error in Section 2 [Urban environment] 67
4.4.7 Code Multipath Error in Section 3 [Dense Foliage environment] 70
4.4.8 Code Multipath Error in Section 4 [Semi-urban environment] 74
4.5 SNR Analysis 75
4.6 Summary 76

Chapter 5 Reliability and Constraints 78

5.1 Introduction 78
5.2 Reliability Theory 78
5.3 Constraints 82
5.4 Accuracy Assessment 84
5.5 Software Implementation 85
5.6 Scenarios 88
5.7 Results 89
5.7.1 Section 1 – Open Sky 89
5.7.2 Section 2 – Urban 94
5.7.3 Section 3 – Dense Foliage 99
5.7.4 Section 4 – Semi-urban 103
5.7.5 Statistics with limiting HDOP 106

5.8 Summary 109

Chapter 6 Inertial Aiding 111

6.1 Introduction 111
6.2 Linear Discrete Kalman Filter 111
6.3 Results 122
6.4 Summary 132

Chapter 7 Conclusions and Recommendations 134

7.1 Introduction 134
7.2 Conclusions 135
7.3 Recommendations 137

REFERENCES 140

APPENDIX A Derivation of the Design Matrix for Applying Constraints Between Antennas 150

APPENDIX B Rotation Matrices 152

B.1 Definitions 152
B.2 Direction Cosines 153
B.3 Simplified Alignment Equations 155

APPENDIX C Calibration 157

C.1 Sensor Biases 157

APPENDIX D Additional Results 161

LIST OF TABLES

Table 2.1: GPS Error sources (Lachapelle, 1998) 19
Table 3.1: MotionPak™ paprmeter specification (Systron Donner, 2000) 35
Table 3.2: Gyro Accuracies from Lab Test (Salychev et al., 2000b) 35
Table 4.1: Average satellite visibility and GDOP - Section 1 55
Table 4.2 : Average satellite visibility and GDOP - Section 2 57
Table 4.3: Average satellite visibility and GDOP - Section 3 60
Table 4.4: Average satellite visibility and GDOP - Section 4 62
Table 4.5 Statistics for code minus carrier differences - Section 1 65
Table 4.6: Statistics for the code minus carrier differences - Section 2 69
Table 4.7: Statistics for the code minus carrier differences - Section 3 72
Table 4.8: Statistics for the code minus carrier differences - Section 4 75
Table 5.1: Non-Centrality Parameter (Leick, 1995) 80
Table 5.2: Average RMS position errors for Section 2 under various scenarios 98
Table 6.1: Average RMS position errors for Day 3 under various scenarios 127
Table 6.2: GAIN1™ attitude error statistics for MotionPak™ (Salychev et al., 2000b) . 132
Table C.1: Gyro bias 158
Table C.2: Accelerometer bias 159
Table C.3: Accelerometer bias and scale factors 160

LIST OF FIGURES

Figure 2.1: GPS L1 signal phasor diagram (Spilker 1994d). 10
Figure 2.2: Typical GPS receiver architecture 11
Figure 2.3: Multipath environment 16
Figure 2.4: Multipath effect on the correlation triangle, (Lachapelle, 1998) 17
Figure 2.5: Principle of Inertial Navigation 20
Figure 2.6: Schuler oscillations 24
Figure 2.7: Body frame of reference 25
Figure 2.8: Principle of azimuth alignment 28
Figure 3.1: Antenna locations on vehicle roof 31
Figure 3.2: Vehicle setup 31
Figure 3.3: Systron Donner's MotionPak™ 32
Figure 3.4: Accelerometer-Theory of Operation, Wuntronic (2000) 33
Figure 3.5: Vibrating tuning fork block diagram (Geier , 1998) 34
Figure 3.6: INS/GPS experimental setup 36
Figure 3.7: Hardware connections 38
Figure 3.8: Section 1 route 39
Figure 3.9: Section 2 route 40
Figure 3.10: Section 3 route 41
Figure 3.11: Section 4 route 42
Figure 4.1: Code Multipath error envelope (Ford, 1998) 44
Figure 4.2: Code – Carrier difference, SV 31, (Elevation - 20°) 48
Figure 4.3: Code multipath error, SV 31, (Elevation - 20°) 49
Figure 4.4: Temporal decorrelation of static multipath error, SV 31 49
Figure 4.5: Satellite visibility for each antenna - Section 1 53
Figure 4.6: GDOP variation for each antenna - Section 1 54
Figure 4.7: Percentage visibility of satellites in Section 1 55
Figure 4.8: Satellite visibility for each antenna - Section 2 56
Figure 4.9: GDOP variation for each antenna - Section 2 57
Figure 4.10: Percentage visibility of satellites - Section 2 58
Figure 4.11: Satellite visibility for each antenna - Section 3 59
Figure 4.12: GDOP variation for each antenna - Section 3 60
Figure 4.13: Percentage visibility of satellites - Section 3 61
Figure 4.14: Percentage visibility of satellites - Section 4 62
Figure 4.15: Code-carrier differences (SV – 17), Elevation (68° - 33°) – Section 1 63
Figure 4.16: Code-carrier differences (SV - 26), Elevation (31° - 14°) - Section 1 64
Figure 4.17: Correlation coefficient (SV - 17), Elevation (68° - 33°) – Section 1 66
Figure 4.18: Temporal correlation (SV - 17), Elevation (68° - 33°) – Section 1 67
Figure 4.19: Code-carrier differences (SV - 17), Elevation (68° - 33°) – Section 2 68
Figure 4.20: Code-carrier differences (SV - 26), Elevation (31° - 14°) – Section 2 68
Figure 4.21: Correlation coefficient (SV - 17), Elevation (68° - 33°) – Section 2 70
Figure 4.22: Code-carrier differences (SV - 17), Elevation (68° - 33°) – Section 3 71
Figure 4.23: Code-carrier differences (SV - 26), Elevation (31° - 14°) – Section 3 71
Figure 4.24: Correlation coefficient (SV – 17), Elevation (68° - 33°) – Section 3 73

Figure 4.25: Correlation coefficient (SV - 26), Elevation (31° - 14°) – Section 3 74
Figure 4.26: SNR for SV – 17, Elevation (68° - 33°) – Section 3 76
Figure 5.1: Type I and Type II errors with non-centrality parameter 80
Figure 5.2: Constraints between antennas 83
Figure 5.3: Piece-wise linearized segment of the road 84
Figure 5.4: Flow chart of the statistical test 87
Figure 5.5: Section 1, GPS and map trajectory 89
Figure 5.6: Absolute error between the GPS and true trajectories – Section 1 90
Figure 5.7: Average RMS agreement between DGPS and map coordinates for various scenarios, Section 1, Day 1 91
Figure 5.8: Average RMS agreement between DGPS and map coordinates for various scenarios, Section 1, Day 2 91
Figure 5.9: External reliability RMS errors for various scenarios, Section 1, Day 1 93
Figure 5.10: External reliability RMS errors for various scenarios, Section 1, Day 2 93
Figure 5.11: Comparison of GPS and digital map coordinates - Section 2 94
Figure 5.12: Absolute error between the GPS and true map trajectory – Section 2 95
Figure 5.13: Average RMS agreement between DGPS and map coordinates for various scenarios, Section 2, Day 1 96
Figure 5.14: Average RMS agreement between DGPS and map coordinates for various scenarios, Section 2, Day 2 96
Figure 5.15: External reliability RMS errors for various scenarios, Section 2, Day 1 97
Figure 5.16: External reliability RMS errors for various scenarios, Section 2, Day 2 97
Figure 5.17: Comparison of GPS and digital map coordinates - Section 3 99
Figure 5.18: Absolute error between the GPS and true map trajectory – Section 3 100
Figure 5.19: Average RMS agreement between DGPS and map coordinates for various scenarios, Section 3, Day 1 101
Figure 5.20: Average RMS agreement between DGPS and map coordinates for various scenarios, Section 3, Day 2 101
Figure 5.21: External reliability RMS errors for various scenarios, Section 3, Day 1 ... 102
Figure 5.22: External reliability RMS errors for various scenarios, Section 3, Day 2 ... 102
Figure 5.23: Comparison of GPS and digital map coordinates - Section 4 103
Figure 5.24: Absolute error between the GPS and true map trajectory – Section 4 104
Figure 5.25: Average RMS agreement between DGPS and map coordinates for various scenarios, Section 4, Day 1 105
Figure 5.26: Average RMS agreement between DGPS and map coordinates for various scenarios, Section 4, Day 2 105
Figure 5.27: Average RMS agreement between DGPS and map coordinates for various scenarios, Section 2, Day 1 106
Figure 5.28: Average RMS agreement between DGPS and map coordinates for various scenarios, Section 3, Day 1 107
Figure 5.29: External reliability RMS errors for various scenarios, Section 2, Day 1 ... 108
Figure 5.30: External reliability RMS errors for various scenarios, Section 3, Day 1 ... 108
Figure 6.1: Kalman filter algorithm 113
Figure 6.2: Feed forward scheme (Open loop) 114
Figure 6.3: Feed back scheme (Closed loop) 115
Figure 6.4: Software algorithm of GAIN1™ (Salychev et al., 2000a) 117

Figure 6.5: GPS/INS integration scheme used in MATNAV (Nayak et al., 2000b) 120
Figure 6.6: Trajectory of Antenna A 122
Figure 6.7: Percentage visibility 123
Figure 6.8: Average RMS agreement between DGPS and map coordinates for various scenarios 124
Figure 6.9: External reliability RMS errors for various scenarios, Day 3 125
Figure 6.10: Integrated DGPS/INS trajectory of Antenna A, prediction limit of 20 s 126
Figure 6.11: Integrated INS/GPS trajectory, without any prediction limit 128
Figure 6.12: Trajectory with a simulated GPS outage of 20s (high dynamics) 129
Figure 6.13: Difference between integrated position and digital map trajectory 130
Figure 6.14: Trajectory with a simulated GPS outage of 20s (benign dynamics) 131
Figure 6.15: Difference between integrated position and digital map trajectory 131
Figure B.1: Attitude parameters 152
Figure B.2: Definition of heading angle (Salychev, 1998) 153
Figure B.3: Sequence of Rotations from Body frame to Local level frame 154
Figure C.1: Gyroscope biases 157
Figure C.2: Autocorrelation of the X-axis gyro measurements 158
Figure C.3: Accelerometer measurements 159
Figure 7.1: Autocorrelation of X-axis accelerometer 160
Figure D.1: Code minus carrier differences (SV – 23),Elevation (88° - 64°)–Section 1 161
Figure D.2: Code minus carrier differences (SV – 23),Elevation (88° - 64°)–Section 2 162
Figure D.3: Code minus carrier differences (SV – 23),Elevation (88° - 64°)–Section 3 162
Figure D.4: Code minus carrier differences (SV – 23),Elevation (88° - 64°)–Section 4 163
Figure D.5: Code minus carrier differences (SV – 3),Elevation (46° - 41°)–Section 1 .. 163
Figure D.6: Code minus carrier differences (SV – 3),Elevation (46° - 41°)–Section 2 .. 164
Figure D.7: Code minus carrier differences (SV – 3),Elevation (46° - 41°)–Section 3 .. 164
FigureD.8: Correlation coefficient (SV – 23), Elevation (88° - 64°) - Section 1 165
Figure D.9: Correlation coefficient (SV – 23), Elevation (88° - 64° - Section 2 165
Figure D.10: Correlation coefficient (SV – 23), Elevation (88° - 64°) - Section 3 166
Figure D.11: Correlation coefficient (SV – 3), Elevation (46° - 41°) - Section 1 166
Figure D.12: Correlation coefficient (SV – 3), Elevation (46° - 41°) - Section 2 167

ACRONYMS

ADC	Analog to Digital Conversion
C/A code	Coarse Acquisition code
C^3NAV	Combined Code and Carrier for GPS NAVigation
DoD	Department of Defence
DC	Direct Current
DGPS	Differential Global Positioning System
DLL	Delay Lock Loop
DOP	Dilution of Precision
GA	Ground Antenna
GAIN	GNSS Aided Inertial Navigation
GDOP	Geometric Dilution of Precision
GPS	Global Positioning System
IF	Intermediate Frequency
IMU	Inertial Measurement Unit
INS	Inertial Navigation System
I/O	Input Output
JPO	Joint Program Office
LORAN	LOng range RAdio Navigation
MATNAV	Multi AnTenna NAVigation
MCS	Master Control Station
MBPS	Mega Bits Per Second
MEDLL	Multipath Estimation Delay Lock Loop
MEMS	Micro Electro Mechanical Systems
MET	Multipath Elimination Technique
MDB	Minimum Detectable Blunder
NCNR	No Constraints No Reliability
NCWR	No Constraints With Reliability
NCO	Numerically Controlled Oscillators
OCS	Operational Control Segment

P code	Precise code
PRN	Pseudo Random Number
RADAR	RAdio Dectection And Ranging
RF	Radio Frequency
SA	Selective Availability
UTM	Universal Transverse Mercator
uv	Ultra Violet radiation
VOR	vhf omnidirectional radio
WCWR	With Constraints With Reliabiltiy
WCNR	With Constraints No Reliability

NOTATIONS

A	Design Martix
B_E	East Accelerometer bias
B_N	North Accelerometer bias
C()	GPS C/A or P code
C_l^{-1}	Covariance matrix of the observations
$\hat{C}_r$	Covariance matrix of the residuals
C_x	Covariance matrix of the parameters
dt	Satellite clock error, nominal
dT	Receiver clock error
D	Navigation Data bits
e	Earth fixed frame
f_{BL}	Base line between two antennas
g	Gravitational acceleration
g_i	Redundancy matrix
H	Design Matrix
H_1	Alternate Hypothesis
H_0	Null Hypothesis
l	Local level frame
N	Integer cycle ambiguity
P	Error covariance matrix of the state vector
Q	Process noise Covariance
R	Measurement covariance
$\hat{r}$	Residuals
T_c	Chip width
X	State Vector
XG	C/A code
X/P	P code

w	wander frame
R_b^l	Rotation matrix
λ	Carrier wavelength
Φ	Carrier phase
ρ	Geometric range between the satellite and the receiver antenna
$d\rho$	Orbital error
d_{ion}	Ionospheric delay
d_{tropo}	Tropospheric delay
ε_p	Code measurement noise
ε_φ	Carrier phase measurement noise
ϕ_k	State transition matrix
W_k	White noise forcing function
V_k	Measurement model noise
$\delta\dot{V}_E^{sh}$	East velocity error component
$\delta\dot{V}_N^{sh}$	North velocity error component
$\dot{\Phi}_E^{sh}$	East misalignment error angle
$\dot{\Phi}_N^{sh}$	North misalignment error angle

Chapter 1

Introduction

1.1 Background

The Global Positioning System (GPS) has been proven to be an accurate positioning sensor for a variety of applications (Daljit and Grewal, 1995) and has made land navigation applications affordable and dependable. The use of GPS for automotive applications has been pursued intensively by French (1995), Geier (1998) to name a few. Over the years, the increasingly falling costs of GPS receivers has rendered the system attractive to automotive applications, where cost is a major factor. Continuous and reliable positioning are two of the important requirements of the automotive sector. One of the major hurdles for reliable navigation in urban and dense foliage environment is multipath. There are many situations where a GPS solution is either unavailable or unreliable. The first case occurs when GPS signals do not reach the antenna due to shading effects resulting for example, from high-rise buildings and underpasses present in an urban environment. The second situation arises from poor satellite geometry and the multiple reflection of signals. Although errors due to the ionosphere, troposphere, multipath and receiver noise limit the achievable accuracy (Parkinson, 1994b), the use of the differential GPS (DGPS) technique improves both accuracy and integrity although it does not reduce multipath (Parkinson and Enge, 1995).

Code multipath is typically the most significant error source for differential vehicular navigation applications, especially in urban and semi-urban areas with buildings and trees. The behaviour of code multipath in dynamic scenarios is very different from the static case. Cannon and Lachapelle (1992) conducted a detailed analysis of multipath in high performance receivers for kinematic applications. In this case, the position of various multipath sources change rapidly and therefore the composite multipath signal is difficult to model. One of the properties of multipath is that it decorrelates rapidly as a

function of distance between the reflecting surface and the receiving antenna. Therefore, two antennas spaced at least 0.5 m apart, may be subjected to different multipath conditions even in a dynamic environment.

Parkinson and Axelrad (1988) demonstrated the concept of using reliability theory to detect gross blunders in GPS pseudorange measurements. Ryan et al., (1999) used a similar approach to detect multipath in a marine environment. Also, from classical least-squares adjustment theory (Leick, 1995), better performance can be achieved by applying constraints. These factors strongly suggest that systems using such concepts can yield better position reliably.

The use of additional sensors for augmenting GPS has been pursued extensively in the past. However, the automobile and land applications market has been constrained by the cost factor, and this has prevented the use of high quality inertial devices in these applications. The new technological advancement in the last few years has resulted in low cost inertial sensors with reduced performance accuracies, which cannot be used as stand alone navigation systems, but when integrated with other systems like GPS, can provide acceptable performance.

The intent of this thesis is to address both the multipath and availability issues through use of multiple GPS antennas as well as through integration with an IMU. The goal is to provide reliable navigation and a measure of the reliability, as well as to increase the availability of the position solution.

1.2 Literature Review

GPS error sources and their characteristics have been analysed in detail by Parkinson (1994b) and Lachapelle (1990). Multipath error is a major error source for DGPS applications (Parkinson and Enge, 1995). It is generally caused by the reflection or defraction of the direct satellite signal from a near-by object. A comprehensive investigation of multipath effects was done by van Nee (1995) and Braasch (1994). Several receiver based multipath mitigation techniques have been developed such as the

Narrow Correlator™ (Fenton et al., 1991; van Dierendonck et al., 1992) which has 0.1 chip spacing and a larger bandwidth at the IF and provides good long delay multipath mitigation. Similar technologies like MEDLL™ (Multipath Estimation Delay Lock Loop, Van Nee, 1995), Edge Correlator™ (Garin et al., 1996), and Strobe Correlator™ (Garin and Rousseau, 1997) use the correlator based approach to mitigate mulitpath. However, code multipath errors can be as large as several tens of metres even with currently available state-of-the-art receiver technologies, and cannot be removed through differential positioning due to its highly localized nature (Braasch, 1994). Ray (2000) has demonstrated the concept of using multiple closely spaced antennas to identify and mitigate code and carrier phase multipath.

Various dead reckoning sensors such as odometers, rate gyros, inclinometers and electronic compasses have very good short-term accuracy; but their errors grow with time (Geier, 1998). In addition, their error behaviour depends on vibration, temperature and acceleration. On the other hand, GPS has a very good long-term accuracy and moderate short-term accuracy. Therefore, these two types of systems are complementary in nature and may be integrated to provide accurate positioning.

The use of dead reckoning sensors to augment GPS for various applications has been studied by Harris (1989), Bullock (1995), Ren and Dedes (1995), Geier (1998), and Weisenburger and Wilson (1999). Krakiwsky et al., (1988) discussed a Kalman filter strategy to integrate dead reckoning, map matching and GPS positioning. Harris (1989) built a prototype for a automatic vehicle location and navigation systems in which kinematic positioning was integrated with GPS and dead reckoning sensors such as a differential odometer and map matching. Bullock (1995) developed a prototype portable vehicle navigation system (PortNav) based on a notebook computer, a PCMCIA-type GPS receiver, and a digital road map.

An IMU (Inertial Measurement Unit) is a measurement system designed to measure specific force and angular rates with respect to the inertial frame in dynamic environments, which when integrated, provide position and attitude. This is a self-

contained system, and when augmented with GPS can provide better availability and integrity of position. Since cost is an important factor in automobile navigation, a low cost IMU in the range of $4000 – $8000 will be considered. This will be used as a prototype system as it is expected that the costs will continue to decrease in the future. The IMU chosen for this research is a three-axis measurement unit called MotionPak™ (Systron Donner, 2000). Zhang (1995) demonstrate the feasibility and effectiveness of using MotionPak™ with GPS. The accelerometers and the gyroscopes are micro-machined solid-state devices, which can measure acceleration and angular rate with a resolution of <10μG and 0.004˚/sec respectively. The bias stability of the accelerometer and gyro for the complete operating range is <1000μG and <2˚/sec respectively (Systron Donner, 2000). Simulation studies conducted by Randle and Horton (1997) indicate the feasibility of using low cost inertial devices for vehicle navigation.

Reliability measures such as blunder detection will be developed as part of the research to identify multipath. Reliability issues for navigation have been addressed by Krakiwsky (1990) and Abousalem (1993). Abousalem (1993) discussed an algorithm to integrate different sensors for a vehicle location system. He compared two filtering approaches, namely, centralized Kalman filter and federated Kalman filter and also discussed quality control issues. The reliability of navigation for automobile applications using external sensors such as a rate gyro and a digital road map was investigated by Sun and Cannon (1997). Ryan et al., (1999) discussed the effect of multipath on various marine receivers and discussed a blunder detection test to identify the measurements containing multipath in a marine environment. Weisenburger, (1997), showed the benefits of using various kinds of constraints with multiple receivers for on-the-fly ambiguity resolution. The above-mentioned approaches such as reliability and constraints have been used collectively to detect blunders in the form of multipath in the current research.

1.3 Research Objectives

The proposed research is aimed at providing reliable positioning in urban areas with good availability and accuracy. The objectives of the proposed research are as follows:

- Analyze the characteristics of code multipath on a moving platform under various environmental conditions such as open sky, urban, semi-urban and under heavy foliage.
- Investigate the impact of multiple GPS antennas for multipath detection and mitigation along with reliability assessment. The accuracy of GPS for vehicular positioning under urban and suburban conditions is affected largely by multipath. One of the properties of multipath is that it decorrelates rapidly as a function of distance. Therefore, two antennas spaced at least 0.5 m apart, may be subjected to different multipath conditions such that through comparative techniques the detection capability may be improved.
- Investigate the benefits of using statistical reliability tests in different environments.
- Use a low cost three-axis IMU to augment GPS and keep the cost of the overall system low. The need to use an IMU arises due to the fact that GPS is a line of sight radio navigation system and this limits its use as a navigation sensor in urban areas with the presence of high–rise buildings.
- Investigate the feasibility of multipath detection and mitigation using IMU measurements and improve the reliability and integrity of the system.

The accuracy goal of the integrated system is to achieve 100% position availability with an accuracy of 5 m (2σ) during GPS availability and 15 m (2σ) during GPS outage to 20 seconds. These goals are set on preliminary simulation results conducted by Randle and Horton (1997). The improved availability and accuracy of position along with the industry's demand for low cost solutions justify the need for a low cost IMU.

1.4 Thesis Outline

Chapter 2 gives an overview of the Global Positioning System, including various error sources that affect GPS signals. This chapter also gives a brief introduction into inertial navigation systems (INS).

Chapter 3 contains a complete description of the test setup and a description of the environment in which various tests were conducted. It also briefly describes the basic principle of micro-machined gyro and accelerometer sensors.

Chapter 4 deals briefly with a description of code multipath characteristics, and introduces a method to characterize multipath on a moving receiver. The results of code multipath detection on a dynamic vehicle under various environmental surroundings are presented. The temporal and spatial correlation of multipath is also shown, along with the tracking performance of the GPS receivers under different conditions.

In Chapter 5, concepts of reliability using statistical test are presented along with a method to use the geometry information between antennas through the application of constraints. Some results with various scenarios and in different environments are also presented.

Chapter 6 describes the concepts and algorithms used for integration of inertial sensors with GPS. This chapter also presents some results of the field tests conducted to study the benefits of integration under various environments.

Some conclusions and recommendations based on the observations made during this research are presented in Chapter 7.

Chapter 2

Fundamentals of GPS and INS

2.1 Introduction

Navigation has been one of the major factors contributing to success of civilizations for centuries. It has come a long way from using landmarks and monuments, angular measurements from stars, magnetic compass to satellite based navigation. French (1995) provides a brief history of navigation describing some of the Chinese inventions. After the invention of radio, a different class of navigation systems were developed and some of these were VHF (Very High Frequency) omnidirectional radios (VORs), long-range radio navigation (LORAN), Radio detection and ranging (RADAR) (Parkinson 1994a). All these systems have major limitations as they can only provide two-dimensional position, and have limited range. Therefore, a cost effective and reliable navigation system that could be used in all terrain and throughout the world was the main consideration for the next generation of navigation systems. The inertial navigation system (INS) can provide navigational capabilities in all terrain and anywhere on the globe, but their use is severely limited by large drifts and hence the necessity for frequent calibration.

2.2 Fundamentals of GPS

The next generation of navigation systems in the 70's and 80's focused on the space based radionavigation systems. The Global Positioning System (GPS) is one such system, which was originally developed as a military force enhancement system in 1973 (GPS Navstar, 1995). GPS provides accurate three-dimensional position, velocity and time information to a user anywhere in the world at any time. Position determination is based on measurements of the transit time of radio signals from at least four satellites (Axelrad and Brown, 1994).

The GPS system consists of three segments: space, control and user segments (Spilker and Parkinson, 1994).

2.2.1 Space Segment

The space segment consists of a constellation of 24 operational satellites placed at an altitude of 20,000 km above the earth, in six orbital planes, each with an inclination of 55° with respect to the equator. Each of the orbital planes contains four satellites and has room for additional spares if required. The current constellation has 27 operational satellites, that is three more than the specification. The satellites have nearly circular orbits with a period of approximately 12 sidereal hours (Spilker and Parkinson, 1994)

Each of the satellites transmits data on two different frequencies L1 (1575.42 MHz) and L2 (1227.6 MHz). These signals carry navigation data bits, which contain information about the satellite position in terms of Keplerian orbital parameters and precise time linked to GPS time. The time on-board the satellite is maintained by highly stable caesium or rubidium atomic clocks. The clocks on all the satellites are synchronized with respect to each other and the offset and the drifts in the clocks are monitored and transmitted as part of the navigation message.

2.2.2 Control Segment

The primary task of the control segment is to monitor the health of each satellite and to update the satellite clock and orbit corrections. The Operational Control Segment (OCS) consists of five monitor stations and three ground antennas (GA). The OCS facilities are based at Hawaii, Colorado Springs, Ascension Island, Diego Garcia in the Indian Ocean, and the Kwajalein Islands in the west Pacific. The OCS in Colorado Springs is also the Master Control Station (MCS). The GA, which is specifically designed, uploads information received from the MCS to all operational satellites and are situated at Ascension Island, Diego Garcia and Kwajalein. Monitor stations continuously track the entire GPS constellation and collect navigation data from all satellites around the clock. The OCS then uses this data to generate a high integrity navigation data set for each

satellite to be used in the future. The generated navigation data for each satellite is uploaded using an "S-band" telemetry channel in the upload stations. The MCS is responsible for all the OCS functions, such as navigation information processing, satellite data upload, vehicle command control and overall system management (Francisco, 1996).

2.2.3 User Segment

The user segment is the largest and the most widely influenced of the three segments. It consists mainly of GPS receivers belonging to a wide spectrum of user requirements. All these receivers use the satellite ranging signals to determine their position and time with the accuracy specified by the Joint Program Office (JPO).

The user segment can be broadly classified into military users and civilian users. Military users have access to the high accuracy Precise Positioning Service (PPS), whereas the civilian users have access to the less precise Coarse Acquisition (C/A) code. Civilian users constitute a major portion of the user segment market, the estimated users in the civilian segment is approximately a few million and is growing every year. The GPS market in the user segment is currently a $2 billion/year market and is expected to grow to $30 billion/year market by 2005 (Cannon, 2000).

GPS receivers compute the range by measuring the transit time of the signal from the satellite to the receiver antenna. To compute position and time, the receivers perform triangulation using range measurements from at least 3 satellites. However, since the receiver local clock is not in synchronism with satellite clocks, an additional measurement is required to solve for the clock offset.

2.2.4 GPS Signal Structure

The GPS L1 frequency contains two signals, namely the Precise (P) code and Coarse Acquisition (C/A) code as shown in Figure 2.1.

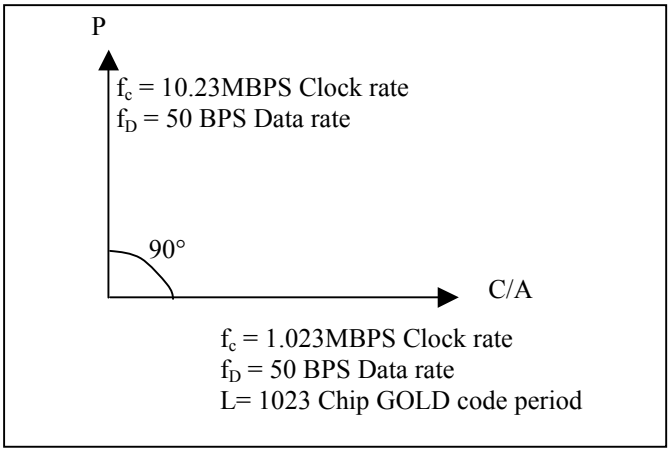

Figure 2.1: GPS L1 signal phasor diagram (Spilker 1994d).

The L1 signal contains two components. The in-phase (C/A) and quadrature (P) signal are both modulated on the same carrier. The C/A code is made up of a maximal length sequence also called as the Gold Code because of its unique autocorrelation properties and has a period of 1 ms and a chipping rate of 1.023 MHz, whereas the P code is a pseudorandom sequence which has a chipping rate of 10.23 MHz and a period of 1 week (actual length of the code is 267 days, but is reset every week). The L1 signal can be expressed as (Spilker, 1994d).

$$f_{L1,i}(t) = A_P XP_i(t) D_i(i) \cos(\omega_1 t + \gamma_1) + A_C XG_i(t) D_i(t) \sin(\omega_1 t + \gamma_1) \quad \textbf{(2.1)}$$

Where,

i	is the satellite index
A_P, A_C	are the in-phase and quadrature signal amplitudes (volt,volt)
XP, XG	are the P and C/A codes respectively
D	is the navigation data bit
ω_1	is the L1 centre frequency (rad/s), and
γ_1	is the small phase noise and oscillator drift component (rad).

2.2.5 Typical Receiver Architecture

A typical GPS receiver has four basic functional blocks, as shown in Figure 2.2. The antenna along with the RF down converter block, signal processing block, navigation processor and reference oscillator (Shenoy et al., 1999). The RF down converter translates the high frequency (> 1GHz) L1 and L2 signals to a low intermediate frequency (IF), typically around 4-16 MHz, which is also digitized by a sampling circuit.

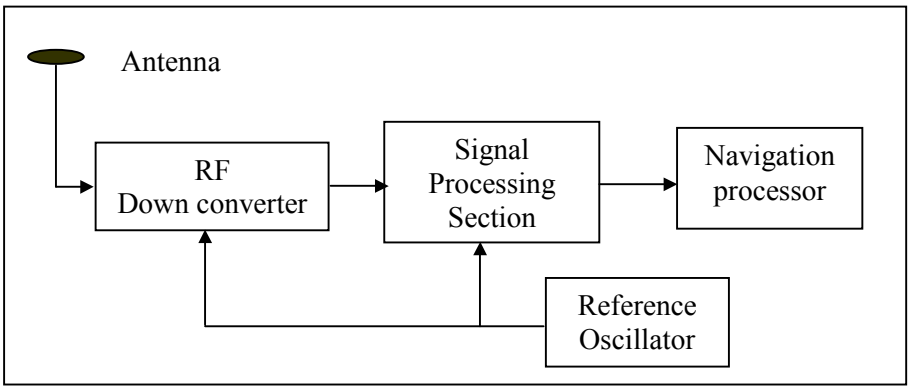

Figure 2.2: Typical GPS receiver architecture

The digitized IF is then processed in the signal-processing block, which basically has a number of correlators, and code and carrier numerically controlled oscillators (NCO) for each channel. Each channel also contains code and carrier tracking loops; code tracking is usually implemented as a delay lock loop (DLL), whereas a costas loop is used for tracking the carrier.

The DLL along with correlators use local code generators, code discriminators and loop filters for individual channels. The DLL aligns the locally generated code with the incoming code to extract the signal which is buried in noise. The Costas Loop uses the in-phase and quadrature-phase versions of the locally generated carrier, carrier discriminator, loop filter, and matches the locally generated carrier with the incoming satellite signal carrier (Spilker, 1994a). The phase error of the carrier discriminator function is used to detect the navigation data. The pseudorange measurements, carrier phase measurements, and Signal-to-Noise-Ratio (SNR) are generated as by-products of the signal tracking loops.

The basic function of the navigation processor is to extract the navigation message and to compute the user parameters (i.e. position, velocity and time). The data bits have a period of 20 milliseconds, and are identified by the Costas loop. Navigation data is made up of five subframes, where each subframe contains 300 data bits. Three of the subframes make up the ephemeris data, which contains Keplerian parameters needed to the compute satellite coordinates. The other two subframes contain a portion of the almanac data, which constitutes a complete message after 12.5 minutes and can be used to compute approximate satellite orbits and positions for the next six months.

2.3 GPS Observables and Error Sources

The pseudorange and carrier phase measurements are the two basic observables from the GPS signal. The pseudorange observations as mentioned before are obtained by measuring the transit time of the signal from the satellite to the receiving antenna. The signal travels through the inhomogeneous space, which has varying effects on code and carrier measurements. The code and carrier phase observables can be expressed as (Lachapelle, 1998)

$$P = \rho + d\rho + c(dt - dT) + d_{ion} + d_{tropo} + \varepsilon_p \quad \textbf{(2.2)}$$

$$\Phi = \rho + d\rho + c(dt - dT) + \lambda N - d_{ion} + d_{tropo} + \varepsilon_\varphi \quad \textbf{(2.3)}$$

Where P is the measured code range (m)

Φ is the measured carrier phase (m)

ρ is the geometric range between the satellite and the receiver antenna (m)

$d\rho$ is the orbital error (m)

dt is the satellite clock error (s)

dT is the receiver clock error (s)

d_{ion} is the ionospheric delay (m)

d_{tropo} is the tropospheric delay (m)

N is the integer cycle ambiguity (cycles)

λ is the wavelength of the signal (m), L1 ≈ 0.19 m and L2 ≈ 0.24 m

ε_p is the code noise (receiver noise + multipath) (m)

ε_φ is the carrier phase noise (receiver noise + multipath) (m)

c is the velocity of light in vacuum (m/s)

From equations (2.2) and (2.3) it can be seen that the carrier phase observable has one additional term compared to the code measurement, which is the ambiguity term. The code phase noise and multipath are replaced with the carrier phase noise and multipath in equation (2.3). Also, the ionospheric error has opposite signs on code and carrier phase measurements.

2.3.1 Orbital Errors

Orbital errors occur due to the discrepancies in the actual position of the satellites as opposed to the position estimated from the broadcast ephemeris. The radial component of this error affects the pseudorange measurements. Absolute values of orbital errors are in the range of 3 – 8 m, however by making use of the DGPS technique this error can be minimized. This improvement is based on the baseline distance between the reference and remote station and as a rule of thumb the improvement is better than 0.5 ppm (Cannon, 2000). Precise ephemeris can be used in post mission to achieve accuracies less than a few decimetres (Zumberge and Bertiger, 1996).

2.3.2 Clock Errors

The satellite clock errors are mainly the offsets in the clock frequency of each satellite with respect to the reference clock. This is monitored by the MCS and the errors are transmitted as coefficients of a polynomial as a part of the navigation message (Navstar GPS, 1995). This error can be on the order of tens of metres but can be completely eliminated by DGPS.

2.3.3 Selective Availability

Selective Availability (SA) was the intentional degradation of the signal by DoD. SA could be implemented in two different ways 1) introducing error into the satellite broadcast orbit (known as the ε-process), and 2) dithering the satellite clock frequency (known as the δ-process). SA was switched off on May 1, 2000 by a Presidential directive. Therefore not much emphasis will be placed on SA. For further details see Parkinson and Enge (1995). SA was present on two of the three data sets collected during the research, however this effect can be completely eliminated by using DGPS since only the satellite clock dither was implemented.

2.3.4 Ionospheric Error

The ionosphere is one of the largest sources of range error for high accuracy GPS users. The ionospheric range error can vary from only a few metres at the zenith to many tens of metres at the horizon. The ionosphere is a dispersive medium; that is the refractive index of the ionosphere is a function of the frequency. Therefore, dual frequency GPS users can make use of this property to measure and correct for the first order range and range rate error effects. The ionosphere can have the following effects on GPS signals 1) group delay of the modulated signal, 2) carrier phase advance, 3) scintillation 4) Faraday rotation to name a few (Klobuchar, 1996).

The ionosphere is made up of ionized plasma and can be classified into four regions, D, E, F1 and F2 respectively. The D region extends from 50-90 km and has a negligible effect on GPS frequencies. The E region extends from 90-140 km and is produced by solar soft x rays and also has a negligible effect on GPS frequencies. The region F1 extends from 140-210 km and has a significant impact on GPS frequencies. F1 is estimated to account for 10% of the daytime ionospheric error. The regions D, E, F1 are associated with the daytime UV (ultra violet) ionization and hence is not present at night. The F2 region extends from 210-1000 km. It is also the most active region and its

influence on GPS frequencies is maximum. F2 region is present at nighttime unlike the D, E, and F1 regions.

The ionosphere also causes a Faraday rotation to electromagnetic signals, which causes a linearly polarized signal to undergo additional rotation along the plane of its polarization. Since GPS signals are circularly polarized, Faraday rotation has no effect on GPS signals (Klobuchar, 1996).

The ionospheric error can be of the order of 2 – 50 m in single point mode and it can be reduced by DGPS. The improvement depends on the base line distance between the reference station and the remote receiver, as the ionosphere decorrelates spatially. The improvement is on the order of 2 ppm with differential corrections (Lachapelle, 1998), but can surpass 17 ppm under high ionospheric conditions (Fortes et al., 2000).

2.3.5 Tropospheric Error

The troposphere is made up of the neutral atmosphere and is situated below the ionosphere. The troposphere is a non dispersive medium, and to model it, information on the atmospheric properties are required. The troposphere produces attenuation effects that are generally on the order of 2-25 m and it varies with the satellite elevation angle and atmospheric conditions (e.g. temperature, pressure and relative humidity).

The dry component of the tropospheric error constitutes around 80% of the total error, and can be modelled within 2-5%. The wet component of the error is due to water vapour in the atmosphere and is more difficult to model. Several models are available to estimate the tropospheric delay such as the Hopfield model (1963) and the Saastamoinen model (1972). Saastamoinen used the models of refraction of the troposphere that estimates the delay versus the elevation angle. The dry atmospheric pressure is modeled using constant lapse rate model for the troposphere (Spilker, 1994b). Hopfield (1963) developed separate zenith models for the dry and wet components of the troposphere. The Tropospheric error can be reduced to 1 ppm in differential mode (Lachapelle, 1998).

All the errors discussed so far can be minimized by applying differential corrections (DGPS). Conversely, multipath and receiver noise cannot be compensated and are discussed below.

2.3.6 Multipath Errors

Multipath is the error caused by reflected signals entering the RF front end and mixing with the direct signal. These effects tend to be more pronounced in static receivers close to large reflectors. As shown in Figure 2.3 the reflectors of electromagnetic signals could be buildings, metal surfaces, water bodies, the ground, etc. Multipath error is specific to a receiver antenna and depends on the surrounding environment. Hence care has to be taken while installing GPS receivers for static applications, such as reference stations.

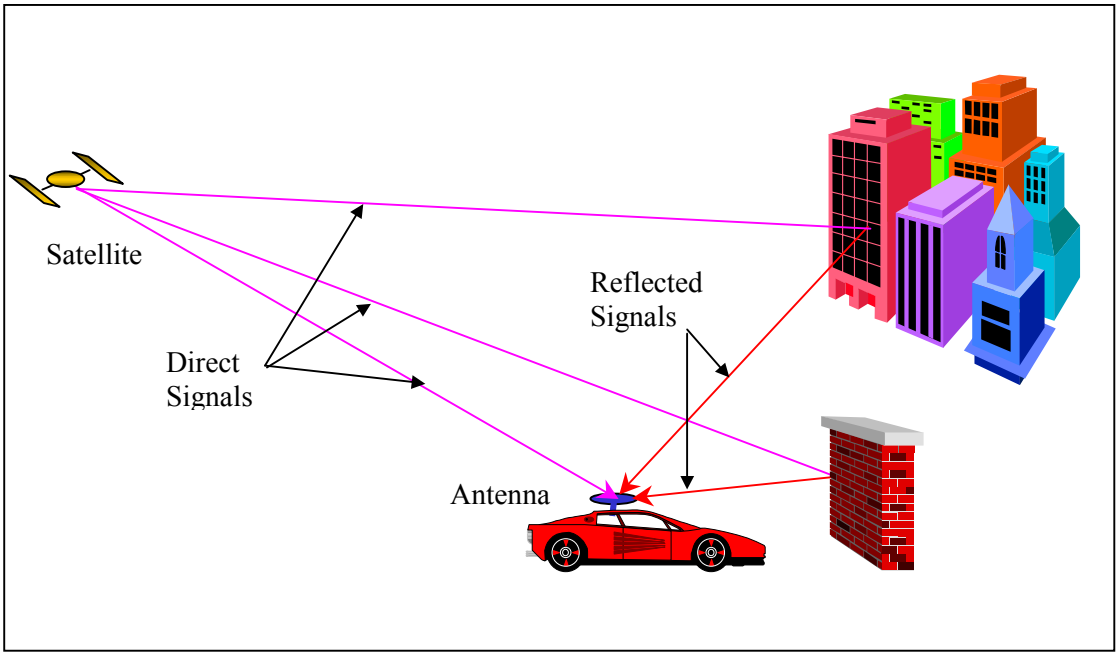

Figure 2.3: Multipath environment

Code multipath errors can be of tens of metres and is highly localized and hence cannot removed through differential techniques. Most of the multipath mitigation technologies are based on the design of suitable architectures in receivers that can minimize multipath,

and there are also special antenna designs such as choke rings, multipath-limiting antennas, which prevent multipath signals from entering the RF section of the receiver.

Code multipath is similar to carrier phase multipath, only its magnitude is several orders of magnitude higher. For code measurements, the multipath signals are always delayed compared to the line-of-sight signals because of the longer travel paths caused by the reflection. The direct and reflected signals will superimpose to produce the composite received signal and in turn affects the correlation property of the C/A code. This is illustrated in Figure 2.4.

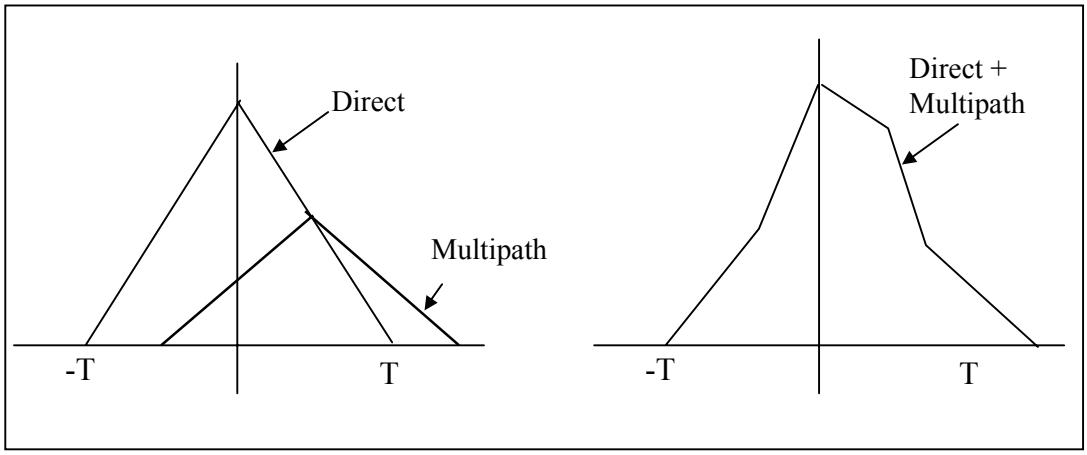

Figure 2.4: Multipath effect on the correlation triangle, (Lachapelle, 1998)

The composite multipath signal can be expressed as (Braasch, 1994),

$$s(t) = -Ap(t)\sin(\omega_o t) - \alpha Ap(t+\delta)\sin(\omega_o t + \theta_m) \quad \textbf{(2.4)}$$

Where,

$s(t)$	is the composite signal
A	is the amplitude of the direct signal
$p(t)$	is the PRN sequence of the C/A code (+/- 1)
ω_o	is the frequency of the direct signal (L1)
α	is the relative power of the multipath signal
δ	is the delay of the multipath signal with respect to the direct signal

θ is the phase of the multipath signal relative to the direct signal

The superposition of direct and the reflected signal can either add or cancel the effective multipath. Hence, on a moving platform usually the multipath tends to average out over time, but can be significant in magnitude and decorrelates rapidly over spatial distances. This property is studied in detail and will be used to detect multipath using multiple antennas. This scheme is discussed in Chapter 4. The magnitude of the multipath error depends on the reflector distance and its strength, the correlator spacing and the receiver bandwidth. The code multipath can be on the order of tens of metres whereas the carrier phase multipath does not exceed 4.75 cm (Ray, 2000). Multipath errors and some of the characterization methods are discussed in detail in Chapter 4.

2.3.7 Receiver Noise

Receiver noise can be considered as white as it is uncorrelated over time and is usually due to the high frequency thermal noise along with the effects of dynamic stresses on the tracking loops (Spilker, 1994a). Also, because of the use of independent signal tracking loops for individual parallel channels there is no correlation due to noise between the channels for measurements taken at the same time. The noise level is a function of code correlation method, receiver dynamics, and satellite elevation (due to the antenna gain pattern) (Lachapelle 1998). Code measurement noise varies from a few centimetres to a few metres depending on the spacing used in the correlators. However, the carrier phase noise is on the order of few millimetres in most modern receivers. The receiver noise increases by $\sqrt{2}$ when differential corrections are applied.

2.3.8 Error Summary

The nominal values of various errors in equations (2.2) and (2.3) are given in Table 2.1.

Table 2.1: GPS Error sources (Lachapelle, 1998)

Error source	Single point (m)	Differential errors (ppm)	Remarks
Orbit	3-8	0.1-0.5	Error in broadcast ephemeris due to residual errors in curve fitting
Clock	10	-	Due to satellite clock drift, can be removed by DGPS
SA	N/A	N/A	Switched off as of May 1, 2000
Ionosphere	2-50	0.5-2	Depends upon elevation angle and solar activity. In DGPS mode the error depends on the spatial decorrelation
Troposphere	2-30	0.1-1	Depends upon the water vapour content in the lower part of atmosphere, and a function of elevation angle. In DGPS mode the error depends on the spatial decorrelation
Code multipath	0.2-3	-	Can be up to 150 m with a correlator spacing of 1 chip and 15 m with a spacing of 0.1 chip. It can not be eliminated by differential corrections
Code noise	0.1-3	-	C/A code noise depends upon receiver technology
Carrier multipath	0.001-0.03	-	Maximum 4.75 cm for L1 and 6.11 cm for L2, and is not affected by differential corrections
Carrier noise	0.0002-0.002	-	Depends on the receiver technology and dynamic stresses

2.4 Fundamentals of INS

The basic principle of inertial navigation is based on integration of accelerations observed by mounting accelerometers on the body of the vehicle. As shown in Figure 2.5, the first integration of the vehicle acceleration provides velocity and the second integration provides the position, however the initial conditions for integration have to be known. In this case the initial velocity and initial position needs to be known. Hence, unlike GPS, an INS is a relative positioning system. To determine the navigation parameters (position and velocity) in the desired navigation frame, the accelerations have to be projected from the body frame (frame on which the accelerometers are mounted) on to the navigation frame of interest before integration (Salychev, 1998). A triad of orthogonally mounted gyroscopes placed coincident with the accelerometers can measure the angular velocity of these accelerations and provide the necessary information to orient the two different frames.

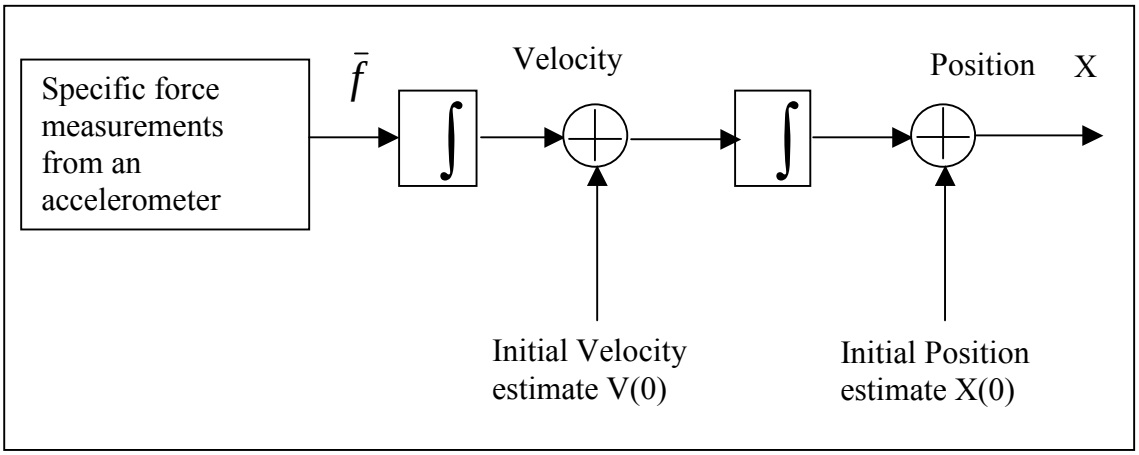

Figure 2.5: Principle of Inertial Navigation

There are two methods to realize the navigation frame. The first deals with physically realizing the navigation frame using a three axis gyro stabilized platform also known as a gimbal system. The second method is to realize the navigation frame analytically using measurements from accelerometers and gyroscopes installed directly on the body of the vehicle. Such a system is referred to as a strapdown INS.

The accelerometers are designed based on the conservation laws of physics (Schwarz and Wei, 1999). Similarly the mathematical models used to realize an INS are based on classical mechanics. Using Newton's second law of motion, the specific force near the surface of the earth can be represented as

$$\bar{f} = \bar{a} - \bar{g}_m \tag{2.5}$$

Where, $\bar{f}$ is the specific force vector measured by the accelerometers

$\bar{a}$ is the absolute acceleration (acceleration with respect to the inertial frame)

$\bar{g}_m$ is the gravitational acceleration

The equation of the absolute acceleration in the inertial frame can be defined as (Salychev, 1998)

$$\bar{a} = \frac{d}{dt}\left[\left.\frac{d\bar{r}}{dt}\right|_I\right]_I = \frac{d}{dt}\left[\bar{V} + \bar{U} \times \bar{r}\right]_I \tag{2.6}$$

Where, $\bar{V}$ is the vehicle velocity in the earth fixed frame

$\bar{U}$ is the angular velocity of the earth

$\bar{r}$ is the position vector in the inertial frame

I represents differentiation with respect to the inertial frame

Equation (2.6) is based on the rule of differentiation of a vector with respect to inertial space and this rule is also referred to as the Coriolis equation. By expanding equation (2.6) the general navigation equation can be derived (see, Salychev, 1998).

$$\bar{f} = \left.\frac{d\bar{V}}{dt}\right|_N + \bar{\omega}_N \times \bar{V} + \bar{U} \times \bar{V} - \bar{g} \tag{2.7}$$

Where, $\left.\frac{d\bar{V}}{dt}\right|_N$ is the differential of the velocity vector in the desired navigation frame

$\overline{\omega}_N$ is the absolute angular velocity of the navigation frame

$\overline{g}$ is the apparent gravity (gravitational acceleration – centripetal acceleration) gravity vector

2.4.1 Mechanization and Error Models

Mechanization equations express the relationship between the raw INS measurements to the navigation parameters. The mechanization of a strapdown INS is briefly discussed in this section.

Strapdown INS, as the name suggests, realizes the navigation frame (Local level frame) mathematically in the onboard computer instead of physically torquing the platform as in the case of a gimbal system. The torquing is realized by the high update rates of the quaternion (50 Hz). A quaternion is a vector that expresses the rotation of the body by a single rotation angle θ about a fixed spatial axis. Hence four parameters are used to represent the rotation matrix R_b^l, one to represent the rotation angle and three to define the direction cosines of the rotation axis in space (see, Salychev 1998; Schwarz and Wei, 1999 for details). The mechanization equations can be expressed in various frames such as the earth fixed (e) frame, the wander frame (w) or the local level (l) frame. For terrestrial navigation, the most popular mechanization is the local level and the wander frame. For detailed description on mechanization see Schwarz and Wei, (1999).

The inertial navigation parameters (position, velocity and attitude), like GPS, are affected by various error sources. The major component of this error, namely Schuler oscillations, repeat periodically with a period of 84 minutes. Schuler oscillations can be modelled as a stationary process. The INS error equations representing this stationary part for the east channel is given by equation **(2.8)** and for the north channel by equation **(2.9)** (Salychev, 1998). The non stationary part is of the inertial errors is given by equation **(2.10)**.

$$\delta\dot{V}_E^{sh} = -g\Phi_N^{sh} + B_E$$

$$\dot{\Phi}_N^{sh} = \frac{\delta V_E^{sh}}{R} + \omega_N^{dr} \quad \textbf{(2.8)}$$

$$\dot{\omega}_N^{dr} = 0, \quad \dot{B}_E = 0$$

$$\delta\dot{V}_N^{sh} = g\Phi_E^{sh} + B_N$$

$$\dot{\Phi}_E^{sh} = -\frac{\delta V_N^{sh}}{R} + \omega_E^{dr} \quad \textbf{(2.9)}$$

$$\dot{\omega}_E^{dr} = 0, \quad \dot{B}_N = 0$$

Where,

$\delta\dot{V}_E^{sh}, \delta\dot{V}_N^{sh}$ are the east and north velocity error components, and represent the time derivatives of east and north velocity errors (m/s)

$\dot{\Phi}_E^{sh}, \dot{\Phi}_N^{sh}$ are the east and north misalignment angles errors (rad/s)

$\dot{\omega}_E^{dr}, \dot{\omega}_N^{dr}$ are the east and north gyro bias (rad/s)

$\dot{B}_E, \dot{B}_N$ are the east and north accelerometer bias (rad/s)

g is the apparent gravity vector (m/s^2)

R is the radius of the Earth (m)

$$\delta\dot{V}_E^{nst} = -g\Phi_N^{nst} + a_N\Phi_{up} + a_E\mu_E$$

$$\dot{\Phi}_N^{nst} = \frac{\delta V_E^{nst}}{R}$$

$$\delta\dot{V}_N^{nst} = g\Phi_E^{nst} - a_E\Phi_{up} + a_N\mu_N \quad \textbf{(2.10)}$$

$$\dot{\Phi}_E^{nst} = -\frac{\delta V_N^{nst}}{R}$$

Where

$\delta\dot{V}_E^{nst}, \delta\dot{V}_N^{nst}$ are the non stationary components of the velocity errors, and represent the time derivative of east and north velocity error components (m/s)

a_E, a_N are the east and north accelerometer measurements in the navigation frame (m/s^2)

$\dot{\Phi}_E^{nst}, \dot{\Phi}_N^{nst}$ are the east and north misalignment angles errors (rad/s)

$\Phi_E, \Phi_N, \Phi_{up}$ are the east, north and up misalignment angles (rad)

The magnitude of the Schuler oscillations depends on the accelerometer and gyro biases, whereas the period depends on ($\sqrt{g/R}$), i.e. gravity and the radius of the Earth. This is evident after solving the differential equation **(2.8)(2.9)**. However on the surface of the Earth the period is approximately 84 minutes. The north and east velocity errors are shown in Figure 2.6. The amplitudes of attitude errors are much smaller because it is inversely proportional to the radius of the Earth.

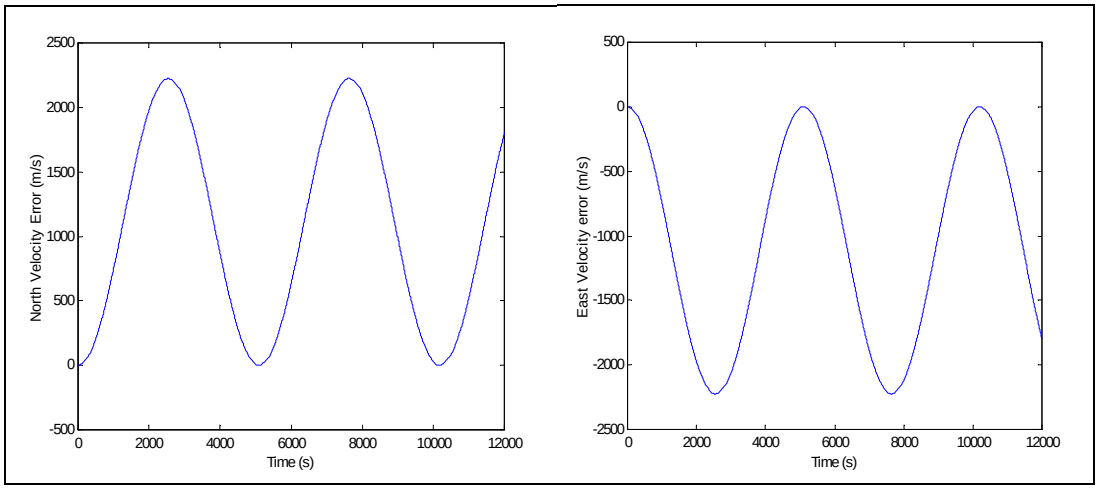

Figure 2.6: Schuler oscillations

Equations **(2.8)** and **(2.9)** are also used to update the state equations of the Kalman filter which is used to model the dynamic model of the process.

2.5 Initialization

Certain initialization procedures like calibration and alignment need to be performed before computing the inertial navigation parameters (Salychev, 1998). The accelerometer and gyroscope triad constituting the IMU is mounted on the body of the vehicle, which is also the body frame, see Figure 2.7.

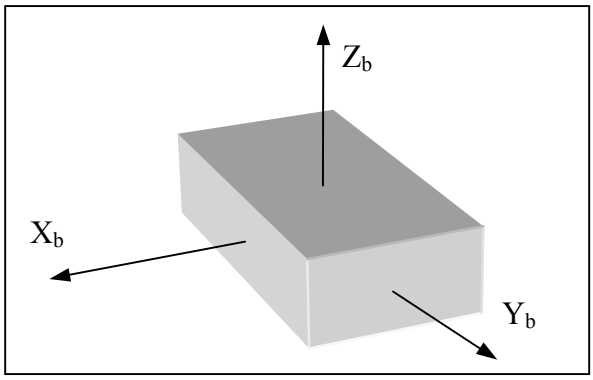

Figure 2.7: Body frame of reference

The Y - axis of the IMU coincides with the longitudinal axis of the vehicle (Y- axis pointing towards the front of the vehicle), Z - axis is pointing upwards and the X - axis completes the right-handed system. The origin of the body frame is located at the centre of the accelerometer and the gyroscope triad.

The strapdown INS initialization algorithm contains the following two stages namely :

1. Calibration mode
2. Alignment mode

2.5.1 Calibration

In most of the high end or navigation grade INS, the gyroscope and accelerometer biases and scale factors are usually factory calibrated and no separate calibration is required every time the sensor is used. Occasional calibration every few months is recommended. However, if low cost sensors are used, then the bias and the drift stability of the gyros are much poorer and frequent calibration, which is every time the sensor is used, becomes a

necessity. Calibration is performed by averaging the raw angular velocities measured from the gyros over a period of 15-20 minutes in static mode. The calibration process for a low cost IMU (e.g. MotionPak™) is described in Appendix C.

2.5.2 Alignment

To start the INS calculations, the initial parameters of the transformation matrix R_b^l (rotation matrix from the body frame to the local level frame, roll, pitch and yaw) is required. The process of computing the initial parameter of the transformation matrix is called the INS alignment procedure. There are two alignment modes, namely the horizontal alignment (roll and pitch) and the azimuth (yaw) alignment. Due to the poor quality of the gyroscopes used in a low cost IMU, azimuth alignment cannot be accomplished, because the gyro drift exceeds the Earth rotation rate. Hence azimuth alignment was done by storing azimuth information by an external aid which was a magnetic compass in this case. The azimuth transfer is achieved by storing the heading obtained from the compass manually, and due to the poor gyro drifts the accuracy of stored azimuth can be on the order of 2° - 4°.

2.5.2.1 Horizontal alignment

Horizontal alignment is the procedure to compute the initial value of roll ($\hat{\gamma}(0)$) and pitch ($\hat{\upsilon}(0)$). The accelerometer axes are mounted to coincide with the body of the vehicle and consequently the accelerometer measurements can be written as

$$\begin{bmatrix} f_x \\ f_y \\ f_z \end{bmatrix}_b = R_l^b \begin{bmatrix} 0 \\ 0 \\ g \end{bmatrix} \qquad \textbf{(2.11)}$$

Where,

f_x, f_y, f_z	are the specific forces in the body frame
R_l^b	is the rotation matrix from the local level frame to the body frame
g	is the apparent gravity vector

If the body frame of the vehicle is assumed to be close to the local level frame, then small angle approximations can be made to the R_l^b matrix (see Appendix B for details) and equation (2.11) can be simplified as

$$\begin{aligned} f_{xb} &= -g\gamma \\ f_{yb} &= g\vartheta \end{aligned} \qquad \textbf{(2.12)}$$

Where,

γ is the roll angle

ϑ is the pitch angle

However, the real accelerometers have additional biases, which result in

$$\begin{aligned} f_{xb} &= -g\gamma + B_{xb} \\ f_{yb} &= g\vartheta + B_{yb} \\ f_{zb} &= g \end{aligned} \qquad \textbf{(2.13)}$$

The objective of the alignment procedure is to make $f_{xb} \cong 0, f_{yb} \cong 0$.

Therefore, equation (2.13) can be rewritten as

$$\begin{aligned} \tilde{\gamma}(0) &= \frac{B_{xb}}{g} \\ \tilde{\vartheta}(0) &= -\frac{B_{yb}}{g} \end{aligned} \qquad \textbf{(2.14)}$$

Equation (2.14) also represents the horizontal alignment errors. Hence, the accuracy of the horizontal alignment procedure is limited by the accelerometer biases.

2.5.2.2 Azimuth alignment

The azimuth alignment is realized by using the gyro measurements. Consider the orientation of the body frame with respect to the local level frame, Figure 2.8. If the misalignment between the two frames in the azimuth direction is ε, U being the magnitude of the angular rotation of the Earth and ϕ the latitude. Then $U\cos\phi$ is the

projection of the Earth rotation rate along the local level north axis and zero along the local level east axis.

The projection of the Earth rate on the body frame is $U\cos\phi\cos\varepsilon$ and $U\cos\phi\sin\varepsilon$ along north and east directions respectively.

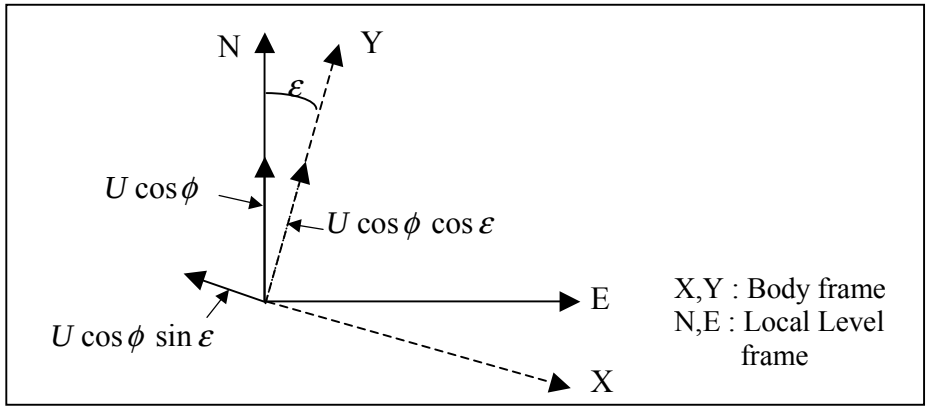

Figure 2.8: Principle of azimuth alignment

The estimate of the azimuth angle can be obtained by the equation

$$\varepsilon = -\tan^{-1}\left(\frac{\omega_x^b}{\omega_y^b}\right) \qquad \textbf{(2.15)}$$

Where,

ω_x^b, ω_y^b are the true angular rates measured by the gyros in the body frame

The gyros not only measure the Earth rate but also contain the run-to-run bias in them; hence the true gyro measurements can be written as

$$\begin{aligned} \omega_x^b &= -U\cos\phi\sin\varepsilon + \omega_{xb}^{bias} \\ \omega_y^b &= U\cos\phi\cos\varepsilon + \omega_{yb}^{bias} \end{aligned} \qquad \textbf{(2.16)}$$

Where,

$\omega_{xb}^{bias}, \omega_{yb}^{bias}$ are the gyroscope run-to-run random biases

Once the coarse azimuth angle ε is known then small angle approximation can be applied to equation (2.16) to derive the relation, which describes the achievable accuracy for the azimuth alignment given in equation (2.17). (For a detailed analysis see Salychev (1998)).

$$\tilde{\varepsilon}(0) = \frac{\omega_{xb}^{bias}}{U\cos\phi} \tag{2.17}$$

Therefore, the horizontal alignment is solely dependent on the gyro bias drift and can be on the order of a few arcmin for a good quality INS to a few degrees for a low cost INS (Salychev et al., 2000). The Earth rotation is 4.166e-3°/s whereas the gyro bias variations can be as large as 1.0°/s in the case of a low cost IMU (e.g. Motion Pak™), which, as mentioned before, means that the gyros can not be used to perform a self contained azimuth alignment.

Chapter 3

System Realization and Inertial Sensors

To achieve the objectives discussed in Chapter 1 various mobile tests were conducted in the city of Calgary. This chapter discusses the setup and the procedures followed during the tests. An insight into the inertial sensors and their characteristics is also presented. Finally a description of the route and the environmental conditions in which the tests were conducted is described.

3.1 Test Vehicle and GPS Receivers

Data was collected from four GPS antenna/receiver systems mounted on a passenger vehicle and a fifth antenna on the roof of the Engineering building at the University of Calgary (UofC). The four antennas on the vehicle were connected to four NovAtel MiLLennium™ GPS receivers. The GPS receivers were operated in the Narrow Correlator™ mode. A NovAtel Beeline™ GPS receiver was mounted on a pre-surveyed pillar on the roof of Engineering building to act as a reference station to generate differential corrections. Although the MiLLennium™ receivers are dual frequency units (whereas the Beeline™ is single frequency), only the L1 data was used during post-analysis. A 5° cut-off elevation angle was chosen while processing the data. NovAtel's high performance active antenna (model 501) was used in the reference station and on the vehicle. The raw binary measurement record (RGEB) and the ephemeris record (REPB) were logged from the remote and reference station receivers at a rate of 1 Hz. Two laptop computers with two serial ports on each were used to log data in the vehicle.

The location of the antennas on the roof of the vehicle is shown in Figure 3.1. The antennas were separated by distances between 76 and 92 centimetres and were designated Antennas A, B, C and D. Two of the antennas labelled A and B were mounted on ski racks and antennas C and D were mounted on magnetic mounts. The complete experimental set up of the four antennas on the roof of the car is shown in Figure 3.2.

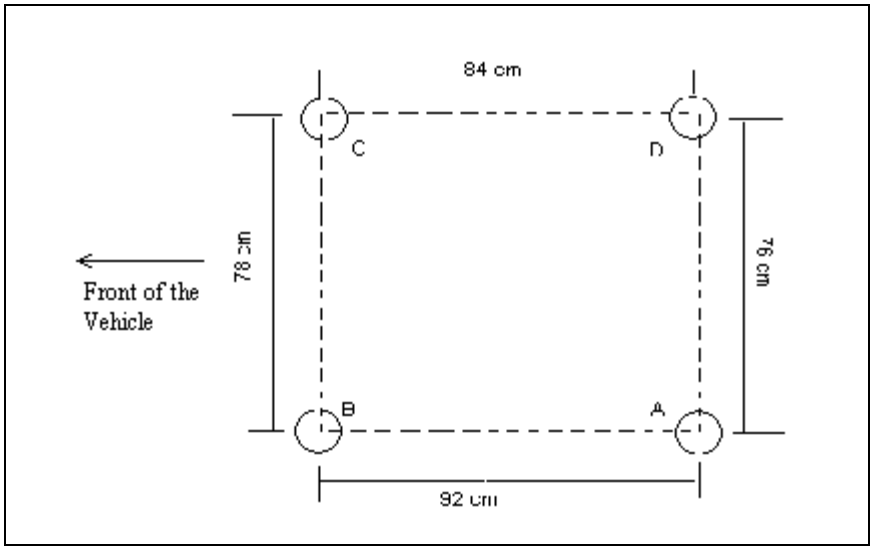

Figure 3.1: Antenna locations on vehicle roof

Figure 3.2: Vehicle setup

Data was collected on June 30 and September 9, 1999 (herein referred to as Days 1 and 2). Another field trial was performed on May 13, 2000 with similar setup but with an IMU device (referred to as Day 3). A detailed description of this test is provided in Chapter 6.

3.2 Inertial Sensor

The MotionPak™ from Systron Donner is a low cost solid-state six degree of freedom inertial sensing system used for measuring linear accelerations and angular rates. It is a highly reliable, compact, and fully self-contained motion measurement package. It uses three orthogonally mounted solid-state micromachined quartz angular rate sensors, and three high performance linear servo accelerometers mounted in a compact, rugged package, with internal power regulation and signal conditioning electronics. Its dimensions are 7.75 x 7.75 x 9.15 cm and it weighs less than 0.9 kg.

Figure 3.3: Systron Donner's MotionPak™

3.2.1 Accelerometer

An accelerometer is a sensor which converts an acceleration from motion and/or gravity to an electrical signal. The accelerometer used in MotionPak™ is a force rebalance servo controlled accelerometer and the operational concept of such a device is shown in Figure 3.4. The accelerometer triad is made up of three surface micro-machined sensors each capable of measuring positive and negative acceleration along their respective axes. Each

sensor consists of a main beam tethered at four points with a number of centre plates at right angles to the main beam as shown in Figure 3.4.

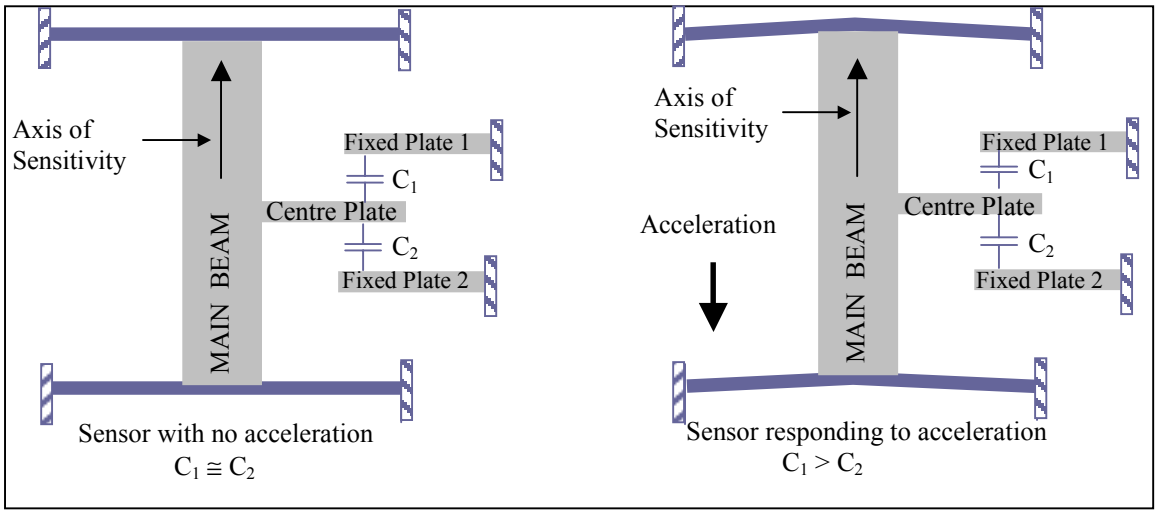

Figure 3.4: Accelerometer-Theory of Operation, Wuntronic (2000)

Each of the centre plates fits between two adjacent fixed plates, forming a capacitive divider. The two fixed plates are driven with equal amplitude but opposite polarity square wave signals. With no acceleration, the two capacitances are approximately equal and the centre plate will be at approximately 0 volts. Any applied acceleration causes a mismatch in plate separation, which in turn results in increased capacitance between the fixed plate closest to the centre plate, and a voltage output can be detected on the centre plate. This voltage output is proportional to the acceleration. A synchronous demodulator is used to extract this acceleration signal and is used in a feedback loop to force balance the sensor. A linear servomechanism is used to bring back the sensor to its 0 position. The balancing force is obtained electrostatically, caused by driving the centre plates to a voltage proportional to the acceleration signal (Doscher, 2000). The force balancing servo loop response is fast enough and flat enough to track a level change, keeping the sensor nearly motionless. This minimizes errors from geometric distortion, spring constant nonlinearity, resonances, mechanical fatigue, etc. that are typical with open-loop sensors (Wuntronic, 2000).

3.2.2 Gyroscopes

Gyroscopes are designed to measure angular velocities and convert them into electrical signals. The principle of operation is again based on the Newton's laws of classical mechanics.

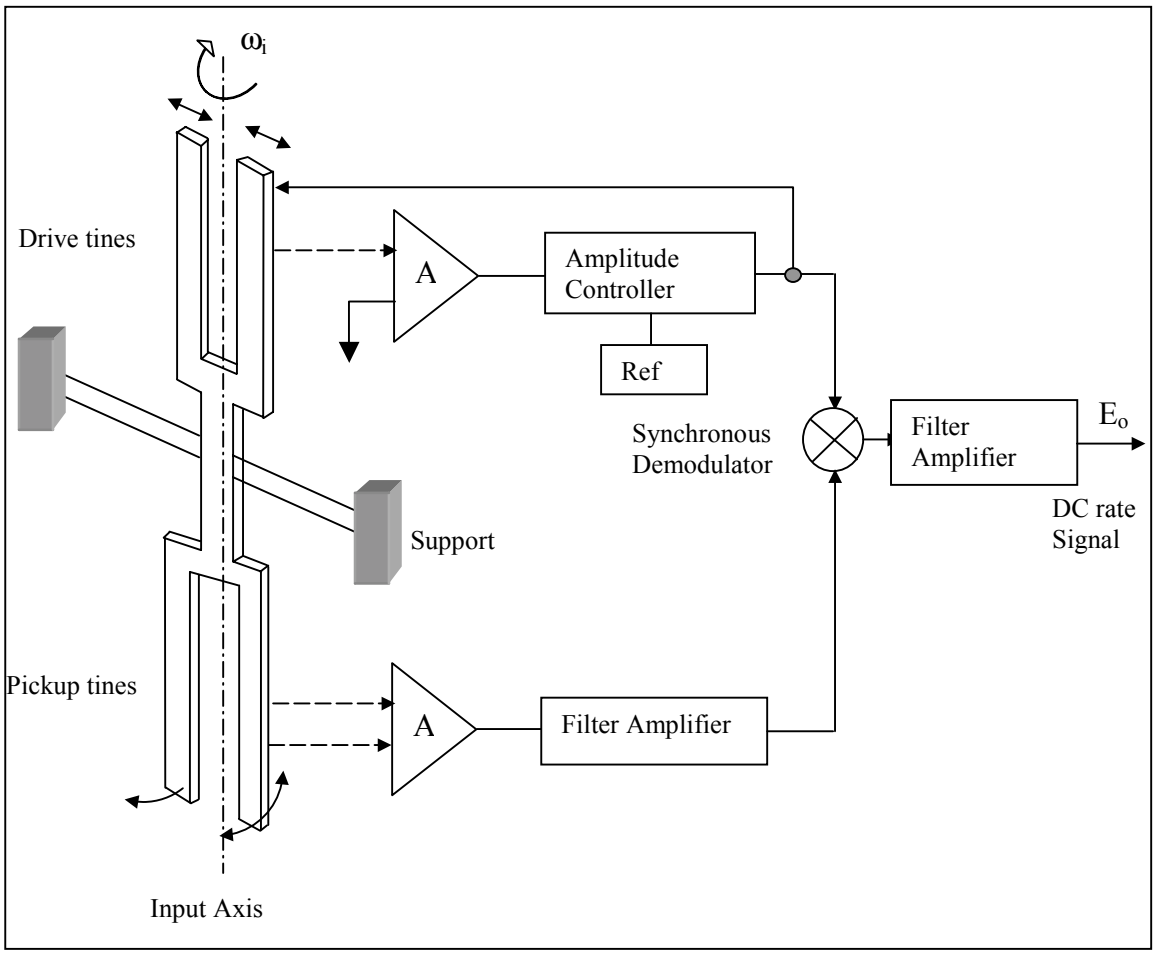

Figure 3.5: Vibrating tuning fork block diagram (Geier , 1998)

The MotionPak™ is made up of a vibrating quartz tuning fork to sense angular velocity and the schematic is shown in Figure 3.5. The sensor is made up of a microminiature double-ended quartz tuning fork and supporting structure, all fabricated chemically from a single wafer of monocrystalline piezoelectric quartz (similar to quartz watch crystals). The use of piezoelectric quartz material simplifies the active element, resulting in enhanced stability over temperature and time. The drive tines, which constitute the active

portion of the sensor, are driven by an oscillator circuit at precise amplitudes and this causes the tines to move toward and away from one another at a high frequency. During rotations each tine will experience a Coriolis force acting on it. The forces are perpendicular to the plane of the fork assembly at each of the tines. This results in a torque proportional to the angular velocity ω_i. The pickup tines respond to the torque by moving in and out of the plane causing the output signals that will be picked up by the pickup amplifier. After amplification these signals are demodulated into a DC signal proportional to the angular rate by the synchronous demodulator (Geier, 1998).

3.2.3 MotionPak™ Characteristics

The parameter specifications of the MotionPak™ sensors are shown in Table 3.1. It is important to note that the equipment accuracy varies from one unit to another even if they have the same factory specifications. A laboratory test was conducted on a particular unit and Table 3.2 shows the best and worst case gyro accuracies that were observed.

Table 3.1: MotionPak™ paprmeter specification (Systron Donner, 2000)

Performance	Rate Channels	Acceleration Channels
Range	± 100 deg/sec	5 G
Bias	<2 deg/sec	<12.5 mG
Alignment to base	<1°	<1°
Resolution	<14 deg /hrs	<10 μG

Table 3.2: Gyro Accuracies from Lab Test (Salychev et al., 2000b)

Gyro Accuracy Parameter	BestCase	WorstCase
day to day (run to run) drift rate bias	< 100 deg/h	< 360 deg/h
drift rate bias in run (averaged within 20 s)	< 60 deg/h	< 180 deg/h
drift rate bias in run (averaged within 250…300 sec)	< 10 deg/h	< 50 deg/h

From the specifications and test results shown, the inertial measurement unit cannot be directly used as a stand alone INS. Firstly, the gyros are not sensitive enough to sense the Earth rate, which means that a self-contained azimuth alignment procedure cannot be performed and as a result a stored azimuth alignment procedure is used. Secondly, the run-to-run gyro bias has a large magnitude that leads to large INS output errors in stand-alone mode. Therefore in order to use such a class of IMU for navigation purposes, it has to be integrated with additional sensors like GPS. Separate calibration and azimuth alignment procedures are also performed.

3.3 Inertial Augmentation Setup

The augmentation of GPS has been studied and used by a number of people for various applications. Bullock (1995), Harris (1988), and Stephen (2000), used dead reckoning sensors to augment GPS. Zang (1995) used a low cost IMU to demonstrate GPS/INS integration. The complete experimental GPS/INS setup is shown in Figure 3.6.

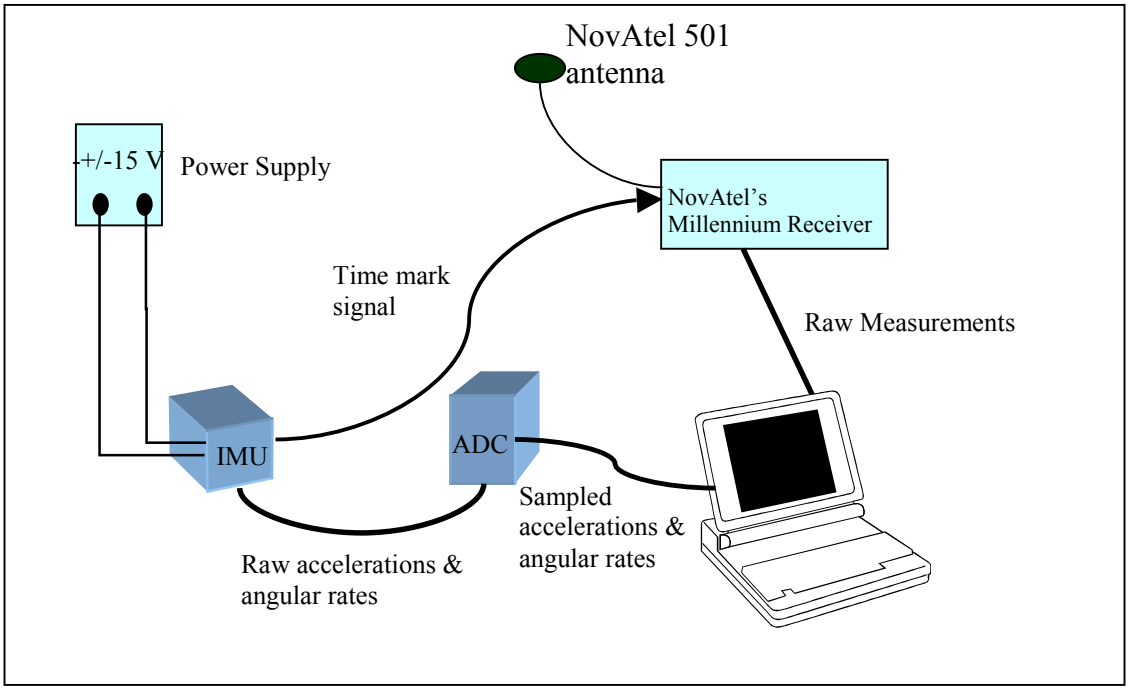

Figure 3.6: INS/GPS experimental setup

The IMU was placed on the floor of the vehicle on a stable platform. The IMU was powered by a +/-15V regulated DC power supply. The sensors are sensitive to the voltage fluctuations, hence a regulated voltage is used. The Y-axis of the IMU was aligned to coincide approximately with the longitudinal axis of the vehicle. The output of the IMU, which is an analog signal is sampled at 50Hz and digitized by a 16bit ADC (Analog to Digital Converter). The digitized signal is then stored in the PC. The PC time stamps are appended to each of the samples before storing. At the end of every 50 samples, the ADC card generates an end of conversion pulse. This pulse is connected to the time mark pin on the Millennium™ card, which responds to the pulse by transmitting a GPS time stamp corresponding to the pulse. The time stamps corresponding to every 50 sample is stored in the PC. A linear clock drift model is assumed within a second and the GPS time stamps corresponding to each of the sample are recomputed. Raw measurements pseudorange (RGEB) and ephemeris (REPB) are recorded at a rate of 1 Hz and stored in the computer. Data from the other three receivers/antennas are also logged simultaneously in another computer at 1 Hz. The antennas are mounted at least 0.5 m apart from each other. The data is then analyzed in post processing mode, using MATNAV (Multi Antennas NAVigation) software developed at the University of Calgary.

The hardware connection among the various components is shown in Figure 3.7. The analog signals from the MotionPak™ are connected to six different analog to digital conversion channels on the DAQPad-MO-16XE-50 data acquisition card. The internal timer is pre-programmed to sample the analog data at 50Hz. The timer generates an end of event pulse (TTL level) at the end of 50 samples, which is connected to the time mark pin (pin 4) on the 9 pin I/O connector of the Millennium™ GPS receiver. The timing uncertainty is limited by the buffering and transmission of data from the DAQPad to the computer, and is expected to be within a few milliseconds.

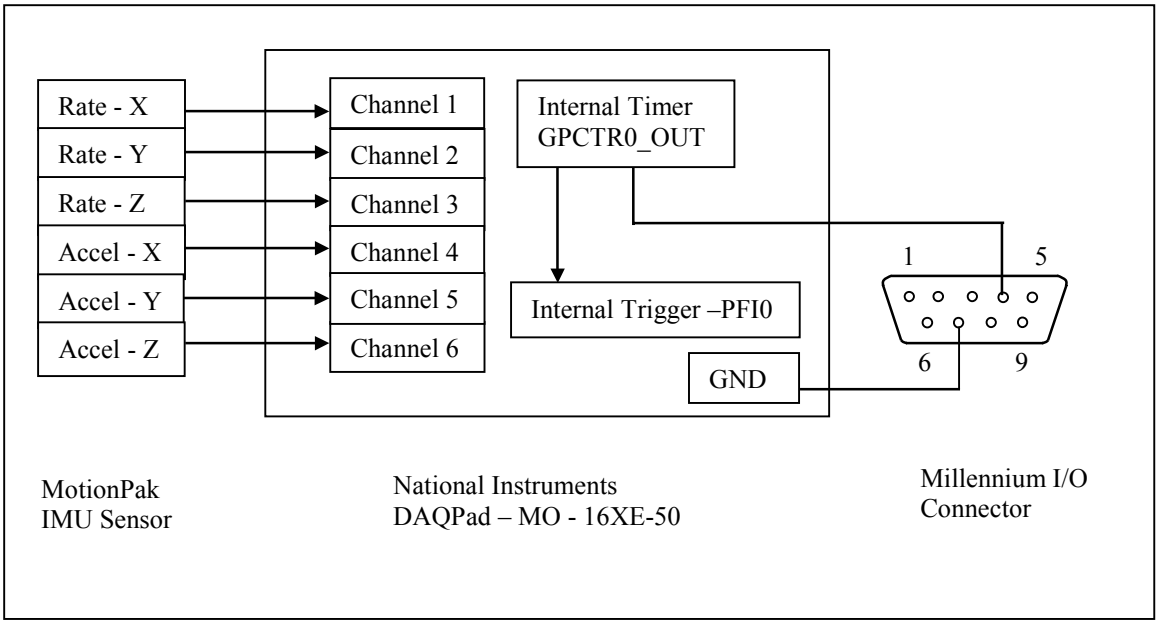

Figure 3.7: Hardware connections

3.4 Test Route Description

A route encompassing various conditions was chosen for the test. The route was divided into four sections each representing a different environmental condition.

The four sections can be classified as:

Section 1: Open sky and suburban, which is free from obstacles for the entire section
Section 2: Dense urban environment in downtown Calgary
Section 3: Heavy foliage environment
Section 4: Open sky in a suburban environment

3.4.1 Section 1 [Open sky and suburban conditions]

The route traversed in Section 1 is shown as a dark red line in Figure 3.8 and has a very clear view of the sky, which is free from obstructions on both sides of the road (Crowchild Trail), but has a few underpasses along the road.

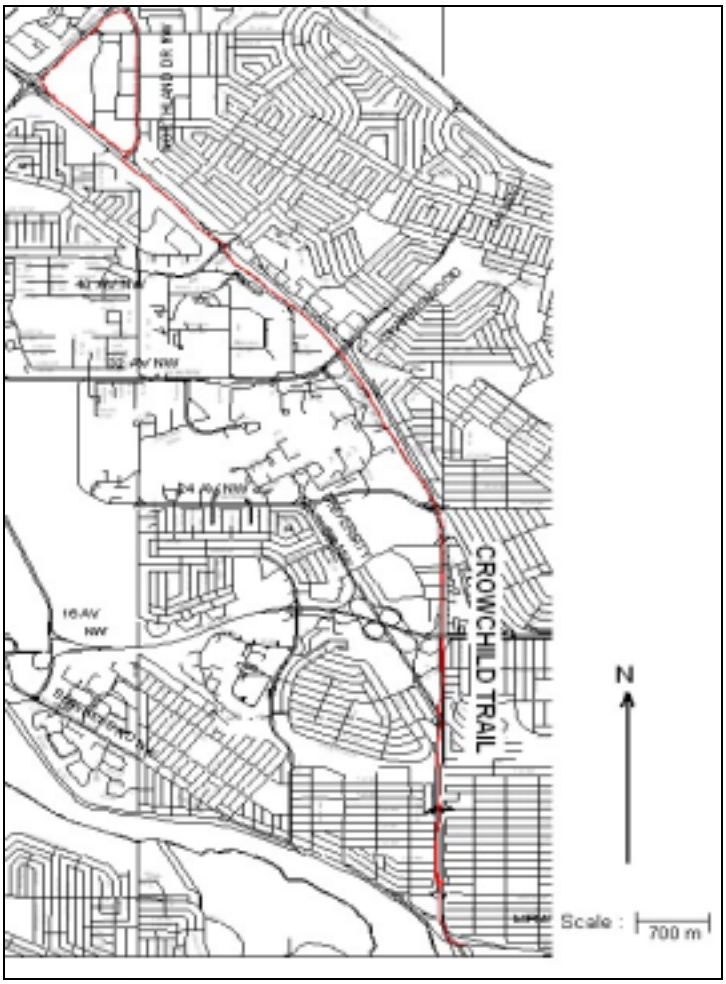

Figure 3.8: Section 1 route

3.4.2 Section 2 [Downtown section]

Section 2 of the test drive starts from Memorial Drive and passes through a rectangular block comprising 9th Avenue, Centre Street, 6th Avenue, and 11th Street in the downtown south west (SW) section of Calgary. The red line in Figure 3.9 shows the chosen route. Memorial Drive has mild foliage on the south side of the road whereas 9th Avenue has high rise buildings along the north side of the road and is fairly open on the south side. Sixth Avenue has high rise buildings on both sides of the road and provides a very dense urban canyon scenario where satellites below elevation angles of 50 degrees are completely masked. Section 2 is approximately 9 km in length. Eleventh Street has clear visibility.

Figure 3.9: Section 2 route

3.4.3 Section 3 [Foliage section]

A residential area in Calgary with sufficiently dense foliage was chosen for Section 3. The route has a variety of foliage characteristics and the majority of the 5.5 km route has moderate to very dense foliage. The most densely covered section is along Montreal Avenue. Trees on both sides of the road branch out to cover the entire street providing very little line-of-sight capability. Satellite visibility is good along 10th Street, as there are no trees on either side of the road. Some sections, like Carleton Street and Montcalm Crescent, have few trees. The route shown in red in Figure 3.10 provided a good variety of foliage attenuation. Detailed description of the foliage in this section can be found in Fotopoulos et al., (1998) who used the same route to test the performance of the WADGPS LandStar™ system under different foliage densities.

Figure 3.10: Section 3 route

3.4.4 Section 4 [open sky and suburban conditions]

The route in Section 4 starts from downtown Calgary and ends at the University of Calgary and is mostly a retrace of Section 1. Satellite visibility varies from sparsely dense to open sky along this section. The route shown in Figure 3.11 is comprised of 17th Avenue, Crowchild Trail and 32nd Avenue. Seventeenth Avenue has low buildings on both sides whereas Crowchild Trail provides a clear and unobstructed view of the sky. The total distance covered in this section is approximately 8km. The wide mix of environmental diversity in the entire route made it ideal for analyzing code multipath on a moving vehicle.

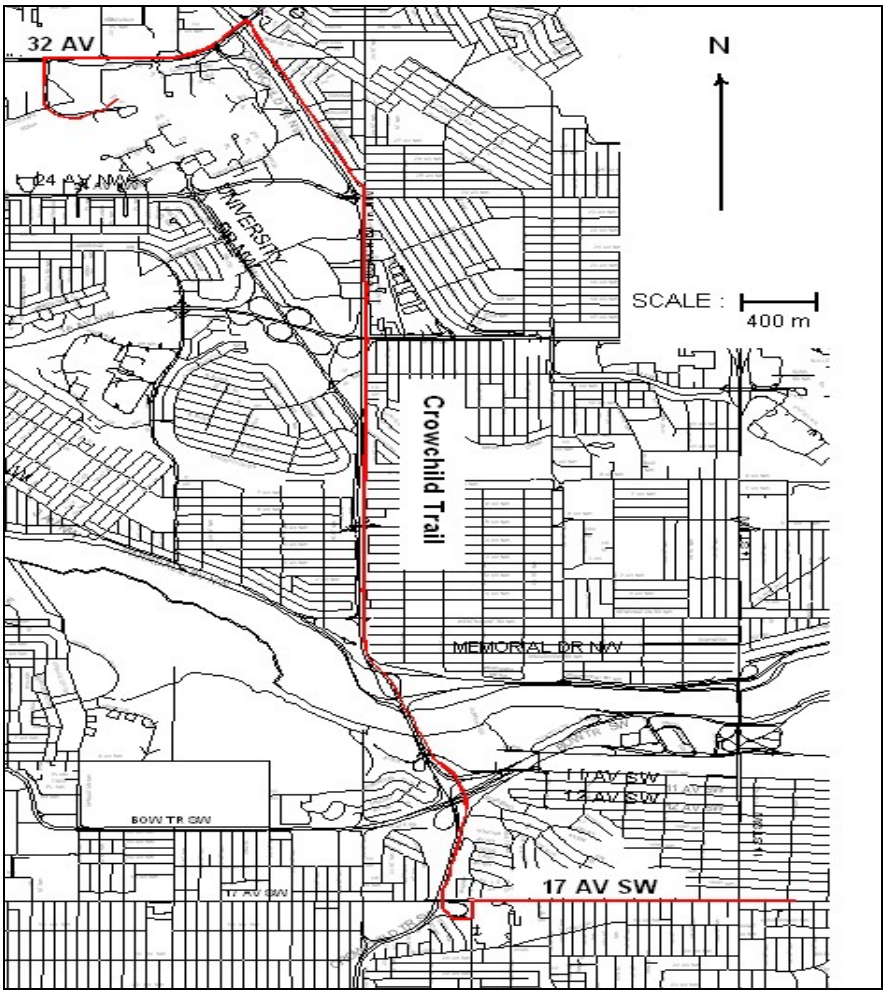

Figure 3.11: Section 4 route

Chapter 4

Code Multipath Characterization

4.1 Introduction

Code multipath error is one of the most significant sources of errors in DGPS applications. The magnitude of code multipath error depends on various factors like the correlator spacing, the precorrelation bandwidth and the antenna reflector distance. Ray (2000) performed a detailed analysis of code and carrier multipath characteristics. This chapter discusses one method of multipath characterization and the results of the code multipath error and correlation properties under various environmental conditions, on a mobile platform.

4.2 Code Multipath

Multipath is the phenomenon whereby a signal arrives at the receiving antenna by multiple paths by reflection or refraction (Braasch, 1996a). Multipath can be classified into diffused reflection, specular reflection and refraction. Diffused multipath results when the GPS signal gets reflected from rough surfaces and specular multipath results when the GPS signal gets reflected from smooth surfaces like water bodies and metal surfaces while refraction occurs due to the bending of the signal. Multipath affects the code and carrier of the GPS signal in different ways, for details see Ray (2000). The multipath signal travels a greater distance compared to the direct signal to arrive at the GPS antenna. The C/A code, which is a composite signal of the direct and the reflected signal, is distorted by the relative amount of phase shift the reflected signal suffers. If the direct signal is in-phase with the reflected signal then the signal power increases, and if they arrive out of phase at the antenna then the signal power at the antenna decreases. This has direct impact on the correlation peak and thus affects the pseudorange (and carrier phase, if applicable) measurements.

The magnitude of code multipath error in a receiver depends on the distance between the reflecting source and the receiving antenna. It also depends on the correlator spacing and the precorrelation bandwidth (Braasch, 1995). Figure 4.1 illustrates relative multipath induced tracking errors encountered among various correlators. The standard correlator has a spacing of 1.0 chip between the early and the late correlators and a precorrelation bandwidth of 2 MHz. In constrast, the Narrow Correlator™ has a precorrelation bandwidth of 8 MHz and a correlator spacing of 0.1 chip between the early and the late correlators (van Dierendonck et al., 1992). From Figure 4.1 it can be seen that the standard correlators are susceptible to substantial multipath errors for C/A code chip delays of up to 1.5 chips, with the most significant C/A code multipath errors occurring at about 0.25 and 0.75 chips (approaching 80 m error). On the other hand, in case of the Narrow Correlator™, multipath susceptibility peaks at about 0.2 chip (about 10 m error) and remains relatively constant out to 0.95 chip, where it rapidly declines to negligible errors after 1.1 chip. The code multipath error envelope for two more techniques MET™ (Multipath Elimination Technique, Townsend and Fenton, 1994) and MEDLL™ (Multipath Estimation Delay Lock Loop, Van Nee, 1995) are also shown in Figure 4.1.

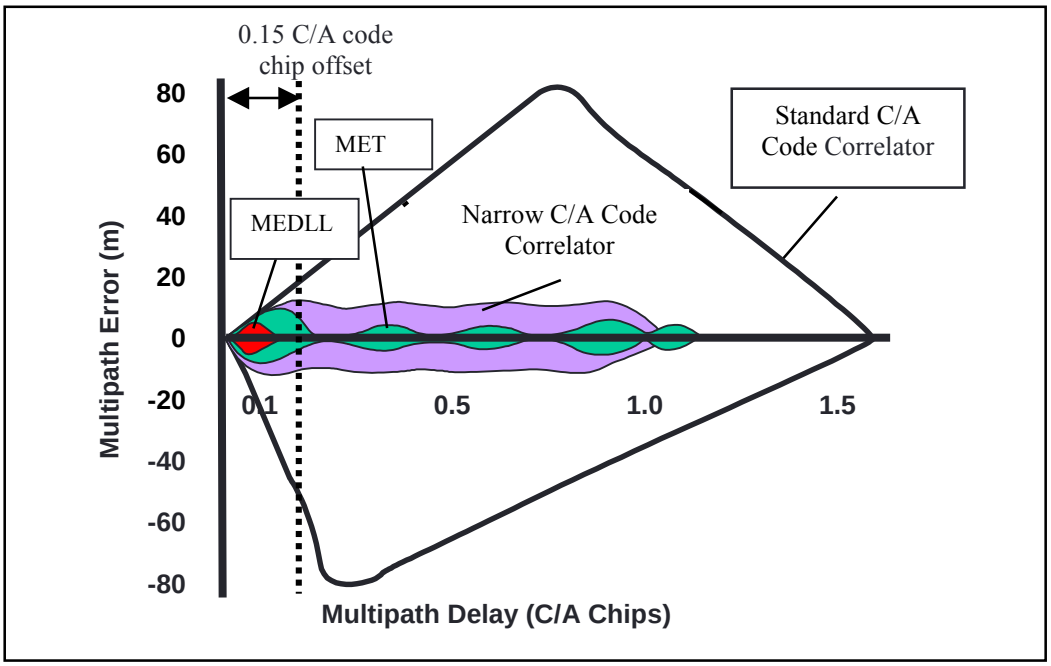

Figure 4.1: Code Multipath error envelope (Ford, 1998)

MET™ is an improvement of Narrow Correlator^{TM} with respect to multipath mitigation (Townsend and Fenton, 1994). It estimates the slope of the two sides of the autocorrelation peak as well as the amplitude, thus estimating for two lines that intersect at the peak, irrespective of the slope. MET™ has a multipath error envelope, which is oscillatory in nature, but is less susceptible compared to the Narrow Correlator™. However, MEDLL™ performs the best under multipath environment. For details on MEDLL™ see Van Nee (1995). MEDLL uses multiple narrow-spaced correlators to estimate multipath and remove it from the correlation function to provide a more pure signal correlation function (Van Nee, 1995). As MEDLL uses multiple correlators the receiver is bulky and expensive and is usually used in reference stations. All correlator based mitigation techniques are effective for long delay multipath errors but are ineffective to short delay multipath. Ray (2000) developed a method to mitigate short delay multipath error for static receivers. All the techniques listed above can remove 50% to 60% of multipath error (Ray, 2000) and the residual multipath error can still be significant on the order of few metres.

The maximum multipath delay (delay between the direct signal and the reflected signal) that can introduce an error in the measurement also depends on the correlator spacing and is given by equation (4.1).

$$M_{delay} = T_C + T_D \tag{4.1}$$

Where,

T_C is the C/A code chip width, and

T_D is the spacing between the prompt and early or prompt and the late correlator spacing

Hence, for a standard corrleator with a spacing of 0.5 chip between early and prompt correlators, the maximum multipath delay can be 1.5 chips, which translates to 450 m. However, for Narrow Corrlelator™ with a spacing of 0.1 chips, the maximum delay that can cause multipath error is 1.05 chips, which translates to 315 m. Therefore a reflector

placed more than 315 m from the receiving antenna will not introduce any code multipath.

Some of the characteristics of code multipath can be summarized as:

- Maximum code multipath error can be up to +/-150 m for receivers with wide correlator spacing (Ray, 2000).
- Affected by multipath signal delayed up to 450 metres.
- Non zero mean (van Nee, 1995).
- Magnitude of multipath error depends on the precorrelation bandwidth.
- Error is high frequency in nature under dynamic conditions.
- Decorrelates rapidly over distance.
- Code multipath has day-to-day repeatability in static receivers, (sidereal time) see, Lachapelle (1998).

For detailed description on the effect of multipath error on the various correlators, discriminator functions refer to Ray (2000).

4.3 Code Multipath Characterization

To characterize code multipath, it has to be detected and isolated. One of the most popular methods to isolate code multipath is the code minus carrier method also described by Braasch (1995). Other techniques involve estimation of multipath by comparing the measured correlation triangle with an accurate reference correlation triangle and estimating the multipath error as in MEDLL™ (van Nee, 1995).

Multipath analysis tends to be performed on the measurement residuals, which are output from an estimator in DGPS mode (e.g. least squares adjustment). This approach is simpler compared to other methods like MEDLL™. Most of the multipath mitigation techniques analyze these residuals to estimate and mitigate multipath, which works well for static applications. However, in kinematic applications the multipath environment is changing continuously and also the multipath characteristics on different antennas will be

different due to differences in satellite visibility (different levels of shading on various antennas). Hence, one of the code minus carrier methods to determine the multipath signature was implemented.

The pseudorange and carrier phase observables can be expressed as in (2.2) and (2.3) respectively.

By subtracting carrier phase measurement from code measurement (P-ϕ), the code minus carrier equation can be written as

$$P - \Phi = r = 2d_{ion} - \lambda N + \varepsilon_{p} + \varepsilon_{\varphi} \quad \textbf{(4.2)}$$

Equation (4.2) contains the ionospheric error (actually twice the ionospheric error), carrier phase ambiguity, code receiver noise and code multipath. Carrier receiver noise and multipath can be neglected since they are very small compared to the corresponding code values. The ambiguity term is a constant if there are no cycle slips and the ionospheric error generally varies slowly over time. A piece-wise linear regression model can therefore be implemented to remove terms due to the ionosphere and ambiguity. Since the ionospheric error changes with time, a regression model was implemented with predefined averaging intervals. An averaging interval of 6 minutes was chosen in the current model. The resulting code minus carrier residual (r), contains multipath and receiver noise which can be used for further analysis.

Figure 4.2 shows the code minus carrier differences for satellite number 31 having an elevation of 20°. The data was collected for a period of one hour. The green line in the figure is the regression fit of the data. The receiver was placed on the roof of the Engineering building and was operated as the reference station. The differences show a slowly varying bias, which is a characteristic behaviour of the ionospheric error with the initial bias due to the integer ambiguity.

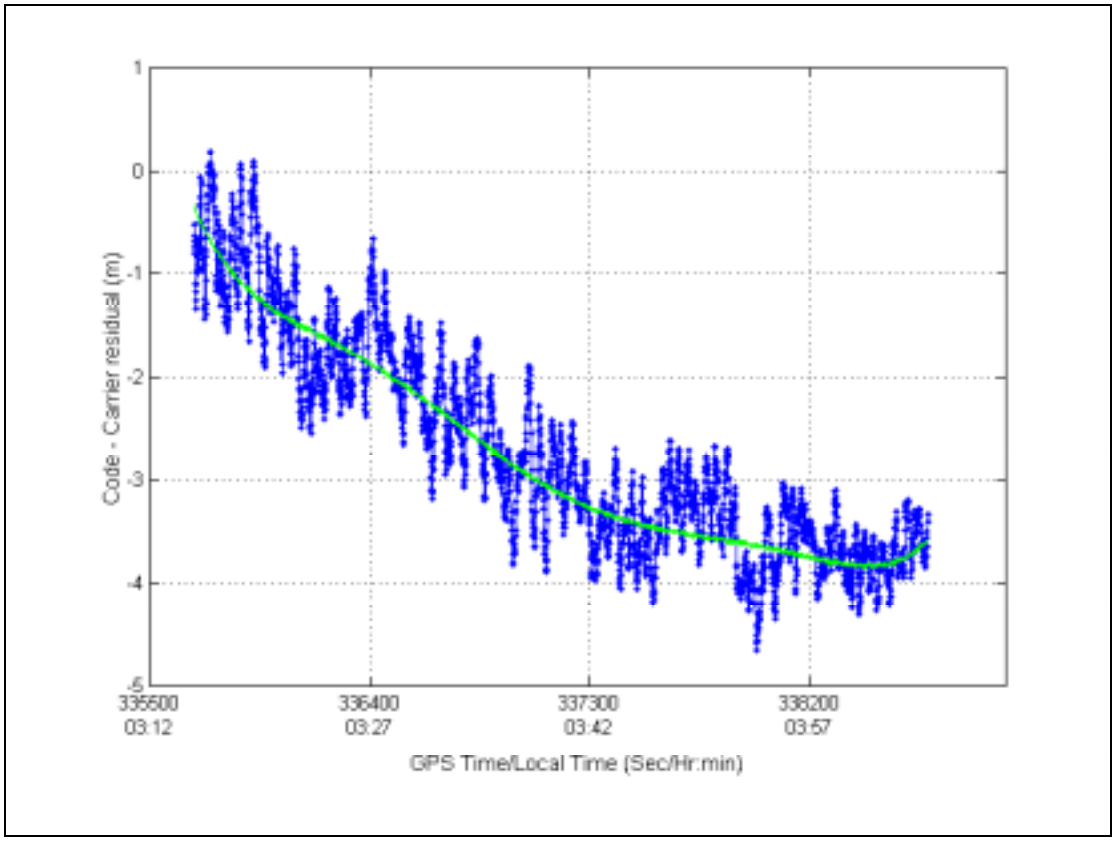

Figure 4.2: Code – Carrier difference, SV 31, (Elevation - 20°)

Figure 4.3 shows the code multipath error after removing the mean error by regression process and Figure 4.4 shows the corresponding temporal decorrelation of static multipath.

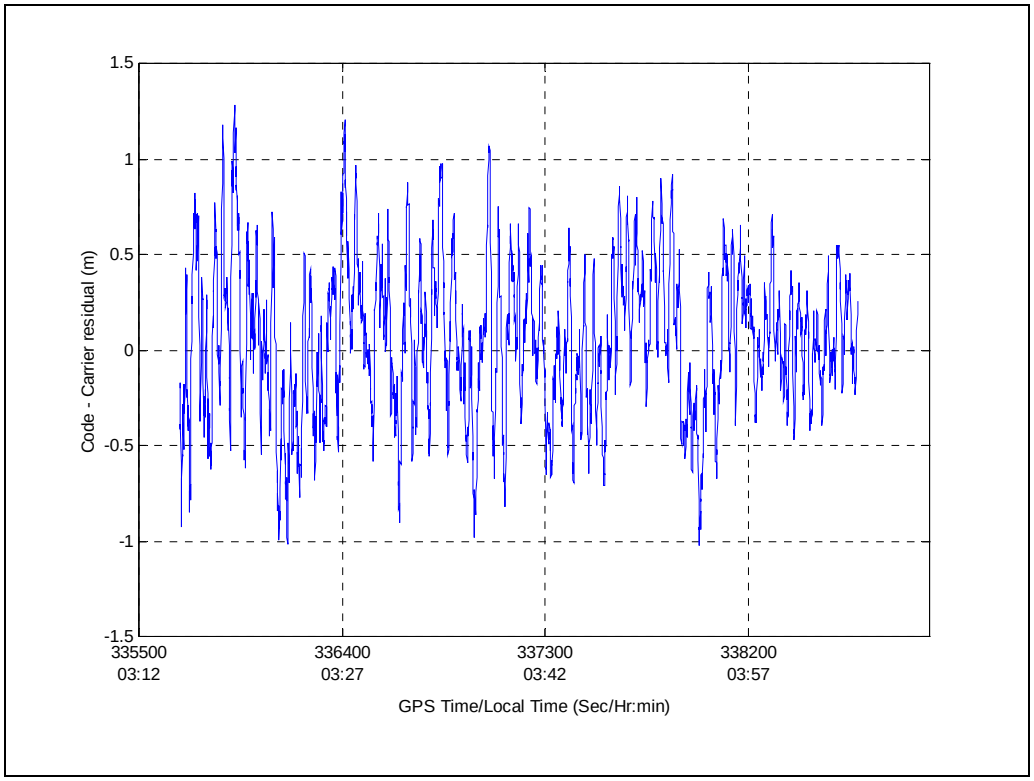

Figure 4.3: Code multipath error, SV 31, (Elevation - 20°)

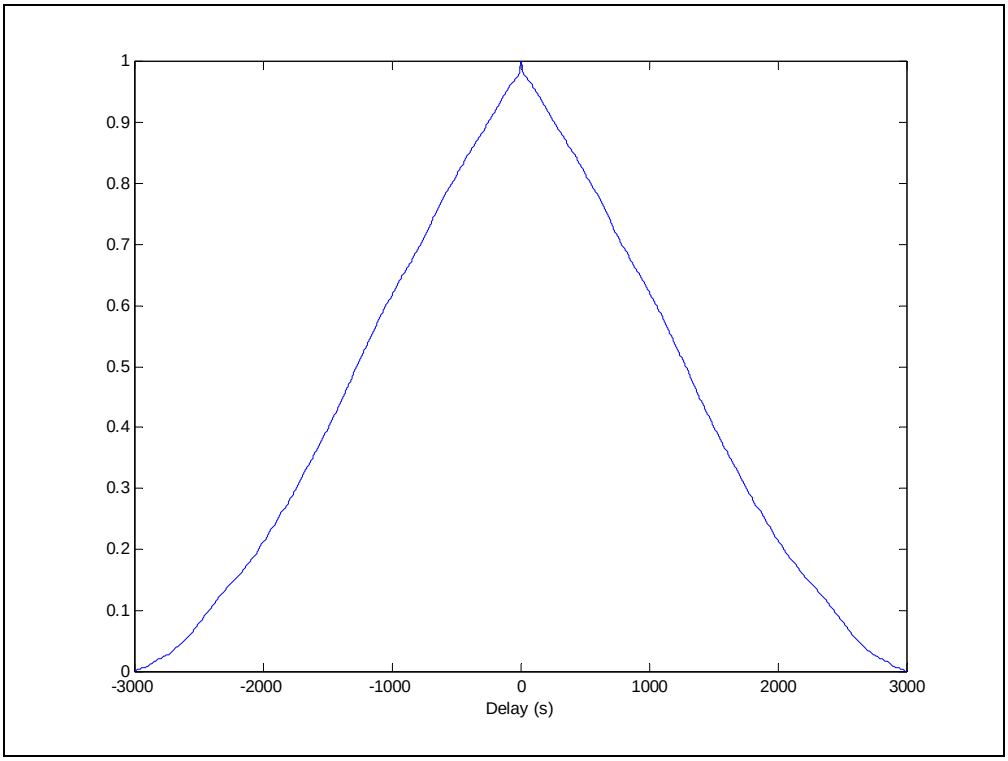

Figure 4.4: Temporal decorrelation of static multipath error, SV 31

Multipath errors up to one metre can be seen from Figure 4.3. To analyze the temporal correlation of multipath in static conditions the auto correlation function was computed from the same sample. The method of computing the autocorrelation function is described in Section 4.3.1.

The temporal decorrelation shows that the multipath error reaches 70% of its value after 10 minutes, which indicates a slowly changing process.

The regression process treats the integer ambiguity and the ionospheric error as a combined bias error and does not try to separate the two. Choosing the right period for the regression interval is also important. If the interval is too large, then the ionospheric error will not be completely removed and some residual errors will remain. If the interval is too small then the multipath error will also be removed as part of the estimation. Hence an optimum time interval has to be chosen. Various intervals were tested and an interval of six minutes was chosen for all the following analysis based on these tests.

Subtracting out the mean as determined from the regression model removes not only the integer ambiguity, but also the bias components present in all of the remaining terms. Code multipath is a non-zero mean process (van Nee, 1995) and this technique only isolates relative multipath effects and not the absolute multipath because the regression process removes the portion of multipath with nonzero mean (Braasch, 1995).

One limitation of this technique is that it cannot be used in real time, as the estimation of ionospheric error using the regression method is a batch process and requires stored data. Ray (2000) demonstrated a real time estimation of multipath, ionospheric error and ambiguity using a Kalman filter.

4.3.1 Multipath Correlation

One of the important reasons for the isolation of multipath error is to analyze its spatial correlation property between multiply spaced antennas. Spatial correlation can be studied by analyzing the cross correlation between the antennas. Correlation provides a measure

of the relationship between two quantities, which is multipath error between two antennas in this case.

The correlation between two signals can be computed from the following equation.

$$\Psi(XY) = E[XY] \tag{4.3}$$

X and Y are real stationary random processes and E[ ] is the expected value operator (Maybeck, 1994). The random variables X and Y can be standardized and the expectation of the product of the standardized variables is a dimensionless quantity known as the correlation coefficient.

The correlation coefficient is given as

$$\rho_{xy} = E\left[\left(\frac{X-\mu_x}{\sigma_x}\right)\left(\frac{Y-\mu_y}{\sigma_y}\right)\right] \tag{4.4}$$

Where,

μ_x, μ_y are the mean of the random variables X and Y, and

σ_x, σ_y are the standard deviations of random variables X and Y

Equation (4.4) can be simplified to (Maybeck, 1994)

$$\rho_{xy} = \frac{\sigma_{xy}}{\sigma_x \sigma_y} \tag{4.5}$$

The correlation coefficient can take values

$$-1 \le \rho_{xy} \le 1 \tag{4.6}$$

The two random variables are perfectly positively correlated if $\rho_{xy} = +1$ and uncorrelated if $\rho_{xy} = 0$. All other values of correlation coefficient give a measure of the similarity between the multipath errors between the two antennas.

4.3.2 Other Effects

Land mobile users are one of the largest users of GPS and foliage and urban environments are some of the most frequently encountered environments by these users.

Foliage attenuation is often characterized as attenuation in dB/m of foliage penetration. The attenuation depends on the nature and height of the tree. When a mobile receiver is moving rapidly past intermittent trees, the mean attenuation should be considered instead of attenuation from a single tree. Spilker (1994c) has provided comprehensive analysis on foliage attenuation of GPS signals on moving and stationary GPS receivers. Lachapelle et al., (1994) conducted tests to study the seasonal effect of foliage on GPS signal availability and accuracy for vehicular navigation.

The intermittent blockage imposes severe stress on the carrier and code tracking loops, which can result in frequent loss of signal lock. Also, the poor signal power (C/N_o) reaching the antenna will severely affect the quality of the measurements and the position estimates.

The Doppler measurement is generated from the carrier tracking loop and as a result is affected by carrier phase multipath. The effect of multipath on code has already been discussed in section 4.1. Unlike code multipath, carrier phase multipath can only have values up to one quarter of a wavelength. A derivation for carrier phase error due to multipath and experimental results can be found in Ray (2000).

Ray (2000) also showed that multipath with 90° phase error with the direct signal introduces phase error, where as a multipath signal with phase error of 0° and 180° does not exhibit phase error in the composite signal but effects the signal amplitude. The change in signal amplitude will cause code multipath error and does not impact the Doppler measurements. Also the error in phase is a function of the distance of the reflector with respect to the antenna and the power of the reflected signal (van Nee, 1995). Ray (2000) has shown that the carrier multipath frequencies are in the order of 0.01 Hz for static case, which can introduce an error of few millimetres/sec in Doppler and its effect is much smaller on a moving platform due to the averaging effect. Therefore, the effect of multipath on Doppler on a moving vehicle can be neglected.

4.4 Results

The receiver tracking performance under different environmental conditions gives a good insight into the ability of the receiver to operate in various environmental conditions. It also gives an insight into the quality of the computed position. This can be analyzed by studying the Geometric Dilution of Precision (GDOP), which is a quality indicator, related to the geometry and in turn a function of the satellites tracked. The tracking performance is discussed before proceeding to the multipath error. All the discussion is based on the data collected from Day 1, and is applicable to Day 2 and Day 3. Data on Day 2 and Day 3 were collected at the same sidereal time as Day1.

4.4.1 Tracking Performance in Section 1 [Open Sky]

Figure 4.5 and Figure 4.6 show the number of satellites tracked by all four antennas and their corresponding GDOP's in Section 1.

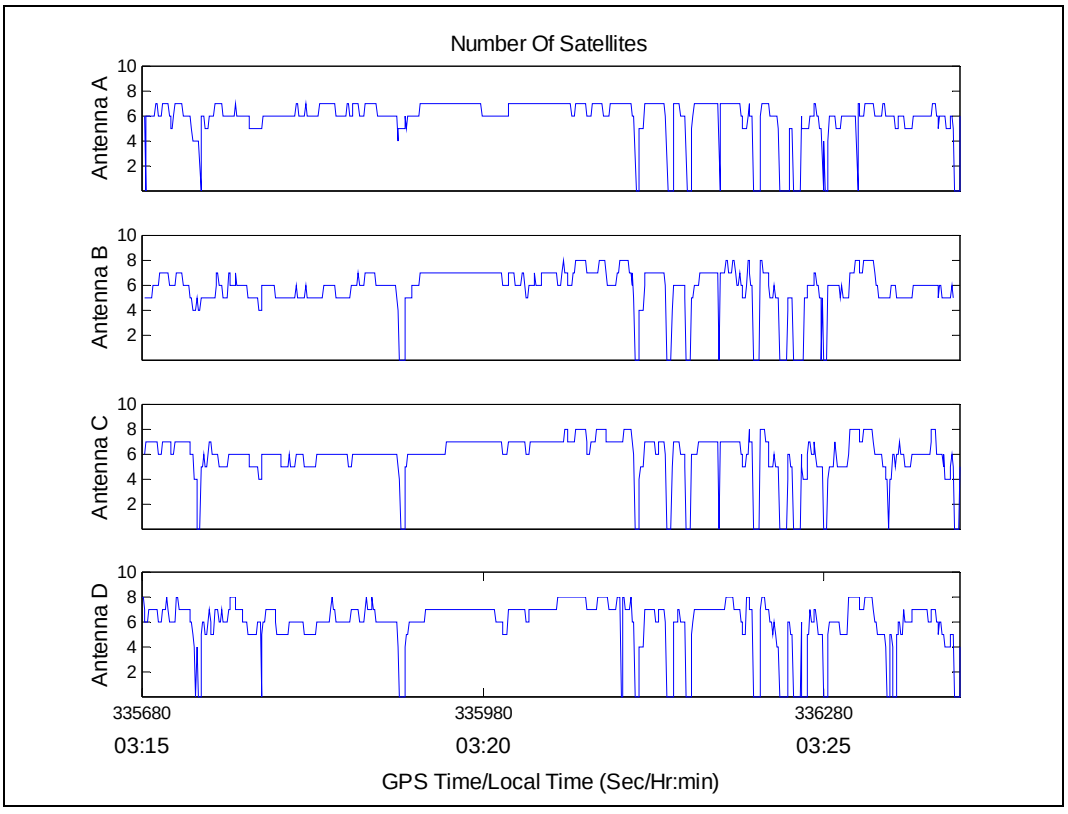

Figure 4.5: Satellite visibility for each antenna - Section 1

Although Section 1 has clear visibility there are some outages in satellite visibility due to underpasses present along the road. Most often these outages are correlated across antennas, which is a characteristic of complete signal masking. In situations when there are less than three satellites a solution is not available, and GDOP is shown to be zero, whereas theoretically it tends to infinity.

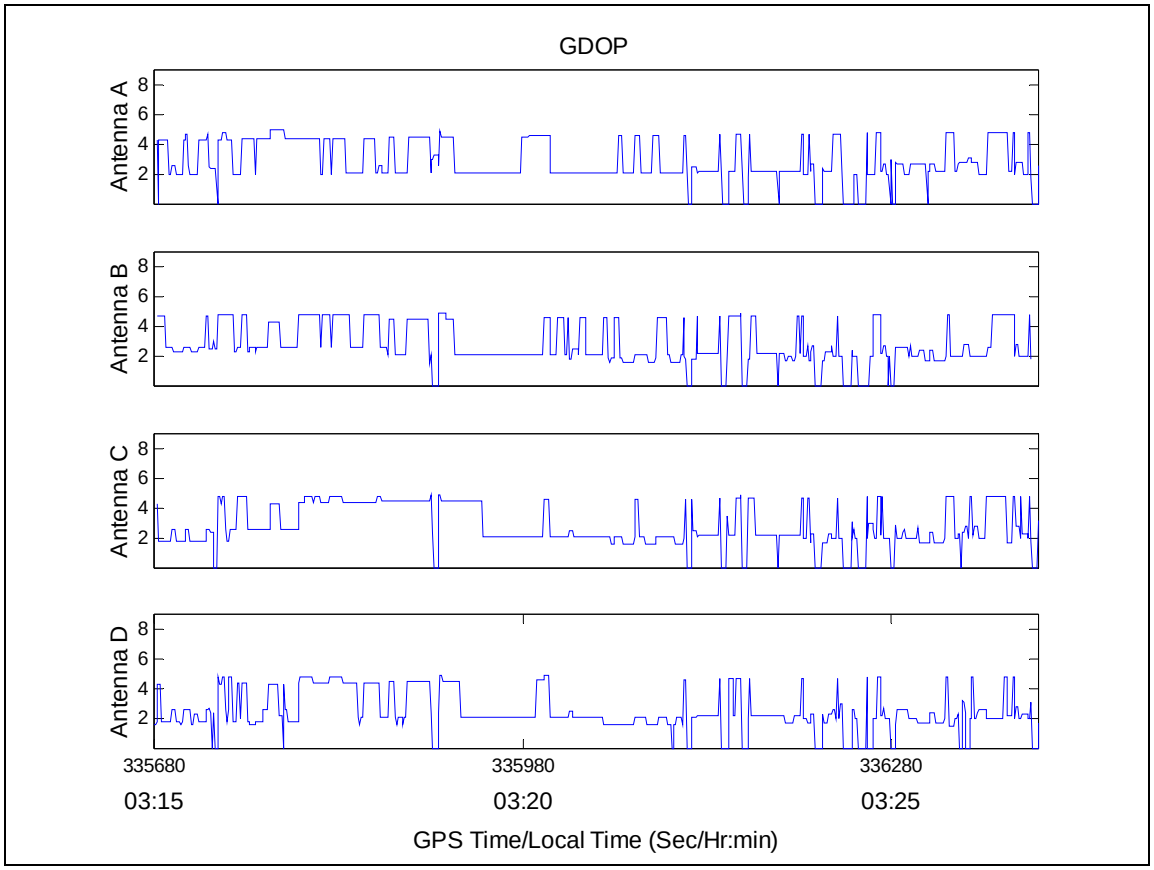

Figure 4.6: GDOP variation for each antenna - Section 1

The variation in the GDOP in all four antennas is between 2 to 6. Despite overall good satellite visibility, there is a large variation of GDOP in all antennas, which can be attributed to the constant changes in geometry associated with the motion of the vehicle and also due to the occasional obstruction of the signal by the neighbouring vehicles.

The average number of visible satellites and GDOP for Section 1 are summarized in Table 4.1. All the plots shown in this chapter are generated from data collected on Day 1.

Similar results were observed on Day 2 hence the results are not shown. The base line separation between antennas is shown in Figure 3.1 and range between 0.7 to 0.9 m.

Table 4.1: Average satellite visibility and GDOP - Section 1

	Antenna A	Antenna B	Antenna C	Antenna D
Average GDOP	3.3	3.5	3.4	3.2
Average number of SVs	5.8	5.7	5.8	4.7

The percentage visibility of the number of satellites tracked in section 1 is shown in Figure 4.7. The graph indicates a given number of satellites (say six) visible as a percentage of the total time during Section 1. For example seven satellites are visible in Antenna A (shown in blue colour in Figure 4.7) 40% of the time. Also, in all antennas, at least six or seven satellites are visible more than 30% of the time.

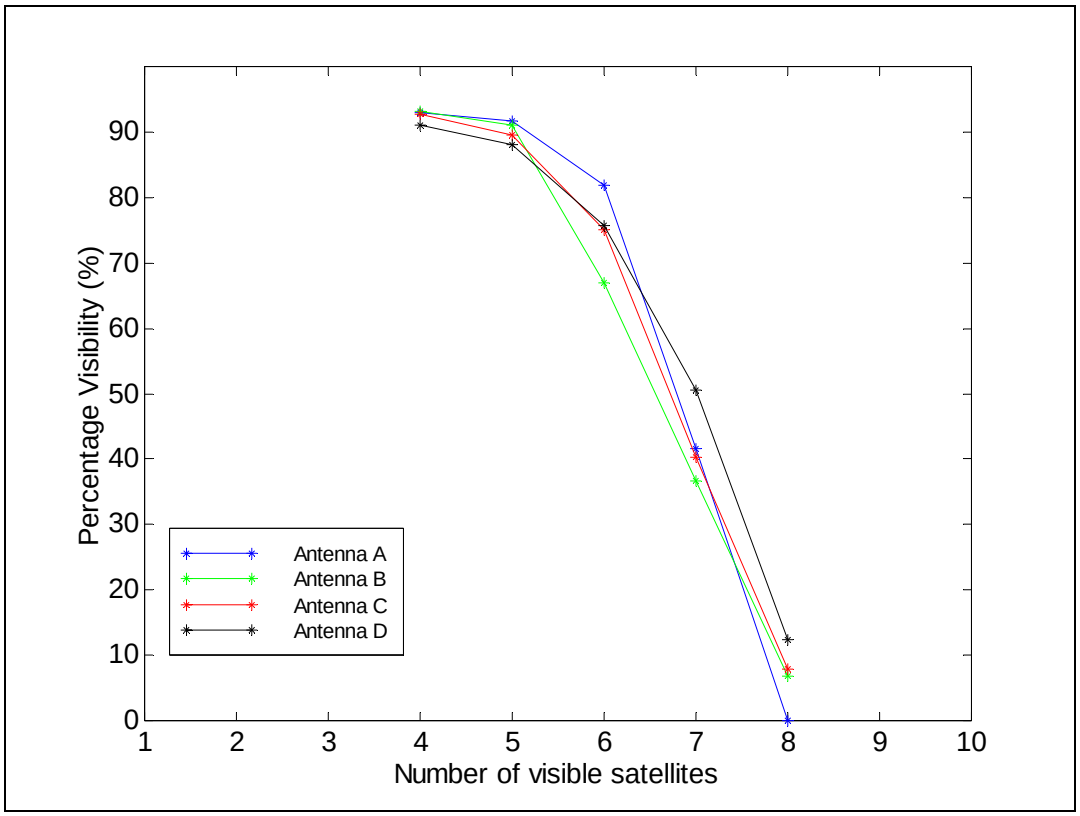

Figure 4.7: Percentage visibility of satellites in Section 1

4.4.2 Tracking Performance in Section 2 [Urban Canyon]

Section 2 contains dense urban conditions and it imposes severe restrictions on the tracking performance of the receivers. Due to the anisotropic nature of the signal masking, the geometry of the satellites is also severely affected. Figures 4.8 and 4.9 show the number of satellites tracked and their corresponding GDOP's for all four receivers.

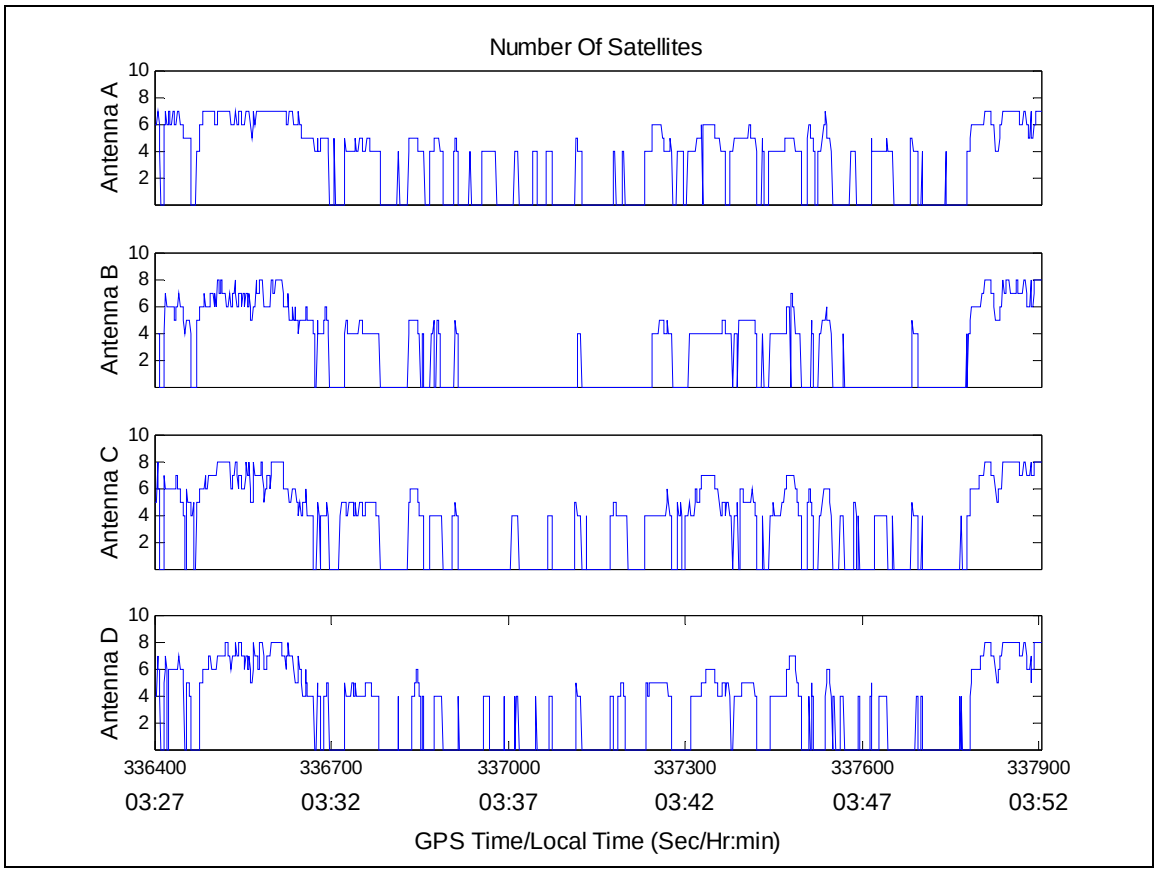

Figure 4.8: Satellite visibility for each antenna - Section 2

There are a lot of satellite outages all through this section and the number of satellites being tracked varies from 3 to 8.

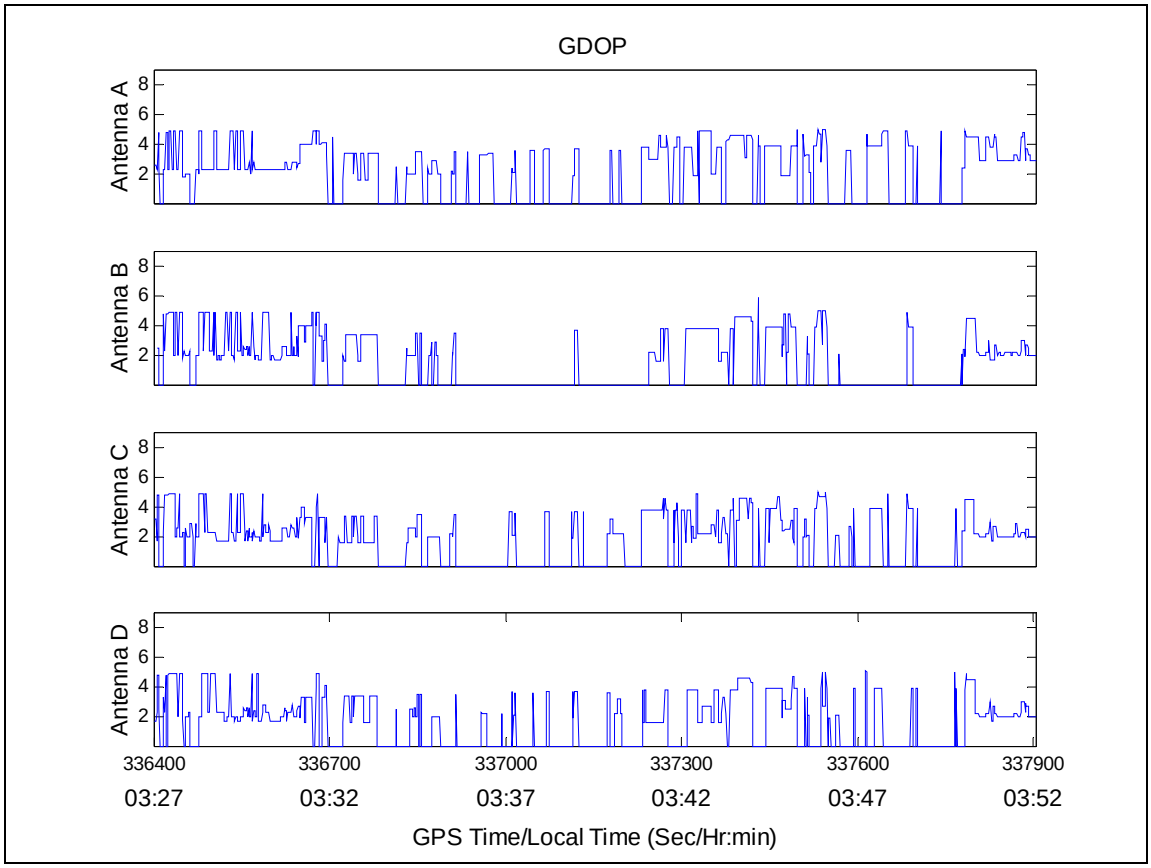

Figure 4.9: GDOP variation for each antenna - Section 2

From the figures severe signal outages can be inferred. The GDOP varies between 2 and 19. The average number of visible satellites and GDOP during Section 2 is shown in Table 4.2.

Table 4.2 : Average satellite visibility and GDOP - Section 2

	Antenna A	Antenna B	Antenna C	Antenna D
Average GDOP	5.6	6.1	5.5	5.9
Average number of SVs	3.2	2.6	3.3	1.2

There is a severe decline in the average number of satellites in all four antennas compared to Section 1 and also the average values of GDOP is larger compared to the values in Section 1. The numbers in the table represents the average satellites tracked for

the entire section, and it includes the epochs when there were no satellites or less than four satellites available. There were sufficient number of satellites available to compute a position fix most of the time and the results are shown below.

Figure 4.10 shows the percentage visibility of satellites for all four antennas. The graph is generated based on the satellites available to compute position from the post processing software and indicates the number of satellites visible as a percentage of the total time of the test.

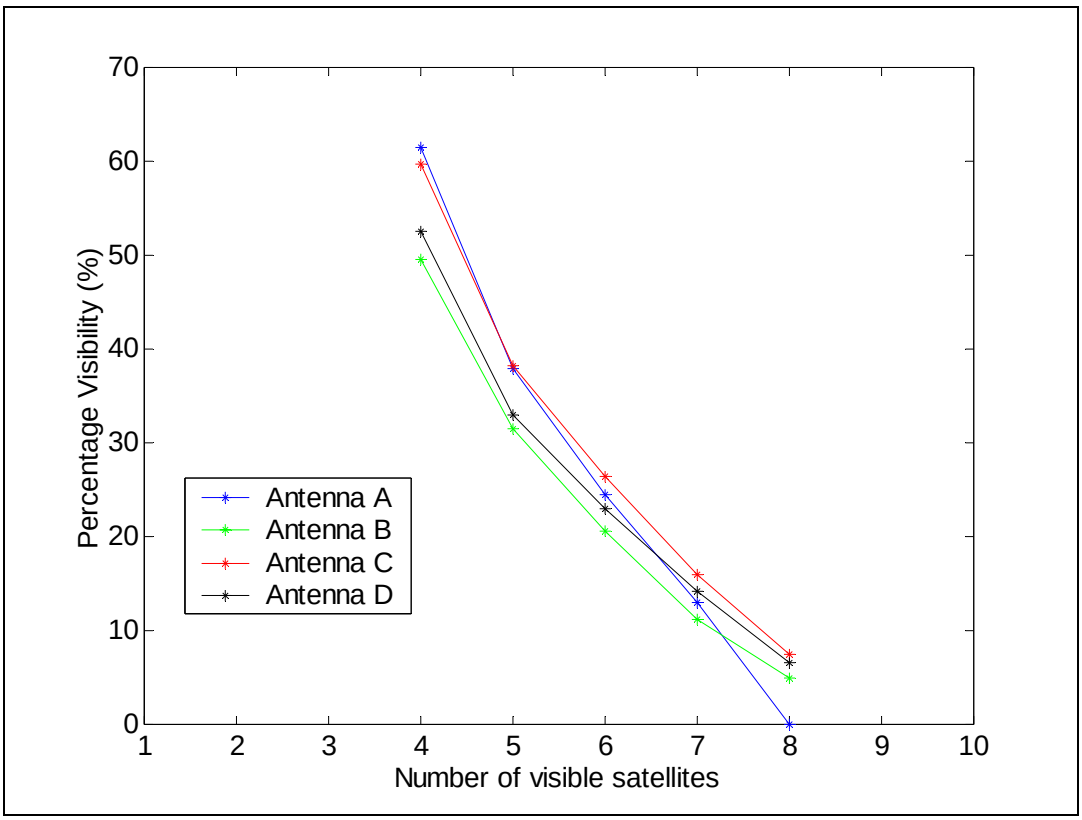

Figure 4.10: Percentage visibility of satellites - Section 2

Most of the time (50-60%) only four satellites were available and no solution was possible for 38.6%, 50.4%, 40.3% and 46.2% in Antennas A, B, C and D, respectively. This means that a solution was available for less than 50% of the time during this test.

4.4.3 Tracking Performance in Section 3 [Dense Foliage]

To address the receiver tracking performance during this section, the satellite visibility graphs, and DOP variations are once again analyzed. Figures 4.11 and 4.12 below show the number of satellites tracked and the GDOP values in each of the four antennas.

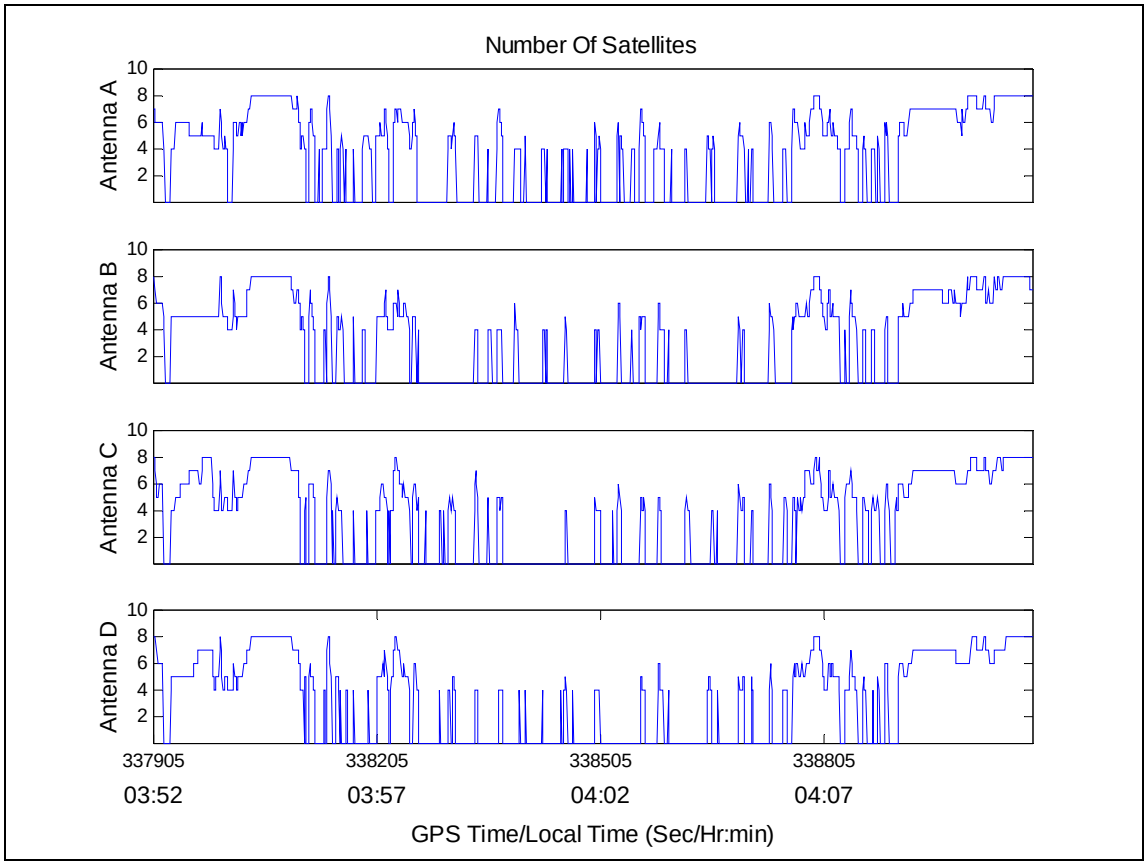

Figure 4.11: Satellite visibility for each antenna - Section 3

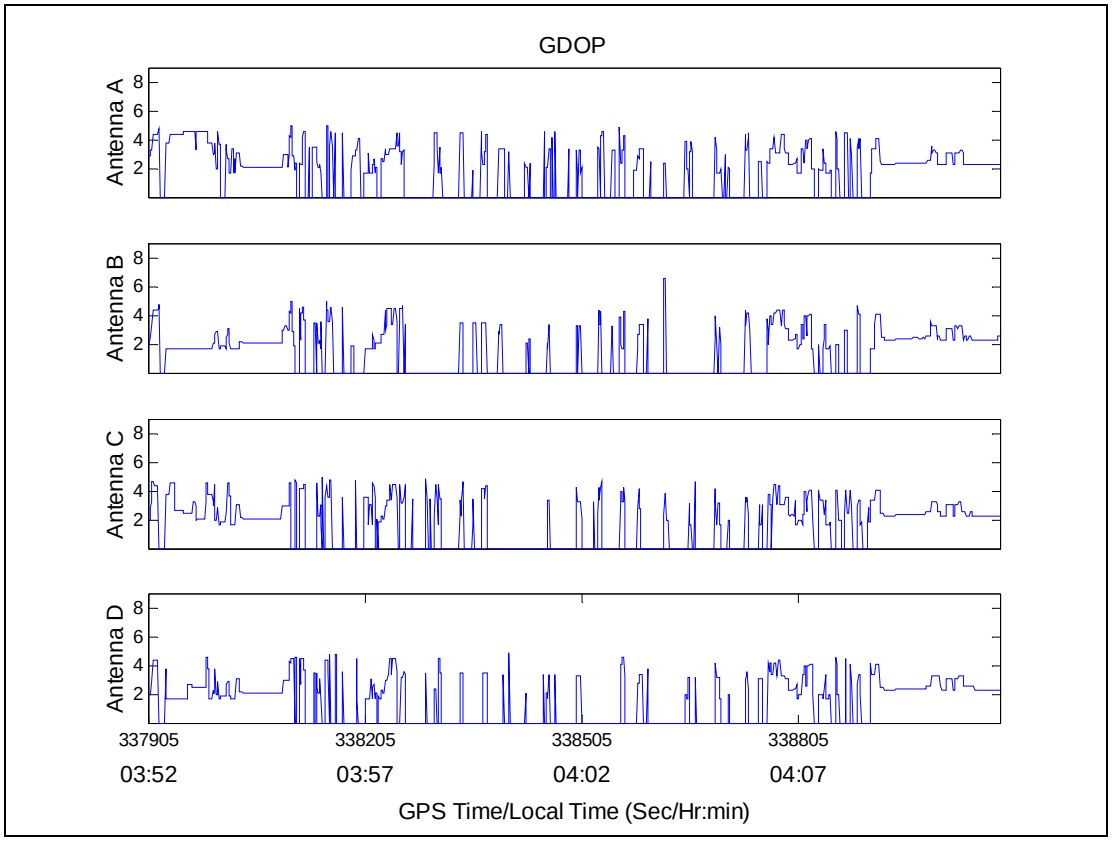

Figure 4.12: GDOP variation for each antenna - Section 3

The GDOP variations are large which is a result of frequent changes in the satellite visibility. The satellite visibility in Figure 4.11 shows large variations, which correlate to the GDOP values in Figure 4.12. However there is a small section at the beginning, which is also the entrance to the 10th Street where the visibility is good.

The average number of visible satellites and the average GDOP during the entire section is shown in Table 4.3.

Table 4.3: Average satellite visibility and GDOP - Section 3

	Antenna A	Antenna B	Antenna C	Antenna D
Average GDOP	4.9	5.9	5.1	5.3
Average number of SVs	3.5	3.1	3.3	2.3

Once again the average number of satellites tracked in this section is less than four as it includes the epochs when there were no satellites or less than four satellites available. However, the actual percentage visibility of each satellite for position computation is shown in Figure 4.13.

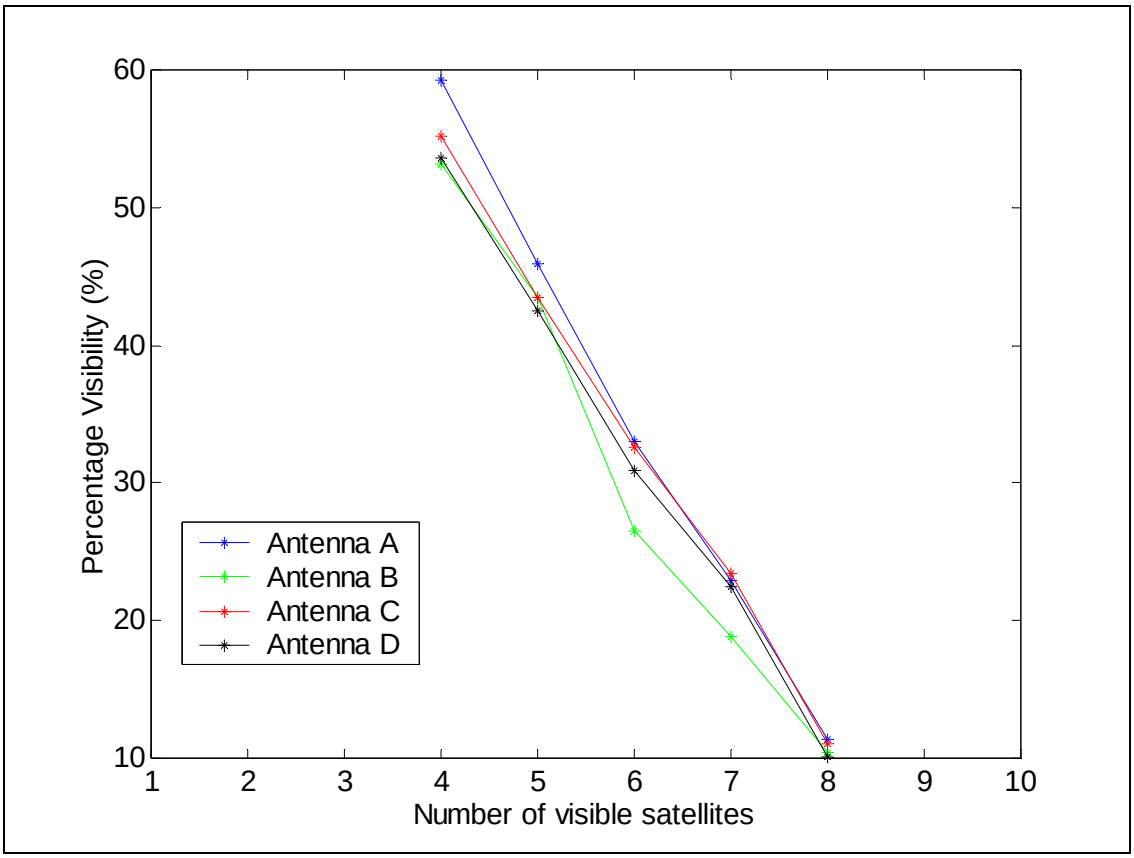

Figure 4.13: Percentage visibility of satellites - Section 3

At least four satellites were visible 55-60% of the time, and less than four satellites were available for 40.6%, 49.1%, 42.7% and 45.3% in Antennas A, B, C and D respectively. This means that a solution was available only 45% of the time on average for all antennas.

4.4.4 Tracking Performance in Section 4 [Semi-urban conditions]

Section 4 is mostly the retrace of section 1 and the results are similar to the section 1. The tracking performance and the GDOP variations among the four antennas are listed in Table 4.4.

Table 4.4: Average satellite visibility and GDOP - Section 4

	Antenna A	Antenna B	Antenna C	Antenna D
Average GDOP	2.9	3.2	3.1	3.2
Average number of SVs	6.7	6.5	6.6	5.7

The visibility performance is similar to section 1 (open sky) and the percentage visibility graph for section 4 is shown in Figure 4.14.

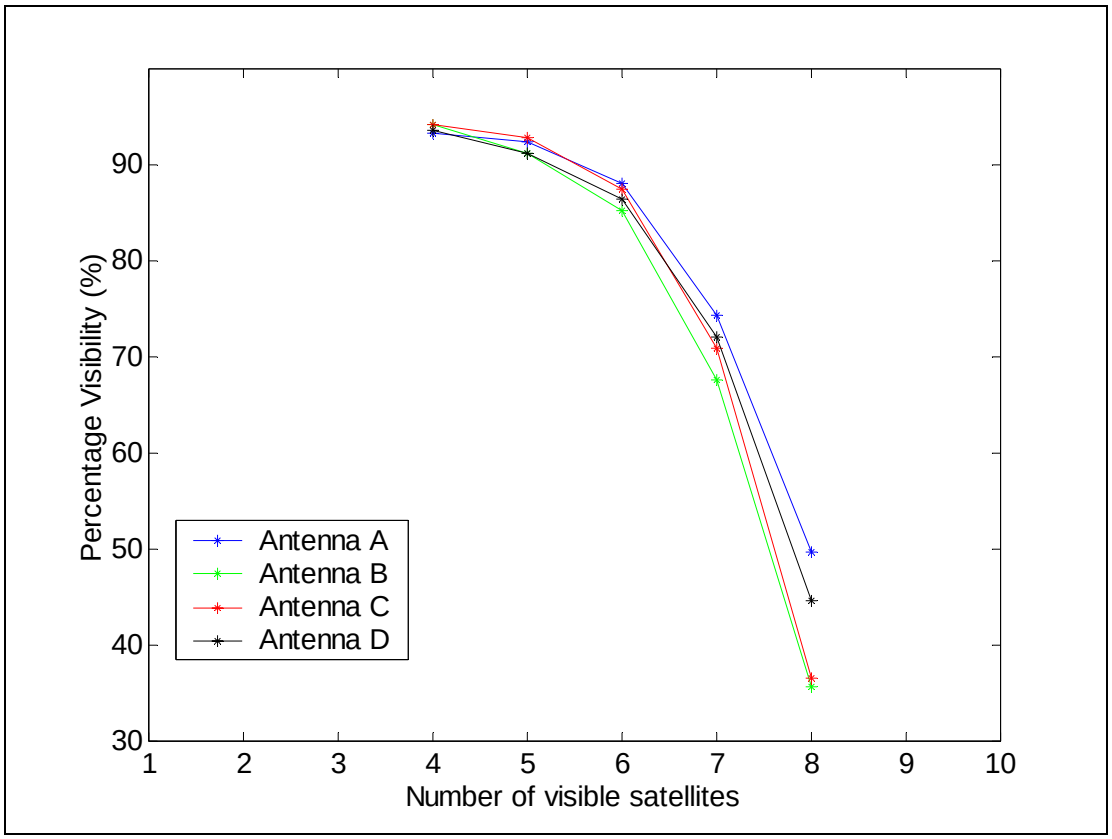

Figure 4.14: Percentage visibility of satellites - Section 4

At least seven or eight satellites were visible for at least 40% of the time and less than four satellites were available for 6.6%, 5.8%, 5.8% and 5.2% in Antennas A, B, C and D, respectively. This means, on average, a position solution was available at least 95% of the time for all receivers.

To provide a reference, the percentage visibility of the reference station was computed. A NovAtel Beeline™ receiver, which is an eight-channel receiver, was setup as the reference station. The base station had eight satellites for almost 100% of the time; the GDOP at the base station was also less than 2.

4.4.5 Code Multipath Error in Section 1 [Open sky]

The results of code minus carrier difference for various sections among different antennas are presented in this section. Code multipath errors in all four receivers for satellites 17 and 26 during Section 1 are shown in Figures 4.15 and 4.16, respectively.

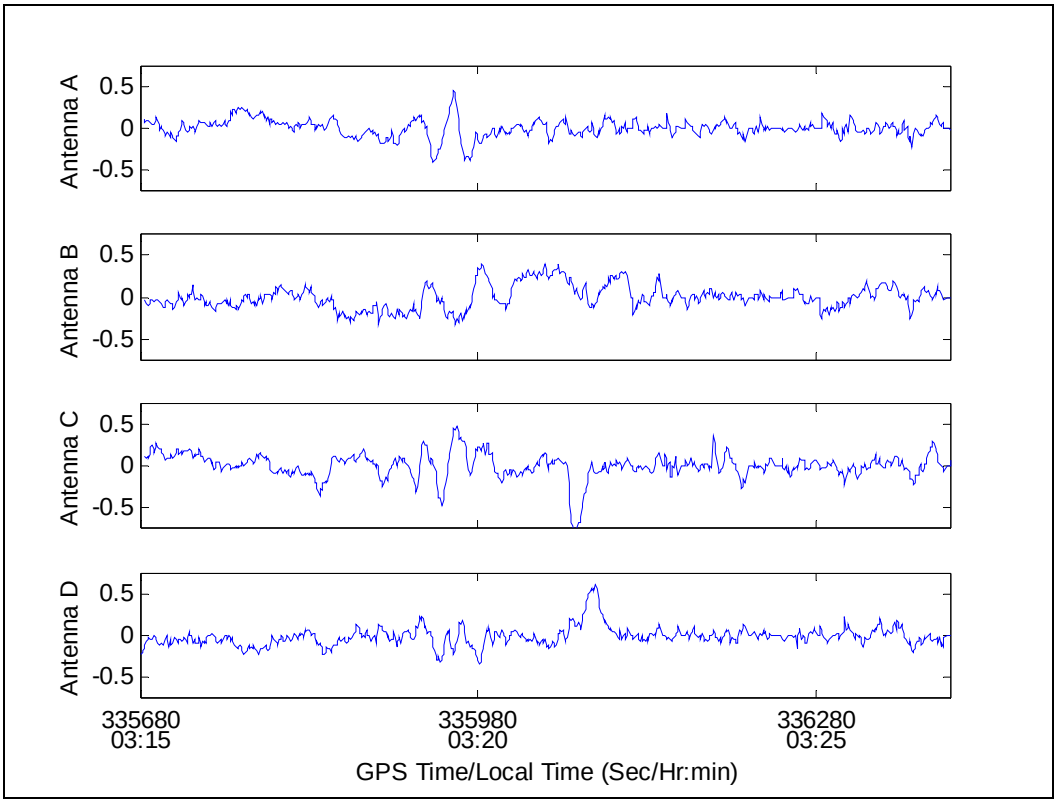

Figure 4.15: Code-carrier differences (SV – 17), Elevation (68° - 33°) – Section 1

The vehicle is in motion during the entire period, except for a few stops at the lights. The multipath errors have magnitudes up to +/-0.75 m and are present in all antennas. Figure 4.16 shows the code multipath error for a slightly lower elevation satellite, which has a higher susceptibility to multipath.

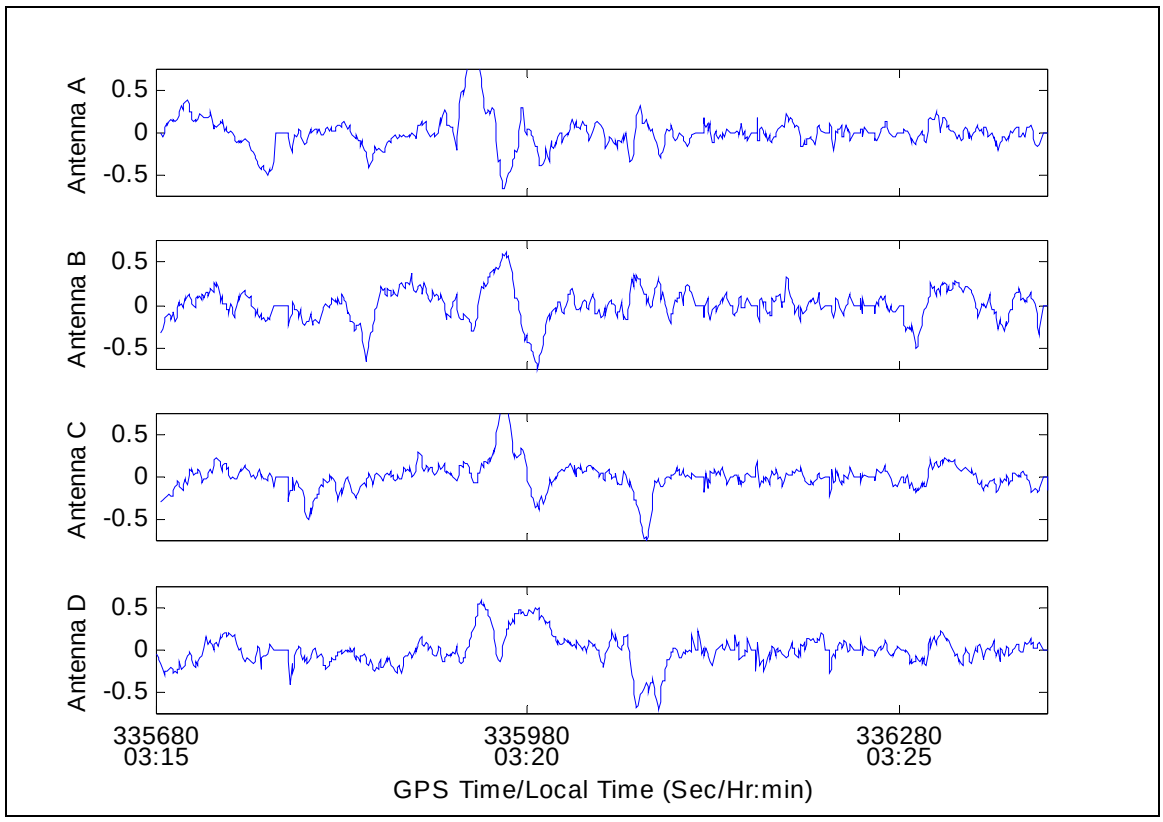

Figure 4.16: Code-carrier differences (SV - 26), Elevation (31° - 14°) - Section 1

The code minus carrier differences in Figure 4.16 has oscillations due to multipath up to magnitudes of 1m. Around GPS time 335980 (3.20 PM local time) multipath oscillations up to 1m can be seen on all four antennas. At this particular time, the vehicle had stopped at traffic lights and the multipath could be due to reflections from surrounding vehicles. Small jumps or spikes are noticeable in the figures, which are due to the restarting of the averaging interval of the regression process used to remove the ionospheric error. Multipath is smaller during the remainder of the run when the vehicle was moving which

agrees in principle with the fact that multipath averages out in dynamic conditions (assuming a relatively open environment).

The mean, and RMS values of these multipath errors for some of the satellites are shown in Table 4.5.

Table 4.5 Statistics for code minus carrier differences - Section 1

	Antenna A		**Antenna B**		**Antenna C**		**Antenna D**	
	Mean (m)	RMS (m)	Mean (m)	RMS (m)	Mean (m)	RMS (m)	Mean (m)	RMS (m)
SV 17 Elv: 68°-33°	0.00	0.11	-0.00	0.16	0.00	0.16	-0.01	0.11
SV 23 Elv: 88°-64°	-0.00	0.16	-0.00	0.13	-0.00	0.16	-0.03	0.13
SV 26 Elv : 31°-14°	0.00	0.20	-0.00	0.19	-0.00	0.18	-0.01	0.18
SV 3 Elv : 46°-41°	-0.00	0.15	0.00	0.14	-0.00	0.19	0.01	0.23
SV 31 Elv : 8°-32°	0.00	0.28	-0.00	0.19	0.00	0.40	0.00	0.27
SV 9 Elv : 6°-24°	-0.02	0.24	-0.01	0.61	0.00	0.23	-0.00	0.31

The RMS value of the multipath error progressively increases (0.11 m to 0.61 m) for lower elevation satellites, which is expected since lower elevation satellites are more susceptible to multipath error. The mean multipath error is also zero in most of the cases. The multipath error in this section is very small less than half a metre in most cases.

To study the multipath spatial correlations properties between antennas on a moving platform the cross correlation between the antennas was computed and the results are shown Figure 4.17. The multipath between antennas, are not entirely uncorrelated but have some oscillations, which are not similar across the antennas. This is because the code multipath delay changes from antenna to antenna and could be totally out of phase

with respect to the first antenna. The multipath oscillations depend on the relative path delay between the direct and the reflected signal (Braasch, 1996).

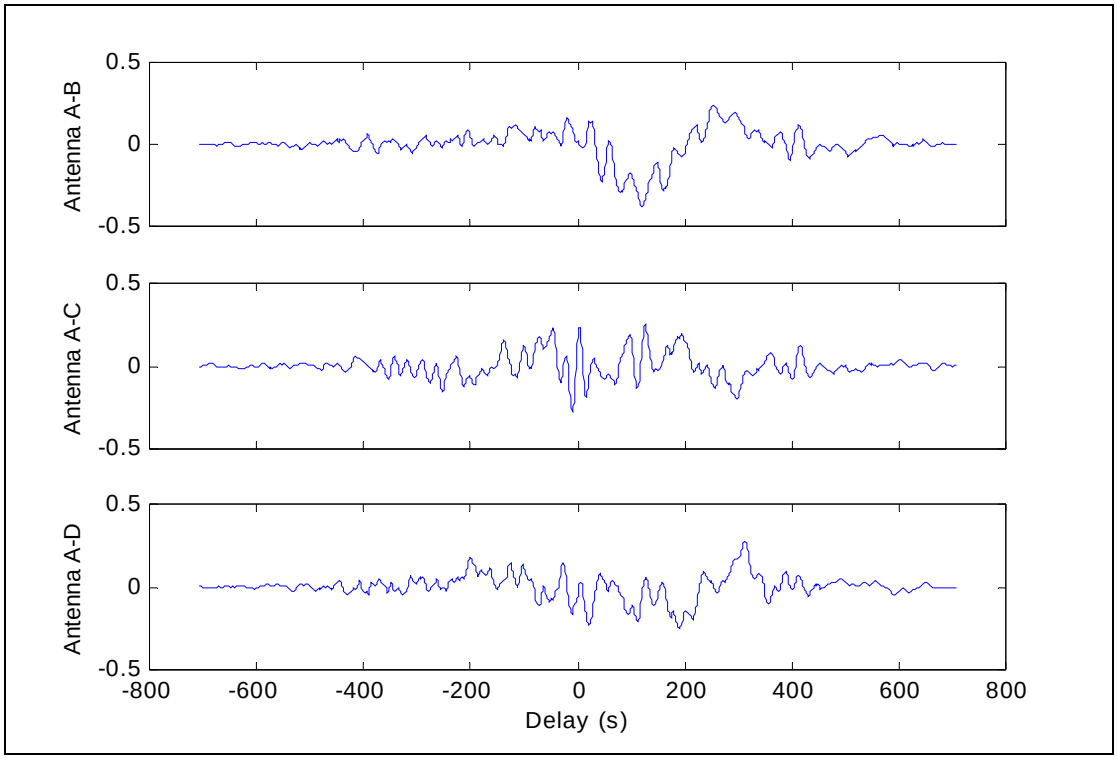

Figure 4.17: Correlation coefficient (SV - 17), Elevation (68° - 33°) – Section 1

If the code minus carrier differences between antennas were uncorrelated then the cross correlation would be a constant. The cross correlation plots above show weak correlation in the code minus carrier differences between antennas. This decorrelation property can be used to identify and remove multipath. The plot also shows multipath correlation between antennas for certain delays. For example, with a delay of 100 seconds a correlation of 0.45 can be seen between Antennas A and B. However, the pseudorange measurements are used in real time and only the multipath errors at zero delay is of real concern. Therefore correlation between two antennas at zero delay should be considered. A maximum correlation coefficient of 0.2 was seen for measurements for various satellites between various antennas. A correlation coefficient of one means perfect correlation and a coefficient of zero represents uncorrelated signals. Therefore, a

correlation coefficient of 0.2 represents very weak correlation between two antennas. To analyze the temporal correlation of multipath in each antenna the autocorrelation of the multipath error was computed and the result for all the four antennas are shown in Figure 4.18.

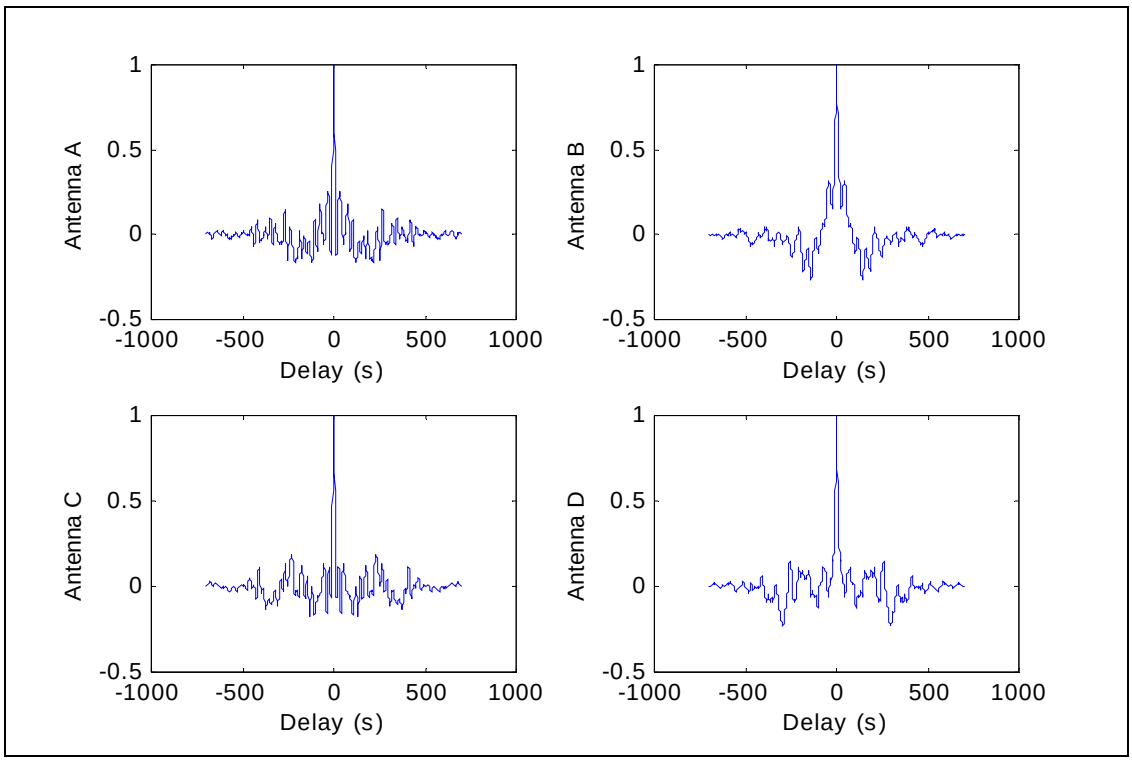

Figure 4.18: Temporal correlation (SV - 17), Elevation (68° - 33°) – Section 1

The temporal correlation shows that multipath error decorrelates to its 50% value within 5 s where as for the static case the decorrelation time is few minutes (Figure 4.4). The temporal correlation shows the averaging nature of multipath in dynamic conditions and does not have any impact on the methodology chosen in this research.

4.4.6 Code Multipath Error in Section 2 [Urban environment]

The results of code minus carrier difference in an urban environment are presented in this section. Code multipath errors in all four receivers for satellites 17 and 26 in Section 2 are shown in Figures 4.19 and 4.20, respectively.

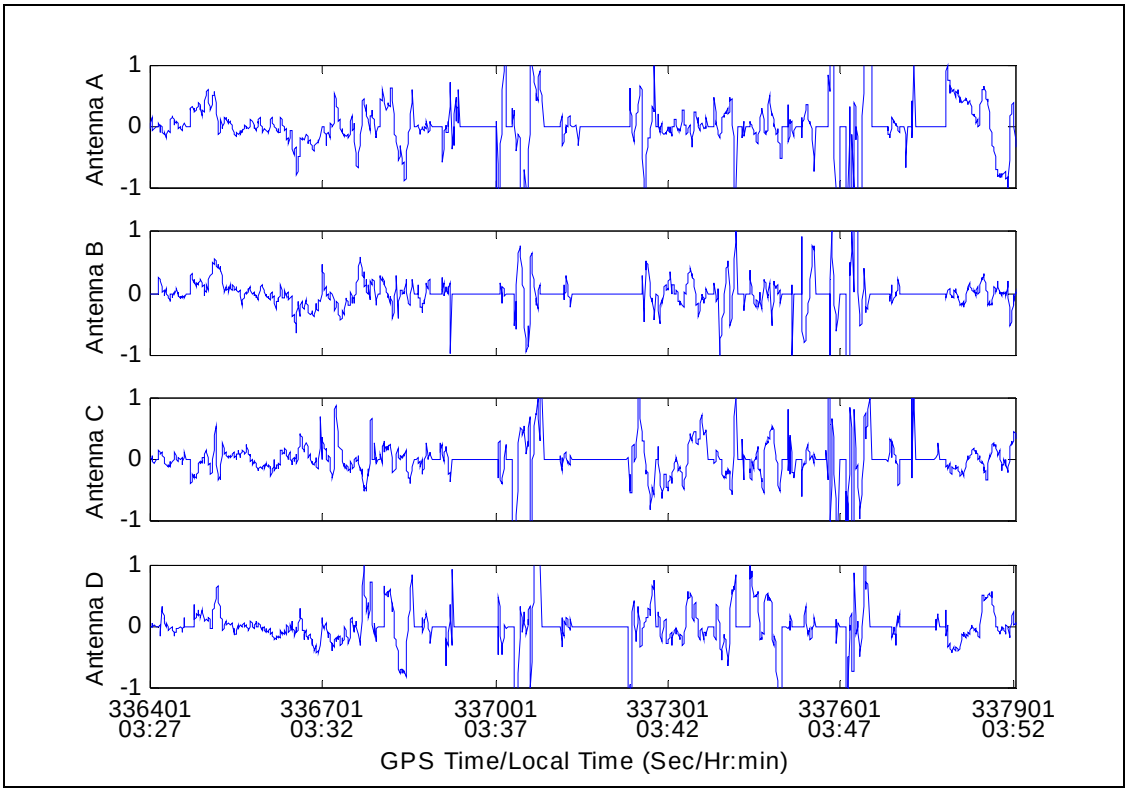

Figure 4.19: Code-carrier differences (SV - 17), Elevation (68° - 33°) – Section 2

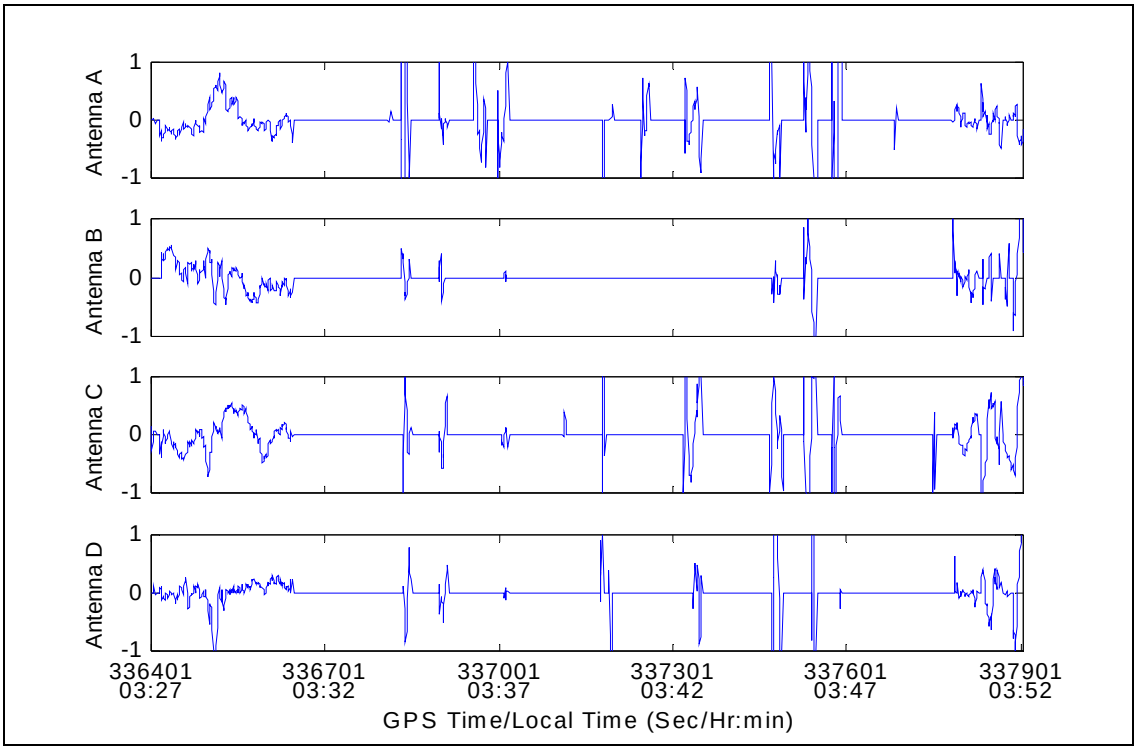

Figure 4.20: Code-carrier differences (SV - 26), Elevation (31° - 14°) – Section 2

The code minus carrier differences in Figures 4.19 and 4.20 show oscillations due to multipath up to magnitudes of 2 m. Due to the high-rise buildings the masking angle is restricted to 50° above the horizon. As a result there are hardly any measurements available for satellite number 26, which has elevation angle less than 30°. The multipath error is random in nature unlike the multipath error in Section 1.

The mean, and RMS values of these multipath errors for some of the satellites are shown in Table 4.6.

Table 4.6: Statistics for the code minus carrier differences - Section 2

	Antenna A		**Antenna B**		**Antenna C**		**Antenna D**	
	Mean (m)	RMS (m)	Mean (m)	RMS (m)	Mean (m)	RMS (m)	Mean (m)	RMS (m)
SV 17 Elv: 68°-33°	0.01	0.47	-0.00	0.29	-0.00	0.36	-0.00	0.35
SV 23 Elv: 88°-64°	0.01	0.26	-0.00	0.19	0.00	0.15	0.02	0.15
SV 26 Elv: 31°-14°	-0.00	0.42	0.00	0.18	0.00	0.37	0.00	0.29
SV 3 Elv: 46°-41°	0.00	0.55	-0.00	0.29	0.00	0.45	-0.00	0.27
SV 31 Elv: 8°-32°	0.00	0.16	-0.00	0.42	0.00	0.19	-0.00	0.19
SV 9 Elv: 6°-24°	0.00	0.23	-0.00	0.28	0.00	0.26	-0.00	0.35

The RMS values of the multipath error for all satellites and in all antennas are larger by an order of magnitude compared to Section 1. The RMS values for low elevation satellites are smaller (0.25m, SV 9) compared to the higher elevation satellites, because most of the time the low elevation satellites were completely blocked by buildings and the RMS errors does not show any multipath during these times. The spatial decorrelation of multipath error across the antenna assembly for satellite 17 is shown in Figure 4.21.

Maximum multipath errors up to 11 m, 5.2 m, 6.2 m, and 6.0 m was seen on Antennas A, B, C and D respectively.

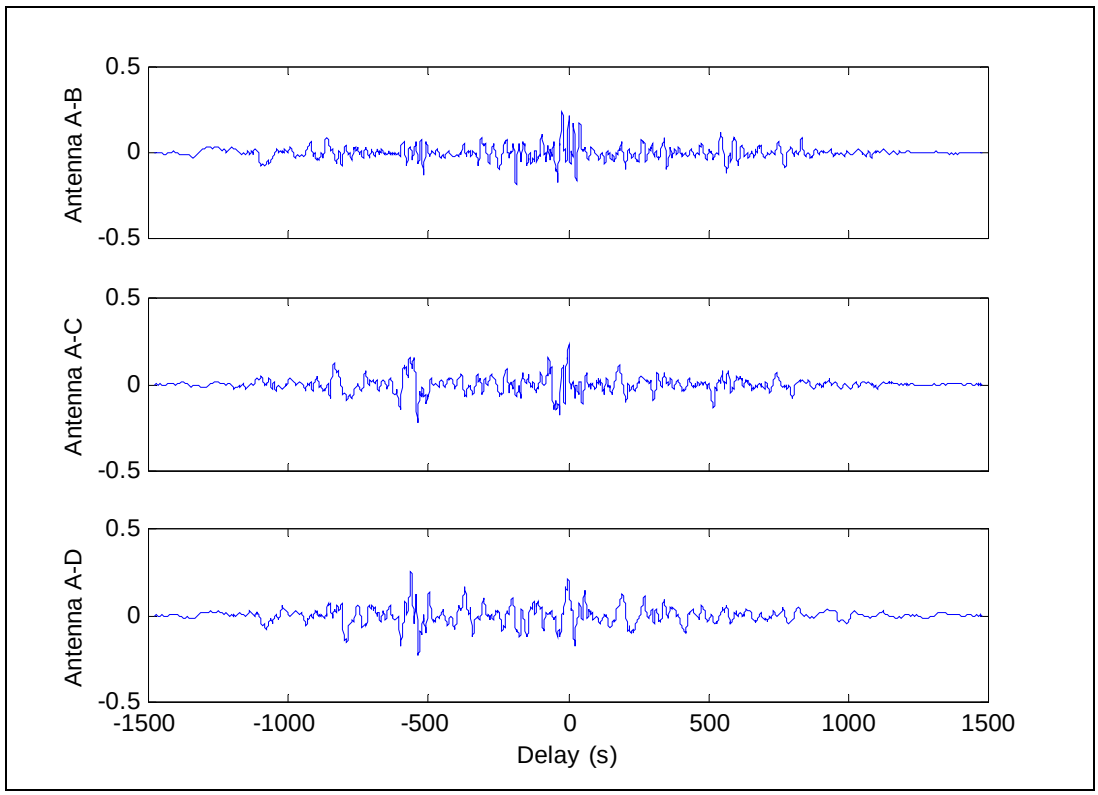

Figure 4.21: Correlation coefficient (SV - 17), Elevation (68° - 33°) – Section 2

The cross correlation plots above show very weak correlation in the code minus carrier differences between antennas. A maximum spatial correlation of 0.3 was seen on some measurements. This shows that multipath is weakly correlated among different antennas and this behaviour will be exploited to detect multipath in the form of blunders, and is discussed in Chapter 5.

4.4.7 Code Multipath Error in Section 3 [Dense Foliage environment]

The results of code minus carrier difference under heavy foliage environment are presented in this section. Code multipath errors in all four receivers for satellites 17 and 26 in Section 3 are shown in Figures 4.22 and 4.23 respectively.

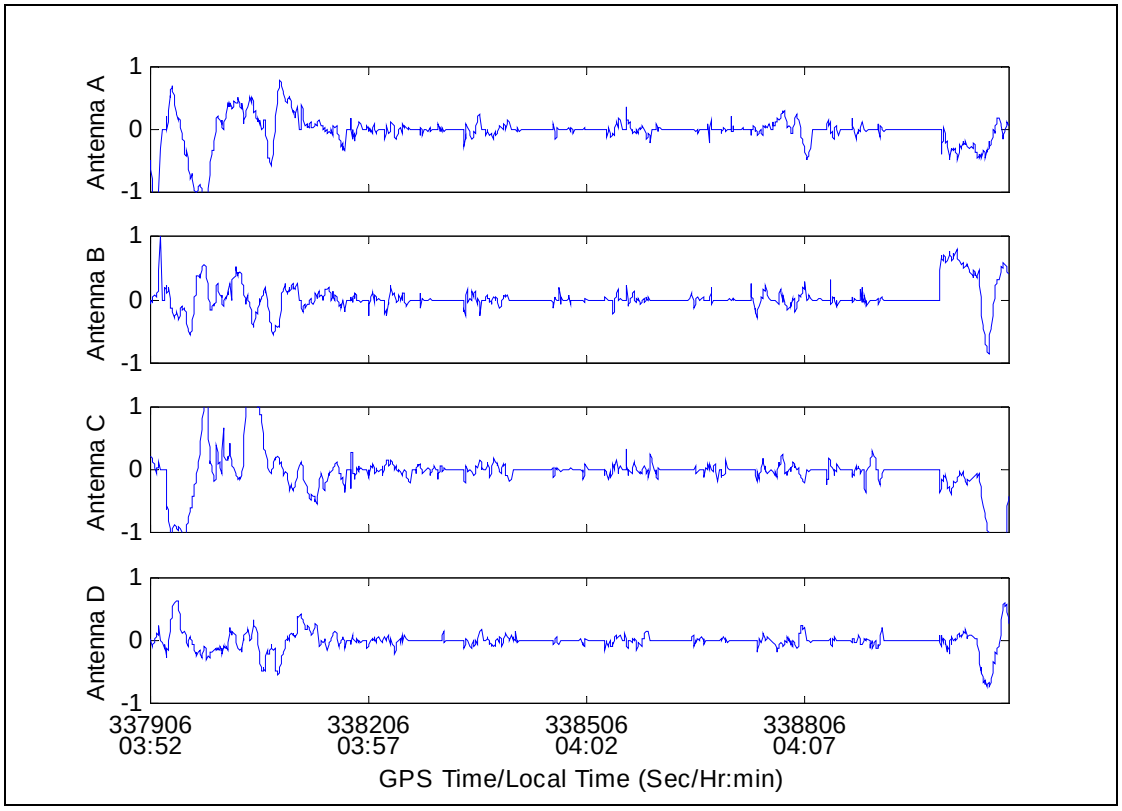

Figure 4.22: Code-carrier differences (SV - 17), Elevation (68° - 33°) – Section 3

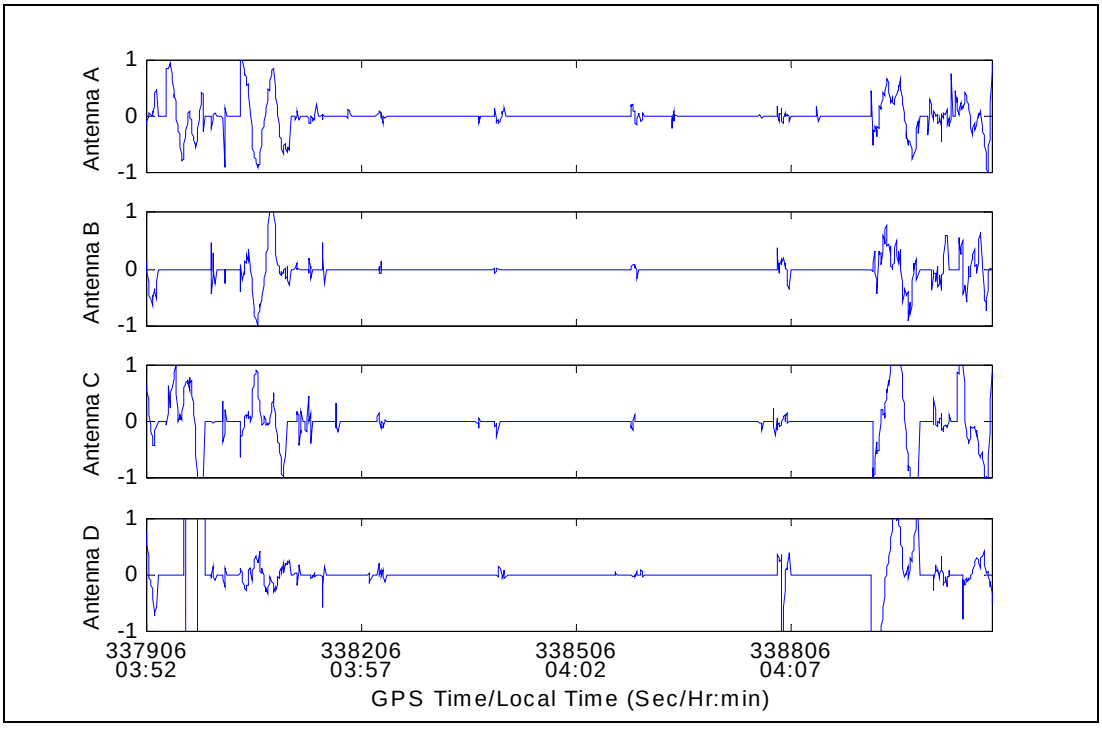

Figure 4.23: Code-carrier differences (SV - 26), Elevation (31° - 14°) – Section 3

The code minus carrier differences show multipath oscillations between GPS time 337906 and 338206 during which time the vehicle was travelling on 10th Street that had fairly good visibility. However, on Montcalm Crescent and Frontenac Avenue large outages can be seen on the code minus carrier differences due to poor tracking as a result of dense foliage. Some satellites with high elevation angle (SV number 23 with an elevation angle of 80˚, Appendix D) show fairly good tracking with small multipath oscillations.

The mean and RMS values of these differences for different satellites are shown in Table 4.7.

Table 4.7: Statistics for the code minus carrier differences - Section 3

	Antenna A		**Antenna B**		**Antenna C**		**Antenna D**	
	Mean (m)	RMS (m)	Mean (m)	RMS (m)	Mean (m)	RMS (m)	Mean (m)	RMS (m)
SV 17 Elv: 68°-33°	-0.02	0.26	0.03	0.20	-0.04	0.35	-0.01	0.15
SV 23 Elv: 88°-64°	0.00	0.27	-0.03	0.23	0.02	0.15	-0.02	0.23
SV 26 Elv: 31°-14°	0.00	0.23	-0.00	0.19	-0.00	0.36	-0.03	1.87
SV 3 Elv: 46°-41°	0.06	0.44	-0.05	0.37	-0.01	0.34	0.03	0.29
SV 31 Elv: 8°-32°	0.06	0.46	0.02	0.37	-0.06	0.57	-0.02	0.53
SV 9 Elv: 6°- 24°	0.06	0.34	0.01	0.41	0.09	0.48	-0.05	0.29

The multipath error in Section 3 is relatively smaller compared to Section 2 for high elevation satellites (0.2 – 0.3 m), this is because foliage, unlike buildings, does not reflect signals but absorbs the energy from electromagnetic signals resulting in attenuation of signal power. The lower elevation satellites have higher RMS errors (0.3 m to 0.6 m); most of the errors are due to the buildings present in the beginning and the end of the test.

The RMS errors are consistent across antennas except on Antenna D for SV 26, which has RMS errors in the range of 1.9 m. There were also a few blunders in Antenna D in the range of 9 m. This is the kind of blunders that the system is expected to detect and eliminate. The correlation coefficients across antennas are shown in Figure 4.24 and Figure 4.25 respectively.

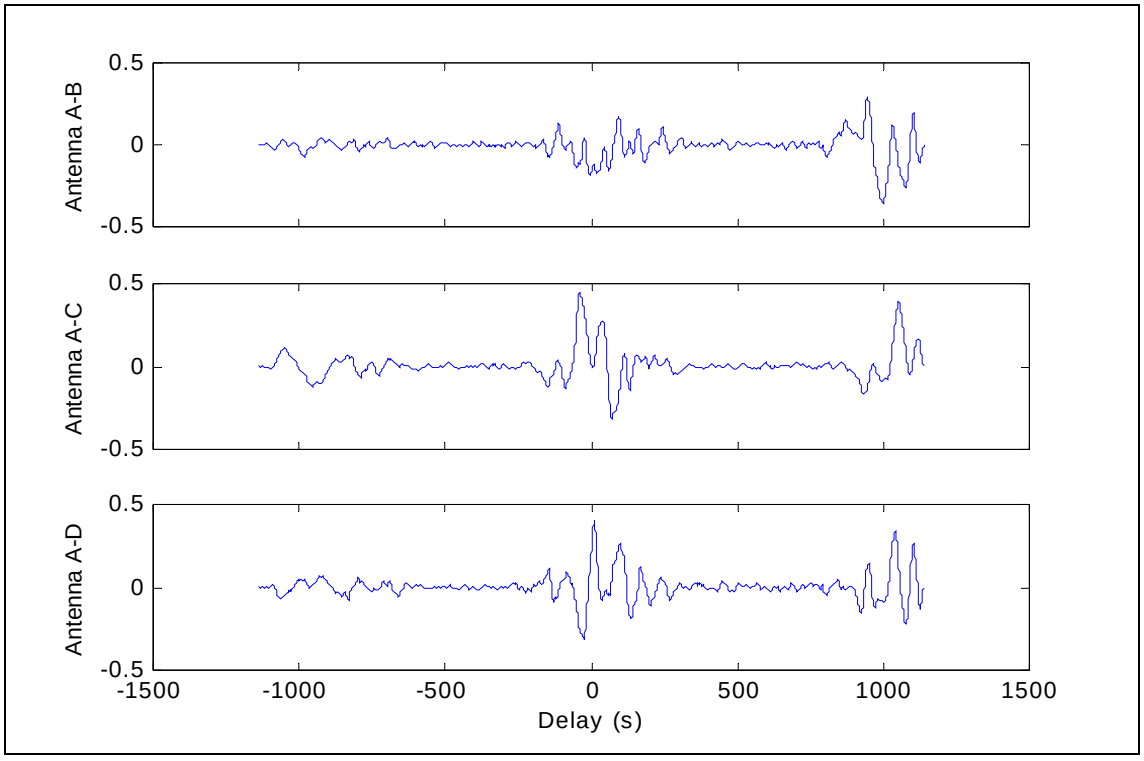

Figure 4.24: Correlation coefficient (SV – 17), Elevation (68° - 33°) – Section 3

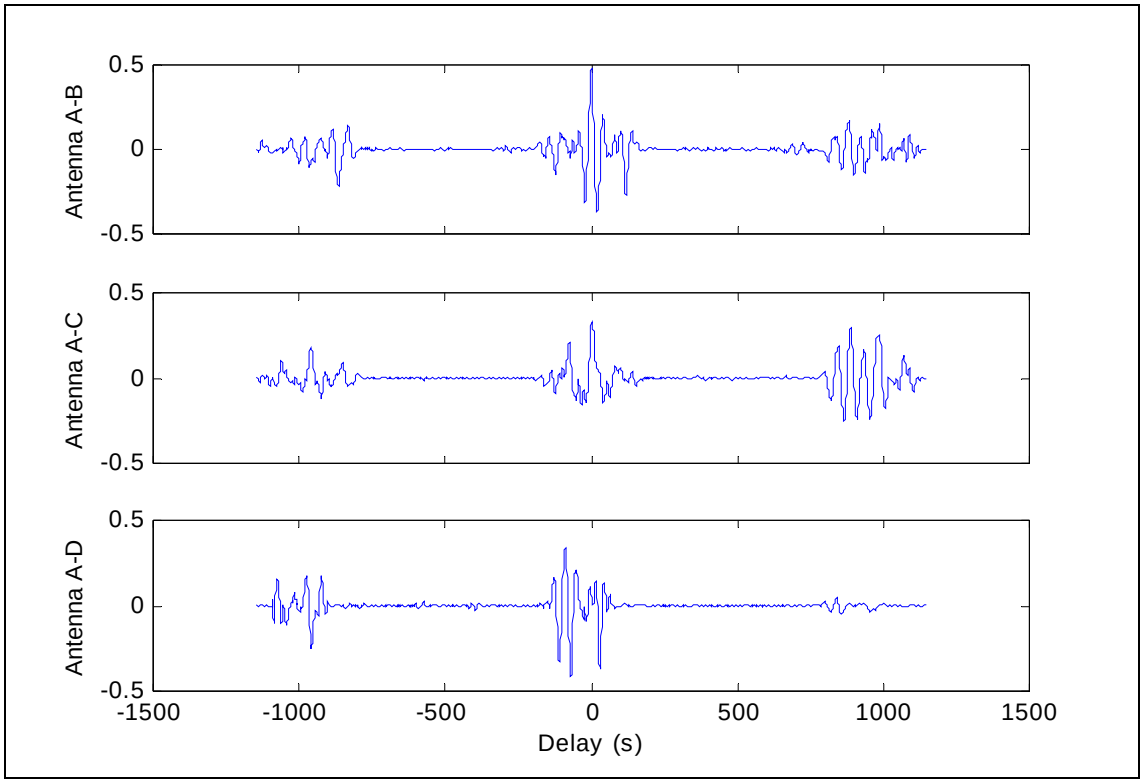

Figure 4.25: Correlation coefficient (SV - 26), Elevation (31° - 14°) – Section 3

The spatial correlation of multipath error among various antennas showed a correlation coefficient of 0.5 between Antenna A and B. The correlation coefficient is similar to Sections 1 and 2, which indicate the weak spatial correlation property of multipath.

4.4.8 Code Multipath Error in Section 4 [Semi-urban environment]

The multipath environment in Section 4 is similar to the Section 1 as this is just the retrace of trajectory in Section 1. The Mean and RMS errors of the multipath error for different satellites are listed in Table 4.8.

Table 4.8: Statistics for the code minus carrier differences - Section 4

	Antenna A		Antenna B		Antenna C		Antenna D	
	Mean (m)	RMS (m)	Mean (m)	RMS (m)	Mean (m)	RMS (m)	Mean (m)	RMS (m)
SV 17 Elv: 68°-33°	0.03	0.21	-0.04	0.29	0.06	0.25	0.01	0.35
SV 23 Elv: 88°-64°	-0.02	0.29	0.04	0.19	-0.03	0.24	0.02	0.22
SV 26 Elv: 31°-14°	0.00	0.27	0.00	0.35	-0.00	0.56	-0.00	0.36
SV 3 Elv: 46°-41°	-0.08	0.30	0.06	0.29	0.02	0.38	-0.04	0.22
SV 31 Elv: 8°-32°	-0.08	0.38	-0.02	0.33	-0.07	0.35	0.03	0.44
SV 9 Elv: 6°- 24°	-0.09	0.35	-0.01	0.43	-0.14	0.66	0.06	0.39

The RMS errors show larger error for low elevation satellites (0.4 m) compared to the high elevation satellites. The RMS errors are similar to the errors in Section 1, hence the multipath error and the spatial correlation graphs are not shown.

4.5 SNR Analysis

The signal-to-noise ratio (SNR) relates to the power of the GPS signal in the receiver. Multipath affects not only the code range and carrier phase measurements, but also affects the power of the composite signal (made up of the direct and the reflected GPS signals). The reflected signal adds constructively and destructively with the direct signal (as the relative phase varies with time). The power of the composite signal also varies with time (Ray, 2000). The signal power can be measured in the receiver from the carrier tracking loop and can be used to estimate carrier and code multipath errors. This technique has been successfully used to estimate carrier phase multipath for static applications (Axelrad, 1994). The SNR of each satellite was also analyzed to study the possibility of using it as an indicator of multipath. The SNR for one of the sections (Section 3) on different antennas is shown in Figure 4.26.

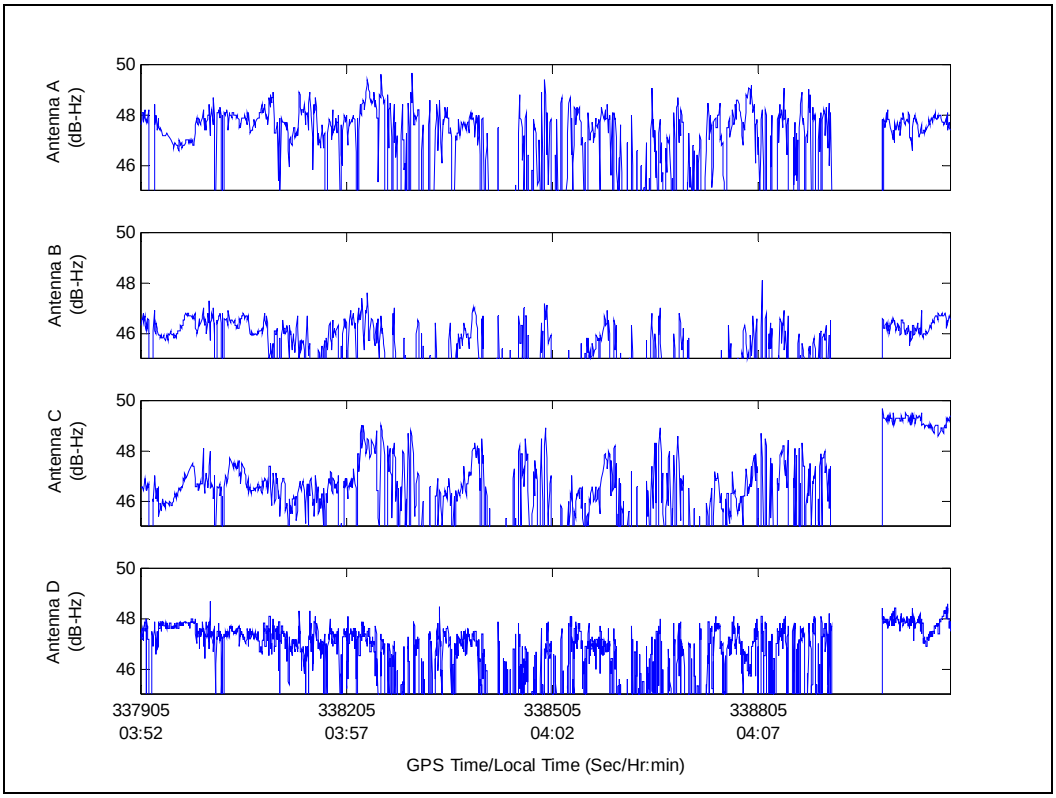

Figure 4.26: SNR for SV – 17, Elevation (68° - 33°) – Section 3

Although SNR variation can be related to multipath it has very large variations due to the signal loss resulting from the environment rather than multipath. Hence the SNR analysis provided inconclusive results in the kinematic situation.

4.6 Summary

A series of tests were conducted in Calgary whereby four antennas were mounted in vehicle and raw GPS data was collected over four sections of urban and suburban routes. Data from the four antennas was processed using code minus carrier technique to analyze the presence of multipath and its correlation from one antenna to another.

The code minus carrier differences provided a good representation of the multipath error. The results of the code minus carrier differences in an open sky, downtown-urban and dense foliage environments show that the multipath error is heavily dependent on the surroundings and the vehicle dynamics. In spite of the harsh multipath environments,

gross multipath errors of few metres (6 – 9m) were observed were observed only few times. This could be due to the high performance Narrow Correlator™ technology used in the Millennium™ receivers. The cross correlation results showed rapid decorrelation of multipath among antennas. Since multipath amplitude and phase change rapidly with the vehicle dynamics it is not possible to use the geometry information between the antenna to detect and mitigate multipath from the pseudorange measurements. Using the SNR to estimate multipath error is also not very effective in kinematic mode as SNR depends not only on the multipath but also on satellite elevation angles, and the surrounding environment.

These results indicate that by combining information from multiple antennas and by performing some sort of blunder detection, multipath errors can be removed. This approach is pursued further in next chapter.

Chapter 5

Reliability and Constraints

5.1 Introduction

An approach to detect multipath is to treat the errors as blunders and then define a statistical test to detect corrupted measurements. This method is similar to the RAIM algorithm proposed by Parkinson and Axelrad (1988). The defined statistical test assumes only one blunder to be present at any given instant, however this assumption may not be always true. Therefore, a reliability measure based on internal and external reliabilities is computed which can be used as a quality indicator. If the statistical test identifies the blunder then the particular measurement is eliminated from the estimation process.

In addition to the statistical test, measurements from several antennas may be combined using constraints before solving for the parameters. This is also expected to improve the reliability. These two concepts are discussed in this chapter, along with some results of this approach.

5.2 Reliability Theory

A brief introduction to the reliability theory and its ability to detect blunders based on some statistical properties are described in this section.

Reliability refers to the ability to detect blunders in the measurements and to estimate the effects of undetected blunders on the solution (Leick, 1995). There are two kinds of reliability, namely internal reliability and external reliability (Krakiwsky and Abousalem, 1995). Internal reliability is defined as the minimum detectable blunder on residuals resulting from a statistical test and the impact of this undetected blunder on the parameters space is defined as external reliability.

The usual course of action followed is to make a statement about the probability distribution of the population and then to test if the sample drawn from the population is

consistent with the statement. In order to detect a blunder on an observation, a statistical test is performed with the underlying assumption that the residuals are normally distributed. Such a statement made about the probability distribution of the population is called a statistical hypothesis. For every hypothesis H_0 (NULL Hypothesis) an alternate hypothesis H_1 exists. A hypothesis is tested by drawing a sample from the population, computing the value of a specific sample statistic, and then making the decision to accept or reject the hypothesis based on the value of the statistic. The hypothesis H_0 cannot result in a certain definite outcome as the test is based on a sample drawn from a sample population and not from the entire population. Hence, four possible outcomes can occur:

1. H_0 is accepted, when H_o is true.
2. H_0 is rejected, when H_0 is true.
3. H_0 is accepted, when H_0 is false.
4. H_0 is rejected, when H_0 is false.

If outcomes (1) or (4) occur then no error is made and the correct action has been taken. Conversely, outcome (2) is known as *Type I error* and outcome (3) is referred to as *Type II error*.

A Type I error occurs when a good observation is rejected and the probability associated with this is denoted as α. A Type II error occurs when a bad observation is accepted and the probability associated with this is denoted as β. Figure 5.1 shows graphically the relationship between Type I and Type II errors. The non-centrality parameter $\left(\sqrt{w_0}\right)$, which is also the bias in the standardized residuals, can be determined by selecting values for α and β from Table 5.1.

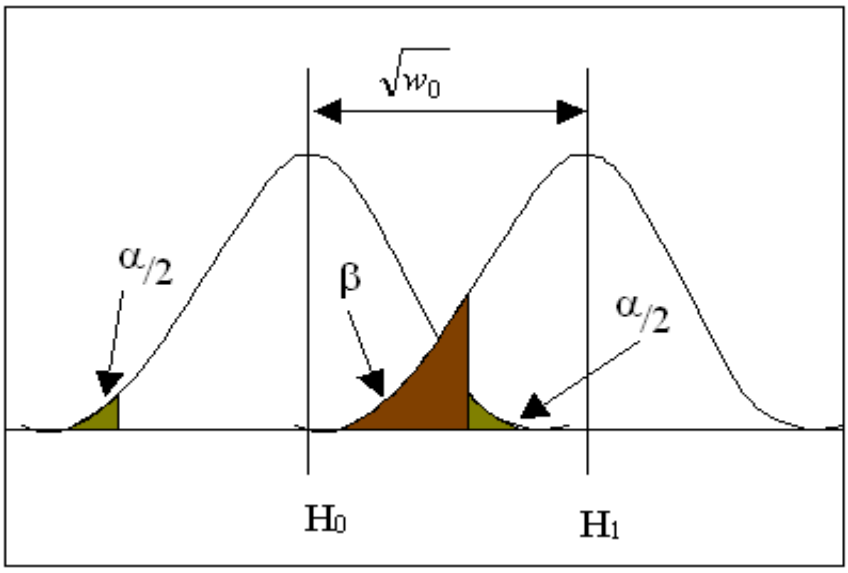

Figure 5.1: Type I and Type II errors with non-centrality parameter

Table 5.1: Non-Centrality Parameter (Leick, 1995)

α	β	$\sqrt{w_0}$
5.0%	20%	2.80
2.5%	20%	3.10
5.0%	10%	3.24
2.5%	10%	3.52
0.1%	20%	4.12
0.1%	10%	4.57

Baarda (1968) introduced this concept of fixing the size of the model error that can be detected at a certain probability level by a certain test. Once $\left(\sqrt{w_0}\right)$is computed, the statistical test shown in equation (5.1) is performed.

$$\tilde{r}_i = \frac{\hat{r}_i}{\sigma_{\hat{r}_i}} \qquad \textbf{(5.1)}$$

Where,

$\hat{r}$ is the residual, and

$\sigma_{\hat{r}}$ is the standard deviation of the residual

The standardized residual is tested against α and has standard normal density ($n(\xi;0,1)$) with mean of zero and a variance of one. The smallest blunder that can be detected through statistical testing is termed as the Minimum Detectable Blunder (MDB). The MDB can be estimated from the relation (Baarda, 1968).

$$MDB = \sigma_{li}\sqrt{\frac{w_0}{g_i}} \quad \textbf{(5.2)}$$

Where, i is the ith observation

$\sqrt{w_0}$ is the non centrality parameter

g_i is the redundancy number of the ith observable, and

σ_{li} is the standard deviation of the ith observable

The redundancy matrix g_i is given as:

$$g_i = (C_{\hat{r}} C_l^{-1})_{ii} \quad \textbf{(5.3)}$$

Where,

$C_{\hat{r}}$ is the variance-covariance matrix of the residuals, and

C_l^{-1} is the variance-covariance matrix of the observations

Once the MDB for each observation has been calculated, the impact of this blunder on the parameter space, which provides a measure of the expected error on the parameters, is given by equation (5.4). This is also referred as External Reliability (Baarda, 1968).

$$\Delta\hat{\delta}_i = -C_{\hat{x}} A^T C_l^{-1} \nabla_0^i \quad \textbf{(5.4)}$$

Where,

$C_{\hat{x}}$ is the covariance matrix of the parameters

A is the design matrix

∇_0^i is a column vector containing all zero's except for the MDB in the ith position

In the current approach, measurements are differentially corrected over a baseline less than 10 km, as a result the ionospheric and tropospheric errors are minimized and only multipath errors and receiver noise are assumed to be present. The receiver noise has a normal distribution whereas multipath errors in a kinematic situation are random in nature and decorrelate rapidly (Nayak et al., 2000a). Therefore, the standardized residuals can be assumed to be normally distributed unless there are multipath errors, in which case the residuals will be biased and can be detected by a statistical test provided there is sufficient redundancy. This test actually eliminates blunders and does not distinguish multipath errors from other errors like integrity failures.

Only one blunder per antenna is considered to exist at any given time. Although this assumption appears insufficient; maximum multipath error is observed in urban conditions where satellite visibility is poor. By eliminating the measurement with the maximum multipath error, the reliability is expected to improve substantially. To achieve better reliability, additional observations in the form of constraints between the antennas can be applied.

5.3 Constraints

If two or more antennas are present, then fixed distance constraints between the antennas can be used as additional observations in the adjustment process. If there are four antennas then six independent constraints can be formed. To apply constraints, the distance between antennas is measured *a priori* with a measuring tape. The model used for a fixed baseline constraint is given by

$$f_{BL} = \sqrt{(x_2 - x_1)^2 + (y_2 - y_1)^2 + (z_2 - z_1)^2} \qquad \textbf{(5.5)}$$

Where $(x,y,z)_1$ and $(x,y,z)_2$ are the WGS84 coordinates of the two antennas. The design matrix for this constraint, which is of dimension 1 x u (where u is the number of parameters), is

$$A = \left[\frac{\partial f_{BL}}{\partial \phi_1} \; \frac{\partial f_{BL}}{\partial \lambda_1} \; \frac{\partial f_{BL}}{\partial h_1} \; \frac{\partial f_{BL}}{\partial \phi_2} \; \frac{\partial f_{BL}}{\partial \lambda_2} \; \frac{\partial f_{BL}}{\partial h_2} \; 0 \; 0 \; 0 \; 0 \; 0 \ldots\ldots \; 0 \right] \qquad \textbf{(5.6)}$$

If the approximate coordinates of the two antennas are known then the following can be derived (Cannon, 1991) (for complete derivation see Appendix A) :

$$\frac{\partial f_{BL}}{\partial \phi} = \frac{\partial f}{\partial x}\frac{\partial x}{\partial \phi} + \frac{\partial f}{\partial y}\frac{\partial y}{\partial \phi} + \frac{\partial f}{\partial z}\frac{\partial z}{\partial \phi}$$

$$\frac{\partial f_{BL}}{\partial \lambda} = \frac{\partial f}{\partial x}\frac{\partial x}{\partial \lambda} + \frac{\partial f}{\partial y}\frac{\partial y}{\partial \lambda} + \frac{\partial f}{\partial z}\frac{\partial z}{\partial \lambda} \qquad \textbf{(5.7)}$$

$$\frac{\partial f_{BL}}{\partial h} = \frac{\partial f}{\partial x}\frac{\partial x}{\partial h} + \frac{\partial f}{\partial y}\frac{\partial y}{\partial h} + \frac{\partial f}{\partial z}\frac{\partial z}{\partial h}$$

Since approximate values of the antenna coordinates are used in the formation of the design matrix, applying baseline constraints can skew the position of all other antennas in the system (Weisenburger, 1997). From Figure 5.2, if the actual antenna position before applying constraints is ABCD then after applying constraints the antenna coordinates could be shifted as indicated by A′B′C′D′.

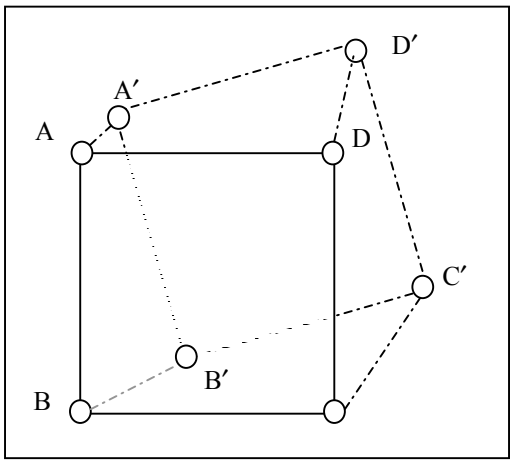

Figure 5.2: Constraints between antennas

This occurs because non-linear mathematical models are used in the design matrix for the constraints. This error can be resolved in a few different ways. One method is to include the second order terms in the design matrix, which is generally neglected during the linearization process (Widnall, 1972). The second method is to increase the estimates of the covariances on the constraints (Weisenburger, 1997). Thirdly, as followed in this research, is to wait for the filter to settle before applying the constraints.

5.4 Accuracy Assessment

One of the ways to access the improvements in accuracy is to compare the position results with some known reference. In this case the positions computed by the post processing software are compared with a highly accurate digital road map of Calgary. The digital road map obtained from the City of Calgary is accurate to within a few centimetres, and was generated by airborne photogrammetric techniques. The coordinates of the map are referenced to the centre of the road and are listed in UTM coordinates. The road is divided into small straight-line segments and the two end coordinates of this segment are stored in the database. The density of the coordinates depends on the geometry of the road and as a result the map co-ordinate density is high on roads with curves. The required trajectory for each test section is selected on a segment-by-segment basis and the corresponding UTM coordinates are exported using the Mapinfo™ software. The true trajectory is then generated by passing straight lines through these coordinates. This method is explained in detail below.

The GPS estimated positions, which are in WGS-84, were converted to UTM coordinates using standard transformation equations (e.g. Snyder, 1993). The digital road map contains piecewise-linearized segments of the road as shown in the Figure 5.3.

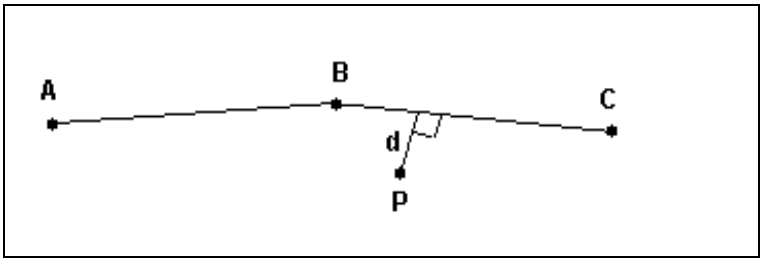

Figure 5.3: Piece-wise linearized segment of the road

From Figure 5.3, segments AB and BC are the linearized segments of the road whereas P is the GPS-derived position. The intention is to compute the distance d from point P to the nearest segment which is BC. The procedure to accomplish this is the following:

1. The node nearest to point P (node B) is identified by computing the minimum distance between P and all the nodes in the database using the equation.

$$d_{\min} = \sqrt{(x_1 - x_2)^2 + (y_1 - y_2)^2} \quad \textbf{(5.8)}$$

2. Distances to the adjacent two nodes A and C are then computed to determine that the nearest segment to P is BC.

3. The shortest distance between P and a straight line segment BC can be computed using the equation for the perpendicular between a point (x1,y1) and a line segment Ax+By+C=0, which is

$$d = \left| \frac{Ax_1 + By_1 + C}{\sqrt{A^2 + B^2}} \right| \quad \textbf{(5.9)}$$

4. The distance *d* then provides the error between GPS coordinates and the reference map data. The errors are computed on a section-by-section basis and the results are discussed in the following sections.

The digital map database contains only two-dimensional topography; therefore it cannot be used to assess the accuracy in the vertical direction. Another inherent problem is that this method does not provide any information regarding the long track error.

5.5 Software Implementation

Data was collected by the test setup described in Chapter 3. The C^{3}NAV™ (Combined Code and Carrier for GPS NAVigation, Cannon and Lachapelle, 1995) software developed at the U of C was modified to become MATNAV (Multiple AnTenna NAVigation), which can process data from up to four antennas and has additional features like reliability testing and constraints, and it is also capable of integrating inertial data from an IMU.

MATNAV reads in an option file, which contains all the parameters for processing multiple antennas. Some of the added features of MATNAV are:

- Multiple Antennas (maximum of four antennas can be processed simultaneously)
- Option to apply constraints between the antennas
- Option to test for blunders using reliability methods
- Option to use inertial data

The differentially corrected measurements from different receivers are independently post-processed in a least squares estimation process using carrier smoothed code and a user selectable cut-off elevation angle (5º in this case).

If the statistical test option is chosen, a 0.1% significance level for hypothesis H_0 and a 10% significance level for hypothesis H_1 is used. This means that the probability of rejecting a good observation is 0.001 and the probability of accepting a bad observation is 0.1, which is highly significant (Mikhail and Gracie, 1998). These are some of the optimal significance levels (Leick, 1995) for which the non-centrality parameter is given in Table 5.1.

The standardized least squares residuals are then tested against this threshold. If any of the residuals fail the statistical test, subsets of the original set of observations are formed. The statistical test is again performed on each of these subsets. If only one subset passes the test, then the blunder is eliminated, and if none of the subsets pass the statistical test then there is more than one blunder and all the observations are discarded. This is a very conservative approach but if this method is used for real time navigation, then a message can be generated to the user to inform about the presence of an undetectable blunder in the measurement. However, if more than one subset passes the statistical test then the subset with the smallest sum of squared residuals is chosen for computing the position. The methodology is detailed in the flow chart shown in Figure 5.4

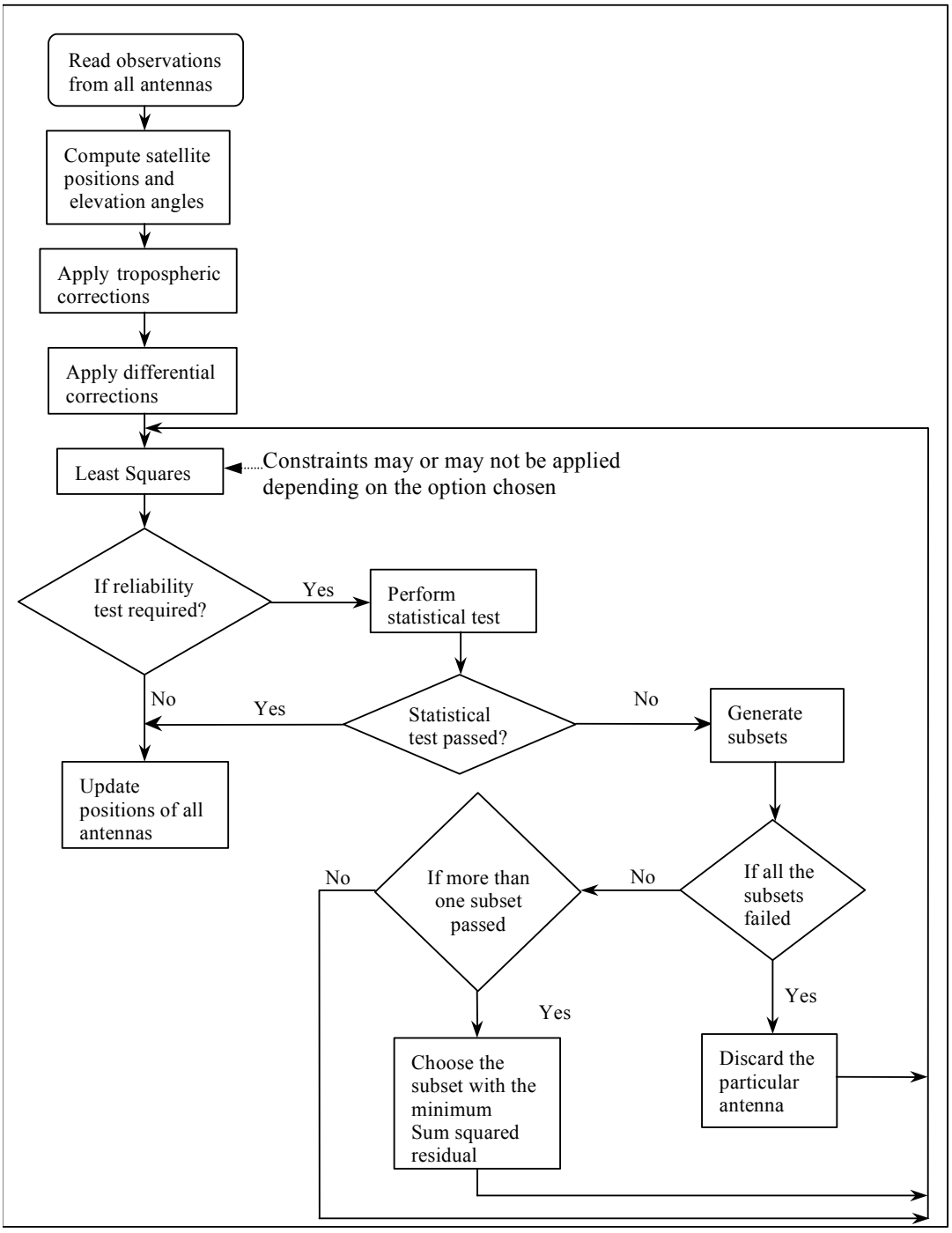

Figure 5.4: Flow chart of the statistical test

In addition to the statistical test, constraints can be applied if there are more than two antennas. The standard deviation of the constraints depends on the external method of

measuring the baseline. For the experiments conducted, the baseline lengths were measured with a tape and a standard deviation of 1 cm was chosen.

To study the performance of reliability and constraints, the data was processed with and without constraints, with and without reliability, for all combinations of antennas.

Latitude (ϕ), longitude (λ), altitude (h) and clock bias (c_b) are the four unknown parameters that are estimated for each antenna using least-squares estimation. If there are four antennas, the total number of estimated parameters is 16. Therefore, according to the prevailing visibility conditions, the number of parameters that are estimated at a given instant may vary from 4 to 16. Then depending on the antennas used at that epoch, appropriate constraints can be applied.

5.6 Scenarios

The data for each section, along with different antenna combinations were processed in the following modes:

- No constraints, No reliability (NCNR)
- No constraints, With reliability (NCWR)
- With constraints, No reliability (WCNR)
- With constraints, With reliability (WCWR)

The results for each of the four sections of the test were analyzed individually and some of the different scenarios are shown below. The position errors (horizontal components) were computed by comparing the MATNAV positions with the highly accurate (< 20 cm) digital map data. The coordinates of the map correspond to the centre of the street. Since the vehicle keeps moving in and out of the centre of the road depending on whether the road is a single lane or a two-lane road, it is practically impossible to estimate the true distance from the centre of the road to the vehicle. Hence the results shown below include these errors due to the motion of the vehicle from the centre.

5.7 Results

The results from the various environments described in Chapter 4 are again presented section wise. The results correspond to two sets of data collected on Day 1 (June 30, 1999) and Day 2 (September 9, 1999). Both sets of data were collected with the same satellite constellation and the same route.

5.7.1 Section 1 – Open Sky

The position coordinates are computed from all four antennas without reliability and constraints. The coordinates from Antenna A are shown in Figure 5.5.

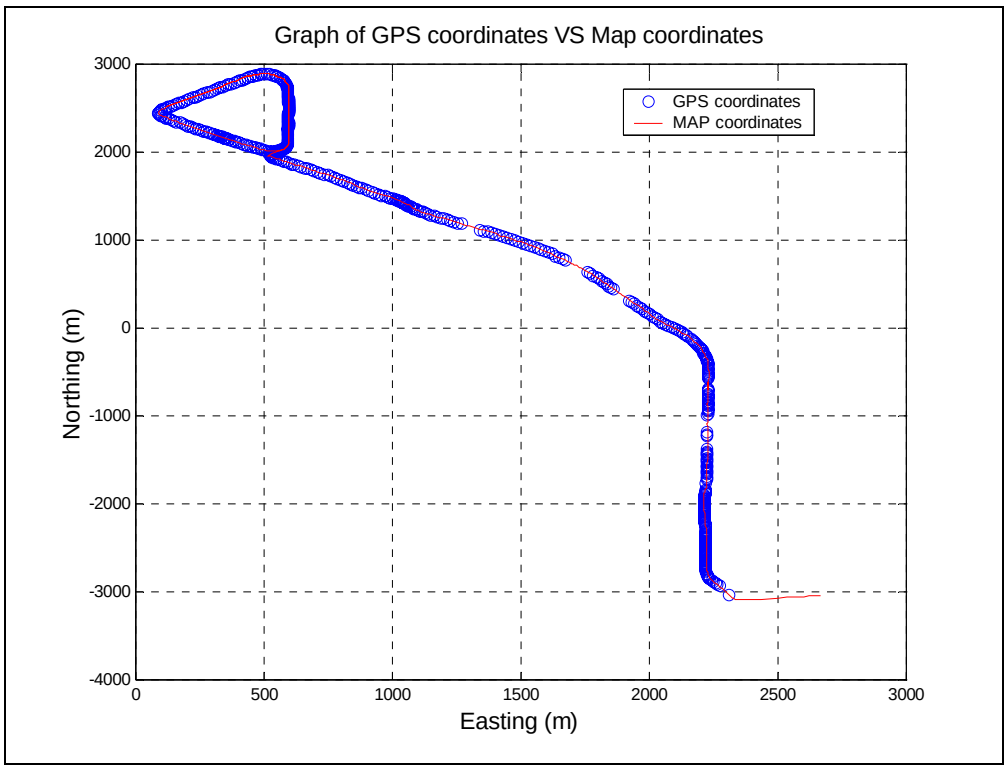

Figure 5.5: Section 1, GPS and map trajectory

The red (black) continuous line in Figure 5.5 is the trajectory extracted from the digital map and the blue (black) circles are the coordinates computed from Antenna A. The trajectories of all the other antennas are similar and hence not shown. There are a few outages in this section due to some underpasses along the road. The error between GPS

and the true reference is shown in Figure 5.6. Comparisons are only done in 2D mode as explained in Section 5.4 of this chapter. The absolute errors have a mean of 2.3m and an RMS of 2.7m. As the digital map corresponds to the centre of the street, the error shown in Figure 5.6 includes the deviations of the vehicle from the centre of the street.

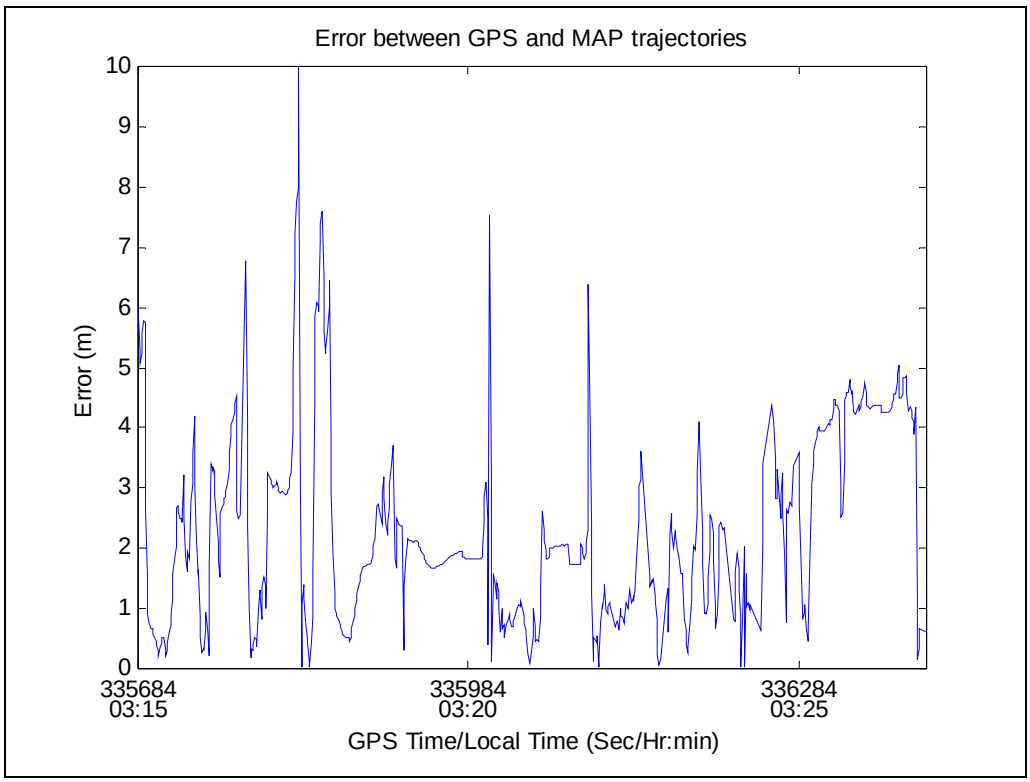

Figure 5.6: Absolute error between the GPS and true trajectories – Section 1

The RMS errors of the absolute position errors for various scenarios on two different days are computed and the results are shown in Figures 5.7 and 5.8 respectively. The mean and RMS values are averaged across antennas and are represented for each reliability-constraint scenario. To apply constraints, at least two antennas have to be selected, and hence the scenario with one antenna and a constraint is not possible. Therefore no results are shown in these figures for the case with one antenna and constraint.

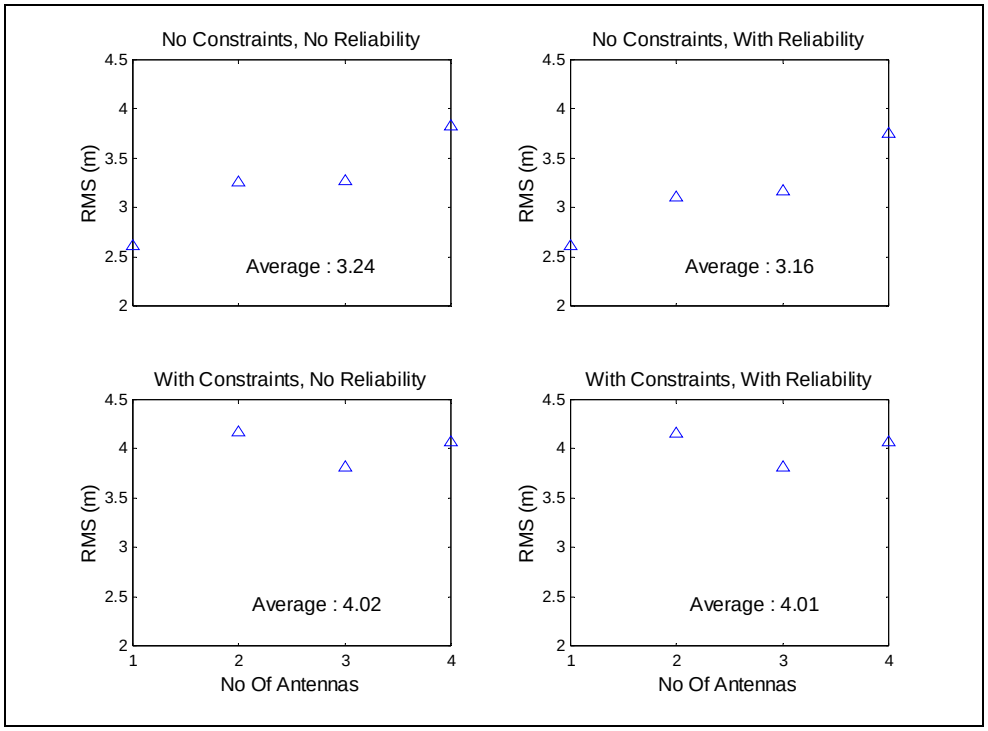

Figure 5.7: Average RMS agreement between DGPS and map coordinates for various scenarios, Section 1, Day 1

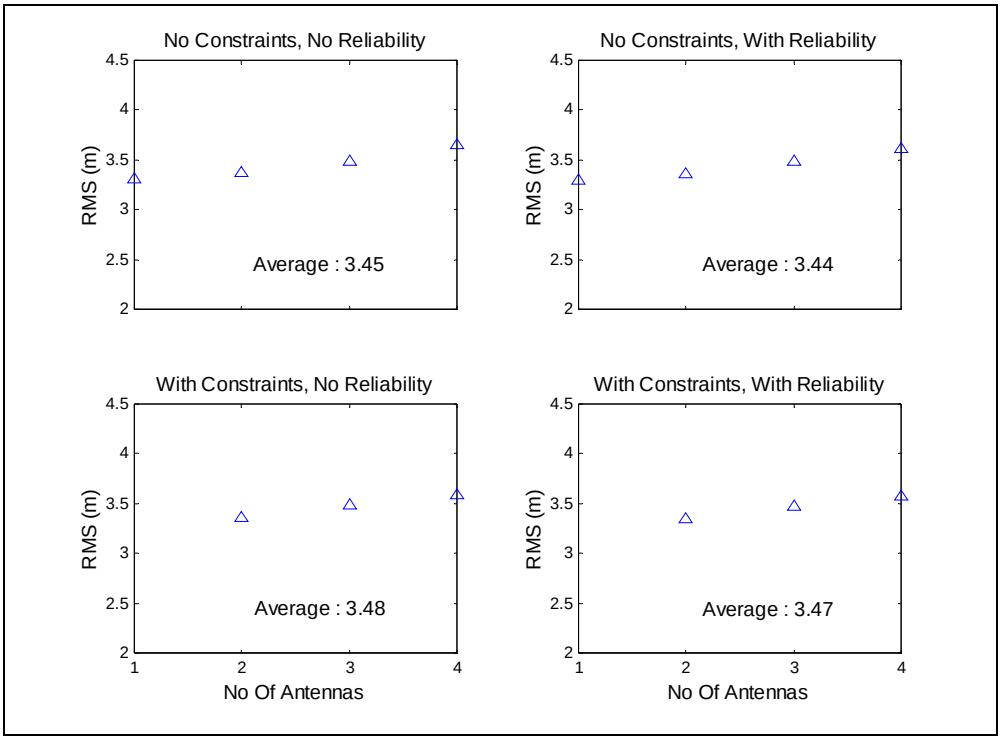

Figure 5.8: Average RMS agreement between DGPS and map coordinates for various scenarios, Section 1, Day 2

The results shown above correspond to the average position error when multiple antennas are used. The average position error increased from 2.6 m to 3.7 m by increasing the number of antennas from one to four in the scenario NCNR on Day 1. This just shows that the average error is bounded to the maximum error amongst all the antennas used. However, the position error improves slightly when reliability tests are conducted but worsen when constraints are applied. This is because constraints are applied with approximate coordinate information and forces the combined solution to be skewed. The reliability tests did not improve the accuracy considerably because this test was in an open area and the multipath errors were small to begin with.

The use of a reliability algorithm with constraints showed marginal improvements in the position domain, but an increase in the accuracy does not mean better reliability. Therefore to assess the reliability of the solution, the maximum expected horizontal position error from the minimum detectable blunder is calculated which is also known as External Reliability in statistical theory, see Section 5.2. The average of these maximum horizontal errors with various scenarios and with data collected on Days 1 and 2 are shown in Figures 5.9 and 5.10, respectively.

The maximum expected horizontal errors improve substantially with the application of constraints. The RMS errors improve from 60 m to 14 m on Day 1 and 16 m to 7 m on Day 2, respectively. An improvement larger than 50% can be seen. This indicates that having additional antennas helps to achieve better reliability as opposed to having a single antenna and performing a statistical test. The improvement is consistent on both days and the results are in agreement with the improvement in MDB by the addition of extra observations (Salzmann, 1991). The improvement in reliability with additional antennas is substantial 19 m (two antennas) to 7 m (with four antennas) on Day 1. The improvement is 40% from two antennas to four antennas on Day 2. The average RMS errors on Day 1 is 68.7 m where as the RMS errors are in the order of 16 m on Day 2, this is because on Day 1 the HDOP values were in the range of 6 – 8 for a duration of 3 minutes due to poor visibility and this directly effects the external reliability.

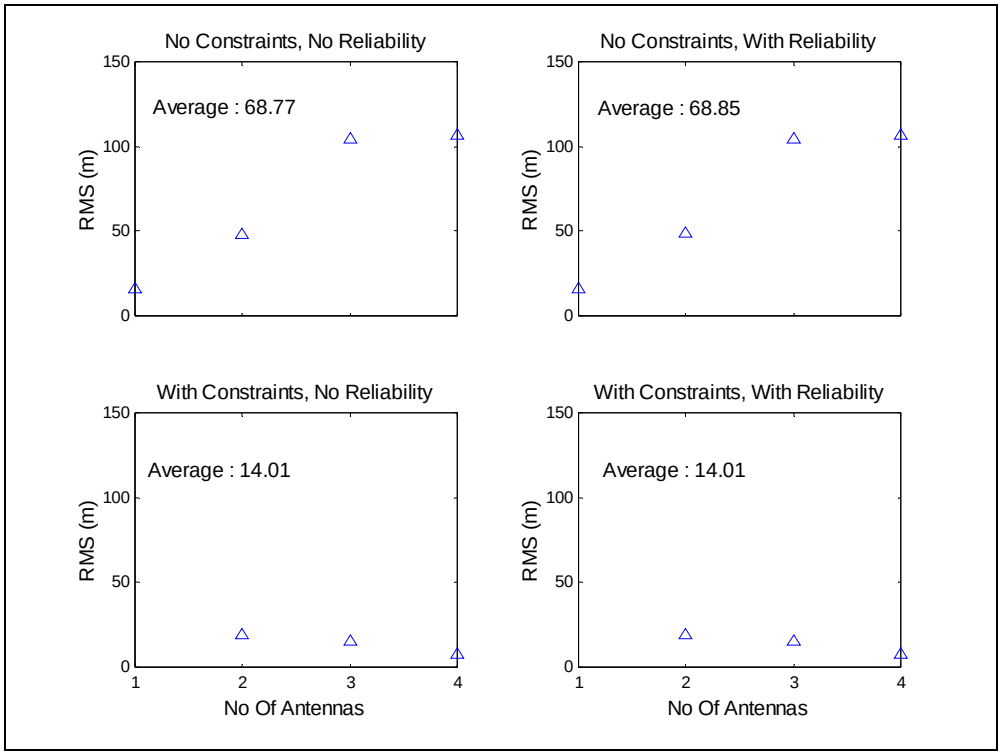

Figure 5.9: External reliability RMS errors for various scenarios, Section 1, Day 1

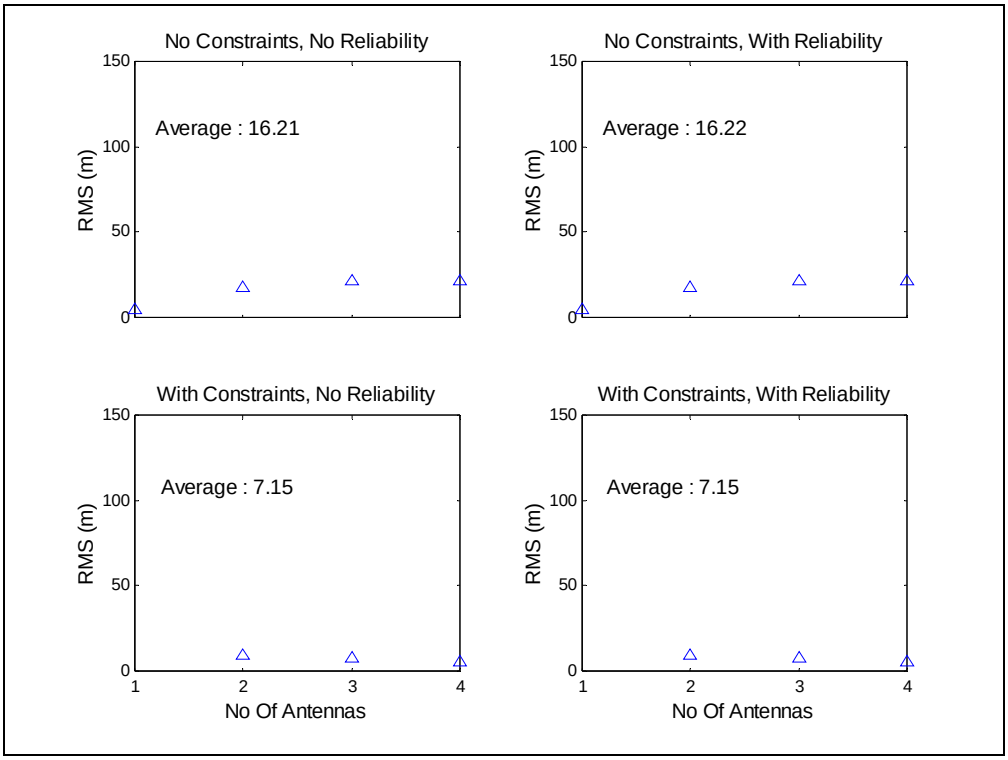

Figure 5.10: External reliability RMS errors for various scenarios, Section 1, Day 2

5.7.2 Section 2 – Urban

The GPS trajectory for Section 2 overlaid on the digital map is shown in Figure 5.11. The GPS coordinates are computed from Antenna A without applying any constraints or performing a reliability test.

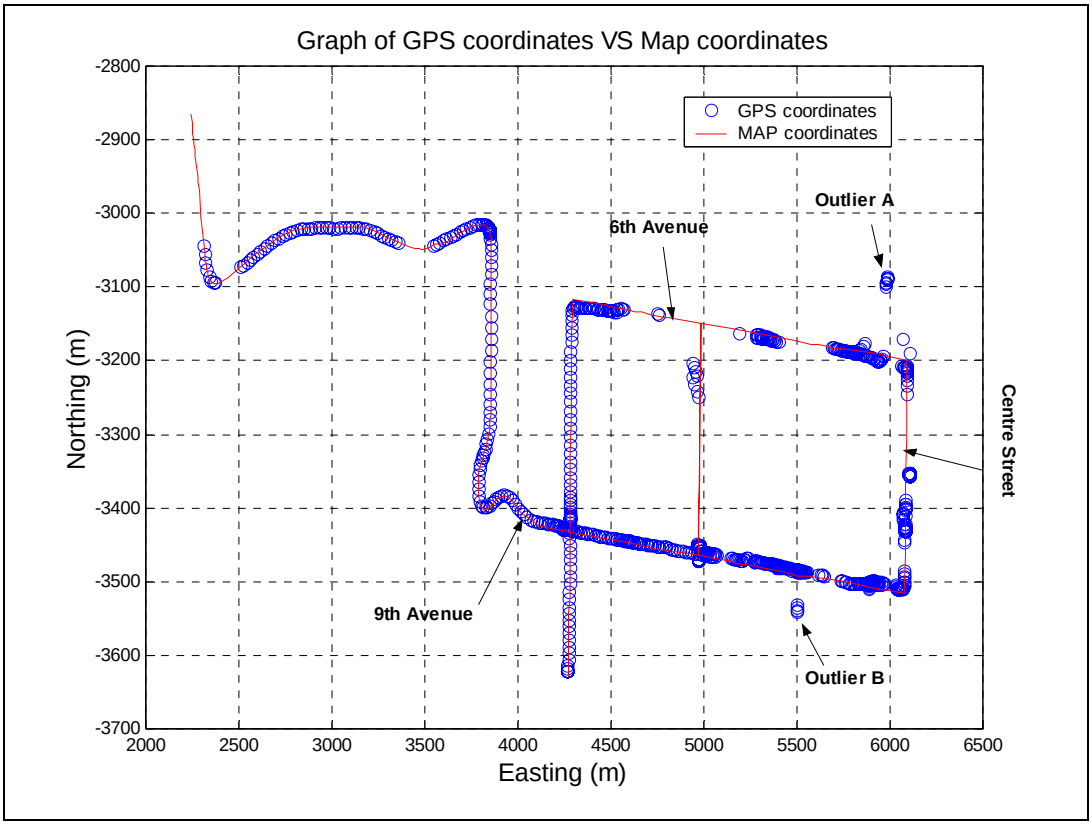

Figure 5.11: Comparison of GPS and digital map coordinates - Section 2

The red (black) continuous line in the figure represents the reference trajectory extracted from the digital map and the blue (black) circles represent the coordinates computed from antenna A on an epoch-to-epoch basis. Two outliers (A and B) shown on the figure are some of the gross outliers clearly visible in section 2. The outlier A is a result of very bad geometry (GDOP > 20) and outlier B is a gross multipath error. The position is erroneous by 100m and 60m at outliers A and B, respectively. Some error is also noticeable at the intersection of Centre Street and 6th avenue. The absolute horizontal error between the two trajectories is shown in Figure 5.12.

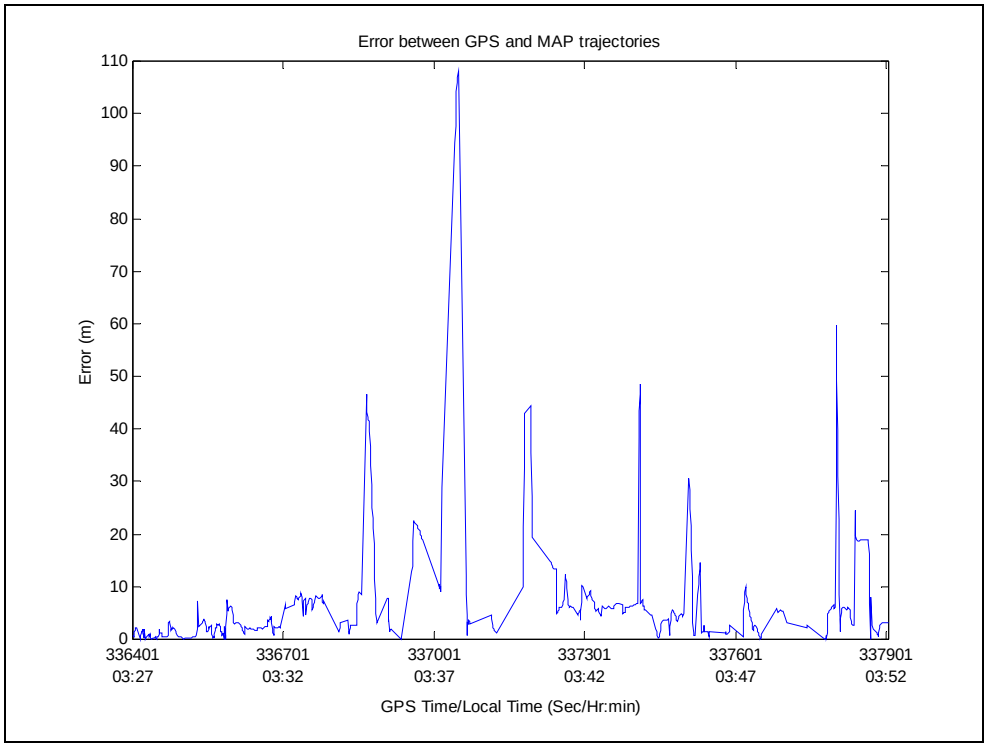

Figure 5.12: Absolute error between the GPS and true map trajectory – Section 2

There are a few large errors (> 20 m) in the above figure. Most of these errors are due to very high DOP values resulting from the urban canyon environment. The mean and RMS values of the position error are 7.0 m and 13.4 m, respectively. The average RMS errors of the position errors for various scenarios on Days 1 and 2 are shown in Figures 5.13 and 5.14. The corresponding maximum horizontal errors computed from the MDB are shown in Figures 5.15 and 5.16.

The statistical tests were able to identify a few multipath errors, but were not very effective because to perform the reliability test successfully, redundant observations are required. Most often the redundancy was affected by poor visibility. Also, most often there were more than one observation corrupted by multipath and also a severe degradation in DOP was observed when some observations were discarded during the reliability test.

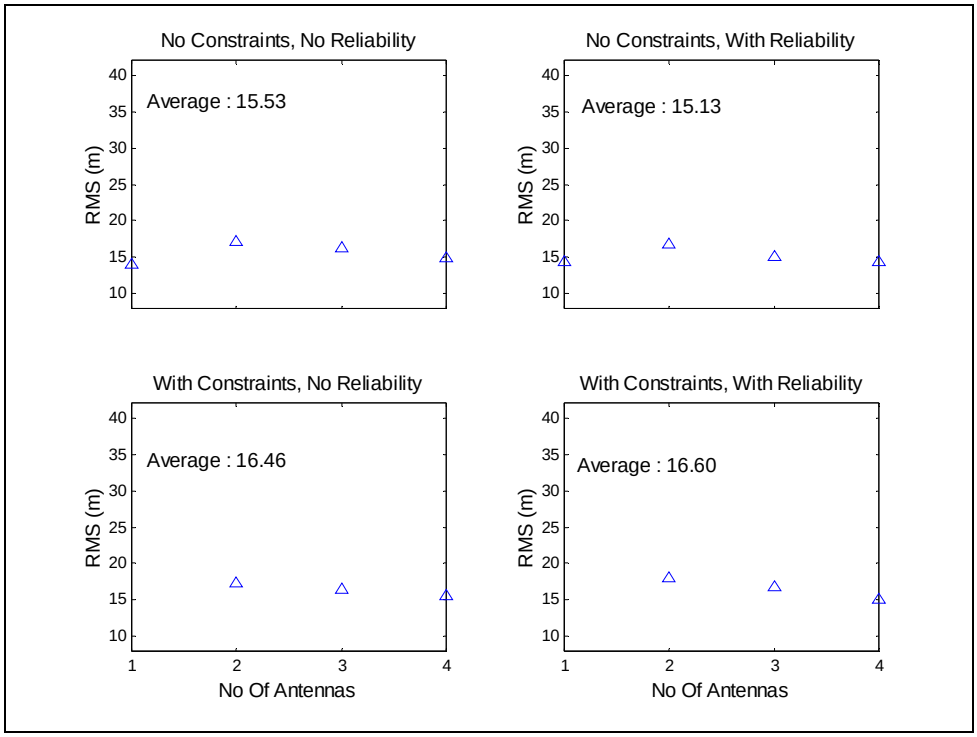

Figure 5.13: Average RMS agreement between DGPS and map coordinates for various scenarios, Section 2, Day 1

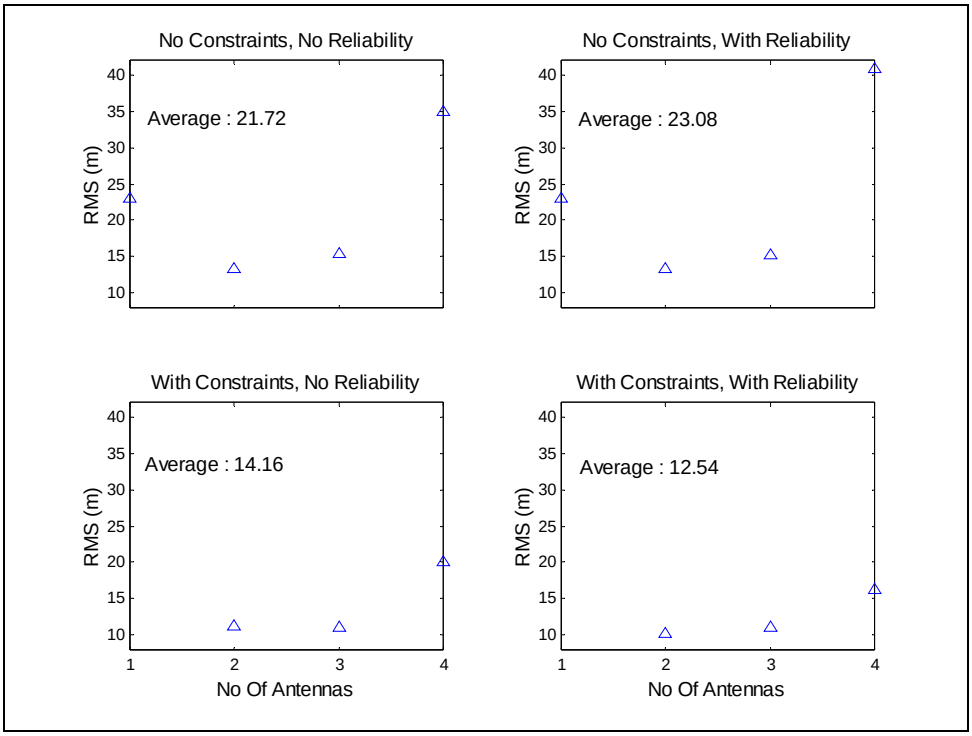

Figure 5.14: Average RMS agreement between DGPS and map coordinates for various scenarios, Section 2, Day 2

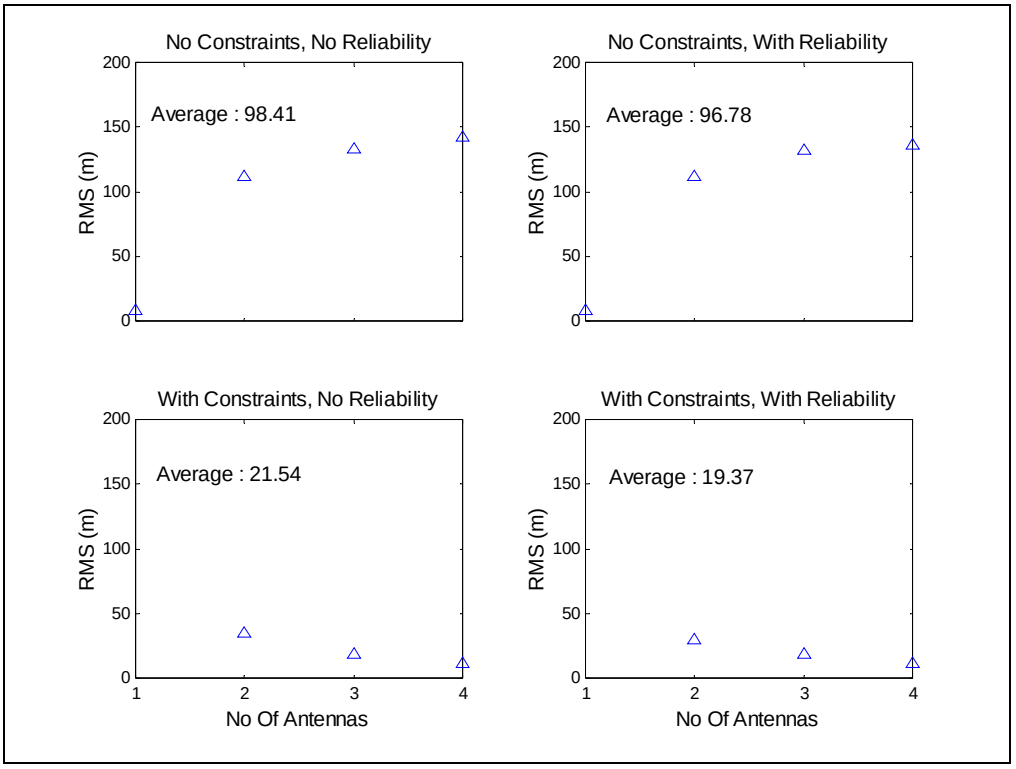

Figure 5.15: External reliability RMS errors for various scenarios, Section 2, Day 1

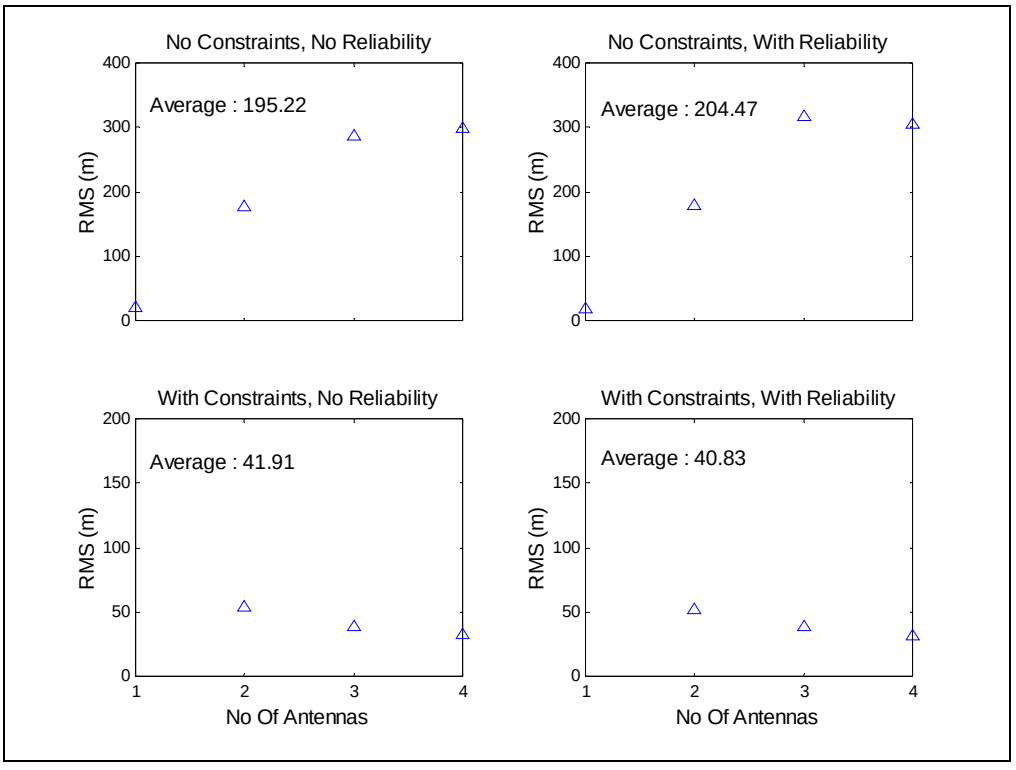

Figure 5.16: External reliability RMS errors for various scenarios, Section 2, Day 2

The maximum horizontal errors (external reliability) reduce from 200 m to 40 m by applying constraints. This clearly shows that the reliability can be improved by having multiple antennas. An improvement of 40% can be seen when reliability and constraints are applied when four antennas are used as opposed to 2 antennas. The average position errors in various scenarios for Days1 and 2 are summarized in Table 5.2.

Table 5.2: Average RMS position errors for Section 2 under various scenarios

Section 2 Day – 1	NCNR[1] RMS (m)	NCWR[2] RMS (m)	WCNR[3] RMS (m)	WCWR[4] RMS (m)
1 antenna	13.96	14.34	N/A	N/A
2 antennas	17.07	16.81	17.36	18.05
3 antennas	16.23	15.07	16.50	16.73
4 antennas	14.87	14.31	15.52	15.03
Section 2 Day – 2				
1 antenna	23.08	23.02	N/A	N/A
2 antennas	13.43	13.27	11.23	10.33
3 antennas	15.41	15.26	11.07	11.07
4 antennas	34.94	40.79	20.17	16.23

1 No Constraints, No Reliability
2 No Constraints, With Reliability
3 With Constraints, No Reliability
4 With Constraints, With Reliability

The increase in the accuracy of the position is marginal with the addition of constraints and reliability, mainly because reliability imposes severe restrictions on geometry (DOP). However on Day 2, an improvement of 53% can be seen from scenario NCNR to WCWR when four antennas were used. There is hardly any improvement on Day 1 by using multiple antennas, however, on Day 2 around 50% improvement can be see when four antennas are used with constraints and reliability as opposed to four antennas without constraints and reliability.

5.7.3 Section 3 – Dense Foliage

The GPS trajectory for Section 3 overlaid on the digital map is shown in Figure 5.17. The GPS coordinates are computed from Antenna A (no constraints or reliability applied).

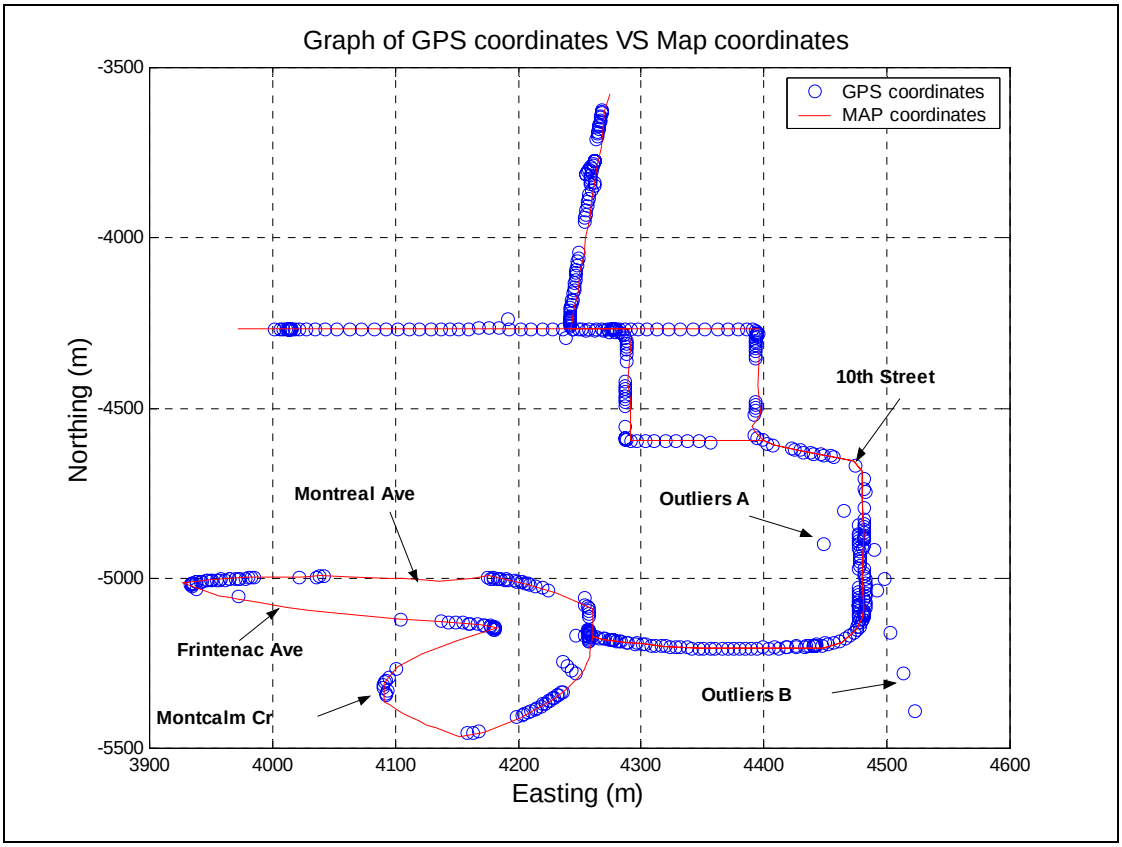

Figure 5.17: Comparison of GPS and digital map coordinates - Section 3

The red (black) continuous line in the figure represent the truth trajectory extracted from the digital map and the blue (black) circles represent the coordinates computed from Antenna A on an epoch-to-epoch basis. Two outliers A and B are shown in the figure above. Outlier A is caused by multipath and is erroneous by 50 m whereas outlier B is 175 m from the reference trajectory and was due to very bad geometry (GDOP > 20). The gross errors mentioned above are seen along the 10th Street, where the visibility is better compared to other streets in this section and the multipath could be due to some of the

buildings present along the street. The error between the two trajectories is shown in Figure 5.18.

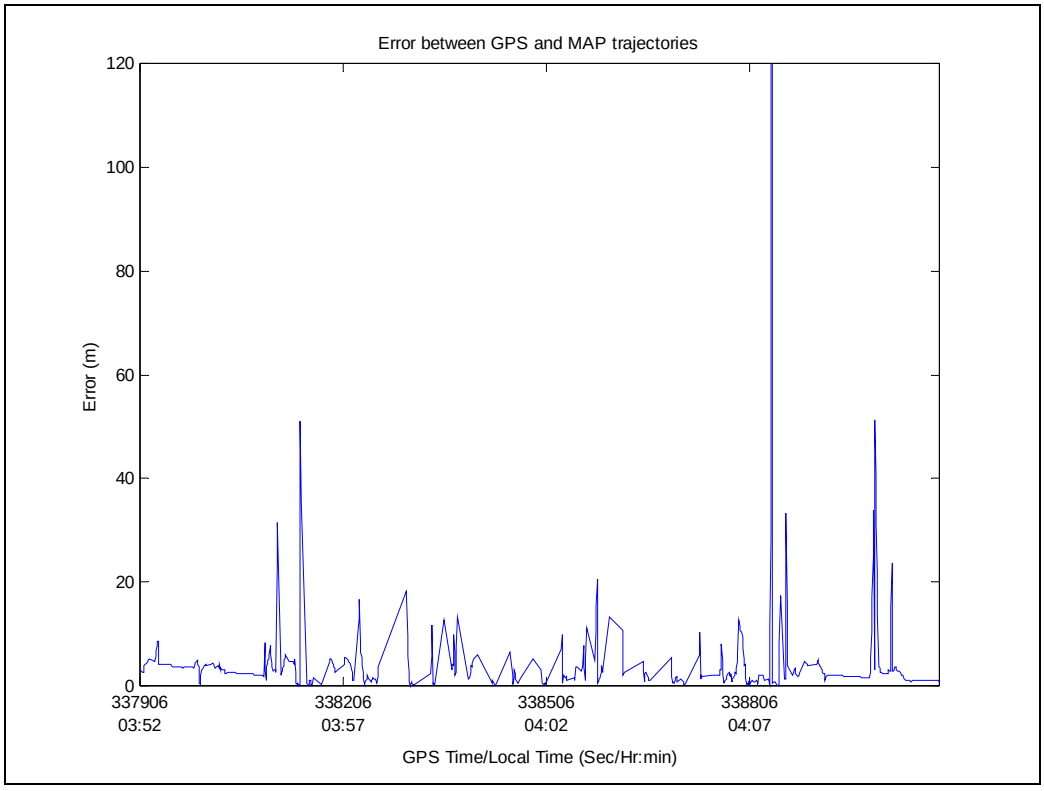

Figure 5.18: Absolute error between the GPS and true map trajectory – Section 3

The mean and the RMS values of the errors are 3.9 m and 9.8 m, respectively. Compared to Section 2, where the mean and RMS errors were 7.0 m and 13.4 m respectively. This indicates that Section 3 is a less multipath prone environment compared to Section 2. There are fewer gross errors in Section 3 compared to Section 2 mainly because foliage causes attenuation of radio signal rather than reflection.

Figure 5.19 and Figure 5.20 show the mean and RMS values of the position error for various scenarios with multiple antennas for Days 1 and 2. There is very little improvement with different scenarios. This is because there was very little multipath error in this section, since most of the time the visibility is poor due to signal loss. Figures 5.21 and 5.22 show the reliability estimates for Days 1 and 2 in this section.

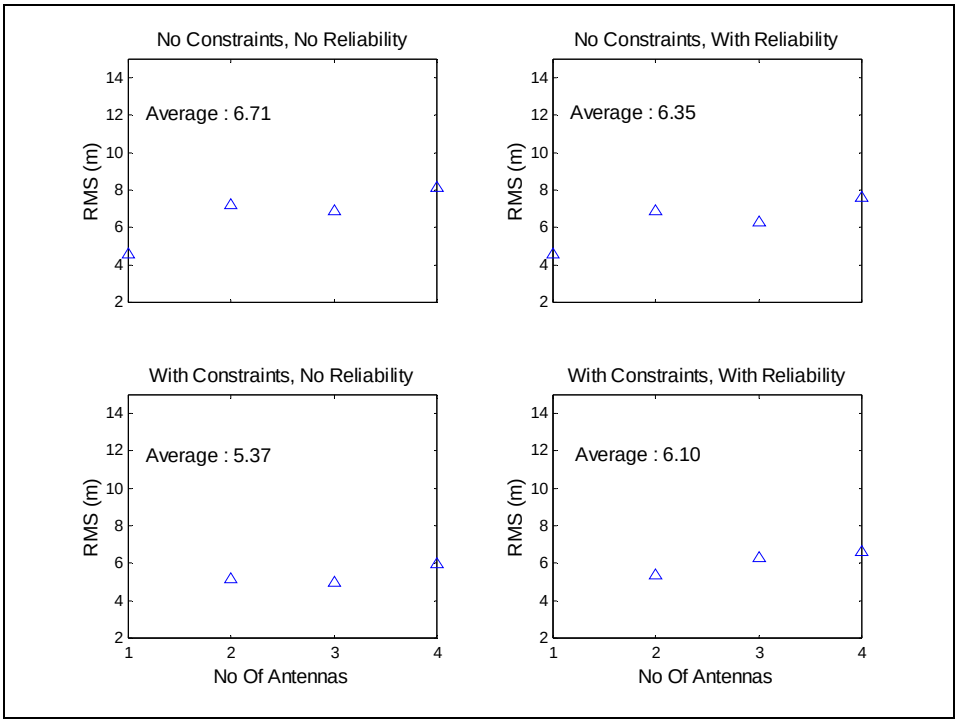

Figure 5.19: Average RMS agreement between DGPS and map coordinates for various scenarios, Section 3, Day 1

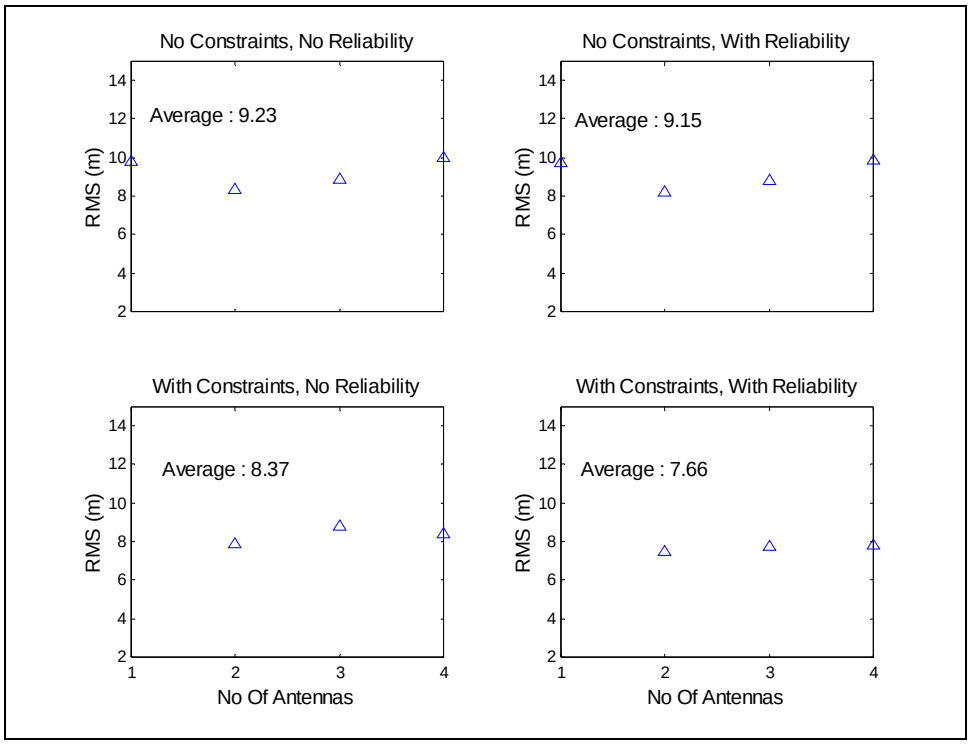

Figure 5.20: Average RMS agreement between DGPS and map coordinates for various scenarios, Section 3, Day 2

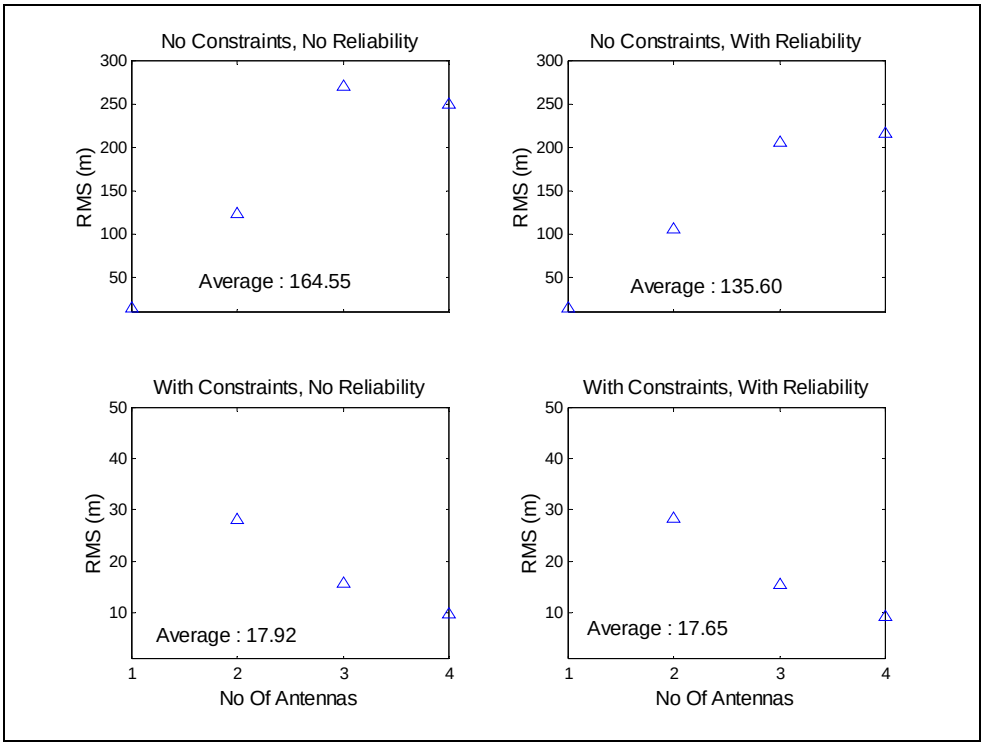

Figure 5.21: External reliability RMS errors for various scenarios, Section 3, Day 1

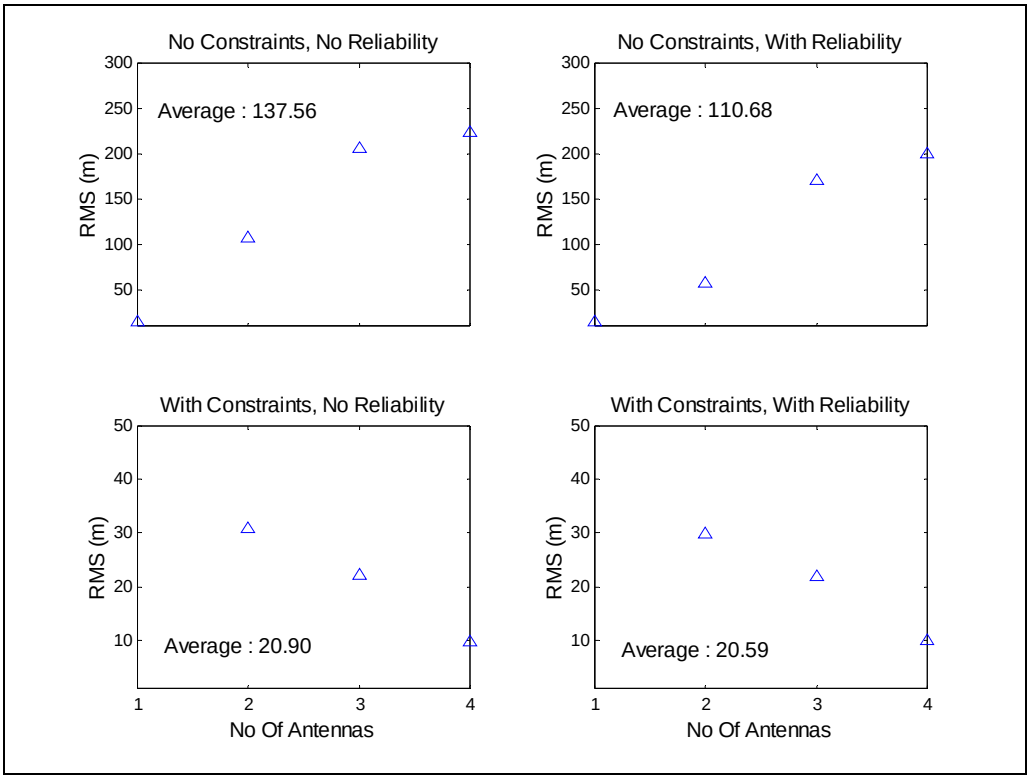

Figure 5.22: External reliability RMS errors for various scenarios, Section 3, Day 2

The improvement in position error is just 9% on Day 1 from scenario no constraints – no reliability to the scenario, with constraints-with reliability and an improvement on 17% was observed with similar scenarios on Day 2. These errors are significantly smaller to the errors in Section 2 (urban environment), where the RMS errors were in the range of 30 m. As mentioned earlier this is because foliage causes attenuation rather than reflection.

The reliability improves with the application of constraints similar to the improvements seen in Sections 1 and 2. The maximum horizontal errors reduce from 100 m to 20 m by applying constraints. The improvement with additional antennas is also significant. RMS errors improved by 50% when constraints and reliability were added to three antennas as opposed to two antennas (Day 1). Also the improvement was 30% from three to four antennas.

5.7.4 Section 4 – Semi-urban

The GPS trajectory for section 4 overlaid on the digital map is shown in Figure 5.23. The scenario 'No constraints, No Reliability' is used to compute the GPS coordinates from Antenna A.

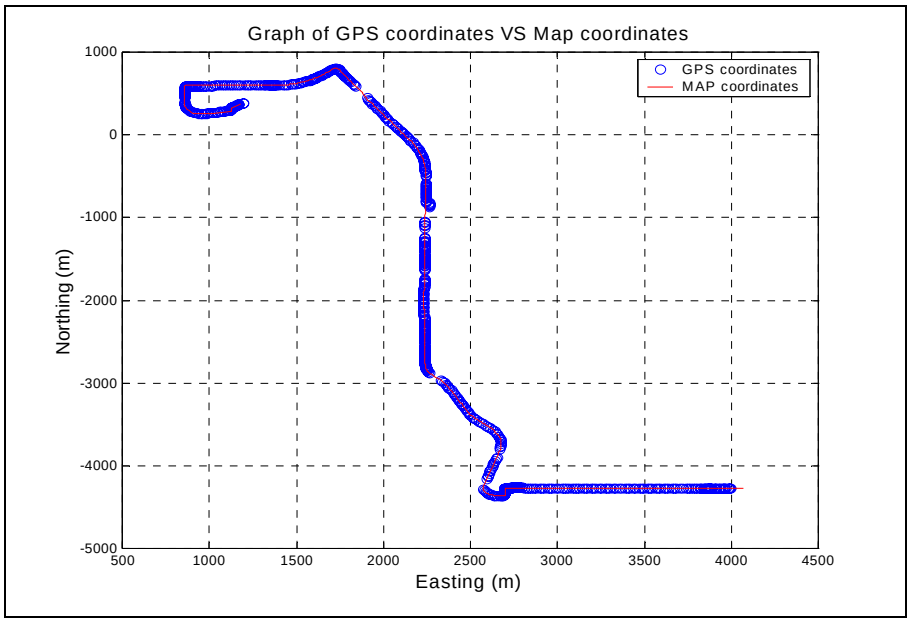

Figure 5.23: Comparison of GPS and digital map coordinates - Section 4

The absolute horizontal position error is shown in Figure 5.24 and the corresponding RMS error statistics with various scenarios for Days 1 and 2 are shown in Figures 5.25 and 5.26, respectively.

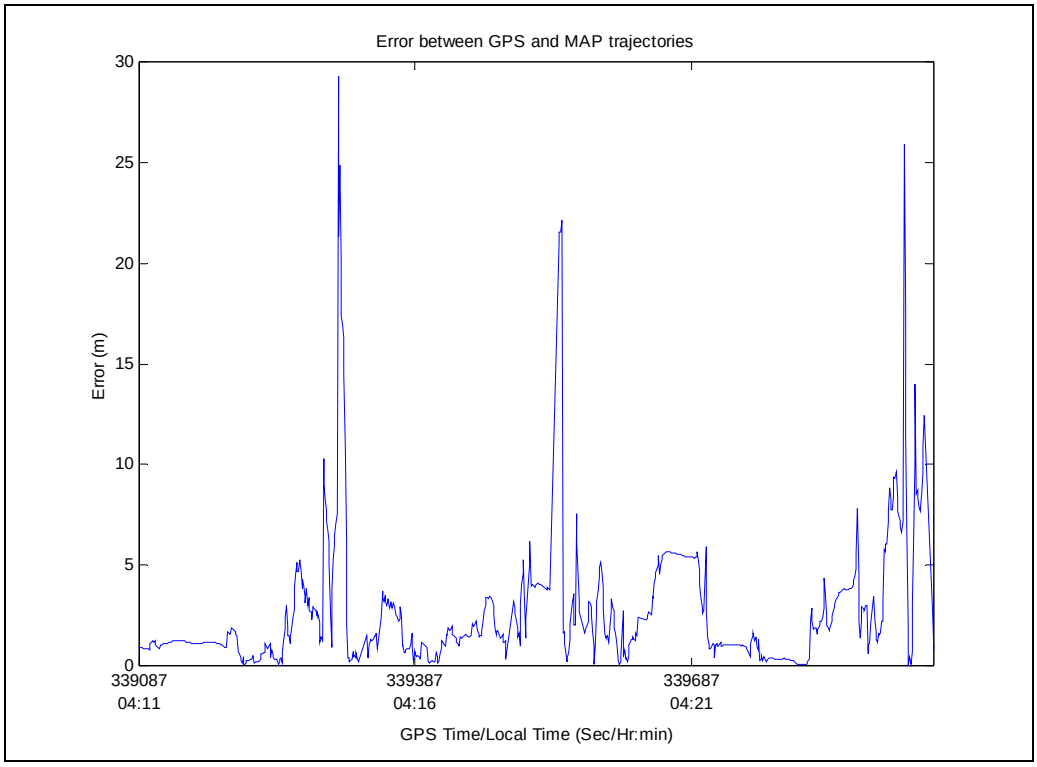

Figure 5.24: Absolute error between the GPS and true map trajectory – Section 4

The position errors, which have a mean of 2.5 m and RMS of 4.3 m is comparable to the errors in Section 1 (Open sky). There are still a few outliers in the range of 20 to 30 m, which are due to blunders in the observations and also due to larger DOP values resulting from obstructions such as underpasses along the route.

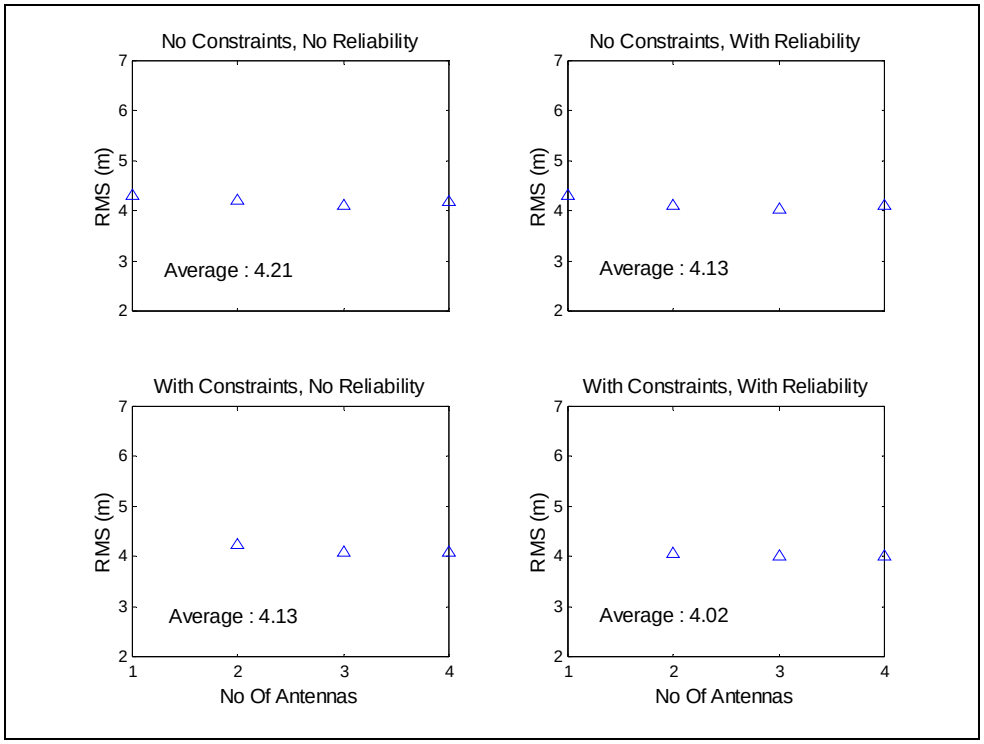

Figure 5.25: Average RMS agreement between DGPS and map coordinates for various scenarios, Section 4, Day 1

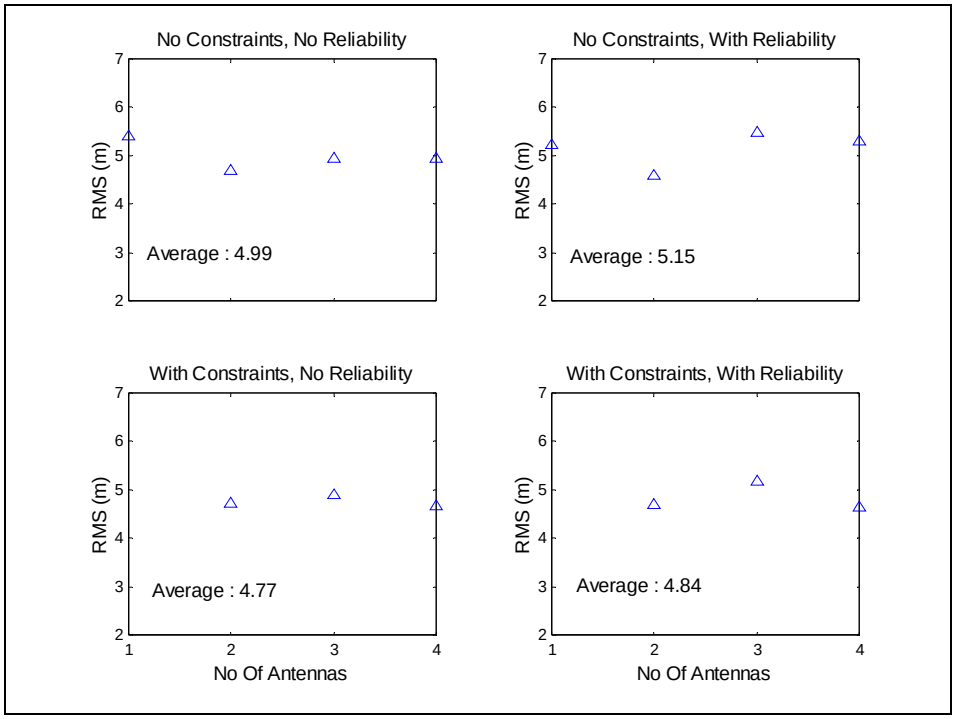

Figure 5.26: Average RMS agreement between DGPS and map coordinates for various scenarios, Section 4, Day 2

A major portion of the route in this section is a retrace of Section 1 and the results are also very similar to the results obtained in Section 1. The average RMS errors are on the order of 5 m in Section 4, which is similar to the results in Section 1 (Open sky). The improvement in reliability as a function of antennas used is not as substantial as in Section 2 (urban environment) or Section 3 (foliage). This is because there are very few blunders in this section.

5.7.5 Statistics with limiting HDOP

To study the impact on the statistics the data was reprocessed with a HDOP limit of 5. The RMS errors in the position domain on Day 1 in Section 2 (downtown) and Section 3 (dense foliage) are shown in Figures 5.27 and 5.28 respectively.

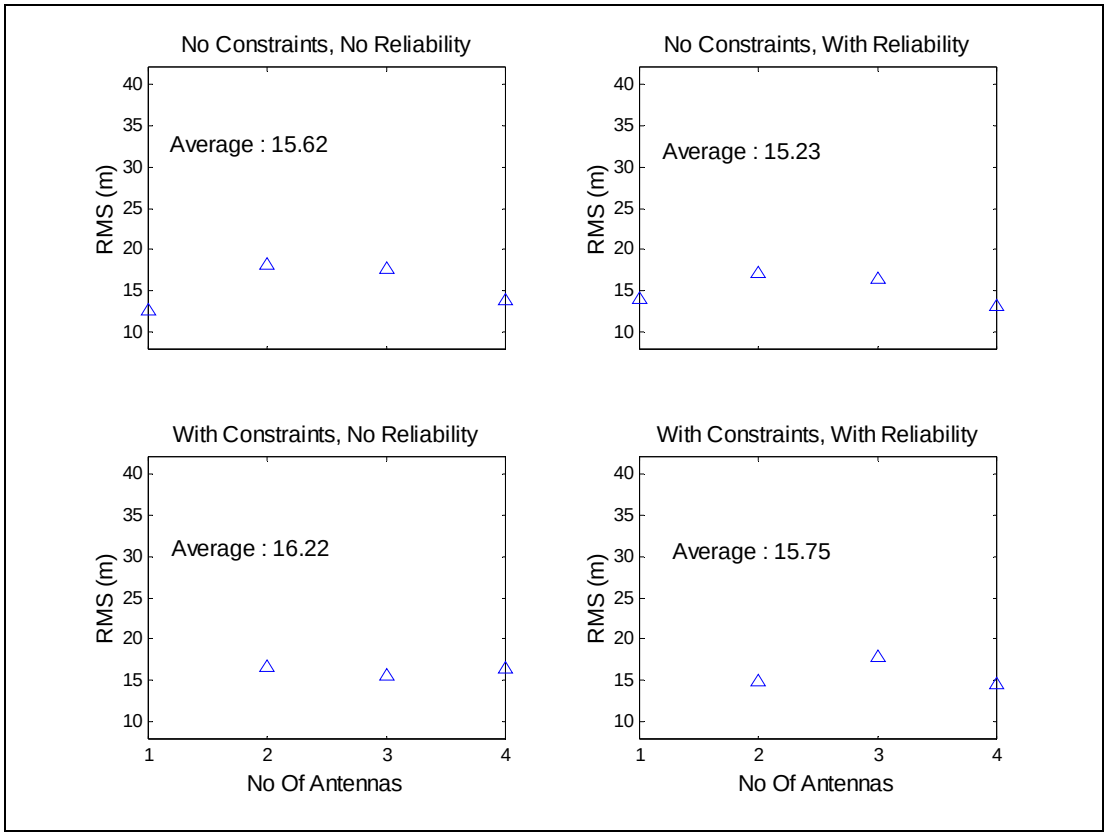

Figure 5.27: Average RMS agreement between DGPS and map coordinates for various scenarios, Section 2, Day 1

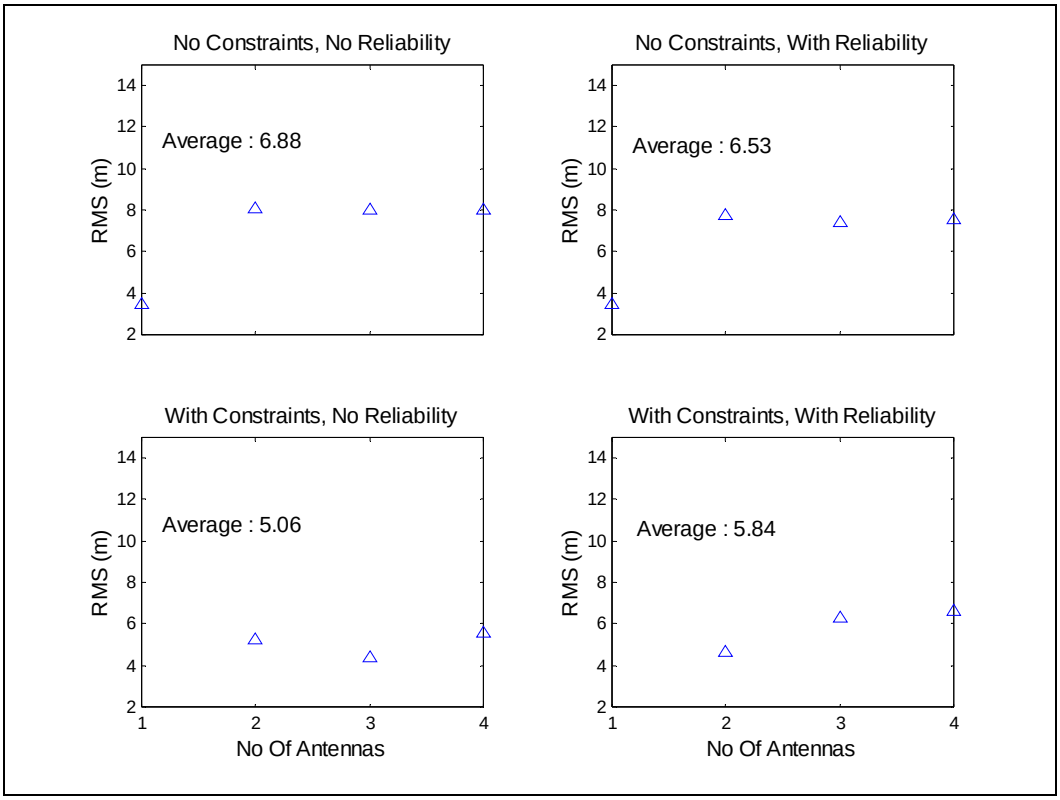

Figure 5.28: Average RMS agreement between DGPS and map coordinates for various scenarios, Section 3, Day 1

The improvements in RMS errors were marginal compared to the unlimited HDOP results shown in Figures 5.13 and 5.19. This is mainly due to the fact that most often the HDOP is within 5 and the occasional explosion is DOP is like an outlier and does not affect the averaged statistics. However, the maximum horizontal errors, which were on the order of 180 m, are now restricted to 60 m.

The impact on the external reliability is shown in Figures 5.29 and 5.30 respectively. The improvement in reliability is considerable as geometry affects the external reliability statistics. An improvement of 13% in Section 2 and 7% in Section 3 for the scenario no constraints and no reliability can be observed. The satellite visibility degraded in this mode. In Section 2 (downtown) there was no solution available for 40%, 50%, 38% and 30% for antennas A, B, C and D respectively.

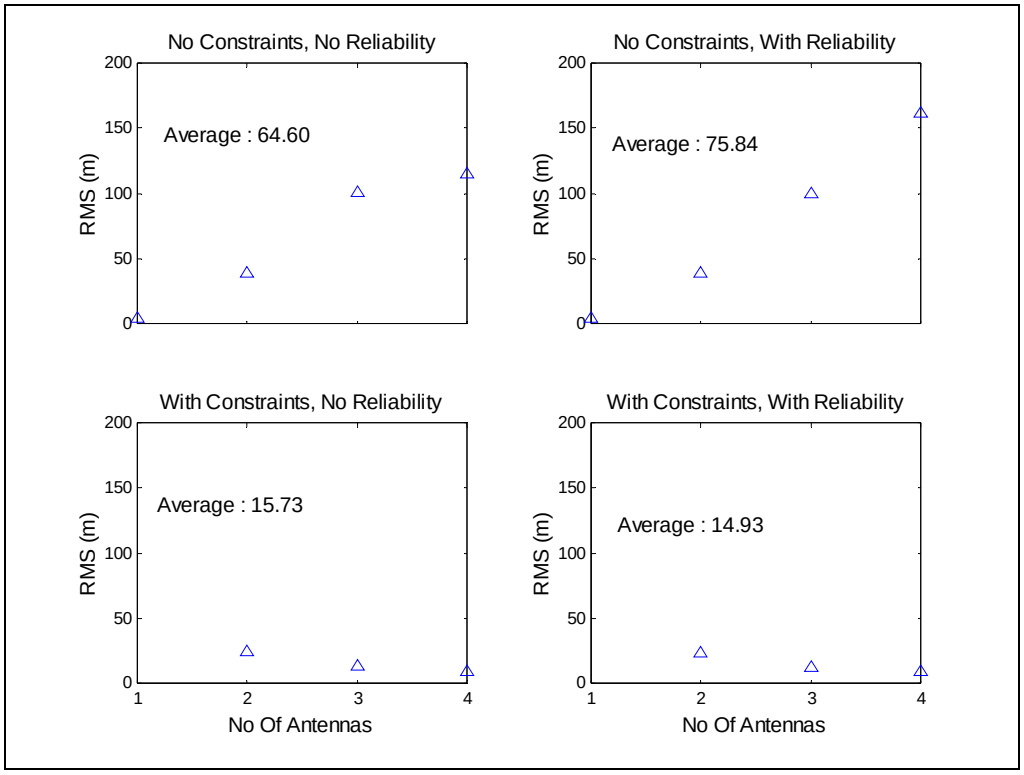

Figure 5.29: External reliability RMS errors for various scenarios, Section 2, Day 1

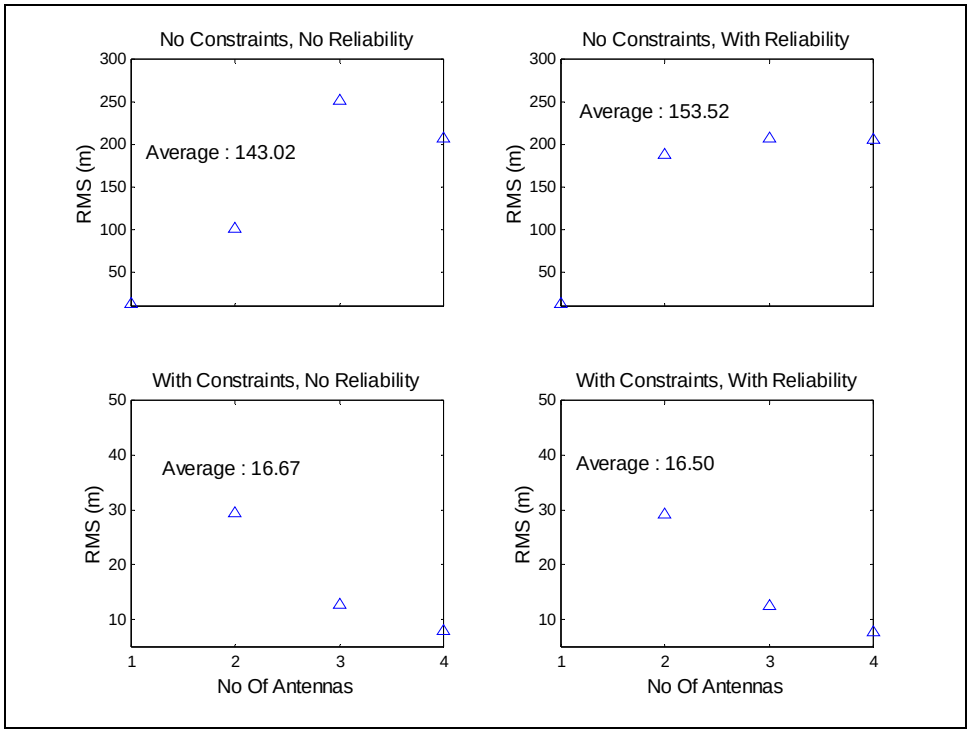

Figure 5.30: External reliability RMS errors for various scenarios, Section 3, Day 1

5.8 Summary

The algorithm used to perform statistical testing did not substantially improve position accuracy in the open sky environment because the blunders or multipath errors in this section were too small to be detected by the statistical test. However, by applying constraints the positions of all the four antennas are bounded by each other, which means that the coordinates of the all the antennas can get shifted.

The results were more promising in urban area (downtown) and foliage sections. The RMS position errors in urban areas on Day 2 with four antennas, and without any constraints and reliability, is around 20 m, but improves to 13 m by applying constraints and performing the reliability test. However, the improvements on Day 1 are much smaller. This is because the multipath environment is different during different runs and the improvement is proportional to the blunder. This method does not eliminate multipath completely but depends on the detection capability of the statistical test.

Some of the blunders were removed with the addition of constraints and reliability tests and sometimes there were more than one blunder in the observation set and the statistical test failed. The average position errors did not improve substantially due to the increase in DOP, which resulted when some measurements were discarded. Also, most often there were not sufficient measurements (redundancy) available to perform a reliability test.

Another important aspect is the choice of the number of antennas to be used. This should be chosen based on the nature of application. For highly critical applications such as collision avoidance where reliable solution is of primary concern, using more antennas/receivers is useful. However, for less critical applications such as position reporting system one or two antenna/receiver system should suffice. This is important because the cost of the total system is a function of the receiver.

The method described in this chapter can detect blunders under certain conditions and also provide an estimate of reliability but cannot provide continuous position updates in

harsh environmental conditions. Therefore the next chapter addresses this issue, where the concepts of integration of low cost inertial sensor with GPS are discussed.

Chapter 6

Inertial Aiding

6.1 Introduction

The use of additional sensors for augmenting GPS has been pursued extensively in the past (Harris, 1989, Bullock, 1995, Zhang, 1995, Geier, 1998, Stephen, 2000). However the automobile, and land applications market in general has been constrained by the cost factor, and this has prevented the use of high quality inertial devices in most of these applications. An attempt has been made here to use a low cost IMU (MotionPak™, $8000) from Systron Donner to augment GPS. The complimentary nature of the INS and GPS errors makes them ideal for integration. Salychev et al., (2000a) describes one such scheme of integration, which is used in this thesis.

In this chapter a brief introduction to Kalman filtering and state space modelling is presented and different popular integration schemes are then discussed. Finally the integration scheme involving GPS and INS along with the results are discussed.

6.2 Linear Discrete Kalman Filter

A Kalman filter is an unbiased linear minimum variance estimator provided the measurement and the system noise can be described as a zero mean Gaussian white noise process (Gelb, 1974). Part of the elegant aspect of this method is the representation of the entire system as a combination of a dynamic model and measurement model. It is basically an algorithm that estimates the state of the system based on the knowledge of system dynamics and a series of measurements corrupted by noise (Gelb, 1974).

The system dynamics in discrete state space form can be represented as

$$X_{k+1} = \phi_k X_k + W_k \qquad \textbf{(6.1)}$$

The measurement process can also be represented in the discrete form as

$$Z_k = H_k X_k + V_k \tag{6.2}$$

Where,

X_k is the state vector at time t_k

ϕ_k is the matrix relating X_k to X_{k+1} in the absence of a forcing function and is purely a state vector update based on the system model

W_k is assumed to be a white noise forcing function with known covariance

Z_k is the vector of measurement at time t_k

H_k is the design matrix relating the measurements to the state vector

V_k is the vector representing the measurement error, assumed to be white sequence with known covariance

The covariance matrix for W_k and V_k vectors are given by Brown and Hwang (1992)

$$\begin{aligned} E\left[W_k W_i^T\right] &= \begin{cases} Q_k, & i = k \\ 0, & i \neq k \end{cases} \\ E\left[V_k V_i^T\right] &= \begin{cases} R_k, & i = k \\ 0, & i \neq k \end{cases} \\ E\left[W_k V_i^T\right] &= 0, \qquad \textit{For all k and i} \end{aligned} \tag{6.3}$$

The relations given in equation (6.3) indicate that measurement noise and system noise are uncorrelated for all instants of time. The relation also shows that system noise is uncorrelated with itself at all time instants except at time t, this is also true with the measurement noise.

Kalman filter concepts and fundamentals are described in detail in Brown and Hwang (1992) and Gelb (1974). In reality the system could be non linear and the noise non-

Gaussian. Various techniques to handle these special cases are also discussed in Brown and Hwang (1992).

The Kalman filter algorithm is comprised of a prediction stage based on the dynamic model and the update stage based on the measurement model. The estimates before measurement updates are denoted by superscript (-) and denoted by (+) after measurement update. The Kalman filter algorithm is shown in Figure 6.1 (Brown and Hwang, 1992).

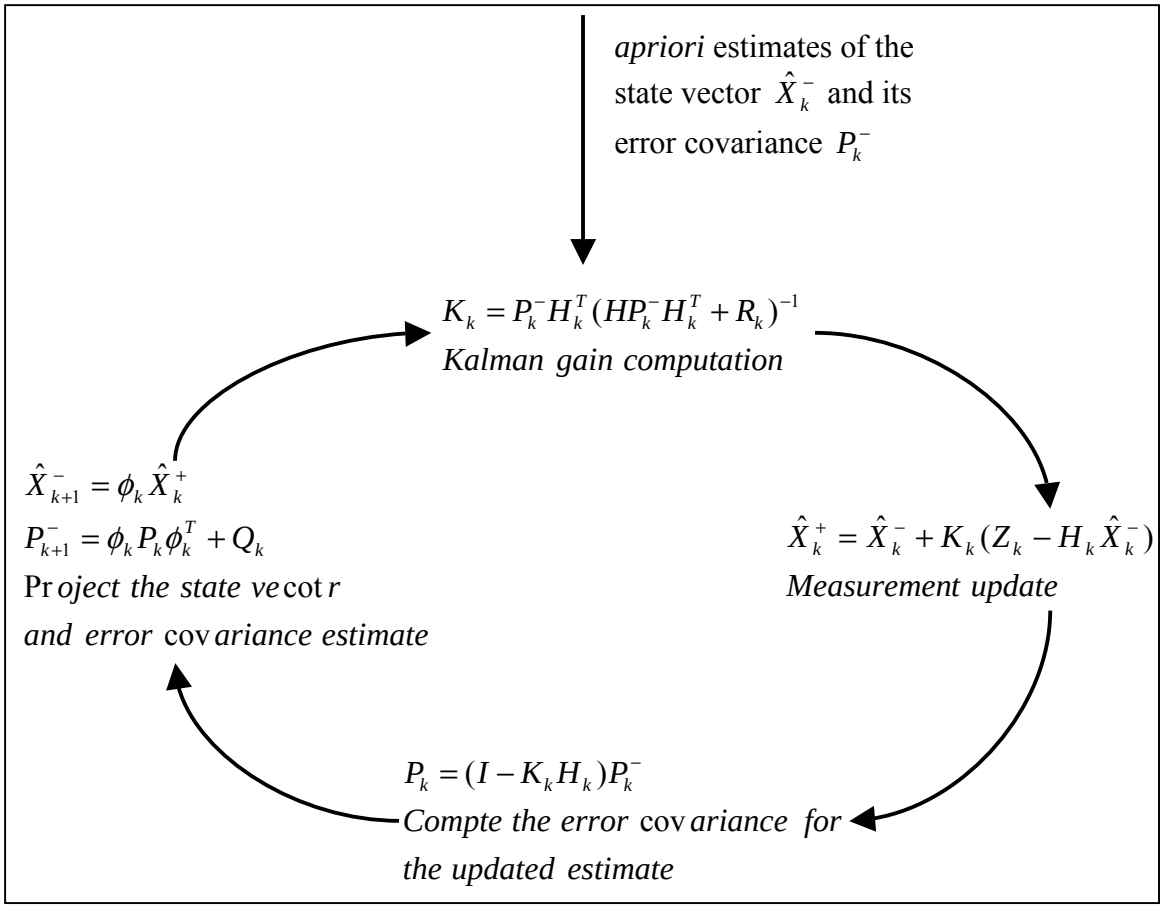

Figure 6.1: Kalman filter algorithm

The detailed derivation of the state transition matrix (ϕ) and, the system process noise (Q) matrix is detailed in Brown and Hwang (1992) and Gelb (1974). The filter is

initialized with the initial estimates of the error covariance matrix P_0 and the initial state vector X_0.

The filter can be operated in three different estimation modes, which are

- Filtering mode
- Smoothing mode
- Prediction mode

In filtering mode the value of the state vector X_k at time t_k is estimated in real-time using all the information including and prior to t_k. In smoothing mode the state vector X_k is estimated in post mission using the information before, including and after time t_k. However, in prediction mode the state vector at time t_k is estimated using information prior to time t_k. Clearly the smoothing mode provides more accurate estimates of the state vector X_k but cannot be used for real-time applications.

Kalman filtering provides an efficient method to integrate various sensors. There are two basic methods of integration, which can be classified into open loop (feed forward) scheme and closed loop (feed back) scheme. The concept of both these schemes are shown in Figure 6.2 and Figure 6.3 respectively.

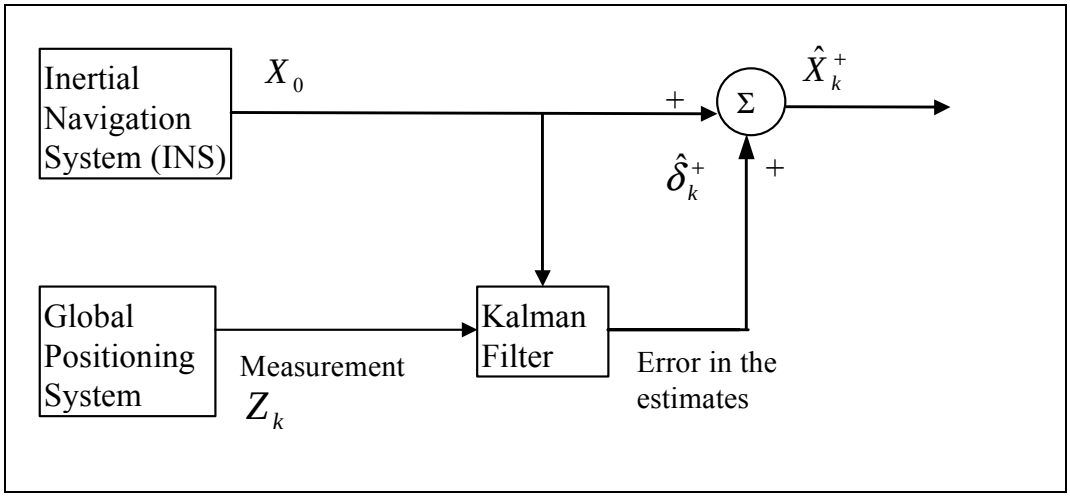

Figure 6.2: Feed forward scheme (Open loop)

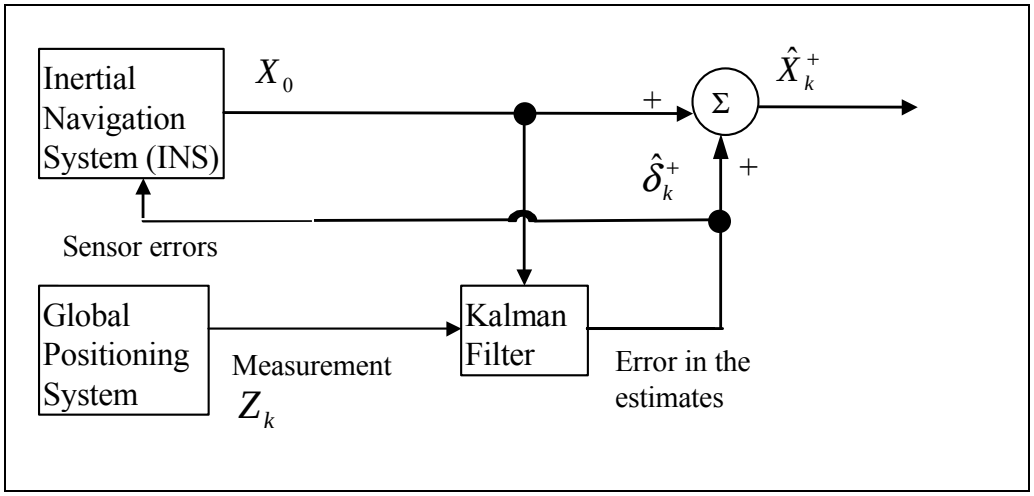

Figure 6.3: Feed back scheme (Closed loop)

Any of these two basic approaches can be implemented in order to integrate the INS with GPS (or DGPS) information. The first one, referred as *open loop*, deals with an estimation of the INS errors using GPS information and does not affect the operation of the INS. The second approach, called a *closed loop*, uses the GPS measurements to estimate the INS errors (sensor errors, such as gyro bias and accelerometer bias) as well as the INS sensor errors, and compensation of sensor errors is performed within the calculation procedure of the INS mechanization scheme. Whereas, in open loop scheme the sensor errors are uncompensated.

In principle, the closed loop scheme is more accurate, but the advantage of this realization depends on the application and on the stand-alone INS accuracy. The state vector estimation accuracy is highly sensitive to the vehicle dynamics and the random part of the estimation components. Hence if the random errors are not modelled properly the filter can become unstable. The open loop scheme operates with output error compensation, and as a result, it is more robust with respect to environmental changes. Therefore, the open loop scheme has been chosen in this research as it guarantees acceptable accuracy for various ranges of inertial sensors.

From the specifications and test results given in Tables 3.1 and 3.2, the MotionPak™ cannot be directly used as an inertial measurement unit (IMU) for a stand-alone INS. Firstly, the gyros are not sensitive enough to sense the Earth rate, which implies that a

self-contained azimuth alignment procedure cannot be performed. Secondly, the run-to-run gyro bias has a large magnitude that leads to nonlinear error behavior in stand-alone mode. In order to use this unit in an open loop integration scheme, a special damping error procedure is introduced using INS/DGPS measurements (see Salychev et al., 2000b).

In order to use the MotionPak™ integrated with GPS, several preliminary procedures have been implemented in the software called GAIN1™ (GNSS Aided Inertial Navigation), which was used in this thesis. This software has been co-developed by Laboratory of Inertial Geodetic Systems and University of Calgary (Salychev et al., 2000c). Several specialized algorithms and procedures have been designed such as

- horizontal alignment based on the acceleration output
- stored azimuth alignment using a magnetic compass or any external heading information
- calibration of the run-to-run gyro drift rate bias.

The GAIN1™ program is designed to process data in post-mission mode, but can be easily modified to operate in real time. Figure 6.4 shows the functional diagram of INS algorithm implemented in GAIN1™. The first step is to compute the run-to-run gyro bias, which is accomplished by the correction step procedure. The next step is to perform horizontal alignment, whereby the azimuth alignment is accomplished by using an external magnetic compass. All these procedures can be realized in real-time and take up to 15 minutes of stationary data. This process is performed on the vehicle before the start of the test. After that, the data processing program switches to navigation mode, which includes the following correction loops:

- INS error damping;
- "Calculated platform" correction using real time GPS output;
- Velocity correction;
- Attitude correction;
- Error model estimation for prediction mode.

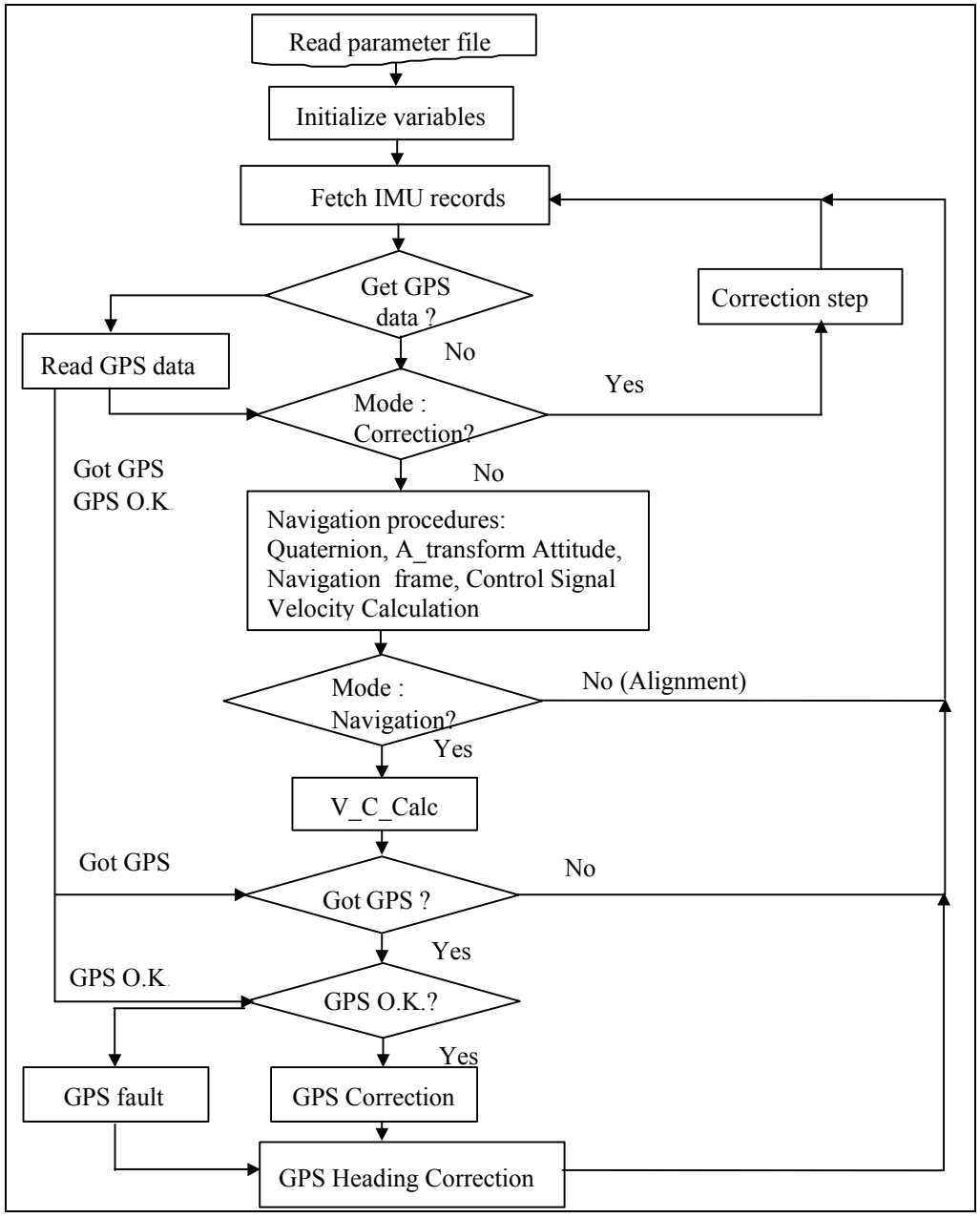

Figure 6.4: Software algorithm of GAIN1™ (Salychev et al., 2000a)

The heading estimate is computed from the GPS-derived velocities using the relation

$$H = \tan^{-1}(V_E / V_N) \qquad \textbf{(6.4)}$$

Where,

H is the heading in radians

V_E is the velocity along the local level East

V_N is the velocity along the local level North

The heading error, δH, in this case depends on the speed of the vehicle and is given as

$$\delta H = \frac{\sigma(DGPS)}{\sqrt{V_N^2 + V_E^2}} \quad \textbf{(6.5)}$$

Where σ(DGPS) is the standard deviation of the DGPS velocity estimates. It can be seen from equation (6.5) that the accuracy of the DGPS-derived heading is inversely related to the speed of the vehicle. Therefore, in order to determine heading angles with acceptable accuracy, a minimum value of the speed (10 m/s) was used. If the speed is below this value, the GPS heading was considered unreliable and was not used.

In the current implementation, a decentralized filter (Geier, 1998) approach is used to estimate the states and as a result two separate Kalman filters are designed to estimate the velocity errors and horizontal component of misalignment angles. The position errors are estimated separately using a least squares filter, which also has algorithms to apply constraints and perform reliability tests.

The state vector that is estimated in the Kalman filter is:

$$X = \left[\delta V_N, \delta V_E, \delta V_{UP}, \delta\varphi_N, \delta\varphi_E, \delta\omega_N, \delta\omega_E, \delta C_{drift}\right]^T \quad \textbf{(6.6)}$$

Where,

δV_N North velocity error component (m)

δV_E East velocity error component (m)

δV_{UP} Vertical velocity error component (m)

$\delta \varphi_N$ North misalignment error angle (radians)

$\delta \varphi_E$ East misalignment error angle (radians)

$\delta \omega_N$ North gyro drift error (rad/s)

$\delta \omega_E$ East gyro drift error (rad/s)

δC_{drift} Clock drift error (m)

The vertical channel in the INS is unstable and hence not computed by the INS algorithm. However, it can be estimated from the GPS measurements and has been included in the estimation process; the azimuth misalignment is estimated separately. The state transition matrix Φ is given by equation (6.7) (see Salychev, 1998 for details). The raw Doppler measurements from the antenna with maximum number of satellites are used as the measurement in the Kalman filter. Since the effect of multipath on Doppler measurements is almost negligible, Doppler from any one of the antennas is sufficient to compute the receiver velocity.

$$\Phi = \begin{bmatrix} dT & 0 & 0 & 0 & gdT & 0 & 0 & 0 \\ 0 & dT & 0 & -gdT & 0 & 0 & 0 & 0 \\ 0 & 0 & dT & 0 & 0 & 0 & 0 & 0 \\ 0 & dT/R & 0 & dT & 0 & 0 & 0 & 0 \\ -dT/R & 0 & 0 & 0 & dT & 0 & 0 & 0 \\ 0 & 0 & 0 & 0 & 0 & dT & 0 & 0 \\ 0 & 0 & 0 & 0 & 0 & 0 & dT & 0 \\ 0 & 0 & 0 & 0 & 0 & 0 & 0 & dT \end{bmatrix} \quad \textbf{(6.7)}$$

Where,

g is the apparent gravity vector (m/s^2)

dT is the interval at which the filter is updated (s)

R is the radius of Earth (m)

In this research, the GAIN1™ software was integrated with C^{3}NAV™ (Cannon and Lachapelle, 1995) to become MATNAV. The integration scheme employed in MATNAV is shown in Figure 6.5.

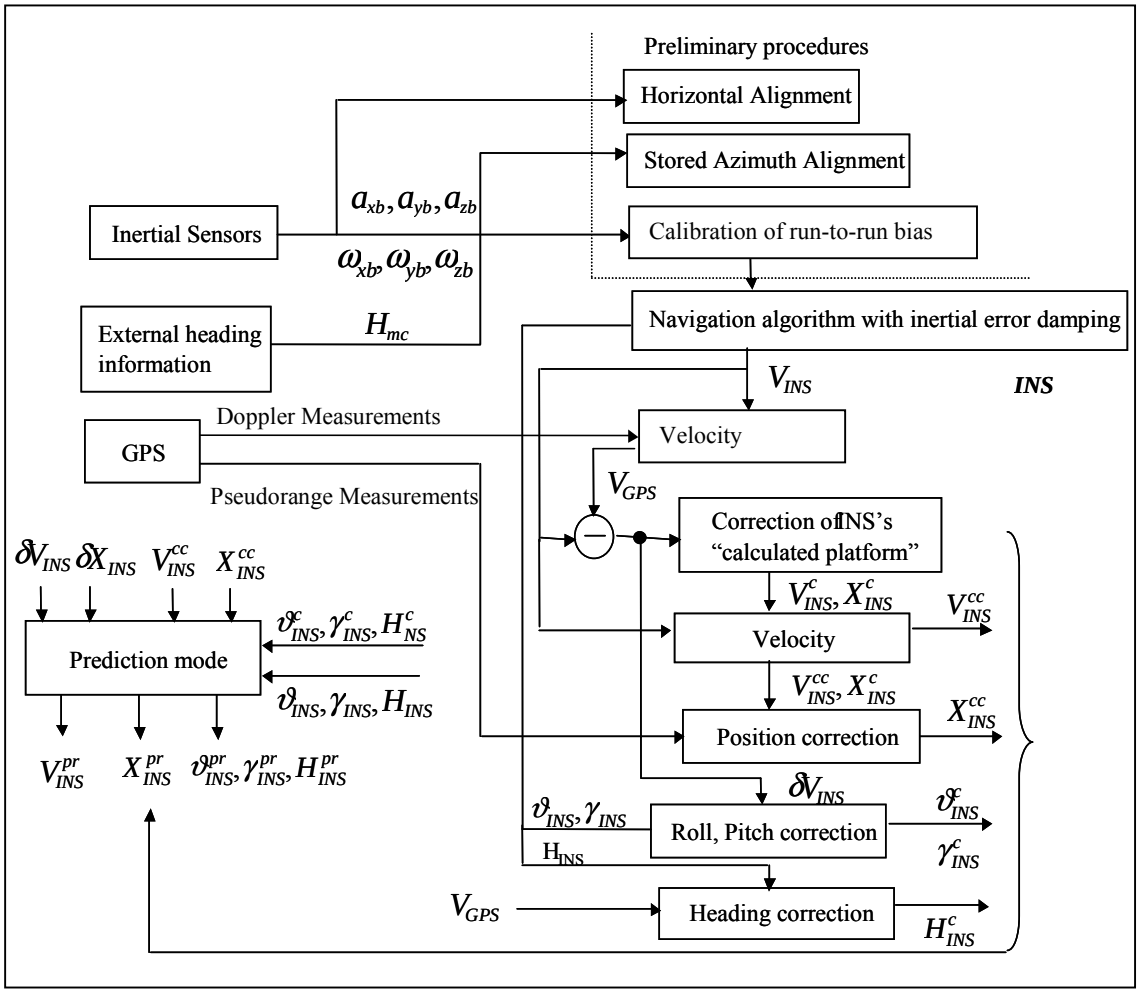

Figure 6.5: GPS/INS integration scheme used in MATNAV (Nayak et al., 2000b)

After the initial run-to-run bias calibration and alignment procedures, the software computes the INS outputs (Position, velocity and attitude) at a rate of 50Hz. The INS-computed velocity is used as the linearization point around which the Doppler measurements are used to estimate the INS velocity and attitude errors. The local level platform corrections are computed based on the GPS corrections. The velocity and the attitude errors are resmoothed using two separate Kalman filters. The velocity estimate is

then updated to the previous position to obtain an estimate of the current position. The updated current position is used as the linearization point in the least squares estimation filter. Latitude (ϕ), longitude (λ), altitude (h) and clock bias (c_b) are the four unknown parameters that are estimated for each antenna using least-squares estimation. The least squares algorithm uses pseudorange measurements from multiple antennas (up to four). If there are four antennas, the total number of estimated parameters is 16 and according to the prevailing visibility conditions, the number of parameters that are estimated may vary from 4 to 16. Therefore, depending on the antennas used at a particular instant, appropriate constraints can be applied.

The heading information is updated using speed information from GPS. The estimates from the Kalman filter are then used in the prediction mode to compute the position and velocity increments during GPS outages. The accuracy and performance of this is shown in the results discussed in the next section.

6.3 Results

Field tests were conducted on May 13, 2000, herein referred as Day 3. Raw GPS and IMU data was collected with the experimental setup described in Chapter 3. The route chosen is similar to the previous route, except that the foliage section has been omitted. The data from receiver D was unusable, most probably due to a faulty power connector; hence data from only three receivers was used for the analysis. The total duration of the test was 50 minutes and a distance of 30 km was covered during this test. The complete trajectory of the route is shown in Figure 6.6.

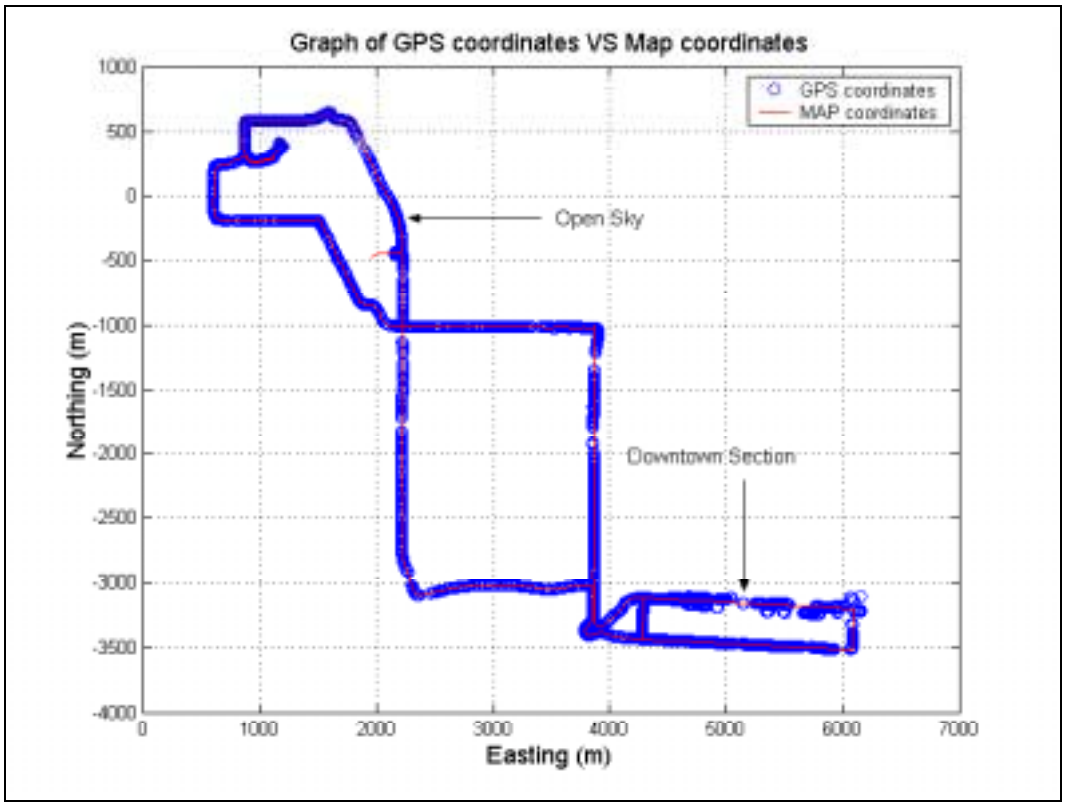

Figure 6.6: Trajectory of Antenna A

The trajectory shown above was computed from a single antenna using GPS-only with no constraints or reliability applied. There are quite a few GPS outages due to underpasses and partial satellite blockage in downtown Calgary. Figure 6.7 shows the percentage of GPS availability for the duration of the test with constraints and reliability, and without

any inertial aiding. Antennas A, B and C had 82.8%, 84.7% and 81.1% GPS availability respectively. The visibility was severely affected in downtown sections, and also due to few underpasses along the route in the open sky section.

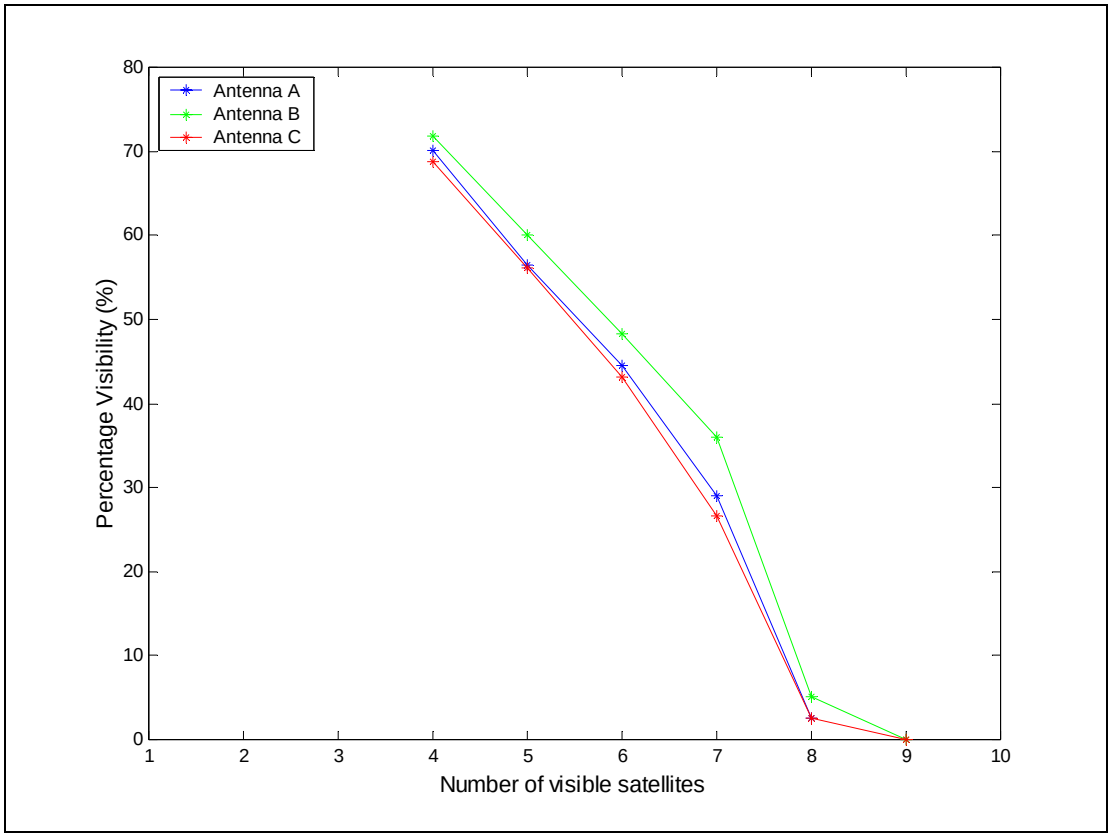

Figure 6.7: Percentage visibility

Horizontal position errors were computed and compared against the digital map of Calgary. The RMS errors for the entire test with different antenna combinations and with different scenarios are shown in Figure 6.8. All the results are with only three antenna/receiver combinations as the data from one of the receivers was unusable as mentioned previously.

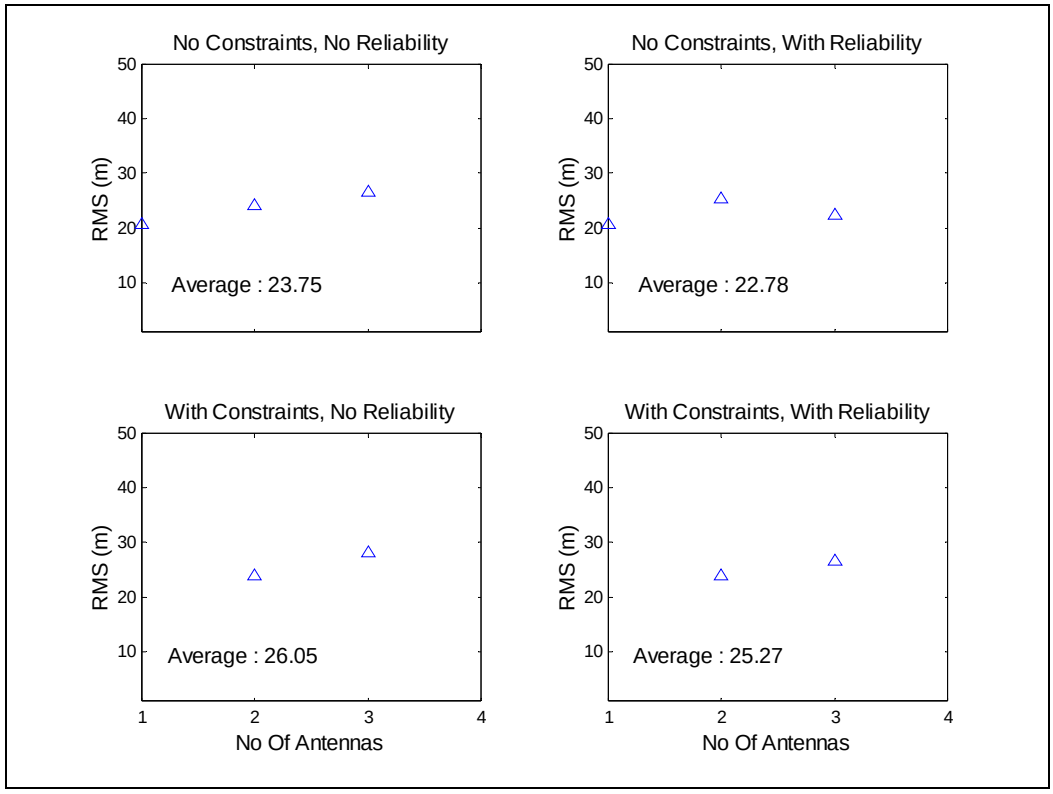

Figure 6.8: Average RMS agreement between DGPS and map coordinates for various scenarios

The RMS errors show a marginal improvement when reliability is applied (scenario No constraints, with reliability) compared to the scenario where no constraints and reliability are applied. However, when constraints are added, the performance deteriorates marginally because constraints can bias the overall solution. These results are similar to the results in Section 5.7. The external reliability, which has been described in Sections 5.2 and 5.3, is also computed for various antennas and scenarios. The results of the reliability tests are shown in Figure 6.9.

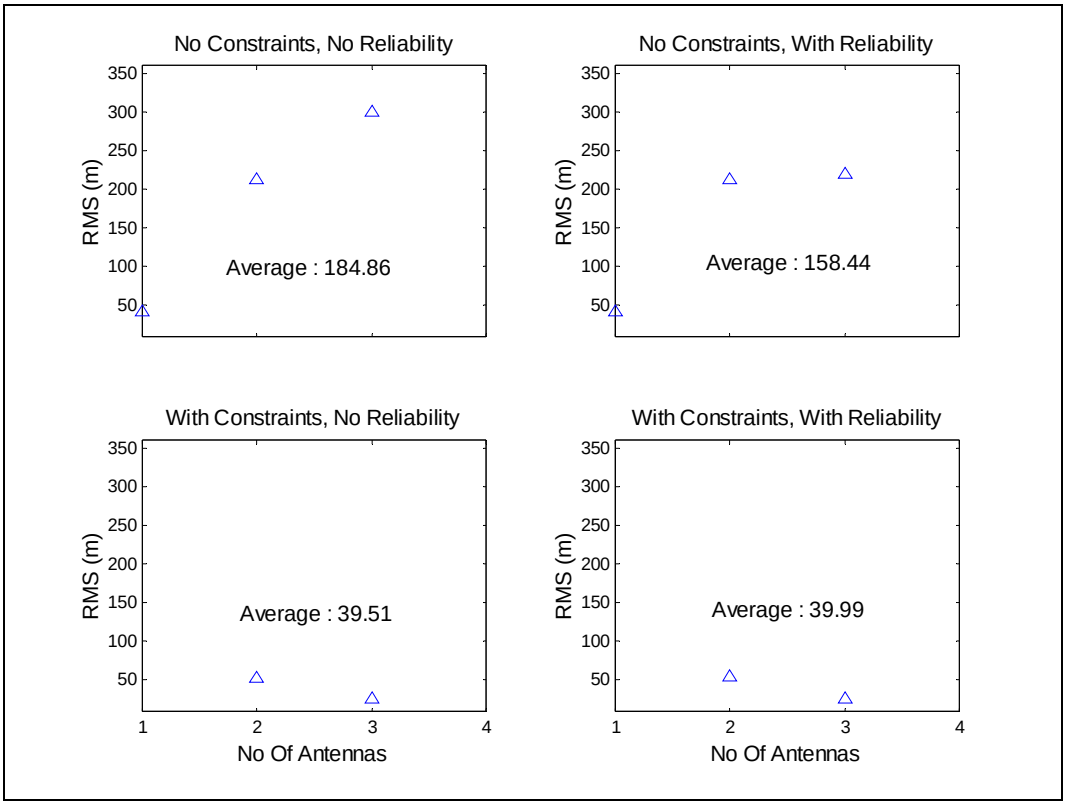

Figure 6.9: External reliability RMS errors for various scenarios, Day 3

The external reliability improves considerably with the application of constraints and also with addition of antennas. This is also consistent with the results shown in Section 5.7.

The DGPS data is then integrated with the inertial data collected at 50 Hz from the MotionPak™. The GPS/INS integrated trajectory for the entire test is shown in Figure 6.10. The integration result shown is generated from only one antenna without applying any constraints or reliability. The continuous red line represents the trajectory of the vehicle extracted from the digital map and the blue circles represent the INS/DGPS integrated trajectory. Most of the data gaps due to underpasses are effectively bridged by the INS. Some outages can be still noticed because the prediction mode is limited to 20 seconds after which there is no position or velocity updates. Hence the GPS availability is not 100% but improves from 84% with GPS-only to 92% with INS/GPS.

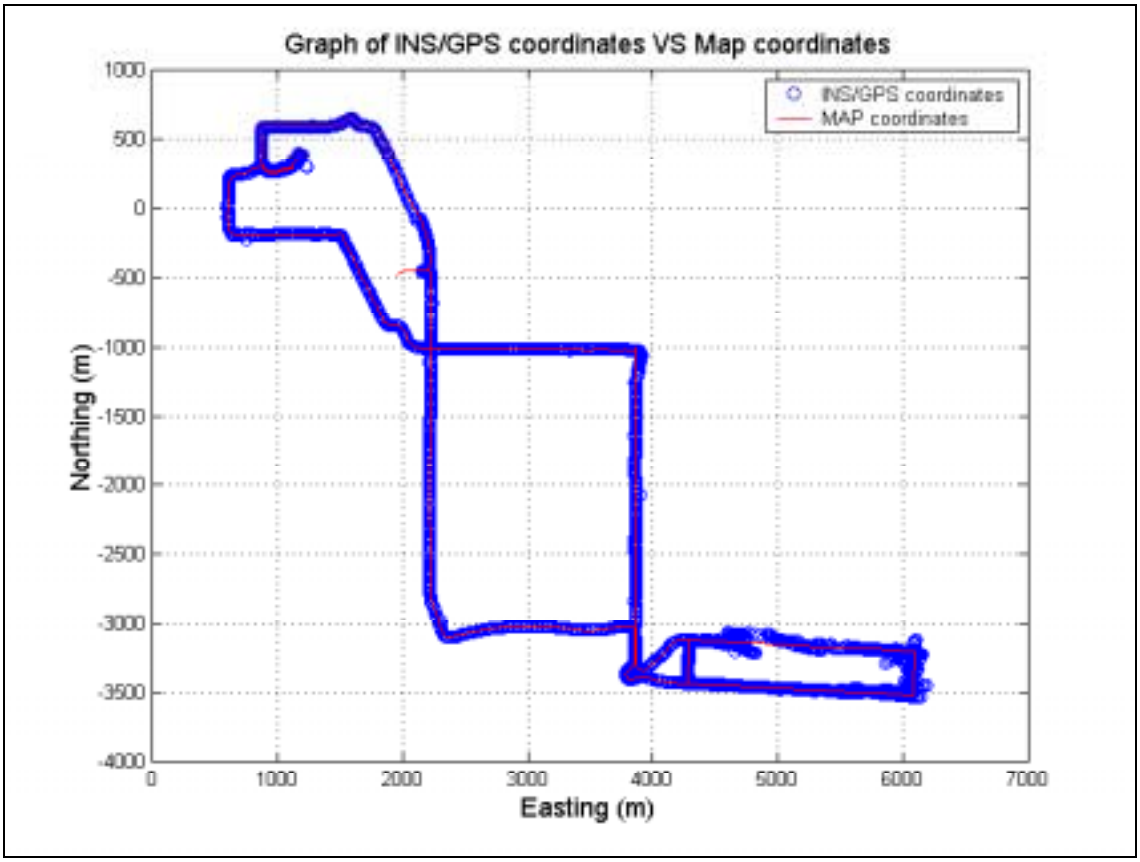

Figure 6.10: Integrated DGPS/INS trajectory of Antenna A, prediction limit of 20 s

A maximum horizontal error up to 160 m was observed in the downtown section. The estimation accuracy of the state variables in this section is poor mainly due to frequent outages. Most often a GPS outage occur before the filter is able to converge and the Kalman filter switches into prediction mode. This makes the filter rely more on the system model, as the measurements are available only sparsely. This system noise model is not able to adequately represent the INS errors and in turn results in large position errors.

The RMS errors of the GPS/INS integrated solution is compared with the digital map and the results are tabled along with the DGPS-only configuration. The results under various scenarios are listed in Table 6.1.

Table 6.1: Average RMS position errors for Day 3 under various scenarios

Day – 3 DGPS ONLY	NCNR RMS (m)	NCWR RMS (m)	WCNR RMS (m)	WCWR RMS (m)
1 antenna	20.5	20.6	N/A	N/A
2 antennas	24.2	25.3	23.9	23.9
3 antennas	26.5	22.5	18.1	26.6
Day – 3 DGPS/INS				
1 antenna	9.5	9.6	N/A	N/A
2 antennas	10.4	12.6	10.1	10.0
3 antennas	12.9	14.2	10.4	10.5

The RMS errors improve by as much as 50% when inertial measurements are used for augmentation. This improvement can be seen in all scenarios, and also with the single and multiple antenna case. This clearly demonstrates the benefit of using an inertial device to augment GPS. Reliability, which is independent of accuracy, depends on the ability to detect blunders in the system. The addition of inertial measurements into the system in the current configuration does not help reliability because the estimation procedure uses a least squares technique and the initial covariance matrix (C_x) of the parameters, which is affected by the inertial measurements is unknown and not propagated in the filter. However, if a Kalman filter was used to estimate the position errors, then the effect of additional measurements from the INS on reliability can be seen to be propagated through the error covariance matrix (P^-).

Figure 6.11 shows the trajectory computed from the GPS/INS integrated system without limiting the prediction interval. The position availability is now 100% whereas the accuracy is poor after about 20 seconds. Horizontal position errors up to 2.5 km can be seen from the figure. The reason for such poor performance is again due to the poor estimation of INS errors in downtown sections and the fast changing drift rates of the

gyros during these outages. This problem can be solved if better quality gyros are used in the IMU.

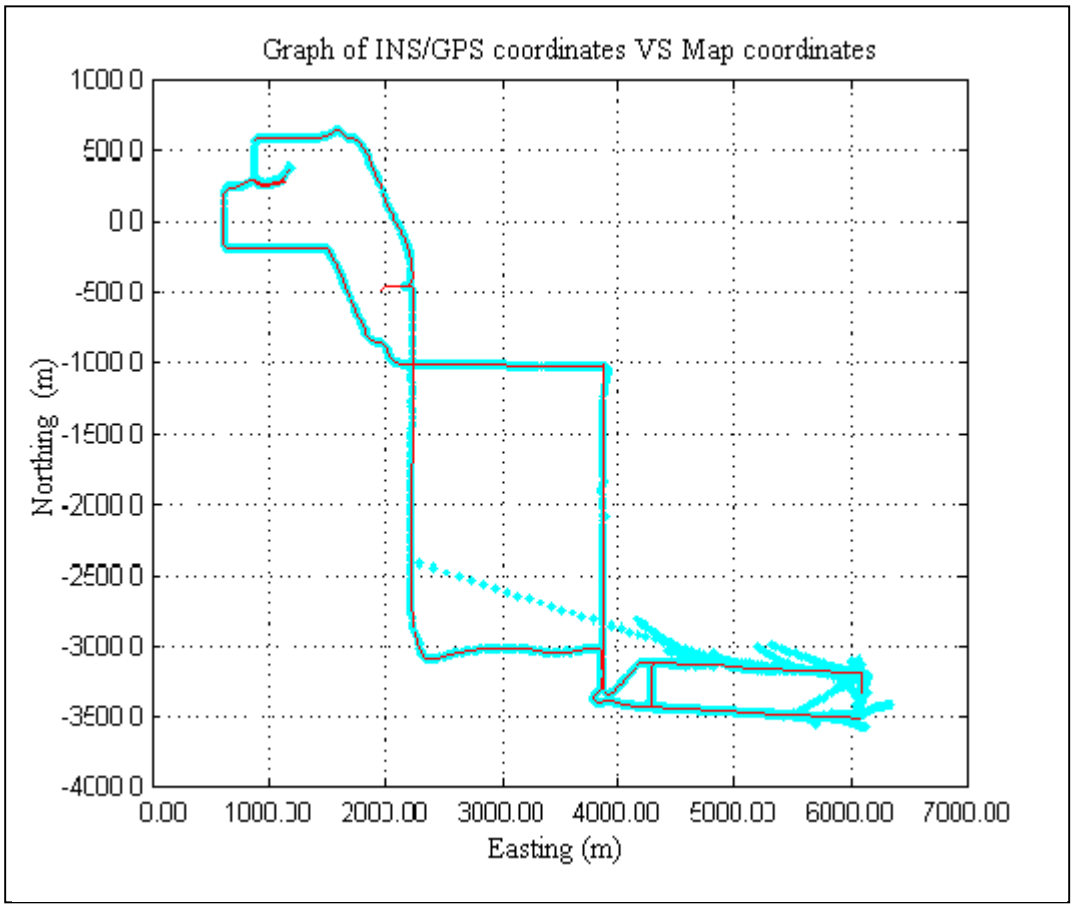

Figure 6.11: Integrated INS/GPS trajectory, without any prediction limit

GPS outages up to 3 minutes were observed in this section mainly when the vehicle had stopped at the lights. There was no improvement in position accuracy with multiple antennas, however, improvements on the order of 50% was seen in reliability estimates when three antennas were used as opposed to two antennas. The improvement in position error was largely due to the external aiding provided by INS rather than multiple antennas.

6.3.1.1 Performance Analyses

To access the performance of the integrated system, GPS outages were simulated along various portions of the test trajectory. The results of two such simulations under different vehicle dynamics are presented below. The accuracy of the predicted positions is then compared with the digital map. A 20 second GPS outage was simulated at a fairly high dynamics of 0.4 m/s^2 along a straight line and the predicted trajectory is shown in Figure 6.12. 'Start' and 'stop' in the figure indicate the beginning and the end of the simulated blockage. An approximate distance of 0.5 km was travelled in this duration. The absolute horizontal error is shown in Figure 6.13.

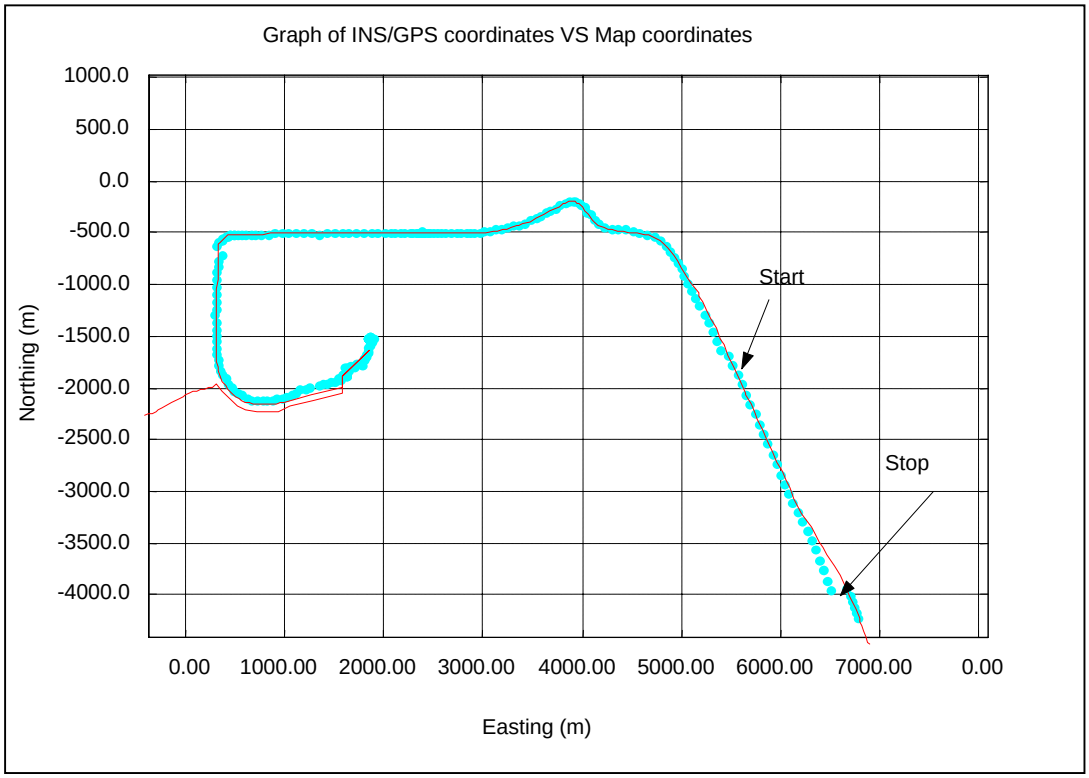

Figure 6.12: Trajectory with a simulated GPS outage of 20s (high dynamics)

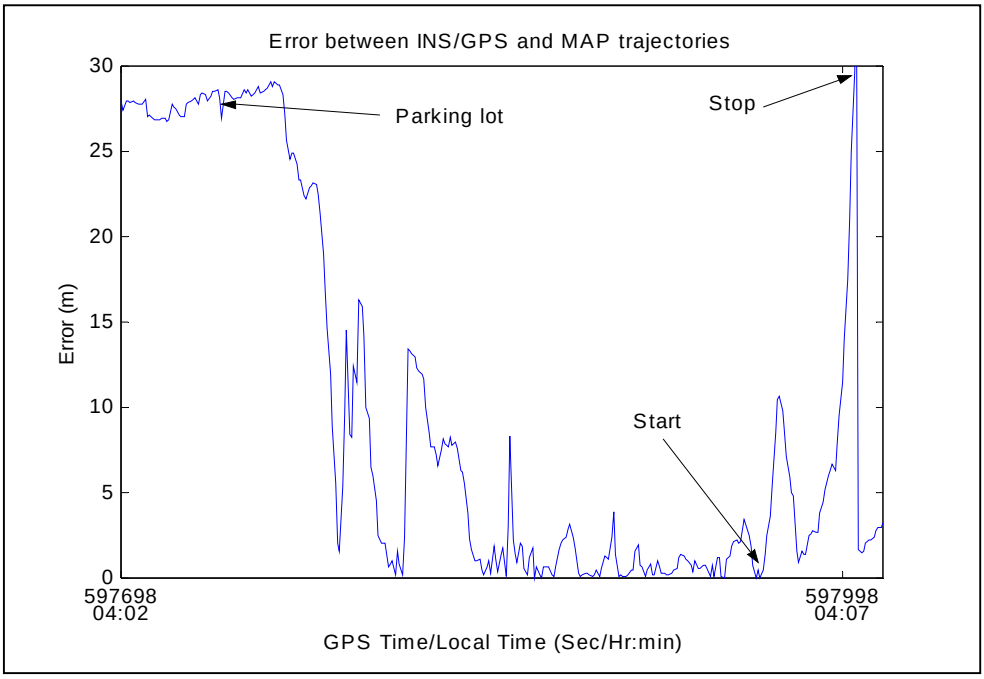

Figure 6.13: Difference between integrated position and digital map trajectory

An error up to 30 m can be seen from Figure 6.13 during the simulated GPS outage. Also an error of 28 m can be seen in the beginning of the test, which is due to non-availability of map coordinates inside the parking area. Map data is available only on the streets and not inside parking areas therefore, as the vehicle moves to the nearest street; the absolute horizontal error decreases.

To study the behaviour of the filter under benign conditions a 20 second GPS outage was simulated at constant vehicle velocity. The start and stop in Figure 6.14 indicate the beginning and end of the simulated outage interval.

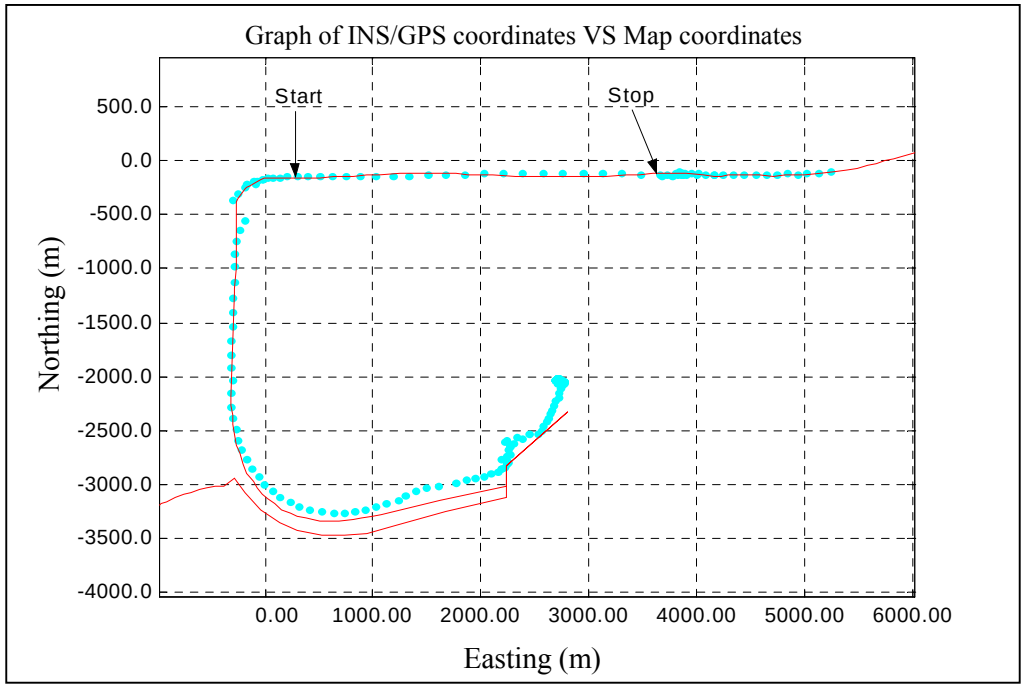

Figure 6.14: Trajectory with a simulated GPS outage of 20s (benign dynamics)

A total distance of 0.38 km was traversed during this time interval, and the absolute horizontal error as compared with the digital map is shown in Figure 6.15.

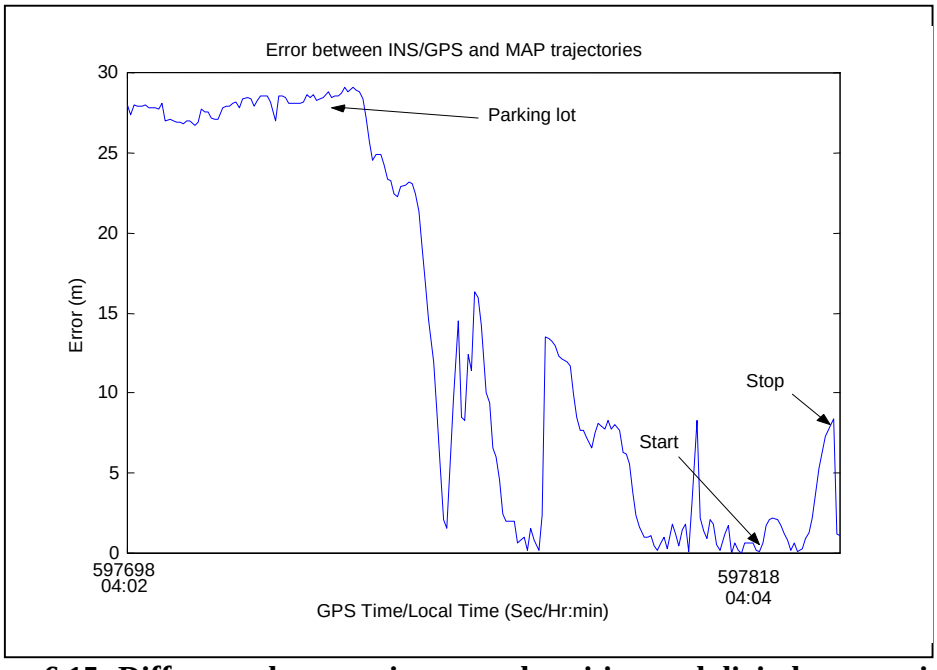

Figure 6.15: Difference between integrated position and digital map trajectory

The absolute horizontal error in this case is limited to 9 m. Once again the large position errors of 28 m in the beginning is due to unavailability of digital map information. These tests clearly show the performance of the Kalman filter under different dynamics. The larger error in case of higher dynamics is because of the poor representation of the system model.

6.3.1.2 Attitude

One of the major benefits of using an inertial device is the availability of attitude information. Although this is not a focal point of this thesis, a brief discussion on the attitude performance of the system is included for completeness. The attitude information can be used to determine the banking of the vehicle during turns and for heading computation. The attitude accuracy of MotionPak™ was compared with a highly accurate Russian I-21 gimbal INS system in airborne mode, for details see Salychev et al., (2000b). The attitude performance of MotionPak™ obtained from GAIN1™ is shown in Table 6.2.

Table 6.2: GAIN1™ attitude error statistics for MotionPak™ (Salychev et al., 2000b)

RMS Error	Pitch (arcmin)	Roll (arcmin)	Heading (arcmin)
	25.1	22.4	43.7

The results indicated errors of few tens of arc minutes, which means although the attitude derived from MotionPak™ cannot be used for precise applications it is still well suited for estimating the banking angle of the vehicle. For further details see Salychev et al., (2000b).

6.4 Summary

This section focused on the detection of multipath blunders based on reliability analysis and multiple antennas with external aiding from a low cost inertial device. Field data was

collected once again to verify the algorithms and to assess their performance under several scenarios.

There is a considerable error in the position domain in the downtown areas (around 30 m) mainly due to poor geometry (GDOP > 15). Some of the blunders were removed with the addition of constraints and reliability tests, but the improvement in position error is marginal. Also, most often there were not sufficient measurements available to perform a reliability test. The results showed that position accuracy did not improve by using multiple antennas, however, there was a substantial improvement in the reliability. Improvements on the order of 50% were seen in reliability when three antennas were used instead of two antennas.

The tests also showed a negative improvement of 11% in position error when only reliability was applied. This was again due to an increased DOP, which is an outcome of discarding satellites resulting from the statistical test. However, an improvement of 6% was observed with the application of constraints and reliability. These results are the average RMS errors for the entire test. Also an improvement of 10% (position availability) is observed by limiting the prediction mode to 20 seconds. However, 100% position availability is possible if no limit is set on the prediction time, but results in reduced accuracy due to the poor quality of the inertial sensors. This can be minimized by using better quality gyros, which have lower drift characteristics, or by improving the estimation of the sensor errors by the Kalman filter using carrier phase observables.

The results shown in this section were much poorer compared to the dead reckoning approach used by Stephen (2000). One of the reasons for this is that the gyro bias was calibrated frequently (every time the vehicle is stationary) unlike the current approach used in this thesis, where the gyro bias is calibrated in the beginning before the start of the test.

Chapter 7

Conclusions and Recommendations

7.1 Introduction

The research had three major components. In the first part of the research a series of tests were conducted in Calgary whereby four antennas were mounted on a vehicle and raw GPS data was collected over four sections covering different environmental conditions such as urban, suburban and dense foliage. The data from all the four antennas was processed using the code minus carrier technique to characterize multipath and its correlation from one antenna to another. The influence of code multipath on multiple antennas separated by less than a metre was analyzed using this approach for spatial and temporal decorrelation effects. GPS receivers tracking performance under different environments were also studied. The possibility of using Signal to Noise ratio (SNR) to estimate multipath was also investigated.

The second part of the research focused on detection and isolation of multipath based on reliability analysis and geometry of multiple antennas/receivers. Field tests were once again conducted to collect data and to verify the algorithms and assess the performance under several operational environments. Various scenarios were formed using combinations of antennas, reliability and constraints. The advantage of each of these scenarios was scrutinized. The horizontal position accuracy for each scenario was computed by comparing the results with an accurate digital road map.

The focus of the third part of this research was to access the benefits of using a low cost inertial device to augment GPS during satellite blockages and to see if better performance in terms of accuracy and reliability could be achieved. A non-conventional GPS/INS integration architecture was discussed (GAIN1™). The software MATNAV was developed by integrating C^3NAV and GAIN1™ along with the options to perform statistical testing and to make use of baseline constraints between multiple antennas.

7.2 Conclusions

From the various tests performed (Days1,2 and 3) the following conclusions can be drawn.

1. The code minus carrier differences provided a good representation of code multipath error in dynamic environments. The code minus carrier differences for Sections 1 (open sky) and 2 (urban) show that the multipath error depends on the surrounding environment and the dynamics of the vehicle. In spite of the harsh multipath environments in section 2, few gross multipath errors of 6 to 10 m were seen. This is due to the high performance Narrow Correlator™ technology employed in the Millennium™ receivers.

2. The cross correlation results showed rapid spatial decorrelation of multipath among antennas. Since multipath amplitude and phase change rapidly with the vehicle dynamics it is possible to use the geometry information between the antennas to detect and mitigate multipath from the pseudorange measurements. The spatial decorrelation (correlation coefficient) among antennas varied from 0.2 to 0.4. The temporal decorrelation of code multipath on a moving platform is also very rapidly changing quantity. The code multipath reduces to 50% of its value within 5 seconds, compared to a few minutes for the static case.

3. Using the SNR to estimate multipath is also not very effective on a moving platform as SNR depends not only on the multipath but also on the vehicle dynamics, satellite elevation angles, and the surrounding environment. SNR is affected more by the loss of signal due to shading effects than multipath, hence SNR cannot be used to identify multipath.

4. Multipath errors up to +/- 6 m were observed in downtown sections, whereas there was hardly any multipath error in section 3 (dense foliage), however the satellite visibility was poor and comparable with the downtown section. Foliage affects the signal by absorbing the power rather than reflecting it.

5. The reliability and constraints algorithms used did not substantially improve the position accuracy in an open sky environment (Section 1). The blunders or multipath errors in this case are too small to be detected by the statistical test, however by applying constraints the positions of all the four antennas are bounded by each other. The results were more promising in urban environment (Section 2) and foliage (Section 3). The RMS position errors in urban areas on Day 2 with four antennas, and without any constraints and reliability, is around 20 m, but improves to 13 m by applying constraints and performing the reliability test. However, the improvements on Day 1 are much smaller. This is because the multipath environment is different during different runs and the improvement is proportional to the blunder. This method does not eliminate multipath completely but the performance depends on the detection capability of the statistical test.

6. Some of the blunders were removed with the addition of constraints and reliability tests and sometimes there were more than one blunder in the observation set and the statistical test failed. The average position errors did not improve substantially due to the increase in the DOP, which resulted when some measurements were discarded. Also, most often there was not sufficient redundancy in measurements to perform a reliability test.

7. The results show that having a reliability test and constraints together is better than having only reliability or constraints. The number of antenna/receivers that needs to be used depends on the reliability requirement of the application. The reliability increases with every additional antenna. The cost of the overall system also increases with every additional antenna/receiver. However, for non-critical automobile navigation applications such as position reporting two antennas with reliability and constraints is adequate.

8. The tests demonstrated that the GPS/INS integrated system shows promising results for accurate navigation with improved position availability using low cost inertial sensors. An improvement of 10% is observed by limiting the prediction

mode to 20 s. However, 100% position availability is possible if the prediction time is not limited, but with reduced accuracy due to the poor quality of the inertial sensors. The sensor errors increase rapidly over time due to their poor stability and to obtain better performance in severe urban conditions integration with map database is an alternate option. These kinds of systems can be widely used for a variety of cost effective navigation applications.

9. The tests conducted with the GPS/INS integrated system showed a negative improvement of 11% in position error when only reliability was applied. This was due to an increased DOP, which is an outcome of discarding satellites as a result of the statistical test. However, an improvement of 6% was observed with the application of constraints and reliability. These results are the average RMS errors for the entire test.

10. The performance of the integrated system is completely dependent on the environment and dynamics of the vehicle, and the results shown in this research represents just one such environment.

7.3 Recommendations

1. One of the methods to improve the MDB is to increase the redundancy. This can be achieved by estimating fewer parameters in the estimation process, which can be accomplished by having a common clock and solving for one clock parameter for all the receivers instead of estimating clock parameters for individual receivers. The benefits of using clock constraints on reliability by using good quality external oscillator needs to be investigated.

2. When GPS is augmented with INS the velocity and attitude accuracy depends on the estimation accuracy of the INS errors. Therefore, by using carrier phase-derived Doppler and range observations, better estimates of velocity can be

obtained, which in turn can be used to propagate position and velocity estimates for longer duration and with better accuracy.

3. The inertial sensors bias and scale factors are usually sensitive to temperature variations; and the MotionPak™ inertial sensor outputs the temperature information along with the acceleration and angular rate measurements. This information is currently not being used. Improved gyro and accelerometer bias drift models can be developed based on the temperature variations.

4. The multipath blunders seen were very small, except for a few large blunders, but generally on the order of few metres due to the Narrow Correlator™ technology used in the receivers, hence the improvements in position accuracy were very small. Similar tests on standard wide correlator receivers may yield different results. Therefore further testing with multiple antenna/receiver configurations along with the low cost inertial device and standard correlator receivers needs to be done.

5. The attitude accuracy that can be achieved with the integrated system needs to be evaluated by comparing attitude derived from highly accurate carrier phase measurements derived from a multi antenna system.

6. The robustness of the system needs to be evaluated by using a additional samples of the inertial sensors by the same manufacturer and also similar sensors from other manufacturers.

7. For the reliability tests only one blunder is assumed to be present, however in reality there could be more than one blunder. Hence, a statistical test that accounts for two or more blunders (Ryan, 2000) also needs to be investigated.

8. One of the benefits of using inertial devices is that it can be used to improve the tracking loop sensitivity by reducing the bandwidth. With low cost inertial devices it may not be possible to do this because of their poor sensor

characteristics. However, the code-tracking loop has low dynamics compared to the carrier loops and the inertial devices can be used to improve the sensitivity of the code tracking loops.

REFERENCES

Abousalem, M.A. (1993), Development of A Robust GPS Kinematic Positioning Module for Automatic Vehicle Location and Navigation, *UCGE Report 20077*, Department of Geomatics Engineering, The University of Calgary.

Axelrad, P. and R.G.Brown (1994), GPS Navigation Algorithms, *Global Positioning System: Theory and Applications, American Institute of Aeronautics and Astronautics,* Vol 1, Ch 9, pp. 409-433.

Baarda, W. (1968), A Testing Procedure for Use in Geodetic Networks, *Neth.Geod. comm. Publ. On Geodesy*, New Series, Vol.5(2).

Braasch, M.S. (1994), Multipath Effects, *Global Positioning Systems: Theory and Applications, Vol.* I, ed. B.W. Parkinson and J.J. Spilker Jr., American Institute of Aeronautics and Astronautics, Washington DC, pp. 547-568.

Braasch, M.S. (1995), Isolation of GPS Multipath and Receiver tracking Errors, *NAVIGATION: Journal of The Institute of Navigation*,Vol 41, No 4, pp 415 – 434.

Brown, R.G. and P.Y.C. Hwang (1992), Introduction to Random Signals and Applied Kalman Filtering*, Second Edition, John Wiley & Sons Inc.*, 502 pp.

Bullock, B.J. (1995), A Prototype Portable Vehicle Navigation System Utilizing Map Aided GPS, *UCGE Report 20081*, Department of Geomatics Engineering, The University of Calgary, 156 pp.

Cannon, M.E. (1991), Airborne GPS/INS with an application to Aerotriangulation, *UCSE Reports No 20040*, Department of Surveying Engineering, University of Calgary.

Cannon, M.E. and G. Lachapelle (1992), Analysis of a High-Performance C/A-Code GPS Receiver in Kinematic Mode, *NAVIGATION: Journal of The Institute of Navigation*, Vol. 39, No. 3, Fall, pp. 285-300.

Cannon, M.E. and G. Lachapelle (1995), *C*^{3}*NAV™ Operating Manual*, Department of Geomatics Engineering, The University of Calgary, 23 pp.

Cannon, M.E. (2000), Satellite Positioning, *ENGO 561 Course Lecture notes*, Department of Geomatics Engineering, University of Calgary, Canada.

Daljit, S and H. Grewal (1995), Autonomous Vehicle Using WADGPS, *Proceedings of the ION GPS-95*, September 12-15,Palm Springs, California, pp-1333- pp 1338

Doscher, J. (2000), Accelerometer Design and Application, *Accelerometer application seminar by Analog Devices,* http://www.analog.com/industry/iMEMS/library/Sensor971.pdf, *(*September 6 2000)

El-Mowafy, A. (1994), Kinematic Attitude Determination From GPS, Ph.D Thesis UCGE Report No 20074, Department of Geomatics Engineering, The University of Calgary

Fenton, P., B. Falkenberg, T. Ford, K. Ng and A.J. van Dierendonck (1991), Novatel's GPS Receiver: The High Performance OEM Sensor of the Future, *Proceedings of ION GPS-91*, Albuquerque, September 9-13, pp. 49-58.

Fortes, L. P., M. E. Cannon, and G. Lachapelle (2000), TESTING A MULTI-REFERENCE GPS STATION NETWORK FOR OTF POSITIONING IN BRAZIL, *Proceedings of ION GPS-2000,* Salt Lake City, Utah, September 20-23, (in press).

Ford, T. (1998), Lead Discussion on NovAtel's Narrow Corrleators, ENGO 625 Course seminar, Department of Geomatics Engineering, The University of Calgary.

Fotopoulous,G., M.E.Cannon, A. Bogle, G. Johnston (1998),Testing Landstar's Performance Under Operational Conditions, *Proceedings of ION NTM 98*,Long Beach CA, January 21 – 23, pp.207-215. (http://www.geomatics.ucalgary.ca/GradTheses.html)

Francisco, S. G. (1996), GPS Operational Control Segment, *Global Positioning System: Theory and Applications, Vol. I*, ed. B.W. Parkinson and J.J. Spilker Jr., American Institute of Aeronautics and Astronautics, Inc., Washington, DC, pp. 435-468.

French R.L, (1995), From Chinese Chariots to Smart Cars: 2,000 Years of Vehicular Navigation, *NAVIGATION: Journal of Institute of Navigation*, Vol 42, No. 1, Spring, pp 235 – 258.

Garin, L., F. van Diggelen and J. Rousseau (1996), Strobe and Edge Correlator Multipath Mitigation for Code, *Proceedings of ION GPS-96*, Kansas City, September 17-20, pp. 657-664.

Garin, L. and J. Rousseau (1997), Enhanced Strobe Correlator Multipath Rejection for Code and Carrier, *Proceedings of ION GPS-97*, September 16-19, Kansas City, pp. 559-568.

Geier, G.J (1998), Integration of GPS with Low Cost Sensors Technology for Automotive Applications, *Lecture Notes ENGO 699.46*, August 10 - 21, The University of Calgary, Summer, 448 pp.

Gelb, A. (1974), *Applied Optimal Estimation*, MIT Press, Massachusetts Institute of Technology, Massachusetts, Cambridge, 374 pp.

Harris, C.B (1989), Prototype For a Land Based Automatic Vehicle Location and Navigation System, *UCSE Report 20033*, Department of Surveying Engineering, The University of Calgary.

Hopfield, H.S. (1963), The Effect of Tropospheric Refraction on the Doppler Shift of Satellite Data, *Journal of Geophysical Research*, Vol 68, No 18, pp. 5157-5168.

Huangqi, S and M.E. Cannon (1997), RELIABILITY ANALYSIS OF AN ITS NAVIGATION SYSTEM, *Proceedings of the IEEE conference on Intelligent Transport Systems*, November 9 – 12, Boston, MA. pp. 1040 – 1046.

Klobuchar, J. A. (1996), Ionospheric Effects on GPS, *Global Positioning Systems: Theory and Applications, Vol I*, ed. B.W. Parkinson and J.J. Spilker Jr., American Institute of Aeronautics and Astronautics, Washington DC, pp. 485-516.

Krakiwsky, E.J., C.B. Harris and R.V.C. Wong (1988) A Kalman Filter for Integration of Dead Reckoning, Map Matching and GPS Positioning, *Proceeding of IEEE Position, Location and Navigation*, November 29 - December 2, Orlando, pp. 39 – 46.

Krakiwsky, E.J. and M.A.Abousalem (1995), Viewgraphs for Adjustment of Observations, *ENGO 411 course notes*, Department of Geomatics engineering, University of Calgary. 99 pp.

Lachapelle,G (1990), GPS Observables and Error Sources For Kinematic Positioning, *Proceedings of International Symposium on Kinematic Systems for Geodessy, Surveying and Remote Sensing*, Banff, September 10 – 13, Springer-Verlag, Vol. 107, pp. 17- 26.

Lachapelle. G., J. Henriksen and T. Melgård (1994), Seasonal Effect of Tree Foliage on GPS Signal Availability and Accuracy for Vehicular Navigation, *Proceedings of ION GPS - 94*, Salt Lake City, Utah, September 20-23, pp. 527 - 532.

Lachapelle, G. (1998), GPS Theory and Applications, *ENGO 625 Course Lecture notes*, Department of Geomatics Engineering, University of Calgary, Canada.

Leick, A. (1995), *GPS Satellite Surveying, 2nd Ed.,* John Wiley &Sons, Inc., New York. 560 pp.

Maybeck, P.S. (1994), *Stochastic Models, Estimation, and Control, Vol. I*, Navtech, Arlington, 423 pp.

Michael, E.M. and G.Gracie (1998), *Analysis and Adjustment of Survey Measurements, Van Nostrand Reinhold Company, New York*, 340 pp.

Navstar GPS (1995*), Global Positioning System Standard Positioning Service Signal Specification, Second Edition*, June 2, 51 pp.

Nayak, R., M. E. Cannon, C.Wilson, and G. Zhang (2000a), Analysis of Multiple GPS Antennas for Multipath Mitigation in Vehicular Navigation, *Proceedings of ION NTM 2000*, Anaheim CA, January 26-28, pp. 284 - 293.

Nayak, R., M. E. Cannon, and C.Wilson, (2000b), Use of Multiple GPS Antennas and A Low Cost IMU for Reliable And Continuous Urban Navigation, *Proceedings of ION, IAIN World congress 2000*, San Diego CA. June 26-28, (in press).

Parkinson, W.B., and P. Axelrad (1988), Autonomous GPS Integrity Monitoring Using the Pseudorange Residual, *NAVIGATION: Journal of The Institute of Navigation,* Vol. 35, No. 2, pp. 255-274.

Parkinson, W.B (1994a), Introduction and Heritage of NAVSSTAR, the Global Positioning System, *Global Positioning System: Theory and Applications, Vol. I*, ed. B.W. Parkinson and J.J. Spilker Jr., American Institute of Aeronautics and Astronautics, Inc., Washington DC, Ch 1, pp. 3-28.

Parkinson, W.B (1994b), GPS Error Analysis, *Global Positioning System: Theory and Applications, Vol. I*, ed. B.W. Parkinson and J.J. Spilker Jr., American Institute of Aeronautics and Astronautics, Inc., Washington DC, Ch 11, pp. 469-483.

Parkinson, W.B and P.K.Enge (1995), Differential GPS, *Global Positioning System: Theory and Applications, Vol. II*, ed. B.W. Parkinson and J.J. Spilker Jr., American Institute of Aeronautics and Astronautics, Inc., Washington DC, pp 3-49.

Randle, J.S and M.A. Horton (1997), Low Cost Navigation Using Micro Machined Technology. *Proceedings of the IEEE conference on Intelligent Transportation Systems*, Boston, November 9-12, pp. 1064 – 1067.

Ray, J. (2000), Mitigation of GPS Code and Carrier Phase Multipath Effects Using a Multi-antenna System, *Ph.D. Thesis, UCGE Report 20136*, Department of Geomatics Engineering, The University of Calgary, Alberta, Canada.

Ren, D and G. Dedes (1995), Nonlinear Smoothing of Dead Reckoning Data with GPS measurements, *Proceedings of ION GPS –95*, Palm Springs, September 12-15, pp. 1285 – 1294.

Ryan, S. J. Stephen, and G. Lachapelle (1999), Testing and Analysis of Reliability Measures for GNSS Receivers in the Marine Environment, *Proceedings of ION NTM 99*, San Diego CA, January 25-27, pp. 505-514.

Ryan, S. (2000), Marine Multipath Blunders and Reliable Navigation, *Graduate Seminar ENGO 609*, Department of Geomatics Engineering, The University of Calgary.

Saastamoinen, J. (1972), Atmospheric Correction for the Troposphere and Stratosphere in Radio Ranging of Satellites, *Geophysical Monograph 15,* American Geophysical Union, Washington, DC.

Salychev, O. (1998), Inertial Systems in Navigation and Geophysics, Bauman MSTU press Moscow, 352 pp.

Salychev, O., V.V.Voronov, M.E.Cannon, R.A.Nayak and G.Lachapelle (2000a), Low Cost INS/GPS Integration: Concepts and Testing, *Proceedings of ION NTM 2000*, Anaheim CA, January 26-28, pp. 98 - 105. (http://www.geomatics.ucalgary.ca/GPSRes/first.html)

Salychev, O., V.V.Voronov, M.E.Cannon, R.A.Nayak and G.Lachapelle (2000b), Attitude determination with GPS-Aided Inertial Navigation System, *Proceedings of IAIN World Congress in association with ION Annual Meeting*, San Diego CA, June 26-28, pp. 705 – 711 (http://www.geomatics.ucalgary.ca/GPSRes/first.html)

Salychev, O., V.V.Voronov, and M.E. Cannon (2000c), GAIN1™ Operating Manual-GNSS Aided Inertial Navigation, Department of Geomatics Engineering, The University of Calgary, 12 pp.

Salzmann, M.A. (1991). MDB: A design tool for integrated Navigation systems, *Bulletin Géodésique*, Vol 65, pp. 109-115.

Schwarz, K.P. (1998), Fundamentals of Geodesy, Lecture Notes ENGO 421, Department of Geomatics Engineering, The University of Calgary, Canada, 189 pp.

Schwarz, K.P and M. Wei (1999), INS/GPS integration for Geodetic Applications, Lecture Notes for ENGO 623, Department of Geomatics Engineering, The University of Calgary, Canada, 112 pp.

Shenoy, M.R., S. M Krishna, N.S. Sudhir, R. Anjan and S. Kiran (1999), NAV2300 – Accord's High Performance Low Cost Receiver Technology with Soft-Correlator™ and Programmatic Interface, *Proceedings of ION GPS-99*, Nashiville, September 14-17, pp 787 - 792.

Snyder, J.P (1993), Map Projections – A Working Manual, *U.S. Geological survey professional paper*, Navtech Seminars, U.S. Government document, 383 pp.

Spilker, J.J. Jr., (1994a), GPS Navigation Data, Overview of GPS Operation and Design, *Global Positioning System: Theory and Applications, Vol I, ed*. B.W. Parkinson and J.J. Spilker Jr., American Institute of Aeronautics and Astronautics, Inc., Washington DC, pp. 121- 176.

Spilker, J.J. Jr., (1994b), Tropospheric Effects on GPS, *Global Positioning System: Theory and Applications, Vol I, ed*. B.W. Parkinson and J.J. Spilker Jr., American Institute of Aeronautics and Astronautics, Inc., Washington DC, pp. 517- 546.

Spilker, J.J. Jr., (1994c), Foliage Attenuation for Land Mobile Users, *Global Positioning System: Theory and Applications, Vol I, ed*. B.W. Parkinson and J.J. Spilker Jr., American Institute of Aeronautics and Astronautics, Inc., Washington DC, pp. 569 - 583.

Spilker, J.J. Jr., (1994d), GPS Signal Structure and Theoretical Performance, *Global Positioning System: Theory and Applications, Vol I, ed*. B.W. Parkinson and J.J. Splileker Jr., American Institute of Aeronautics and Astronautics, Inc., Washington DC, pp. 57 - 119.

Spilker, J.J. Jr. and B.W. Parkinson (1994), Overview of GPS Operation and Design, *Global Positioning System: Theory and Applications, Vol. I*, ed. B.W. Parkinson and J.J. Spilker Jr., American Institute of Aeronautics and Astronautics, Inc., Washington DC, pp. 29-56.

Stephen, J. (2000), Development of a Multi-Sensor GNSS Based Vehicle Navigation System, UCGE Reports No 20140, Department of Geomatics Engineering, The University of Calgary.
(http://www.geomatics.ucalgary.ca/GradTheses.html)

Systron Donner (2000), " BEI MotionPak™ Multi-Axis Inertial Sensing System ", http://www.systron.com/prodinfo/MotPk.html, (2 September, 2000).

Townsend, B. and P. Fenton (1994), A Practical Approach to the Reduction of Pseudorange Multipath Errors in a L1 GPS Receiver, *Proceedings of ION GPS-94*, Salt Lake City, September 20-23, pp. 143-148.

van Dierendonck, A. J., P. Fenton, T. Ford (1992), Theory and Performance of Narrow Correlator Spacing in a GPS receiver, *NAVIGATION: Journal of the Institute of Navigation*, Vol 39. No 3, pp.265-283.

van Nee, R.D.J. (1995), Multipath and Multi-Transmitter Interference in Spread-Spectrum Communication and Navigation Systems, *Delft University Press, Delft, The Netherlands,* 208 pp.

Widnall, W.S. (1972), Enlarging the region of Covariance of Kalman Filters that Encounter Nonlinear Elongation of Measured Range, Proceedings of the AIAA Guidance and Control Conference, August, Stanford CA, pp. 1 – 7.

Weisenburger, S. (1997), Effect of Constraints and Multiple Receivers for On-The-Fly Ambiguity Resolution, *UCGE Reports No 20109*, Department of Geomatics Engineering, The University of Calgary.

Weisenburger.S and C. Wilson (1999), An Integrated Vehicle Positioning System for Safety Applications, *Proceedings of ION NTM-99*, San Diego CA, Jan 25-27, pp 361 – 368. (http://www.geomatics.ucalgary.ca/GradTheses.html)

Wuntronic, "34100 A Theory of Operation", Accelerometer theory of Operation. http://www.wuntronic.de/accelerometer/34_theo.htm, (26 July, 2000).

Zhang, G (1995), A Low Cost Integrated INS/GPS System, *UCGE Reports No 20078*, Department of Geomatics Engineering, The University of Calgary.

Zumberge, J.F. and W.I. Bertiger (1996), Ephemeris and Clock Navigation Message Accuracy, *Global Positioning System: Theory and Applications, Vol. I*, ed. B.W.

Parkinson and J.J. Spilker Jr., American Institute of Aeronautics and Astronautics, Inc., Washington DC, pp. 585-600

APPENDIX A

Derivation of the Design Matrix for Applying Constraints Between Antennas

If the coordinates of the two antennas are (x_1, y_1, z_1) and (x_2, y_2, z_2) then the baseline distance between the two antennas can be expressed as

$$f_{BL} = \sqrt{(x_2 - x_1)^2 + (y_2 - y_1)^2 + (z_2 - z_1)^2} \tag{A.1}$$

The design matrix for this constraint which is of dimension mxu (where u is the number of parameters and m is the number of observations) is given by

$$A = \left[\frac{\partial f}{\partial \phi_1} \frac{\partial f}{\partial \lambda_1} \frac{\partial f}{\partial h_1} \; 0\,0\,0\,0\,0 \; \frac{\partial f}{\partial \phi_2} \frac{\partial f}{\partial \lambda_2} \frac{\partial f}{\partial h_2} \; 0\,0\,0\,0\,0 \ldots\ldots 0 \right] \tag{A.2}$$

Where

$$\begin{aligned} \frac{\partial f}{\partial \phi} &= \frac{\partial f}{\partial x}\frac{\partial x}{\partial \phi} + \frac{\partial f}{\partial y}\frac{\partial y}{\partial \phi} + \frac{\partial f}{\partial z}\frac{\partial z}{\partial \phi} \\ \frac{\partial f}{\partial \lambda} &= \frac{\partial f}{\partial x}\frac{\partial x}{\partial \lambda} + \frac{\partial f}{\partial y}\frac{\partial y}{\partial \lambda} + \frac{\partial f}{\partial z}\frac{\partial z}{\partial \lambda} \\ \frac{\partial f}{\partial h} &= \frac{\partial f}{\partial x}\frac{\partial x}{\partial h} + \frac{\partial f}{\partial y}\frac{\partial y}{\partial h} + \frac{\partial f}{\partial z}\frac{\partial z}{\partial h} \end{aligned} \tag{A.3}$$

If the approximate coordinates of the two antennas are known then the following partial derivatives can be formed (Cannon, 1991):

$$\begin{aligned} \frac{\partial f}{\partial \phi_1} = {} & \frac{-(R_N + h_1)\sin\phi_1 \cos\lambda_1 (x_1 - x_2)}{d_{12}} + \frac{-(R_N + h_1)\sin\phi_1 \sin\lambda_1 (y_1 - y_2)}{d_{12}} \\ & + \frac{[R_N(1 - e^2) + h_1]\sin\phi_1 (z_1 - z_2)}{d_{12}} \end{aligned} \tag{A.4}$$

$$\frac{\partial f}{\partial \phi_2} = \frac{(R_N + h_2)\sin\phi_2\cos\lambda_2(x_1 - x_2)}{d_{12}} + \frac{(R_N + h_2)\sin\phi_2\sin\lambda_2(y_1 - y_2)}{d_{12}} + \frac{[R_N(1-e^2) + h_2]\cos\phi_2(z_1 - z_2)}{d_{12}} \quad \textbf{(A.5)}$$

$$\frac{\partial f}{\partial \lambda_1} = \frac{-(R_N + h_1)\cos\phi_1\sin\lambda_1(x_1 - x_2)}{d_{12}} + \frac{(R_N + h_1)\cos\phi_1\cos\lambda_1(x_1 - x_2)}{d_{12}} \quad \textbf{(A.6)}$$

$$\frac{\partial f}{\partial \lambda_2} = \frac{(R_N + h_2)\cos\phi_2\sin\lambda_2(x_1 - x_2)}{d_{12}} + \frac{(R_N + h_2)\cos\phi_2\cos\lambda_2(x_1 - x_2)}{d_{12}} \quad \textbf{(A.7)}$$

$$\frac{\partial f}{\partial h_1} = \frac{\cos\phi_1\cos\lambda_1(x_1 - x_2)}{d_{12}} + \frac{\cos\phi_1\sin\lambda_1(y_1 - y_2)}{d_{12}} + \frac{\sin\phi_1(z_1 - z_2)}{d_{12}} \quad \textbf{(A.8)}$$

$$\frac{\partial f}{\partial h_2} = \frac{-\cos\phi_2\cos\lambda_2(x_1 - x_2)}{d_{12}} + \frac{-\cos\phi_2\sin\lambda_2(y_1 - y_2)}{d_{12}} + \frac{-\sin\phi_2(z_1 - z_2)}{d_{12}} \quad \textbf{(A.9)}$$

And,

$$R_N = \frac{a}{\sqrt{1 - e^2\sin^2\phi}} \quad \textbf{(A.10)}$$

Where

a is the WGS84 semi-major axis, and

e is the ellipsoidal eccentricity

APPENDIX B

Rotation Matrices

B.1 Definitions

Rotation matrices represent the relationship between the body frame and the navigation frame. The attitude matrix also provides the three orientation parameters namely roll (γ), pitch (υ) and yaw (η). These parameters are illustrated in Figure B.1.

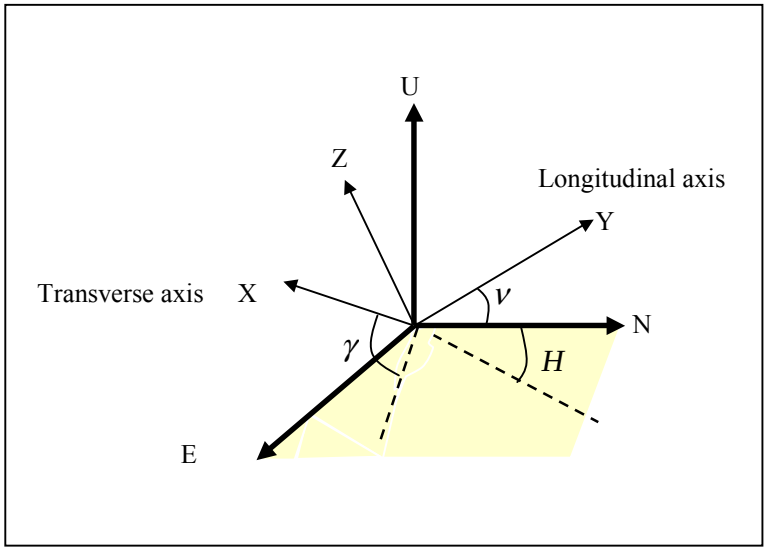

Figure B.1: Attitude parameters

The N, E, U axes in the figure represent the local level coordinate system, whereas the X, Y, Z axes represent the body frame, with the body longitudinal axis coinciding with Y axis.

H represents the heading angle (angle between the projection of the longitudinal axis on the horizontal plane and the North direction). The relationship between the heading angle, azimuth angle, and yaw is shown in Figure B.2.

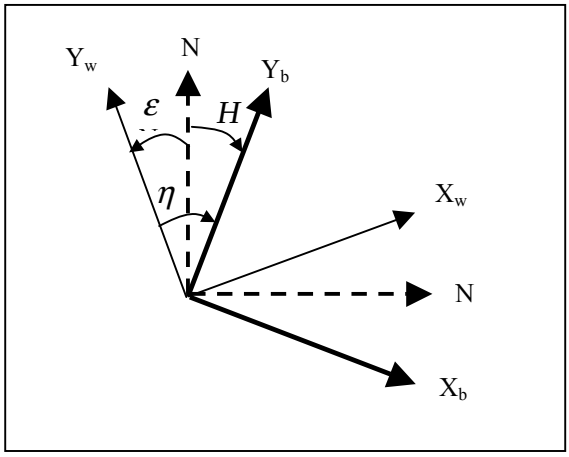

Figure B.2: Definition of heading angle (Salychev, 1998)

Yaw angle (η) is the angle between the projection of the longitudinal axis of the vehicle on the horizontal and the Y-axis of the navigation frame (Salychev, 1998). Clearly from the figure if the navigation frame is local level frame then $H = \eta$ and if wander frame is chosen as the navigation frame then

$$H = \eta - \varepsilon \tag{B.1}$$

Where, ε is the wander angle.

B.2 Direction Cosines

The transformation from the body frame to the navigation frame can be expressed as

$$\begin{bmatrix} x \\ y \\ z \end{bmatrix}_l = R_b^l \begin{bmatrix} x \\ y \\ z \end{bmatrix}_b \tag{B.2}$$

In the Equation B.2 R_b^l is the transformation matrix or the direction cosine matrix from the body frame to the local level frame. If the precise rotation of the body is known then the elements of the matrix can be computed by incrementally transforming the body frame and compute the direction cosine between the axes each time. This is illustrated in the Figure B.3.

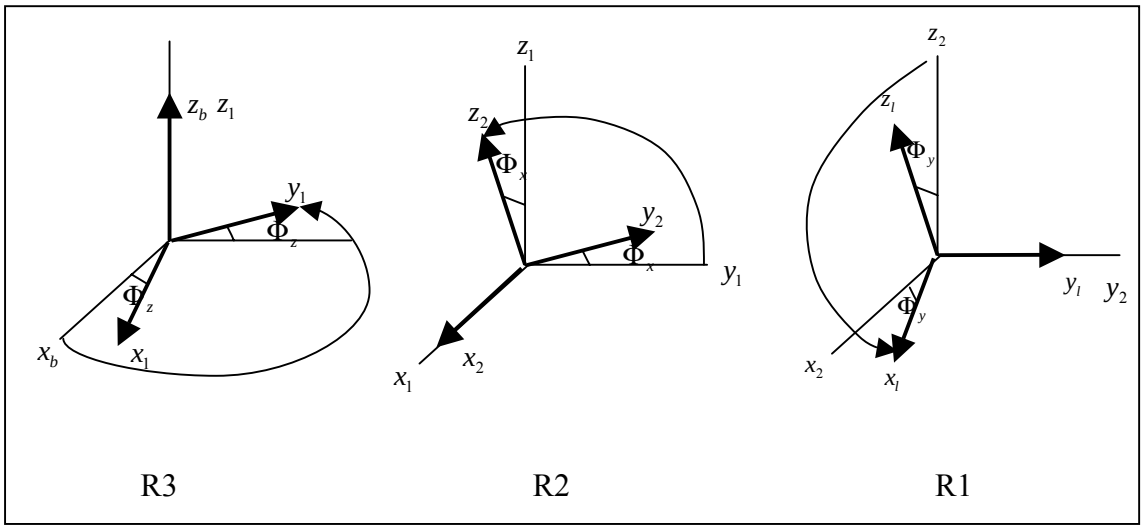

Figure B.3: Sequence of Rotations from Body frame to Local level frame

The individual rotations R3, R2, and R1 can be expressed as (Schwarz, 1998)

$$R3 = \begin{bmatrix} x_1 \\ y_1 \\ z_1 \end{bmatrix} = \begin{bmatrix} \cos\Phi_z & \sin\Phi_z & 0 \\ -\sin\Phi_z & \cos\Phi_z & 0 \\ 0 & 0 & 1 \end{bmatrix}$$

$$R2 = \begin{bmatrix} x_2 \\ y_2 \\ z_2 \end{bmatrix} = \begin{bmatrix} 1 & 0 & 0 \\ 0 & \cos\Phi_x & \sin\Phi_x \\ 0 & -\sin\Phi_x & \cos\Phi_x \end{bmatrix}$$

$$R3 = \begin{bmatrix} x_l \\ y_l \\ z_l \end{bmatrix} = \begin{bmatrix} \cos\Phi_y & 0 & -\sin\Phi_y \\ 0 & 1 & 0 \\ \sin\Phi_y & 0 & \cos\Phi_y \end{bmatrix}$$

Therefore, the total transformation matrix is

$$R_b^l = R_3 R_2 R_1$$

$$R_b^l = \begin{bmatrix} \cos\Phi_z \cos\Phi_y - \sin\Phi_x \sin\Phi_y \sin\Phi_z & \cos\Phi_y \sin\Phi_z \sin\Phi_y & -\cos\Phi_x \sin\Phi_y \\ -\cos\Phi_x \cos\Phi_z & \sin\Phi_z & \sin\Phi_y \cos\Phi_z + \sin\Phi_x \cos\Phi_y \sin\Phi_z \\ \sin\Phi_y \cos\Phi_z + \sin\Phi_z \cos\Phi_y \sin\Phi_z & \sin\Phi_y \sin\Phi_z - \sin\Phi_x \cos\Phi_y \sin\Phi_z & \cos\Phi_x \cos\Phi_y \end{bmatrix}$$

(B.3)

Now, Φ_x, Φ_y, Φ_z can be replaced by the pitch (ϑ), roll (γ) and yaw (η) which are equivalent.

The roll, pitch and yaw can be computed from the R_b^l matrix as

$$\begin{aligned} pitch(\vartheta) &= \tan^{-1}\left(R_b^l(2,3) \Big/ \sqrt{R_b^l(1,3)^2 + R_b^l(3,3)^2}\right) \\ roll(\gamma) &= -\tan^{-1}\left(R_b^l(1,3) / R_b^l(3,3)\right) \\ yaw(\eta) &= \tan -1\left(R_b^l(2,1) / R_b^l(2,2)\right) \end{aligned}$$

(B.4)

The computation of the rotation matrix from the raw angular rate measurements involves parameterization and solution of linear equations. For details refer Salychev (1998), Schwarz (1998), or El-Mowafy (1994).

B.3 Simplified Alignment Equations

If the body frame is closely aligned to the local level frame, then small angle assumptions can be made to the transformation matrix given in equation (B.3).

Therefore,

$$\begin{aligned} \sin\Phi &\cong \Phi \\ \cos\Phi &\cong 1 \end{aligned}$$

(B.5)

Hence, equation (B.3) can be simplified as

$$\begin{bmatrix} 1+\gamma\vartheta\eta & \eta+\gamma\vartheta & -\gamma \\ -\eta & 1 & \vartheta \\ \gamma & -\vartheta & 1 \end{bmatrix} \quad \textbf{(B.6)}$$

Since, γ, ϑ, η is close to zero, the product terms can be neglected. The equation (B.6) can be further simplified to

$$R_b^l = \begin{bmatrix} 1 & \eta & -\gamma \\ -\eta & 1 & \vartheta \\ \gamma & -\vartheta & 1 \end{bmatrix} \quad \textbf{(B.7)}$$

APPENDIX C

Calibration

The low cost sensors used in this research have poor stability and needs calibration every time this sensor is used. The gyro bias calibration procedure explained in this section was performed on the vehicle before beginning the test.

C.1 Sensor Biases

This sections shows the gyro and accelerometer bias when the sensor was mounted on the vehicle. The sensor data was logged for 15 minutes while the vehicle was stationary. Figure C1 shows the gyro biases (sensor output) as measured by the 3 independent sensors.

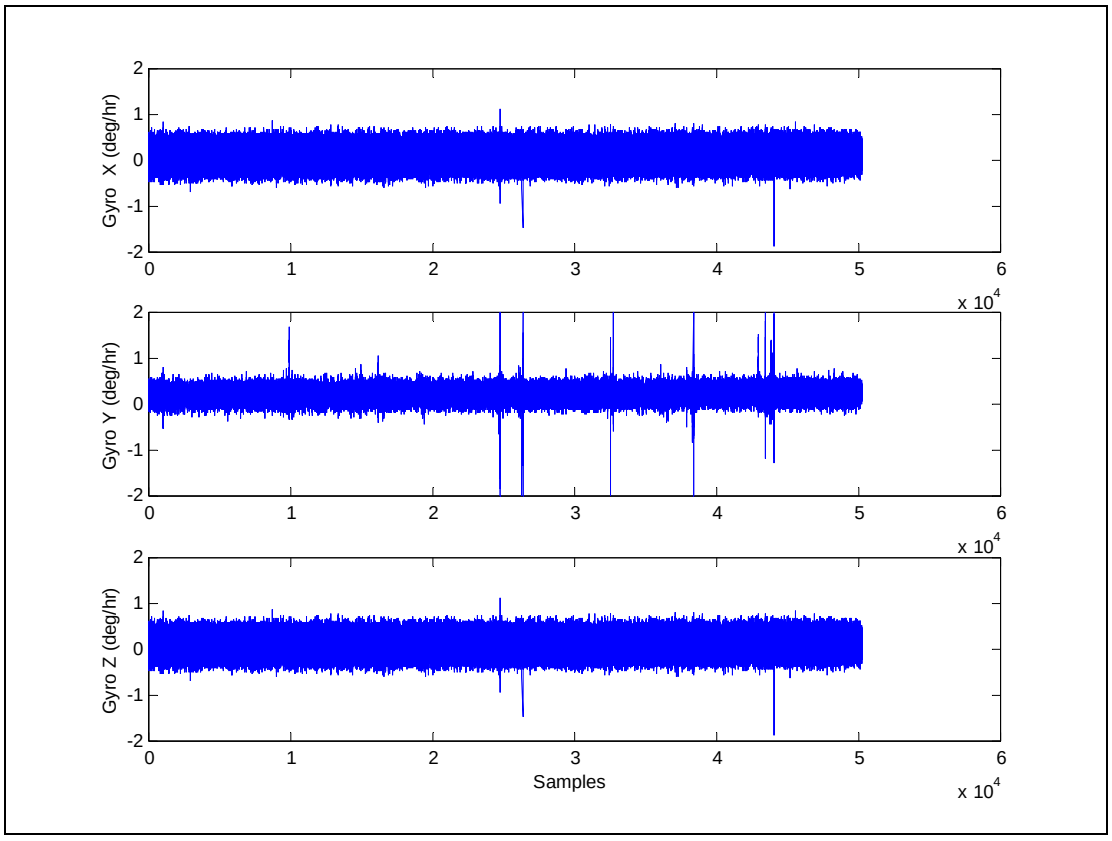

Figure C.1: Gyroscope biases

The data was logged at 50Hz for duration of 15 minutes. The raw gyro measurements have a random nature with some outliers. The averaged gyro bias and the corresponding standard deviation are shown in Table C.1.

Table C.1: Gyro bias

	Gyro Bias (deg/s)	**Standard Deviation (deg/s)**	**Scale factor (deg/v) manufacturer**
X - Axis	0.226	0.205	1/24.893e-3
Y – Axis	0.217	0.196	1/24.843e-3
Z - Axis	0.108	0.295	1/25.028e-3

The gyro bias is a function of temperature and also changes every time the sensor is switched on. The autocorrelation function of the X-axis gyro bias is computed after filtering out the high frequency components. The normalized correlation is shown in Figure C.2. The correlation time 5000 s was observed from the graph. The correlation time can be used to model the gyro drift as a Gauss-Markov process.

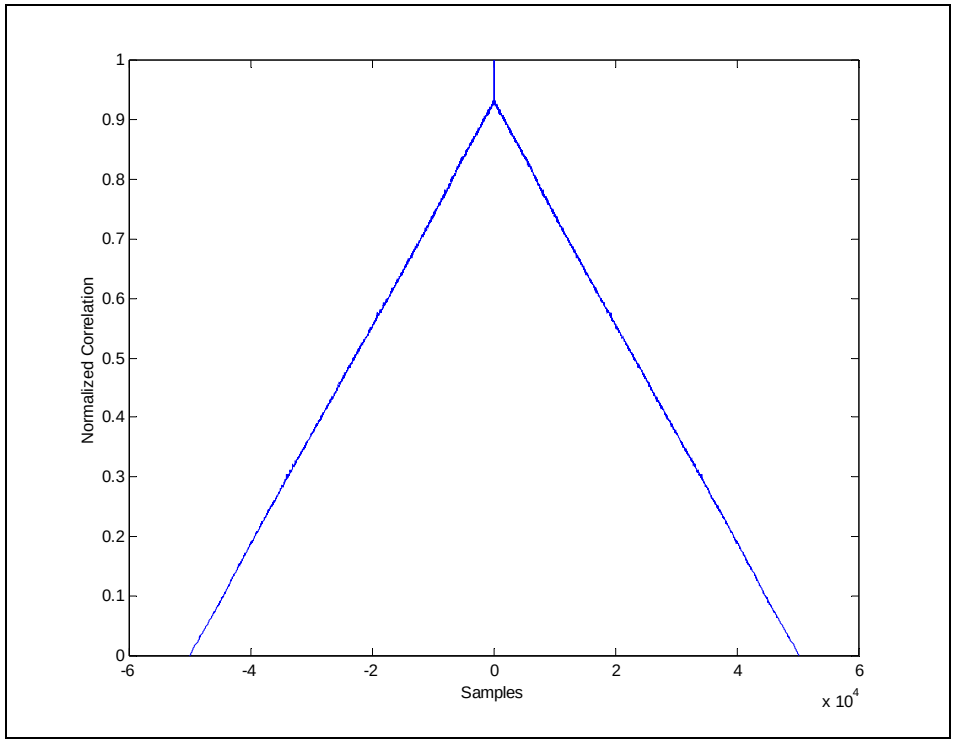

Figure C.2: Autocorrelation of the X-axis gyro measurements

The raw accelerometer measurements in all 3 axes are shown in Figure C.3.

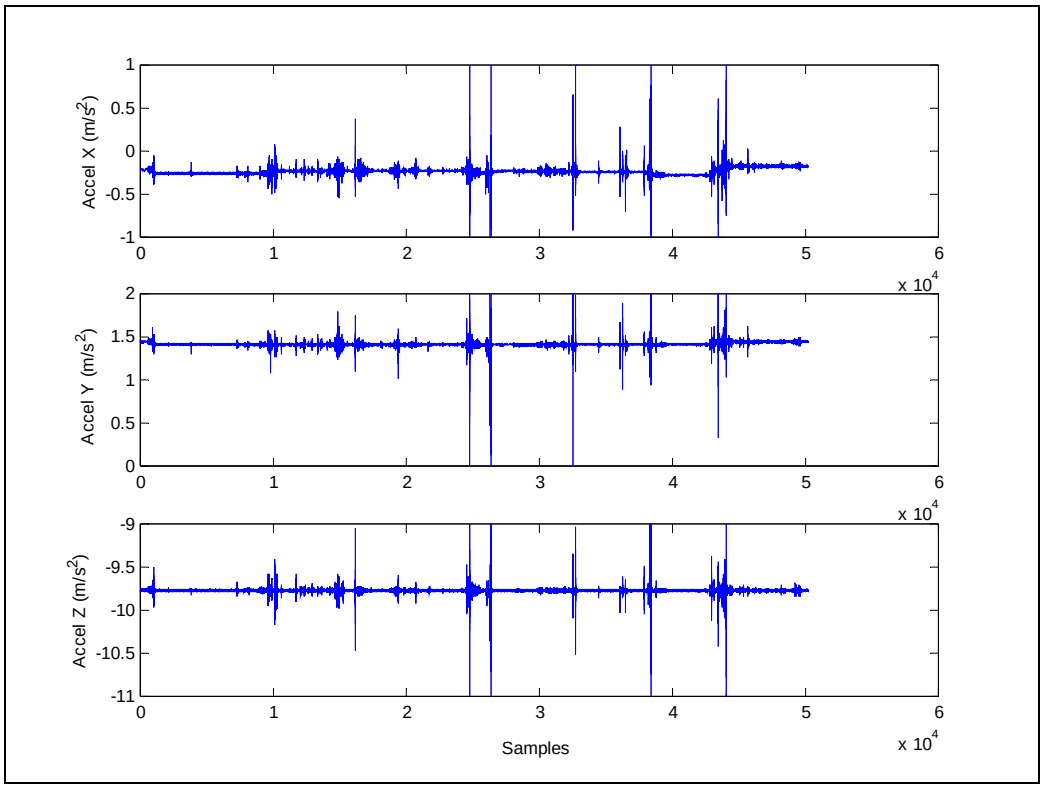

Figure C.3: Accelerometer measurements

The accelerometer shows a larger bias but has smaller standard deviation compared to the Gyro measurements. The results are tabulated in Table C.2, which are basically for the case when IMU is in static mode and include the gravity components due to non levelled body frame in them.

Table C.2: Accelerometer bias

	Accelerometer Bias (m/s^2)	**Standard Deviation (m/s^2)**
X - Axis	-0.234	0.055
Y – Axis	1.414	0.032
Z - Axis	-9.773	0.043

The autocorrelation of the raw accelerometer measurement is shown in Figure C.4.

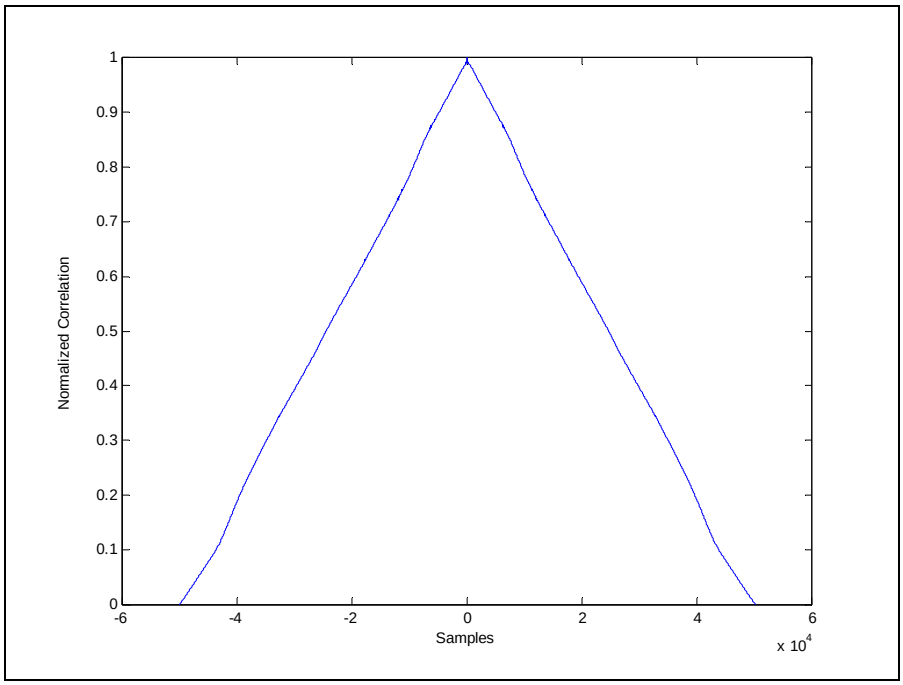

Figure 7.1: Autocorrelation of X-axis accelerometer

The accelerometer bias and scale factor calibration was performed in the lab as described in Salychev (1998) and the results are shown in Table C.3.

Table C.3: Accelerometer bias and scale factors

	Accelerometer Bias (mg)	**Accelerometer Scale factor (mg)**
X – Accelerometer	-46.61	2.84
Y – Accelerometer	-24.51	3.08
Z - Accelerometer	5.44	2.55

The accelerometer bias, scale factor and the gyro scale factor values computed from the lab test was determined to understand these errors, and was not used in the test. However, the values provided by the manufacturer were used in the test. These values are much different from the results in Table C.2 as in the lab the gravity component is eliminated by rotating the sensor in various directions.

APPENDIX D

Additional Results

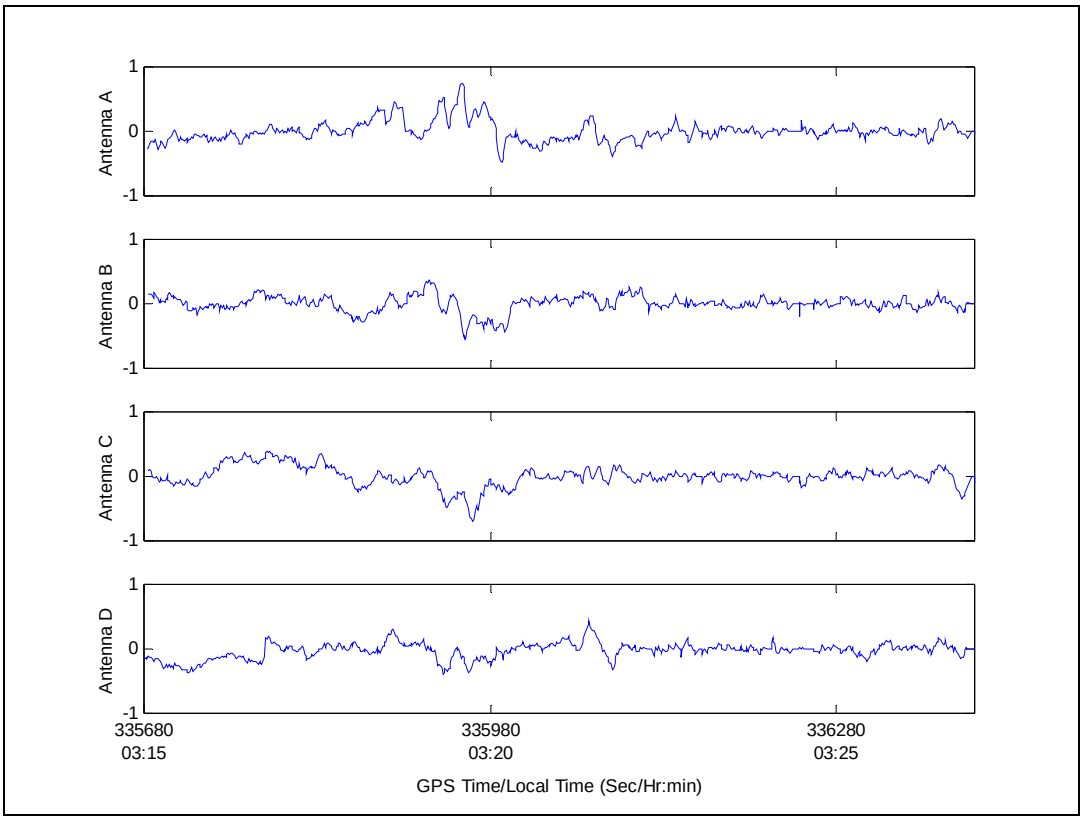

Figure D.1: Code minus carrier differences (SV – 23),Elevation (88° - 64°)–Section 1

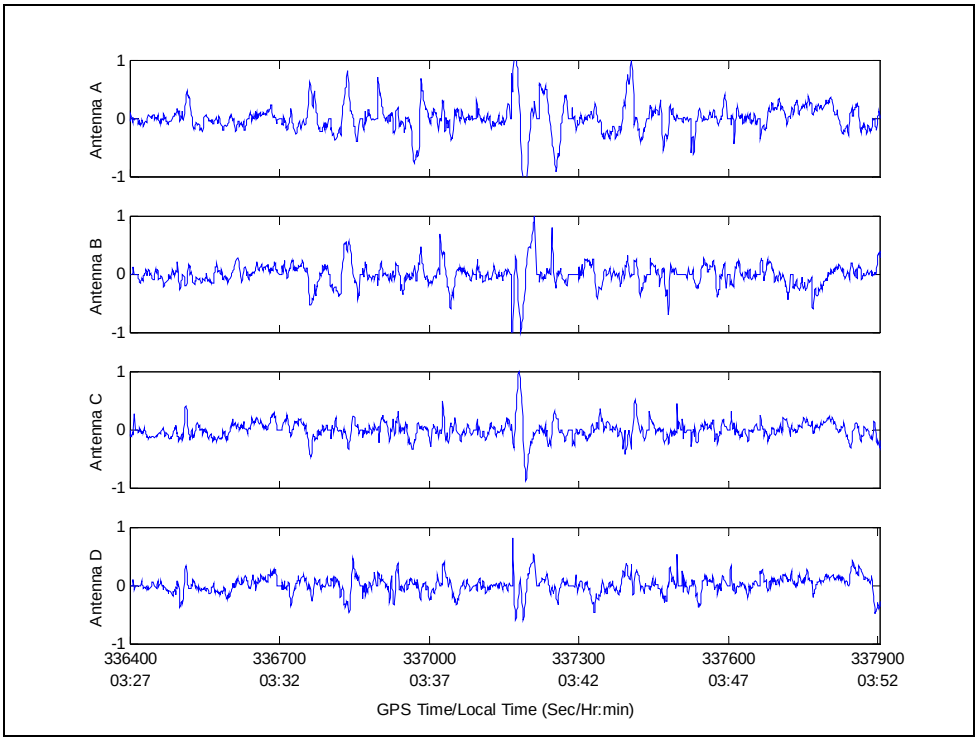

Figure D.2: Code minus carrier differences (SV – 23),Elevation (88° - 64°)–Section 2

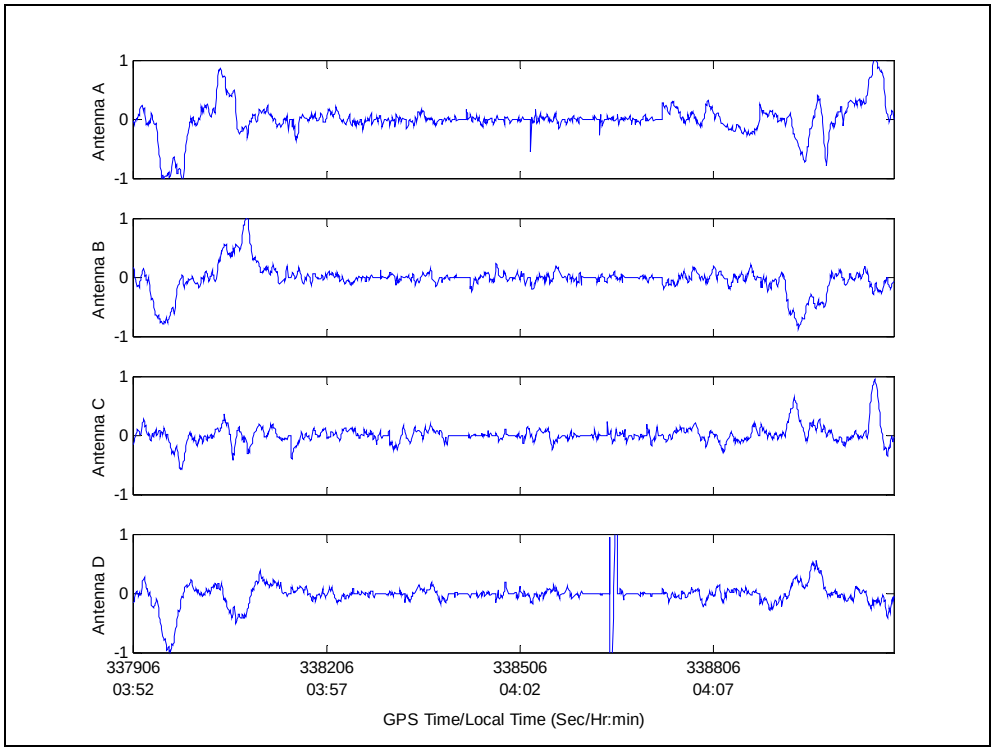

Figure D.3: Code minus carrier differences (SV – 23),Elevation (88° - 64°)–Section 3

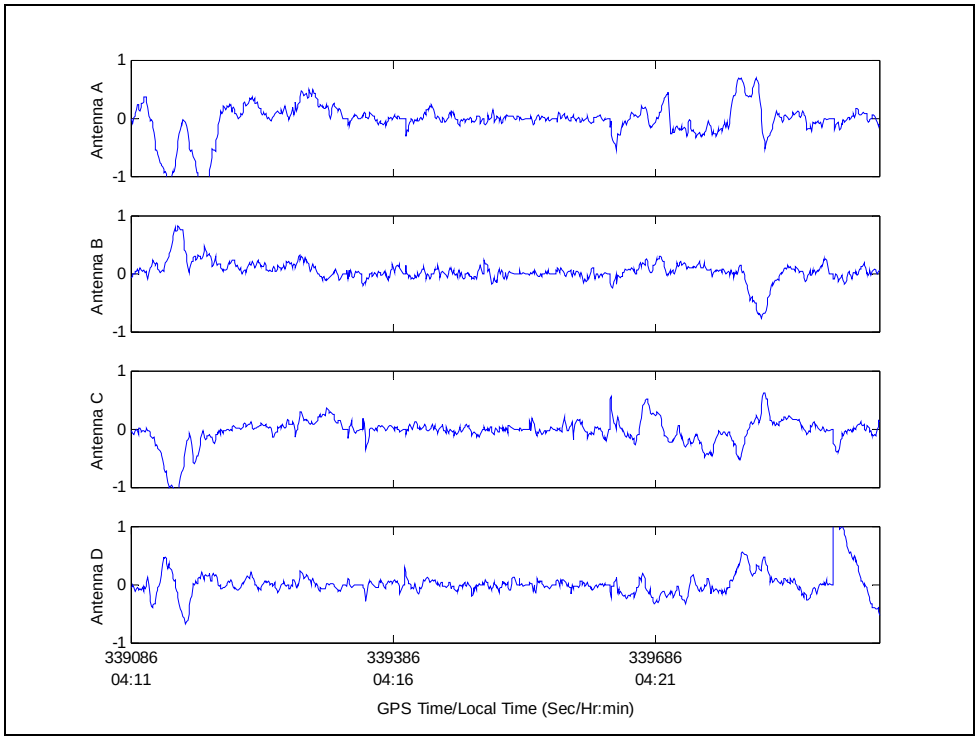

Figure D.4: Code minus carrier differences (SV – 23),Elevation (88° - 64°)–Section 4

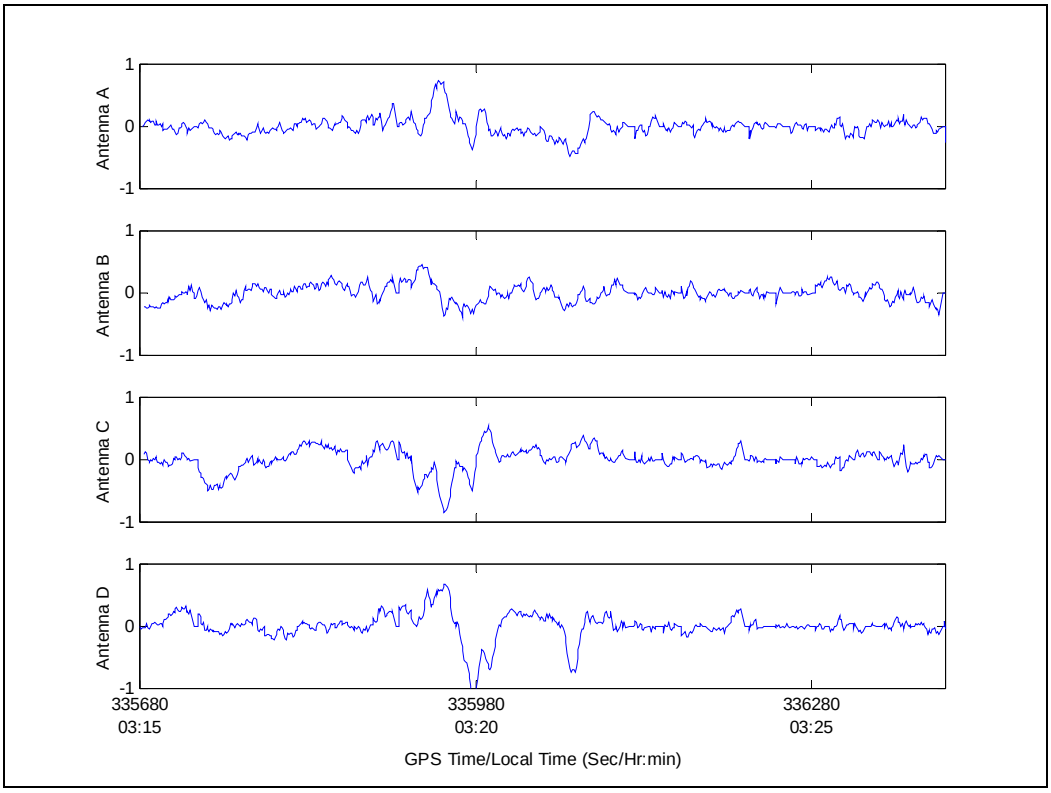

Figure D.5: Code minus carrier differences (SV – 3),Elevation (46° - 41°)–Section 1

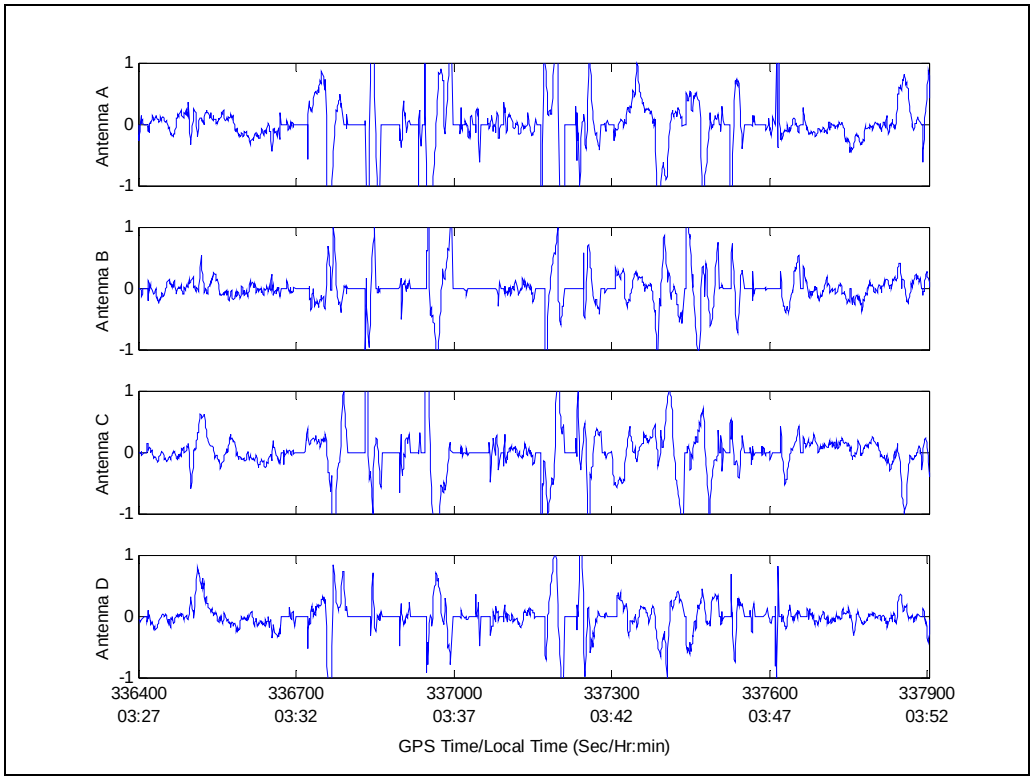

Figure D.6: Code minus carrier differences (SV – 3),Elevation (46° - 41°)–Section 2

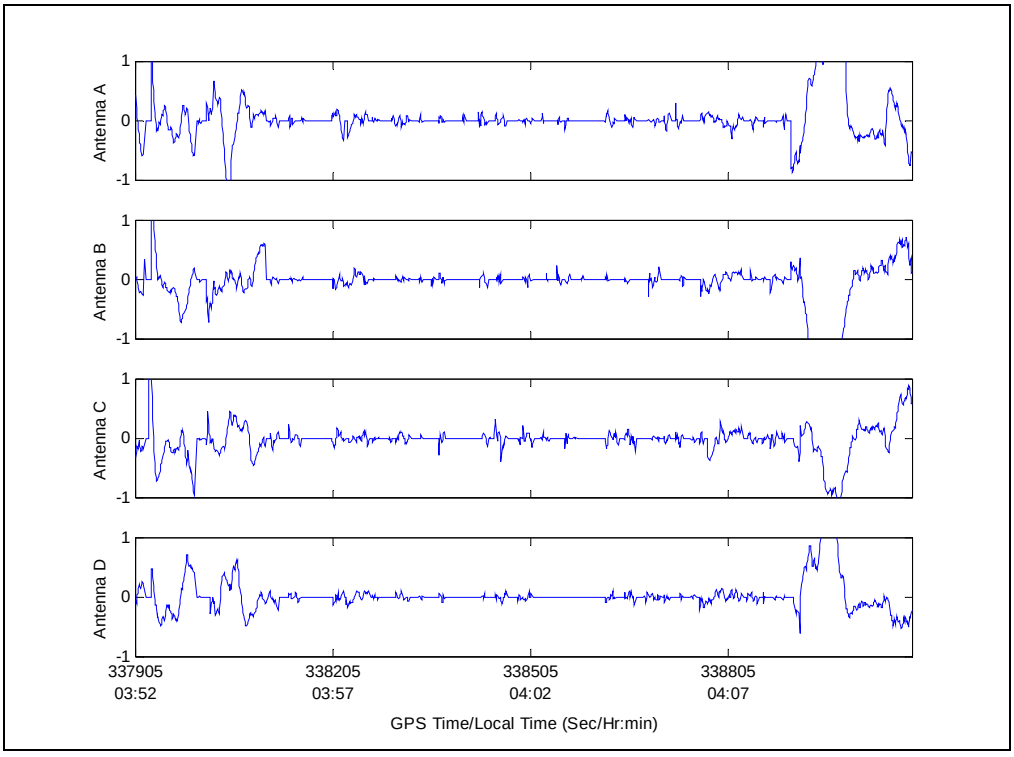

Figure D.7: Code minus carrier differences (SV – 3),Elevation (46° - 41°)–Section 3

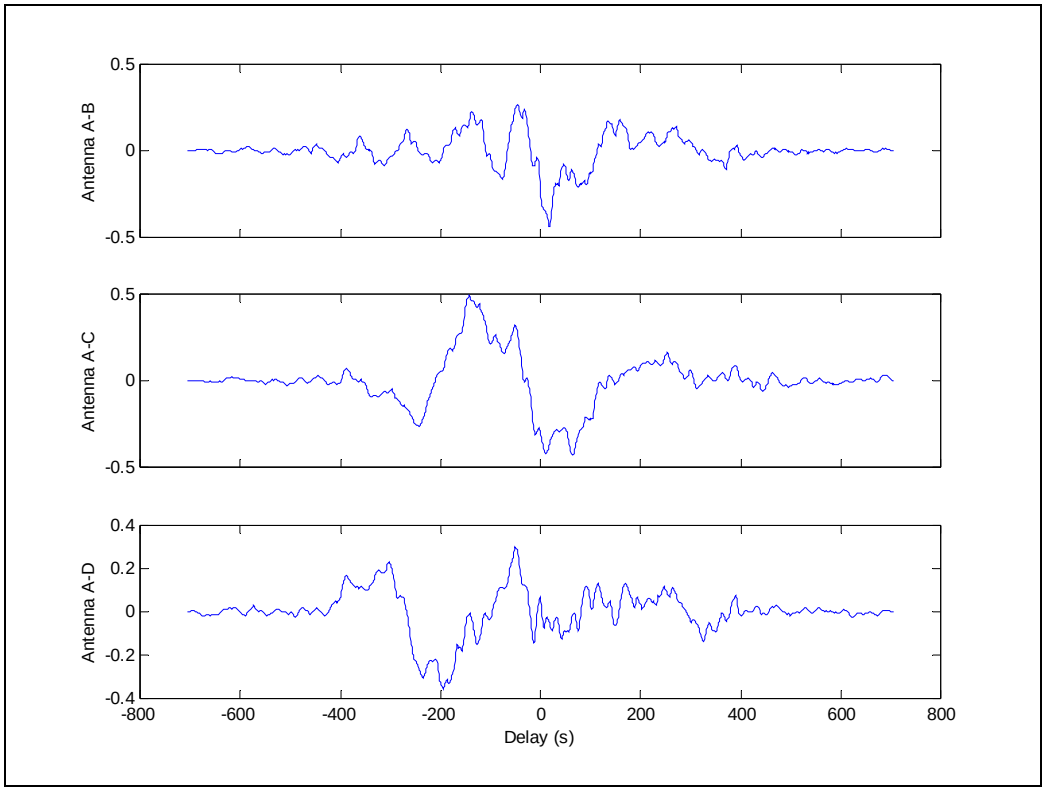

FigureD.8: Correlation coefficient (SV – 23), Elevation (88° - 64°) - Section 1

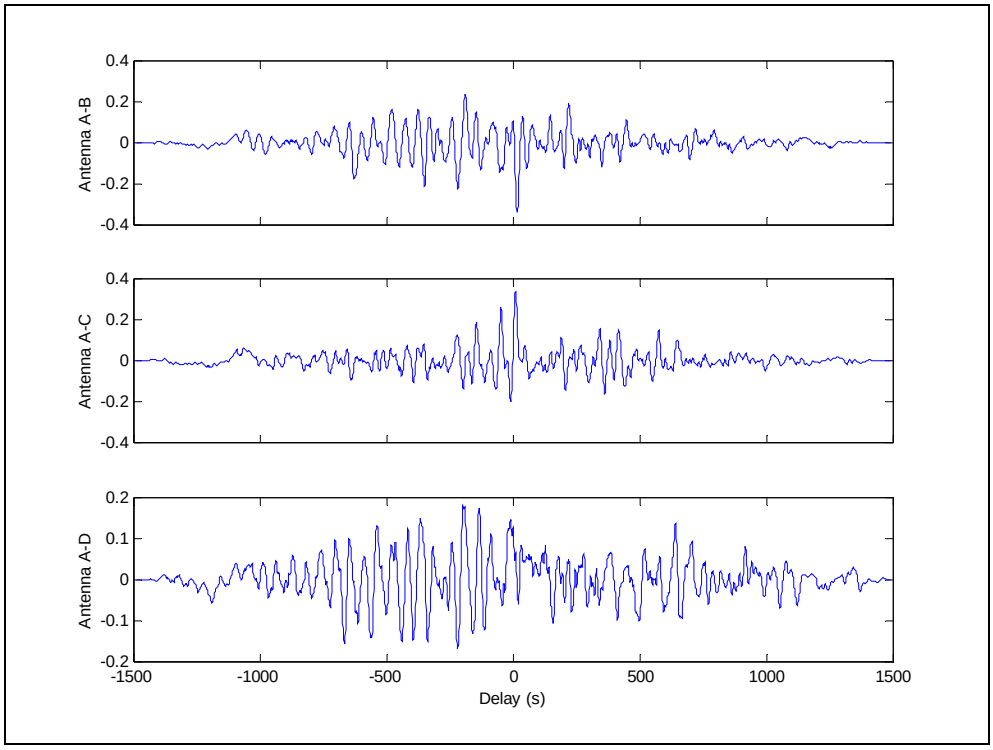

Figure D.9: Correlation coefficient (SV – 23), Elevation (88° - 64° - Section 2

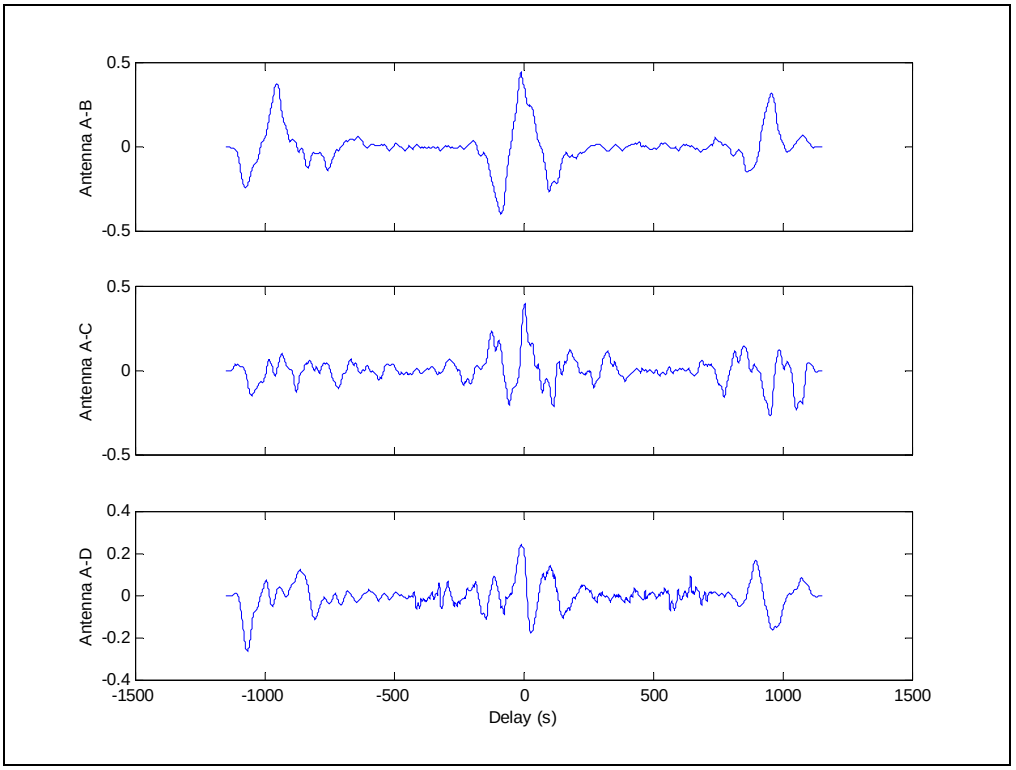

Figure D.10: Correlation coefficient (SV – 23), Elevation (88° - 64°) - Section 3

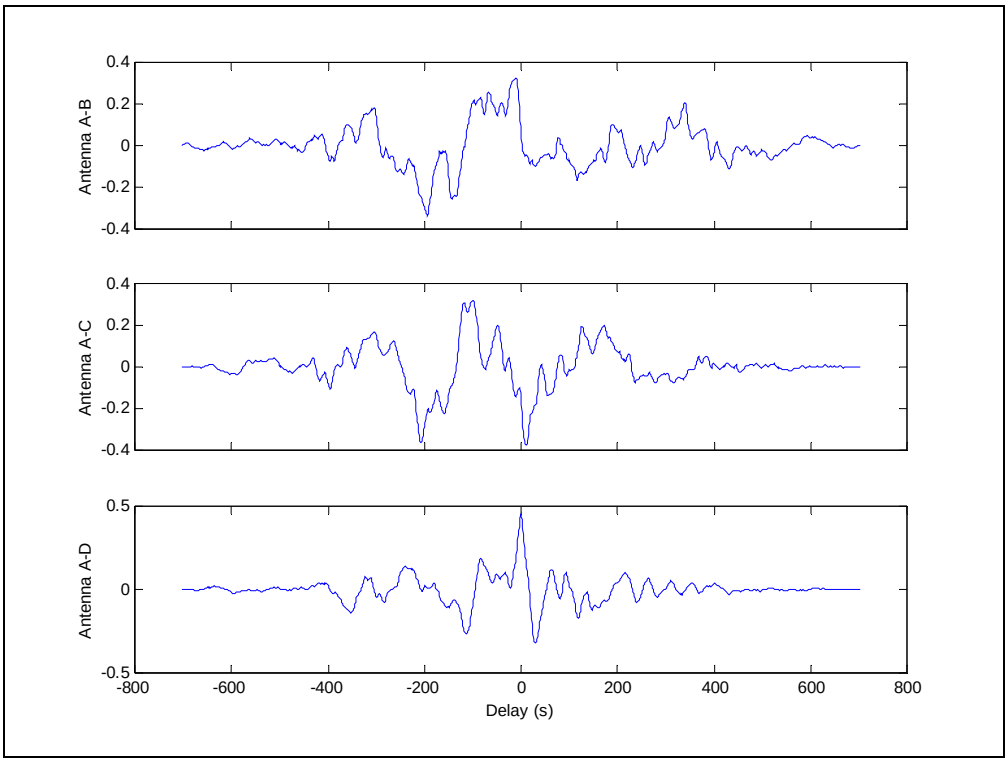

Figure D.11: Correlation coefficient (SV – 3), Elevation (46° - 41°) - Section 1

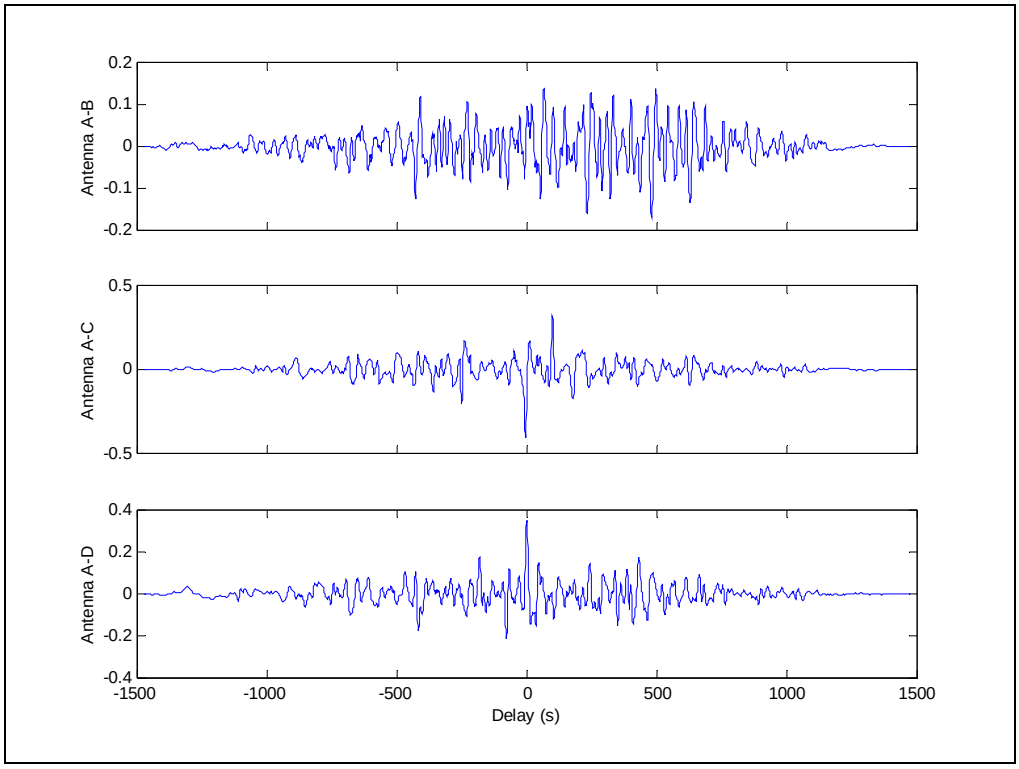

Figure D.12: Correlation coefficient (SV – 3), Elevation (46° - 41°) - Section 2